A New Atomistic Simulation Framework for Mechanochemical Reaction Analysis of Mechanophore Embedded Nanocomposites

by

Bonsung Koo

A Dissertation Presented in Partial Fulfillment
of the Requirements for the Degree
Doctor of Philosophy

Approved February 2017 by the
Graduate Supervisory Committee:

Aditi Chattopadhyay, Chair
Lenore Dai
Hanqing Jiang
Yang Jiao
John Rajadas

ARIZONA STATE UNIVERSITY

May 2017

ABSTRACT

A hybrid molecular dynamics (MD) simulation framework is developed to emulate mechanochemical reaction of mechanophores in epoxy-based nanocomposites. Two different force fields, a classical force field and a bond order based force field are hybridized to mimic the experimental processes from specimen preparation to mechanical loading test. Ultra-violet photodimerization for mechanophore synthesis and epoxy curing for thermoset polymer generation are successfully simulated by developing a numerical covalent bond generation method using the classical force field within the framework. Mechanical loading tests to activate mechanophores are also virtually conducted by deforming the volume of a simulation unit cell. The unit cell deformation leads to covalent bond elongation and subsequent bond breakage, which is captured using the bond order based force field. The outcome of the virtual loading test is used for local work analysis, which enables a quantitative study of mechanophore activation. Through the local work analysis, the onset and evolution of mechanophore activation indicating damage initiation and propagation are estimated; ultimately, the mechanophore sensitivity to external stress is evaluated. The virtual loading tests also provide accurate estimations of mechanical properties such as elastic, shear, bulk modulus, yield strain/strength, and Poisson's ratio of the system. Experimental studies are performed in conjunction with the simulation work to validate the hybrid MD simulation framework. Less than 2% error in estimations of glass transition temperature (Tg) is observed with experimentally measured Tgs by use of differential scanning calorimetry. Virtual loading tests successfully reproduce the stress-strain curve capturing the effect of mechanophore inclusion on mechanical properties of epoxy polymer; comparable changes in Young's modulus and yield strength are observed

in experiments and simulations. Early damage signal detection, which is identified in experiments by observing increased intensity before the yield strain, is captured in simulations by showing that the critical strain representing the onset of the mechanophore activation occurs before the estimated yield strain. It is anticipated that the experimentally validated hybrid MD framework presented in this dissertation will provide a low-cost alternative to additional experiments that are required for optimizing material design parameters to improve damage sensing capability and mechanical properties.

In addition to the study of mechanochemical reaction analysis, an atomistic model of interphase in carbon fiber reinforced composites is developed. Physical entanglement between semi-crystalline carbon fiber surface and polymer matrix is captured by introducing voids in multiple graphene layers, which allow polymer matrix to intertwine with graphene layers. The hybrid MD framework is used with some modifications to estimate interphase properties that include the effect of the physical entanglement. The results are compared with existing carbon fiber surface models that assume that carbon fiber has a crystalline structure and hence are unable to capture the physical entanglement. Results indicate that the current model shows larger stress gradients across the material interphase. These large stress gradients increase the viscoplasticity and damage effects at the interphase. The results are important for improved prediction of the nonlinear response and damage evolution in composite materials.

This dissertation is dedicated to my parents, Mr. Ja-Keon Koo, Ms. Ui-Shin Kim, and

mother-in-law, Ms. Song-Sik Song

as well as

my wife Tae-Kyoung Kang, son David Hyun-Mo Koo, and daughter Hannah Koo,

for love, support, and encouragement that helped me reach here.

ACKNOWLEDGMENTS

Completion of the research presented in this dissertation was the result of efforts by many people to whom I owe much appreciation. The advice, encouragement, and challenge provided by my advisor, Regents' Professor Aditi Chattopadhyay, has developed in me a passion for research and allowed me to achieve my academic goals. I am sincerely grateful for her supervision and support throughout my doctoral studies. I would also like to thank the members of my supervisory committee, Prof. Lenore Dai, Prof. Hanqing Jiang, Prof. Yang Jiao, and Prof. John Rajadas for volunteering their time to provide valuable insight and advice in regards to my research.

I have had the pleasure of working with every person that has been a part of Prof. Chattopadhyay's group and Prof. Dai's group at ASU, and I would like to specifically thank those including Nithya Subramanian, Ashwin Rai, Siddhant Datta, Christopher Sorini, Guoyi Li, Ryan Gunckel, and Drs. Elizabeth Nofen, Jinjun Zhang, Joel Johnston, Luke Borkowski, Jin Zou, Rajesh Neerukatti, Inho Kim, Yingtao Liu.

I would like to acknowledge the financial support from the Army Research Office, Grant Number W911NF1510072, Program Manager Dr. David Stepp and the Air Force Office of Scientific Research, grant number FA9550-12-1-0331, Program Manager Dr. David Stargel.

Last but not least, I thank God the Father for allowing me to meet all these people, sustaining my family and me each and every day, and making all these things possible.

TABLE OF CONTENTS

Page

LIST OF TABLES

Table Page

Table Page

LIST OF FIGURES

Figure Page

Figure Page

Figure Page

Figure Page

Figure Page

Figure Page

Figure Page

Figure Page

Figure Page

Figure Page

Figure Page

Figure Page

CHAPTER

1. INTRODUCTION

1.1. Motivation and Background

Polymer matrix composites (PMCs) are being increasingly used today for primary load carrying structures in industrial, civil, and military applications. PMCs have several advantages over traditional metallic structures, such as strength, lightweight, tailorable mechanical properties, and resistance to environmental effects [1]. However, PMCs present challenges in terms of the design, maintenance, and repair due to strong heterogeneity. Although the primary constituents in PMCs (such as fiber and matrix material) have been successfully characterized, the interphase region between fiber and the polymer matrix, on the other hand, is still not well-understood and can lead to complex material response [2].

Damage detection is a particularly challenging problem in PMCs, which due to their heterogeneous structure, are susceptible to a wide range of failure mechanisms, such as matrix cracking, fiber failure, fiber pullout, and intra/interlaminar failure, thereby limiting their optimal potential as load bearing materials. As such, detection and quantification of damage in PMCs has become an important and highly fertile area of research. Several researchers have investigated the use of surface bonded or embedded transducers to detect in situ damage in PMC structures[3-6]. Sohn et al. [3] demonstrated a method to detect delamination in multilayer composites by combining two techniques, piezoelectric transducer (PZT) and laser Doppler vibrometer. Hiche et al. [4] used fiber Bragg grating (FBG) sensors with PZT in another study to locate low energy impact damage on PMC; here, PZT generates the waves and FBG sensors are used to capture the waves. The impact

damages were then identified by monitoring distortion in the propagated waves. In yet another study, a piezoelectric paint sensor was developed to detect damage precursors by checking voltage changes [5].

The primary focus of the above studies, however, has been the development of sensors and sensing technologies suitable for macroscopic damage detection. However, detection of microscale damage, and, more important, understanding damage initiation and precursors remain a critical area of research. Since damage initiation typically occurs at the molecular level [7-9], there is a growing need for nanoscale sensing technologies that can offer valuable advantages in damage precursor detection. Carbon nanotube (CNT)-based membrane (also known as buckypaper) has been reported as a nanoscale strain sensor for composite materials [10]. CNTs have been used to detect damage initiation by measuring the change in electrical resistance of single-lap composite joint during the mechanical loading test [11]. However, the effect of CNTs' type, distribution, alignment, and volume fraction on electrical resistance should be addressed clearly for practical usage. Recently, mechanophores or force-sensitive molecular units, have been developed, which can offer remarkable nanoscale damage detection capabilities [12-16]. When external mechanical loading is applied to mechanophores, the resulting deformation of the molecular structures of the mechanophores and subsequent change in the material property is manifested in the mechanophores' change in color. A color change in the mechanophore-embedded nanocomposites can potentially indicate the initiation of damage in the system. Different types of mechanophores have been implemented experimentally and have demonstrated damage detection capability by emitting fluorescence during mechanical loading tests [12, 13].

Despite the experimental implementation of the mechanophore embedded composites, there is still a strong need for developing physics-based models of these novel materials because existing spectroscopic techniques do not adequately capture the nanoscale phenomena. The development of such models to simulate the nanoscale material behavior is highly desirable to improve our understanding of both the mechanochemical reaction in the composites as well as the interaction between host material and mechanophores. An accurate physics-based model will not only help to optimize the design process, but also add to our seminal understanding of damage precursors and propagation in PMCs, as well as serve as an alternative to existing experimental limitations.

The focus of this dissertation is to develop a molecular dynamics (MD) simulation framework that mimics the entire experimental process, from specimen synthesis to a range of experiments for analyzing material properties. This new framework will require accurate simulation of the mechanochemical reaction of mechanophores, along with an epoxy curing process and nanoscale damage initiation/evolution, in conjunction with covalent bond breakage. To develop the framework, two different mechanophores, cyclobutane- and anthracene-based mechanophores are used. These mechanophores are synthesized and incorporated experimentally into an epoxy-based thermoset polymer matrix, and then are modeled and simulated in this work using the MD method. Material properties, such as thermal and mechanical response, are analyzed using a range of assessment tools, including differential scanning calorimetry (DSC), dynamic mechanical analyzer (DMA), and mechanical load frame. The experimental results are also used to validate the modeling and simulation methodology. In addition to the mechanophore embedded nanocomposite model, a molecular model of fiber/matrix interphase is developed to capture the dynamic

behavior of the interphase region of PMCs by extending the MD simulation framework. The physics-based molecular model of fiber/matrix is expected to provide reasonable estimations of the material responses of the interphase region, which is critical to understanding damage initiation and propagation in the composites. Existing studies related to mechanophores, both experimental and computational, are discussed in the following sections.

1.1.1. Mechanophores

Mechanophores are molecular units that respond to an external force by emitting fluorescence from deformed molecules resulting from their covalent bond breakage. A natural application of these materials, therefore, is in structural health monitoring, with emphasis on understanding damage initiation. The covalent bond breakage at the nanoscale activates the mechanophores, resulting in a fluorescent emission, which can be used as an indication of impending material failure prior to damage propagation to the higher length scales. Crenshaw et al. [17] studied a mechanophore which has a unique activation mechanism wherein it is not activated by covalent bond breakage, but rather changes color due to the electronic distribution between dye molecules. This type of mechanophore depends on changes in physical molecular packing modes, and can be used as strain sensors. In the same study, Crenshaw and co-workers also demonstrated that tensile loading can lead to substantial changes in the molecular packing, resulting in changes in luminescent properties in the mixture of linear low-density polyethylene (LLDPE) and two dye molecules, (1,4-bis(R-cyano-4-methoxystyryl)-2,5-dimethoxybenzene (BCMDB) and 1,4-bis(R-cyano-4-meth- oxystyryl)benzene (BCMB): two mixtures, LLDPE/BCMDB and

LLDPE/BCMB. Figure 1.1 shows the fluorescent emission from these mechanophores under excitation with ultraviolet (UV) light of a wavelength of 365 nm. However, these mechanophores cannot be considered good candidates for sensing damage growth in PMCs since their activation mechanism does not require covalent bond breakage.

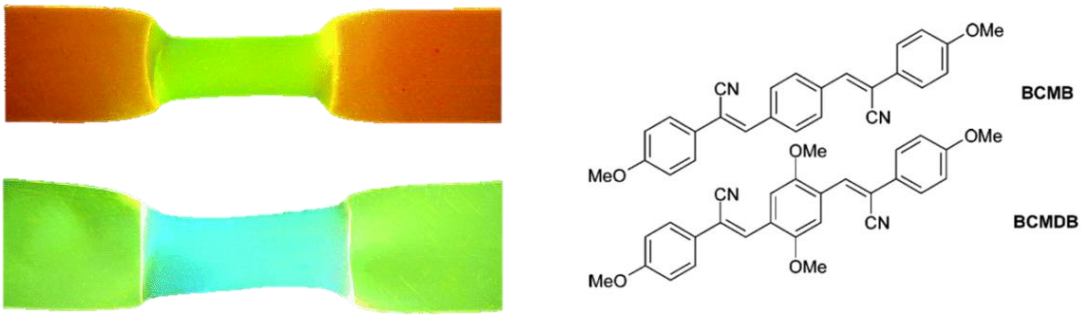

(a) (b)

Figure 1.1. (a) Picture of LLDPE with BCMB (top) / BCMDB (Bottom) and (b) Chemical Structure of Dye Molecules[17].

In the literature, there are examples of mechanophores that have been activated by covalent bond breakage, and as such, are suitable as crack sensors for composite structures. Chen et al. [18] showed luminescence at very low stress level using polymers that incorporated the bis(adamantly)-1,2-dioxetanes mechanophore unit as a way to convert mechanical energy into optical energy by opening the dioxetane ring. As shown in Figure 1.2, the molecular structure of the mechanophore is seen to change, followed by a change in color as the specimen deforms. Since the luminescence color can be changed by suitable acceptors with different wavelengths, this mechanophore can be a potentially effective

stress or strain range indicator. However, in Chen's study, the luminescence was seen to fade away quickly, thus limiting the observation time, and in turn restricting its capabilities in damage sensing applications.

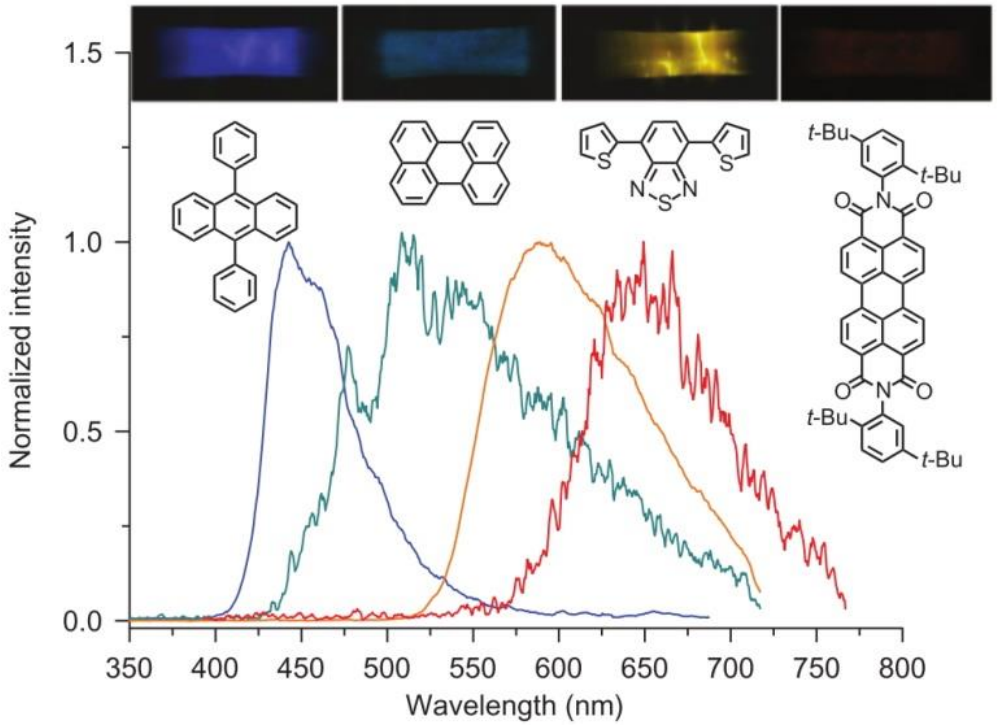

Figure 1.2. Mechanically Induced Decomposition of a Polymeric 1-2 Bis(Adamantyl) Dioxetane and Color Spectrum According to the Deformed Molecular Structure During Mechanical Loading Test [18].

Pyran-based mechanophores, such as spiropyrans, spirooxazines, and naphthopyrans that change color when light conditions change, have also been studied in several works [19-21]. Although the pyran-based mechanophores have exhibited molecular transformations by changing from a colorless form to a colored form due to

photodegradation of a specific functional group, they are considered inadequate for sensing and detecting mechanically induced damage. In a recent study, Davis et al. [14] grafted spiropyran molecules to thermoplastic polymer chains, which act as force sensors in response to the external mechanical loading, thus successfully developing mechanically activated spiropyran molecules. Fluorescence emission was observed with the application of tensile loading to the spiropyran embedded thermoplastic polymer. During the mechanical loading test, the transferred local force was observed to induce oxygen-carbon covalent bond dissociation, which transforms colorless spiropyran into colored merocyanine, as shown in Figure 1.3. Since fluorescence from merocyanine is visible to the naked eye, researchers have used it in various elastomeric or thermoplastic polymer systems such as poly(methyl methacrylate) (PMMA) [22], and poly(dimethylsiloxane) (PDMS) [23]. However, to observe fluorescence from merocyanine, the spiropyran-based mechanophore polymers need large deformations (> 200 % strain), which is well beyond yield strain, making the system infeasible for damage precursor detection.

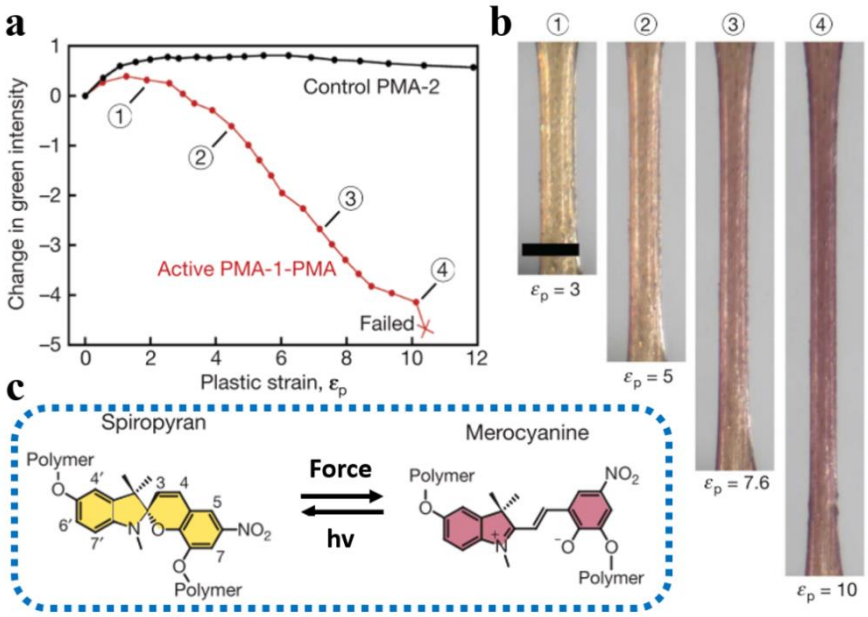

Figure 1.3. (a) Accumulation of Plastic Strain and Relative Change in Green Intensity for Two Samples: One with Spiropyran and the Other One without, (b) Optical Images of the Sample with Spiropyran After the Loading Cycles Indicated in Inset **a**, and (c) Schematic of a Hypothesized Conversion Between the Colourless Spiropyran and Coloured Merocyanine Forms [14].

Cycloalkane-based mechanophores developed through UV photodimerization have also been explored for damage sensing applications. Cyclobutane rings formed from cycloaddition of the cinnamoyl groups can act as mechanophore units. The cyclobutane ring reverts back to monomeric fluorescent cinnamoyl group after damage occurs in the polymeric system (see Figure 1.4 [16, 24, 25]). The strained cyclobutane ring structure is used as mechanophores to produce a mendable poly(butylene adipate) network through functionalization with cinnamoyl groups [26] and to quantify the effect of acoustic stimulations on the mechanophore activation using monocyano and dicyano-substituted cyclobutanes [27, 28].

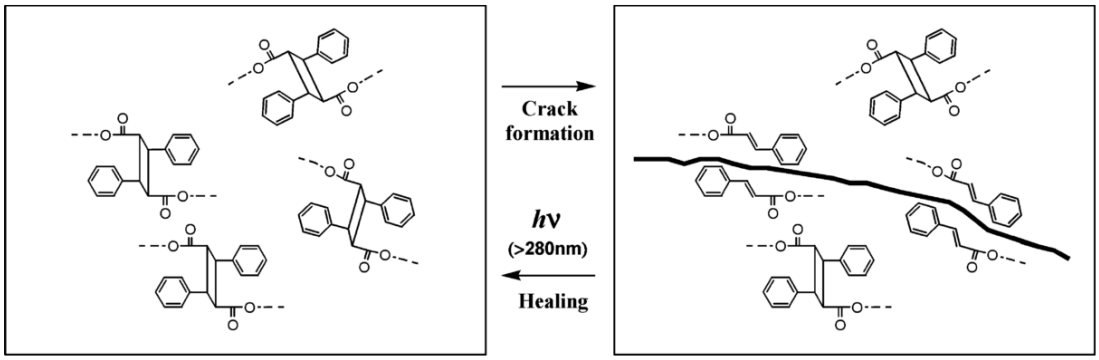

Figure 1.4. Schematic Showing Polymerized Cyclobutane Mechanophores Before an Applied Force/Crack (Left), Reversion to Fluorescent Cinnamoyl Groups along Damaged Area/Crack (Right), and Healing to the Left Image under UV Light [16, 25].

Anthracene, consisting of three fused benzene rings, has been also a commonly used as a fluorescent component to quantify the extent of mechanical damage by emitting fluorescence in quartz [29, 30]. Under the UV light, anthracene derivatives can be photodimerized into several different structures, for example, some for self-healing [31] and others for shape memory applications [32]. In a few recent studies, anthracene molecules have been used as damage precursors as they have significantly higher absolute fluorescence quantum yield compared to other mechanophores, which brings the excitation/emission to longer wavelengths, and thus enables visible light emission [33]. Two cyclooctane-based polymers, dimerized from poly(9-anthraldehyde) and poly(9-anthracenecarboxylic acid), have been successfully utilized as crack sensors in poly(vinyl alcohol) coatings, as seen in Figure 1.6 [15].

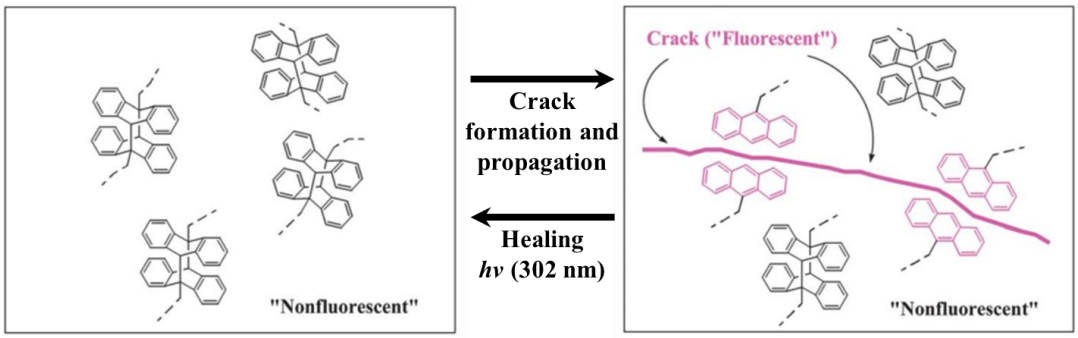

Figure 1.5. Schematic of Crack Sensor Activation Mechanism using Anthracene-Based Mechanophore [15].

It is worth noting that the previously mentioned work on spiropyran, cyclobutane, and anthracene as mechanophores involves thin films, elastomeric, or thermoplastic matrices; in other words, there has been limited study of mechanophores within thermoset polymer systems and engineering composites such as PMCs [34-36]. Additionally, the damage precursor or early damage signal detection capability of mechanophores, critical to determining the course of maintenance *before* catastrophic failure occurs, has not been addressed successfully in these works. For early damage detection, it is important to detect the anomaly in the system (structure) before the yield point. Therefore, mechanophores that undergo covalent bond breakage before the yield point are considered more appropriate for the damage precursor detection scenario in which the molecular deformation due to external mechanical loading can be hypothesized to represent impending material damage.

In this work, cycloalkane-based mechanophores, activated via cycloreversion upon damage to yield fluorescent signals are the chosen damage sensors. As part of the first stage of this research, experiments were conducted focused on incorporating cyclobutane-based

mechanophore into epoxy-based thermoset polymer. The cyclobutane-based mechanophore, a tris(cinnamoyloxymethyl) ethane (TCE) polymer, was formed by UV dimerization, transforming cinnamoyl groups into the cyclobutane rings [12]. The fluorescent signals achieved in this cyclobutane-based mechanophore occurred after the yield point. Thus, another mechanophore, dimeric (9-anthracene carboxylic acid) (Di-AC) was developed and synthesized within epoxy composites [13]. The use of Di-AC allowed for damage precursor detection, as this mechanophore exhibits over 10 times the absolute fluorescence quantum yield compared to the cyclobutane-based mechanophore due to the three conjugated benzene rings [15]. The quantum yield can be used to quantify the amount of damage in the system. The experimental results are used to validate and further refine the model and methodology of the developed simulation framework.

1.1.2. Modeling of Mechanophore Embedded Nanocomposites

New nanomaterial manufacturing and synthesis techniques are the primary drivers of innovation in the nanotechnology field. Currently, nanotechnology advances are being further accelerated by use of a broad array of computational techniques (e.g., quantum mechanics-based methods, molecular-based simulation methods, and coarse-grained modeling), particularly since the design and development of these novel materials require a comprehensive understanding of intermolecular/intramolecular interactions, which cannot be fully attained through experiments alone [37]. Mechanophores have been incorporated into various polymers to impart self-sensing capability to the polymers using novel photosynthesis-based manufacturing techniques; however, characterizations of individual constituents and interactions between different phases in these nanocomposites

have yet to be addressed successfully. This is primarily due to the fact that small-scale phenomena are extremely difficult to capture in experiments, and atomistic scale simulation methods, such as MD, are required to effectively capture the intermolecular/interatomic interactions. Li and co-workers [38] performed MD simulations for graphene embedded nanocomposites to investigate the effect of graphene layer alignment on mechanical property improvement. Zhu et al. [39] performed MD simulations on a unit cell consisting of a single wall carbon nanotube and epoxy-based thermoset to estimate the stress-strain relation. Subramanian and Rai [40, 41] investigated the effect of polymer-nanotube chemical bonding on critical load transfer from CNT to polymer matrix using MD simulations.

Unlike graphene or CNT embedded nanocomposites, the existing literature on the modeling of mechanophore embedded nanocomposites is very sparse. The spiropyran-embedded thermoplastic polymer model was developed by Silberstein et al. [42] to analyze local force distribution and mechanophore activation. A three-prong method that included use of quantum theory, a traditional MD simulation, and a finite element approach, was used to analyze the kinetics of the spiropyran, the local force distribution on the molecules, and the macroscopic stress in the polymer specimen, respectively. Estimation of local forces applied to spiropyran in the thermoplastic matrix using a classical force-field was conducted by Dreiding [43]. A reference force, required for transforming the spiropyran to the merocyanine, was calculated using the quantum theory-based method. The mechanophore activation was observed when the estimated local force exceeded the reference force during virtual deformation tests.

While the method proposed by Silberstein et al. represents a pioneering modeling effort for mechanophore-embedded nanocomposites, it has several limitations that need to be addressed to improve the reliability of the local force analysis. For example, in Silberstein's study, the traditional MD method using classical force-fields was used. This approach is limited to the study of a system around its equilibrium state [44-47]; therefore, it is not appropriate for investigating plastic deformation pertaining to covalent bond dissociation, which occurs away from the equilibrium state. Figure 1.6 illustrates this issue and shows that the force in the backbone steadily increases with strain, which is not physically meaningful. Additionally, the force does not become zero even at large values of strain (100% strain). Since external forces propagate through a polymer network during the deformation test and the network might be disconnected due to covalent bond dissociation, local force applied on the mechanophore will vary as the polymer network deforms. Hence, capturing covalent bond dissociation during the virtual deformation test is critical for accurate estimation of local force. In addition, the molecular nanocomposite model of the matrix was a simplified one in the Silberstein et al. study since it did not include spiropyran molecules and only considered PMMA as thermoplastic backbone and ethylene glycol dimethylacrylate (EGDMA) as a crosslinker.

It is important to note that the experimental system used in Silberstein et al. consisted of PMMA, EGDMA, and spiropyran. The local force information for mechanophore activation was not estimated from the spiropyran, but rather from the crosslinker (EGDMA). Therefore, it is necessary to develop a simulation framework incorporating a special force-field, capable of capturing covalent bond dissociation, and an accurate method for constructing realistic molecular model of the experimental process.

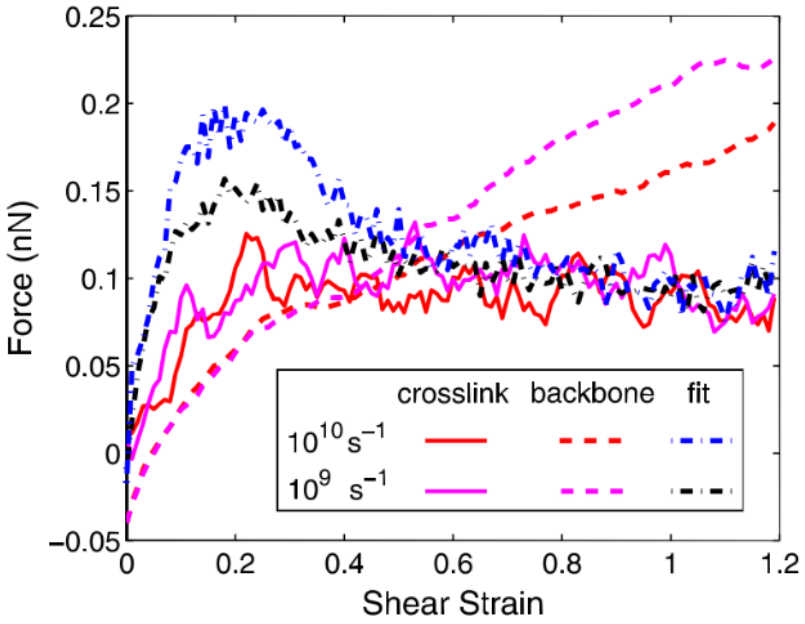

Figure 1.6. Local Force vs. Shear Strain for the Crosslinks and Backbone Including Result of Function Used to Convert Stress to Local Force [42].

1.1.3. Atomistic Virtual Loading Test

There is a critical need for nanoscale damage models that capture atomistic level damage such as covalent bond breakage and molecular sliding under mechanical loading [48-50]. Since the mechanophore is activated by the covalent bond breakage, a study of its damage model must also involve close observation of the mechanochemical reactions that take place. A significant amount of research, both modeling and experiments, has been reported addressing damage and damage evolution in composites at the microscale and the macroscale. As classic homogenization method [51] using a single-fiber representative volume element (RVE), was extended by Asp et al. [52] to explore damage initiation and evolution in composite materials by investigating the location of the maximum dilatational

energy density in the matrix. Trias et al. [53] developed a model using a statistical representative volume element (SRVE) to describe material behaviors accurately. Trias's model was extended to predict the intralaminar fracture [54-56]. To estimate the macroscopic damage response from the micromechanics damage model, Raghavan and Ghosh [57] developed a continuum damage mechanics method using the asymptotic homogenization method [58]. In addition to modeling work, several experiments have been performed with X-ray radiography [59-61] and thermography [62, 63] to detect damage in carbon fiber composites. However, the phenomena occurring at the nanoscale, specifically, the intra/intermolecular interactions in the nanocomposites under mechanical loading, which is necessary to fully investigate the capabilities of nanoscale sensing techniques, have not been fully explored. This can be attributed to the complexities in developing a realistic molecular model as well as the computational expense. Experimental validation of such information also is limited by the resolution/sensitivity of existing experimental tools.

A number of MD studies are available in the literature that focuses on performing deformation simulations to estimate mechanical response of epoxy-based nanocomposites [64-74]. Li and Strachan [65], for example, estimated mechanical properties, such as tensile/shear/bulk moduli of the epoxy polymer (resin DGEBF (Di-Glycidyl Ether of Bisphenol F) and hardeners DETDA (Di-Ethyl Toluene Di-Amine)). Figure 1.7 shows the estimated stress-strain curves and calculated Young's moduli therefrom. In another study, Strachan and co-workers used the MD method to predict mechanical response to cyclic loading using DGEBF and 33DDS (3,3 Diamino Diphenyl Sulfone) [66]. Valavala et al.

[67] and Bandyopadhyay et al. [68] studied the effect of epoxy conversion degree on mechanical properties of the same epoxy matrix.

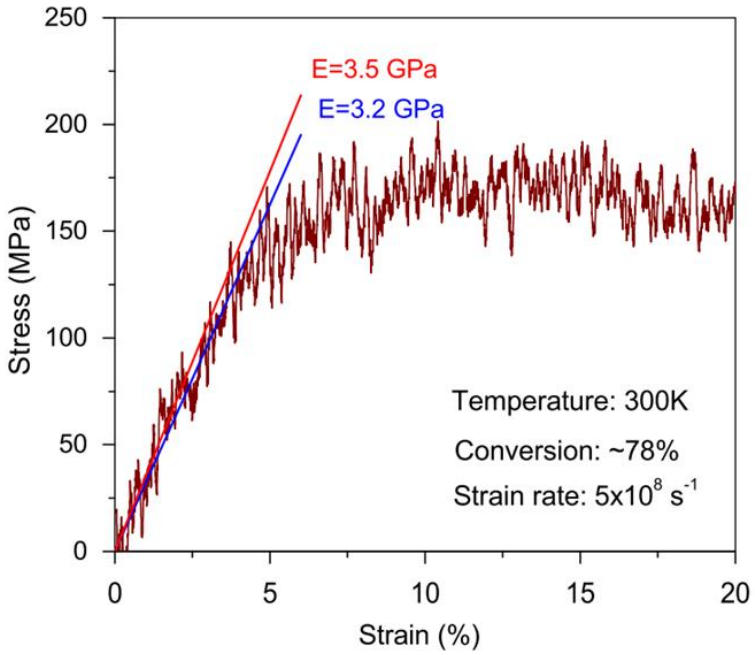

Figure 1.7. Predicted Stress-Strain Curve under the Tensile Loading [64].

The MD studies mentioned above, however, were all performed with classical force fields, and as such, the plastic deformation leading to damage initiation and propagation has yet to be captured successfully. To overcome this limitation, several MD simulation techniques have been developed. In early studies, for example, researchers sought to modify the finitely extensible nonlinear elastic (FENE) force-field [75-78] to yield a quartic bond potential that could enable studying covalent bond dissociation. Moller et al. [79] recently developed an approach for capturing covalent bond dissociation. Their method involved using classical force fields to monitor the covalent bond length during

mechanical deformation. If the bond length went beyond a specific threshold, then it was eliminated and the information was deleted from the system database during the virtual deformation test.

While the above two approaches (modified FENE and Moller's approach) capture fracture behavior successfully, a large deformation (>100% strain) is required to observe this failure, as shown in Figure 1.8. Such a deformation is not realistic since material failure of epoxy polymeric systems appears at smaller strains (<10% strain) [48-50]. Therefore, it is necessary to develop a method capable of accurately describing plastic deformation in an amorphous thermoset polymer system and with the application of mechanical load.

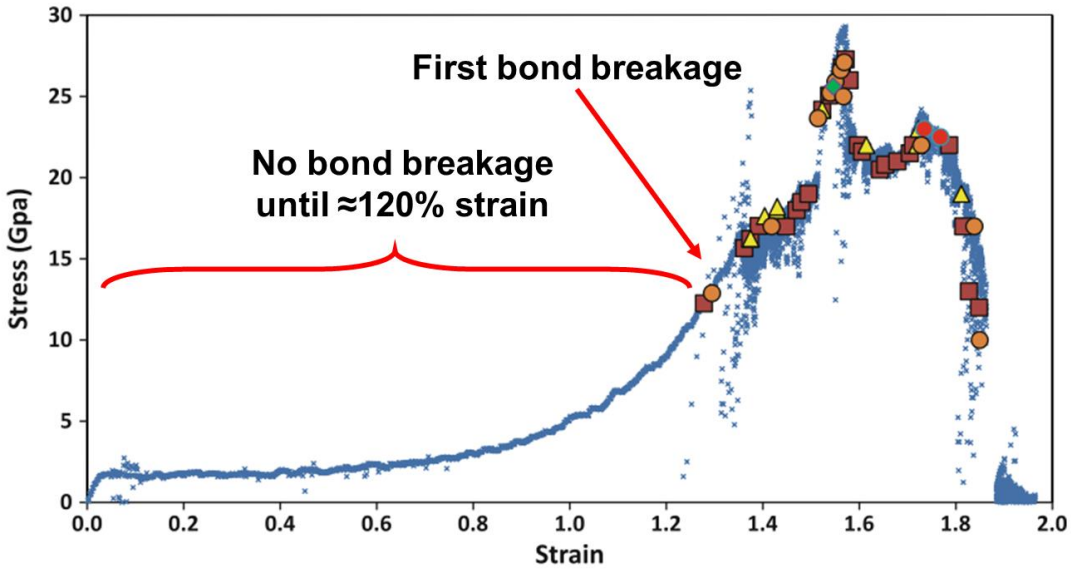

Figure 1.8. Stress–Strain Curve Estimation. Symbols Indicate the Type of Bond Broken and the Strain at Which They Occurred [79].

1.1.4. Atomistic Modeling of Fiber/Matrix Interphase

There is a considerable body of research that shows fiber/matrix interphase in PMCs as critical to the performance of the composite system. However, the ability to characterize this interphase region through testing is significantly limited due to its associated length scale; therefore, measuring interphase properties and estimating their impact on the composite structural response and damage is challenging [80]. Several modeling efforts have been reported based on indirect observation of the composite behavior. Reifsnider [81] developed a micromechanical strength model that investigated the effect of the interphase region on the strength and life of the composites. Asp et al. [82] assumed symmetric and periodic conditions to model a quarter of the fiber in a polymer matrix while studying the effects of interphase thickness on the response. The authors also used finite element analysis (FEA) to conduct a parametric study of various interphase properties. Souza et al. [83] developed a multiscale FEA model incorporating viscoelasticity in the micromechanics and a cohesive zone law representing the interphase to determine the effect of damage under impact loading. FEA has also been used to model representative volume elements (RVEs) consisting of multiple fibers with the interphase represented using bilinear cohesive laws [84, 85].

Although the above-mentioned studies have employed interfacial laws to account for the fiber/matrix interaction, these microscale interfacial laws were based on larger scale coupon testing, with assumptions/hypotheses that have latent uncertainties. In order to improve the interphase modeling study, some experimental efforts have been made with single fiber specimen test [86-88]. The Broutman test, for example, was originally designed to measure the interphase transverse tensile strength for glass fiber PMCs [87]. This

method, which has now been extended to carbon fiber PMCs (Figure 1.9 [88]), calculates the transverse tensile strength using the difference in Poisson's ratios between the fiber and polymer matrix under a compressive loading condition. However, the transverse modulus is difficult to obtain due to the challenge in extracting strain information of the interphase region. Although these experimental studies have the capability to estimate the interphase properties, the indirect method of estimation involves uncertainty propagation, which cannot be addressed by current experimental techniques.

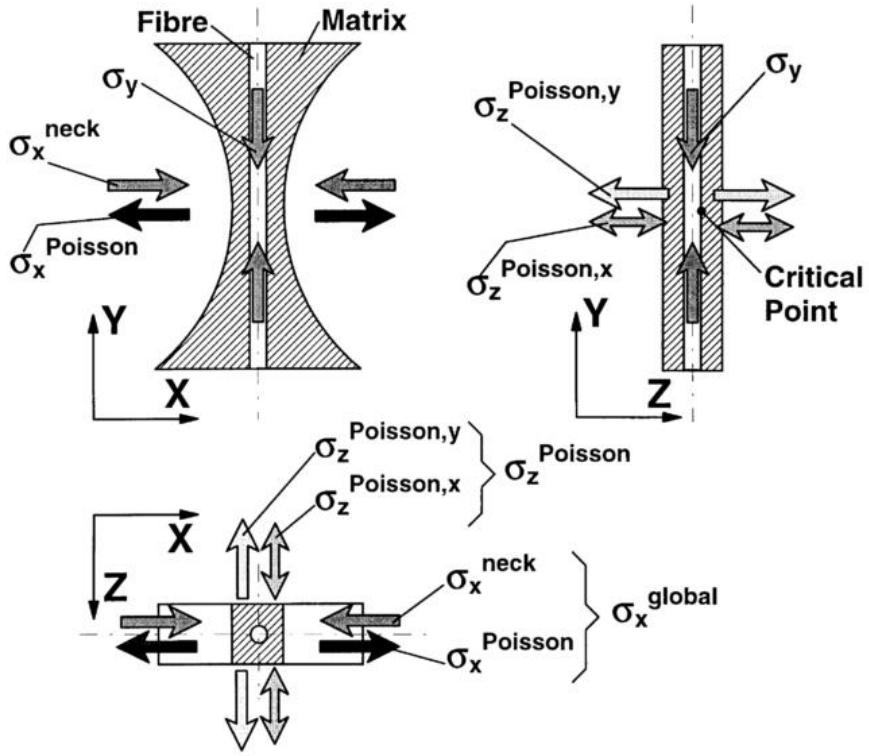

Figure 1.9. Stress Components in the Broutman Specimen [88].

To overcome the nanoscale experimental limitations, several computational methods have been introduced for estimating the molecular scale properties of composites. They include ab-initio quantum chemistry, density functional theory (DFT), and a range of MD methods [69-72, 89-91]. Hadden et al. [89] used a generalized method of cells to integrate MD generated properties of graphene nanoplatelets in epoxy within a multiscale model. Jiang et al. [90] modeled the macroscopic behavior of CNT-reinforced nanocomposites using a form of the rule of mixtures. In their work, the interphase between the polymer matrix and a CNT is modeled as a wavy surface and a cohesive stress law is formulated based on the Lennard-Jones potential (non-bonded potential). Mousavi et al. [91] studied the elastic regime of CNT/polymer composites by using a coarse-grained model, which allowed the scaling of crosslinking and molecular interactions to larger length scales. In these molecular modeling methods, carbon fiber is often approximated as graphene or CNT so that the number of atoms needed to fully represent the fiber is reduced. Zhang et al. [85] estimated the mechanical properties of a carbon fiber/polymer interphase by representing the fiber as multiple layers of graphene and constructing a cohesive law using the van der Waals interactions between the constituents (Figure 1.10). Most of these molecular interphase models are formulated using only the Lennard-Jones potential, which does not account for mechanical entanglements or covalent bond within the constituents. In addition, graphene and CNTs are crystalline structures, whereas carbon fiber is semi-crystalline with chains of carbon atoms randomly folded and/or interlocked together [92-95]. Due to the complexity of the carbon fiber, CNT and graphene molecular models cannot represent carbon fiber correctly. It is critical, therefore, to develop a new carbon fiber surface model to accurately capture elastic and plastic behavior in the interphase region. In this

dissertation, the representation of the semi-crystalline carbon fiber surface has been explored using stacked graphene layers with void.

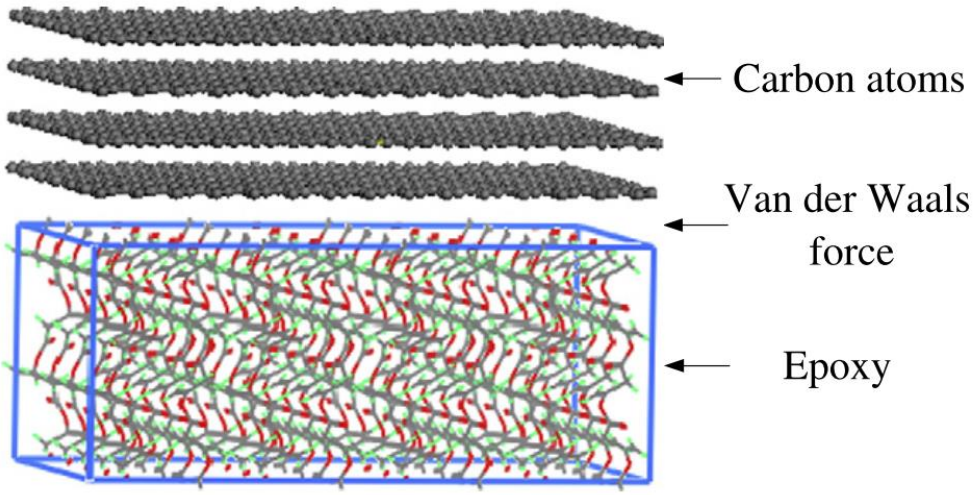

Figure 1.10. Schematic Diagram of Molecular Simulation of the Interface Between Carbon Fiber and Epoxy [85].

1.2. Objectives

The primary objective of this research is to accurately model mechanochemical reactions of mechanophores and to develop atomistic simulation methodologies for effectively emulating mechanophore activation and estimating material properties of mechanophore embedded nanocomposites. A fiber/matrix interphase model is also developed by extending the existing molecular modeling technique. The matrix/fiber interphase study is fundamental to understanding the effects of the interphase on the PMC response and developing rigorous multiscale damage evolution laws that span the relevant length scales. Physics-based model developments are steered by a closed-loop design and

validation plan that incorporates both experimental and computational modeling approaches as shown in Figure 1.11. Following are the specific goals of the current research.

(1) Modeling of Epoxy-based Thermoset

A molecular model of the thermoset polymer matrix based on epoxy curing process is developed first. Since the activation of the mechanophore is governed by the interaction among the mechanophores and the host material surrounding it, developing a realistic model of the host materials is essential for reliable simulations. In order to allow both random distribution of molecules and stochastic covalent bond generation features with meaningful assumptions (for example, cutoff distance ≈ van der Waals radii) in the simulation of epoxy network generation, a numerical covalent bond generation method between epoxy resin and hardener (also known as crosslinker) is developed. A standard procedure for running the MD simulation for the epoxy system needs to be established and experimentally validated. Next, a molecular model of the mechanophore embedded nanocomposites is developed by incorporating mechanophore molecules into the epoxy-based polymer model. Using this nanocomposite model, the interaction between two different constituents (epoxy matrix and mechanophore) and the effect of the constituent parameters on mechanochemical responses, including mechanical/thermal properties and mechanophore activation sensitivity, is investigated.

(2) Mechanophore Reaction Simulations

An appropriate atomistic simulation methodology that captures mechanophore reaction entailing covalent bond breakage simulations is developed. Traditional MD simulations are

suitable for molecular conformational studies, which analyze the system around equilibrium state. Bond breakage, however, occurs away from the equilibrium state. Quantum mechanics (QM)-based method can account for the chemical reactions including covalent bond breakage and covalent bond formation; however, QM-based methods are not applicable for a large size system, which is necessary for this study since nanocomposites are bulk polymer systems. A combination of both MD-based method and QM-based methods, therefore, are employed in this research wherein actual physical parameters activating the mechanophore in the nanocomposites are investigated. This aspect of the research will aid in understanding mechanophore activation mechanisms as well as the ability to optimize the performance of the self-sensing polymer.

(3) Development of Nanoscale Damage Model

Current MD simulation methods to emulate mechanical loading test for epoxy-based thermoset do not capture bond breakage at lower strains in the stress-strain curve as mentioned previously in the section 0. Unlike experimental observations, the estimated stress-strain curve of epoxy-based thermoset shows ductile behavior and demonstrates covalent bond breakage at unrealistically high strain. This limitation in current MD simulation methods must be addressed to improve the reliability of the MD approaches. A few MD and QM-based methods have been developed to simulate the covalent bond dissociation during single molecular deformation; however, a method to capture the bond breakage during the nanocomposite (bulk system) deformation has not been established correctly. In this dissertation, the limitations of the current methods are identified through exhaustive simulations with various parameters such as temperatures, strain rates,

boundary conditions, force fields, etc. From the simulations, hypotheses to resolve the limitations are proposed.

(4) Development of Fiber/Matrix Interphase Model

A methodology to model the interphase between the fiber and matrix using MD simulation is developed to provide meaningful estimation of interphase properties and understanding of the nanoscale damage process. Existing models that adopt the ‘perfect bonding’ or ‘non-bonded’ assumption between the fiber and the matrix cannot account for the semi-crystalline structure of carbon fiber surface that can be physically entangled with the polymer matrix. The models that assume ‘perfect bonding’ overestimate the mechanical properties of the interphase relative to experiments and the models based on the ‘non-bonded’ assumption underestimate the properties [96-99]. In this dissertation a more accurate interphase model is developed to estimate damage initiation of PMCs. Although the methodology presented is applicable to any interphase system, the focus of this study is on the interphase between carbon fiber and thermoset matrix.

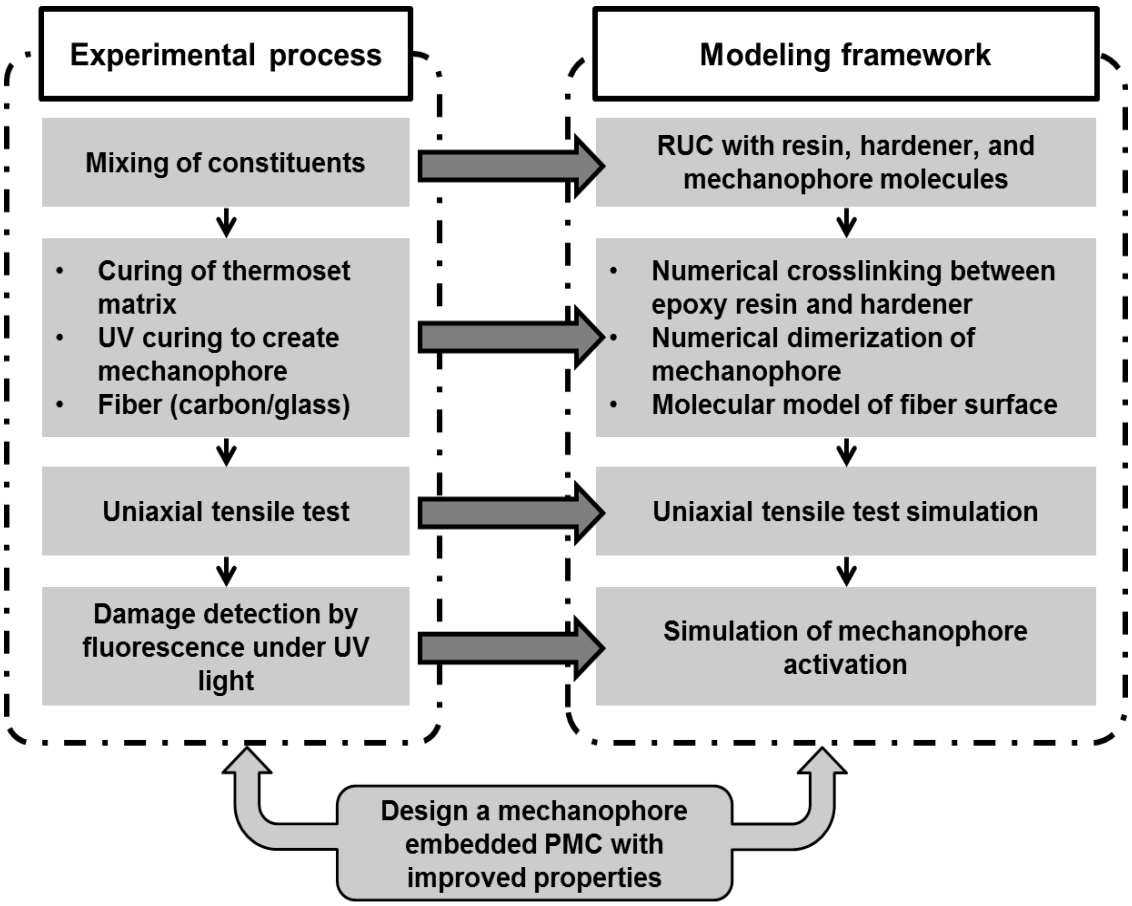

Figure 1.11. Flowchart for Closed Loop Validation by Connecting Experimental Results and Simulation.

1.3. Outline of the Dissertation

This dissertation is organized as follows:

Chapter 2 introduces a new atomistic scale simulation framework that can capture mechanochemical reaction of mechanophores in an epoxy-based thermoset matrix. The purpose of this framework development is to create a realistic model that can generate physically meaningful output. The framework includes four essential elements to achieve this goal: i) modeling of epoxy-based thermoset polymer and UV dimerized

mechanophores; ii) simulation of covalent bond dissociation; iii) emulation of mechanical loading tests; iv) analysis of force and energy distribution in the nanocomposites. Detailed descriptions of methodology for each element will be provided for users to reproduce the outputs.

Chapter 3 presents experimental validation of the framework. Material properties including glass transition temperature (Tg), fluorescence intensity of activated mechanophore, elastic modulus, and yield strength are predicted using the framework, and are measured experimentally using DSC, fluorescence microscope, and uniaxial load frames, respectively. Effectiveness of the framework is evaluated by comparing experimental results against simulation results.

Chapter 4 discusses a new MD model and simulation methodology to simulate damage initiation and propagation in epoxy-based thermoset polymer at the nanoscale. Two requirements are introduced: i) employing a special force-field capable of capturing chemical reaction, especially bond dissociation; ii) reducing molecular thermal vibration during the nanoscale deformation test. A quasi-continuum method that meets the two requirements is demonstrated. An alternative for improving computational efficiency over the quasi-continuum method is also introduced.

Chapter 5 presents a molecular interphase model capable of capturing physical coupling between carbon fiber and thermoset polymer matrix. A computational method transforming graphene layers into a molecular model representing semi-crystalline carbon fiber surface is introduced. A simulation procedure to make the interphase model by entangling the transformed graphene layers with epoxy polymer is demonstrated. Using this interphase model, the elastic/plastic material responses of the interphase region is

predicted. Various existing interphase models are introduced to compare with the proposed interphase model.

Chapter 6 summarizes the research reported in this dissertation and highlights its main contributions and findings. Potential areas and recommendations for future research work are also discussed at the end of the chapter.

CHAPTER

2. A HYBRID MOLECULAR DYNAMICS SIMULATION FRAMEWORK

2.1. Introduction

In the late 1950s, Alder et al. [100] first used molecular dynamics (MD) to demonstrate evidence of phase transition between liquid and solid states (also known as 'first-order phase transition') in a system of hard spheres. Kirkwood et al. [101] predicted phase transition based on an approximated theoretical analysis prior to conducting a computational study, even though this was not widely accepted due to a lack of rigorous theoretical work. Alder's simulation work, however, had in essence successfully validated Kirkwood's theoretical hypothesis. After these two historically significant studies, atomistic simulation methodologies have attracted considerable attention as a method capable of estimating material responses, especially in cases where experimental approaches are not feasible. Currently, atomistic simulation techniques are generally used in many fields, including physics, chemistry, material science, biophysics, structural biology, and pharmaceutics.

Three atomistic simulation methods, in particular, have gained popularity in materials science research: Monte Carlo (MC), molecular mechanics (MM), and molecular dynamics (MD). The MC atomistic simulation method was developed by Metropolis et al. [102] in the early 1950s. This method was the first atomic simulation performed on the MANIAC (Mathematical Analyzer, Numerical Integrator, and Computer) using a computer-generated random number. Since this random number decides the next trajectory of the atoms, it is useful in low density systems with multiple energy minima; however, it has no dynamics information of molecules of constituents. This method depends on the randomly

generated value for the system evolution; it is not relevant for a system whose dynamics has not been well defined.

MM was developed to analyze stereochemical conformation of a molecular system using the potential energy calculated by a set of parameters and functional forms (also known as 'force-field') obtained by quantum chemistry and experiments. The MM method is especially useful for the study of equilibrium geometry of the system as well as potential energy surface as a function of the molecular structure/geometry. However, MM is not appropriate for a system at the high temperature (> 0 K) inducing thermal vibration and molecular mobility. Therefore, MD has been devised to analyze intermolecular interaction by calculating the potential energy at every time step using the force-field. The historical work mentioned at the beginning of this section was performed by the MD method using the Lennard-Jones (LJ, non-bonded) potential, which is a mathematical functional form for van der Waals interaction among atoms in the system. Since the MD method evaluates system evolution using Newton's second law of motion, unlike the MC and MM methods MD can hold dynamical information accurately, which allows capture of the phase transition due to temperature variation.

In this dissertation, the MD method is employed to establish the atomistic scale simulation framework. The traditional MD method that uses the classical force-fields is very effective in conformational studies of molecules; however, traditional MD itself has limitations in capturing all the mechanochemical reaction phenomena of interest. Although the traditional MD method is implemented within the proposed framework for the conformational study, appropriate force-fields to capture particular phenomena (non-

equilibrium state) have to be added, relevant methodologies developed, and effective data analysis methods incorporated into the framework.

In this chapter, the basic theory of MD algorithm is discussed first as a preliminary study. Next, the four essential elements of the framework which are mentioned in the introduction are elaborated.

2.2. Traditional Molecular Dynamics

The MD simulation algorithm is based on Newton's motion equation (the number of atoms: N) and the force is determined by negative spatial gradient of potential energy (V),

$$m_i \frac{\partial^2 \boldsymbol{x}_i}{\partial t^2} = \boldsymbol{F}_i = -\frac{\partial V}{\partial \boldsymbol{x}_i}, i = 1 \dots N. \quad (2.1)$$

Using Taylor expansion, the position vectors of atoms are reduced to,

$$\boldsymbol{x}_i(t + \Delta t) = \boldsymbol{x}(t) + \frac{\dot{\boldsymbol{x}}_i(t)\Delta t}{1!} + \frac{\ddot{\boldsymbol{x}}_i(t)\Delta t^2}{2!} + O(\Delta t^3). \quad (2.2)$$

Substituting Equations 2.1 into 2.2, acceleration at $t+\Delta t$ is obtained,

$$\ddot{\boldsymbol{x}}_i(t + \Delta t) = -\frac{1}{m_i}\frac{\partial V\left(\boldsymbol{x}_i(t + \Delta t)\right)}{\partial \boldsymbol{x}_i}, i = 1 \dots N. \quad (2.3)$$

After applying Euler's method to the velocity, acceleration at *t* is expressed as

$$\frac{\dot{\boldsymbol{x}}_i(t + \Delta t) - \dot{\boldsymbol{x}}(t)}{\Delta t} = \ddot{\boldsymbol{x}}_i(t). \quad (2.4)$$

Using the midpoint method, Equation 2.4 can be modified to

$$\frac{\dot{\boldsymbol{x}}_i(t + \Delta t) - \dot{\boldsymbol{x}}(t)}{\Delta t} = \ddot{\boldsymbol{x}}_i\left(t + \frac{\Delta t}{2}\right). \quad (2.5)$$

Since the right-hand side of the Equation 2.5 can be considered as the average acceleration,

$$\ddot{\boldsymbol{x}}_i\left(t + \frac{\Delta t}{2}\right) = \frac{\ddot{\boldsymbol{x}}_i(t + \Delta t) + \ddot{\boldsymbol{x}}(t)}{2}. \quad (2.6)$$

The left-hand side of Equation 2.5 and the right-hand side of Equation 2.6 reduce to:

$$\frac{\dot{\boldsymbol{x}}_i(t+\Delta t)-\dot{\boldsymbol{x}}(t)}{\Delta t}=\frac{\ddot{\boldsymbol{x}}_i(t+\Delta t)+\ddot{\boldsymbol{x}}(t)}{2}. \qquad (2.7)$$

Using the position at *t* and acceleration at *t* and $t+\Delta t$, velocity at $t+\Delta t$ will be calculated by

$$\dot{\boldsymbol{x}}_i(t+\Delta t)=\dot{\boldsymbol{x}}(t)+\frac{\Delta t}{2}\left(\ddot{\boldsymbol{x}}_i(t+\Delta t)+\ddot{\boldsymbol{x}}(t)\right). \qquad (2.8)$$

Using this method (also known as the velocity-Verlet algorithm [103]), the states of atoms at $t+\Delta t$ such as acceleration, velocity, and position can be obtained. Through the evaluation of motion of atoms and molecules in the system, dynamic response of the molecular system is captured precisely. In order to use discrete MD simulations to estimate continuum material responses representing experimental measurements, statistical mechanics – a theory of calculating macroscopic thermodynamic properties from microscopic simulations, is introduced.

In statistical mechanics, averages are defined as 'ensemble' averages. Ensemble means a collection of possible systems that have different microscopic states but have an identical macroscopic state; hence, the ensemble averages enable the representation of macroscopic properties. In MD, the ensemble average can be calculated in two ways under the assumption that the system is in equilibrium state: 1) integrate time and spatial averages using a set of short trajectories that are initiated from an equilibrium state of each system and run for the same period of simulation time; 2) calculate time average using a single very long trajectory that has passed through all possible states. Although the first method is in complete accord with the definition of ensemble average, making a set to include all possible states is extremely difficult, whereas the second method is more practical and can

be statistically meaningful by means of one of the fundamental axiom ‘ergodic hypothesis’ in statistical mechanics. The ergodic hypothesis was postulated by Willard Gibbs in the thermodynamics research field [104]. In this hypothesis, time averages become equivalent to ensemble averages when the simulations are conducted for a long enough period of time and consistent average values are observed from the simulations. The rigorous mathematical expression of this hypothesis allows the use of MD simulations to estimate macroscopic thermodynamic properties. There are four ensembles popularly used in MD simulation:

1. NVE ensemble (Microcanonical ensemble): The number of moles (N), volume (V), and energy (E) are constant. This ensemble conserves the system total energy; it is typically useful in studies on energy exchange between potential and kinetic energy.
2. NVT ensemble (Canonical ensemble): The number of moles (N), temperature (T) and volume (V) are constant. Since this ensemble conserves the temperature of the system, it is useful for the system related to exothermic/endothermic processes.
3. NPT ensemble (Isothermal-Isobaric): The number of moles (N), pressure (P), and temperature (T) are constant. The volume is not constant, but pressure and temperature are constant; therefore, this is equivalent to laboratory conditions, and the system is allowed to change its volume freely as a result of constituent conformations, especially for the polymeric system.
4. NPH ensemble (Isoenthalpic-Isobaric): The number of moles (N), pressure (P) and enthalpy (H) are constant. Volume (V) becomes a dynamic variable with kinetic energy given by PV. The enthalpy H = E + PV is kept constant, while the internal energy E and the kinetic energy PV are allowed to change.

Although Newtonian equation itself allows the exploration of the constant energy surface of the molecular system, ensemble averages achieved by controlling the temperature and pressure condition during the simulation are much more meaningful to mimic experimental conditions. Therefore, design constraints can be imposed on the simulations to produce ensemble averages that consistently represent the same state of the system as in experiments; these design constraints are imposed in the form of statistical ensembles for equilibration. Researchers can choose ensembles according to experimental conditions that need to be mimicked.

Additionally, computing the bulk properties of the epoxy-based system is of primary interest; as the number of particles increases, more statistically meaningful properties can be obtained. However, only systems with a finite and relatively small number of particles can be simulated. This small number limitation introduces the problem of surface effects. For example, in a simulation of a simple cubic crystal consisting of 1000 particles, 512 will be at the surface. A general way to mitigate the problem of surface effects is to impose periodic boundary conditions (PBC). In this scheme, it is envisioned that the cubic simulation box containing the particles is replicated throughout space to form an infinite lattice. This boundary condition is illustrated in the two-dimensional case in Figure 2.1. If a particle moves out of the main simulation box, one of its periodic replicas from a neighboring box moves in to replace it.

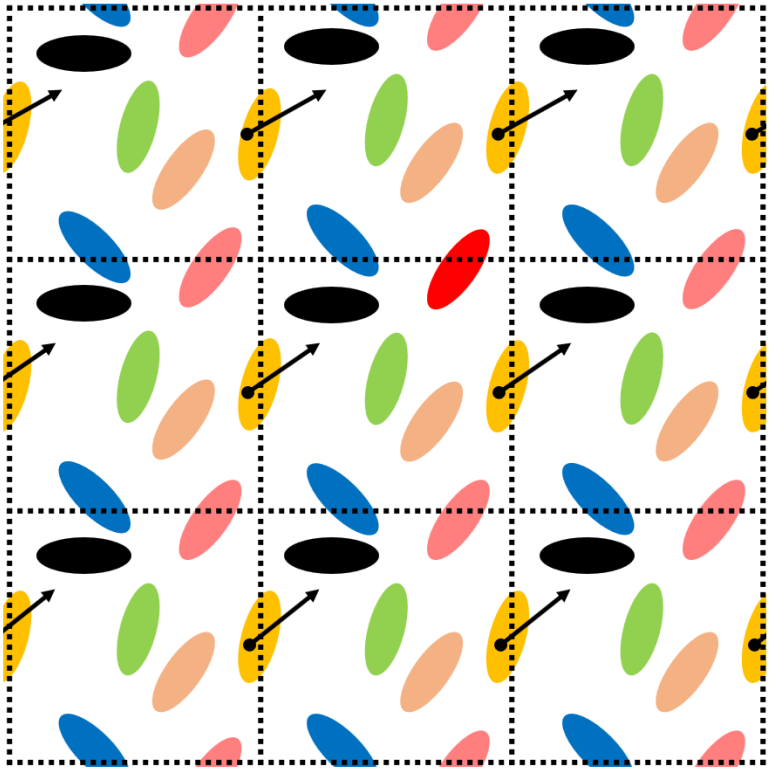

Figure 2.1. Illustration of Periodic Boundary Conditions in MD Simulations.

2.2.1. Classical Force-field for Traditional MD Simulation

The force in Newton's motion equation in the previous section is calculated by the potential energy of the system in the molecular model, which is estimated by the 'force-field' that is chosen based on materials. The force-field is generally defined as a set of functions and parameters in the atomistic simulation research field and is strongly material dependent; hence, the selection of the right force-field for the system of interest is very important. Merck Molecular Force Field (MMFF) is a classical force-field that is employed to deal with the inter/intramolecular potential energy of neat epoxy and mechanophore embedded epoxy nanocomposite (smart polymer) [47, 105-108]. With MMFF, Large-scale Atomic Molecular Massively Parallel Simulator (LAMMPS) is used as an MD simulator

[109]. MMFF is derived from computational data calculated using *ab initio* quantum mechanics-based methods and has been validated by chemists and crystallographers. Through these calculations, MMFF-based MD simulations have enabled to reproduce experimental results accurately in the pharmaceutical and chemical engineering research field [110-112]. The experimental data, which come from X-ray and neutron diffraction, microwave spectroscopy, and electron diffraction, are maintained by the Cambridge Crystallography Data Centre (CCDC), a major international resource for chemical and pharmaceutical research [113]. Based on MMFF, topologies and force-field parameters of all the molecules are provided by a web-based molecular structure generator, which is developed by Swiss Institute of Bioinformatics (SIB)- an international research foundation providing organic chemistry resources [114]. The MMFF force-field is implemented in conjunction with LAMMPS, which has versatile functions such as unit cell deformation, and the ability to create/delete atoms. It is worth noting that although LAMMPS does not support MMFF itself, this research is able to use MMFF in LAMMPS because SIB converts the MMFF functional forms into the Chemistry at HARvard Macromolecular Mechanics (CHARMM) force-field functional form which is available in LAMMPS.

$$E_{CHARMM} = E_{bond} + E_{angle} + E_{dihedral} + E_{improper} + E_{vdW} + E_{coulomb}. \qquad (2.9)$$

Classical force-fields consist of two potentials: bonded potential and non-bonded potential. Bond, angle, dihedral, and improper potential are all included in bonded potential, and van der Waals and Coulomb potential are included in non-bonded potential. Table 2.1 shows the functional forms of each potential where K_{bond} is the bond force constant, and r_0 is the equilibrium bond distance, K_{angle} is the angle force constant, θ_0 is the equilibrium angle between three bonded atoms, $K_{dihedral}$ is the dihedral force constant, n is the

multiplicity of the function, φ_0 is the equilibrium dihedral angle, $K_{improper}$ is the improper force constant, λ_0 is the equilibrium improper angle, ε is the depth of the potential well, σ is the finite distance at which the intermolecular potential between the two particles is minimum, $K_{Coulomb}$ is Coulomb's constant, and q_1, q_2 are the signed magnitudes of the charges. In the case of bonded potential, the functional form and parameters are optimized around an equilibrium point; therefore, the optimized topology information is invalid if the research goal is the material response of the system away from the equilibrium state. In this study, the results calculated from the classical force-field, including the optimized topology, shows good agreement with experiments when the MD estimates the material response (e.g. density, glass transition temperature, etc.) of the system around the equilibrium state. All the coefficients in the force-fields are dependent on the atom type and molecular geometries. To enumerate the potential energy plot of all the geometry cases, Figure 2.2-Figure 2.7 show all the chemical structures involved with covalent bond and non-bonded potential, corresponding to their potential energy plots. Since this research is about mechanophores, all the chemical topologies in the figures are from a mechanophore, namely TCE.

Table 2.1. CHARMM Functional Form for Potential Energy Calculation

	Functional form	
Bond	$K_{bond}(r - r_0)^2$	(2.10)
Angle	$K_{angle}(\theta - \theta_0)^2$	(2.11)
Dihedral	$K_{dihedral}(1 + cos(n\,\varphi - \varphi_0))$	(2.12)
Improper	$K_{improper}(\lambda - \lambda_0)^2$	(2.13)
van der Waals	$4\,\varepsilon[\left(\frac{\sigma}{r}\right)^{12} - \left(\frac{\sigma}{r}\right)^{6}]$	(2.14)
Coulomb	$K_{coulomb}\frac{q_1\,q_2}{r^2}$	(2.15)

In MD simulation, all the topologies such as bond, angle, dihedral, and improper strongly interact with each other, and potential energy is calculated using the functional forms of those topologies. Since the material response is determined by the accuracy of the potential energy calculation, finding very accurate and appropriate force-field of the molecular system is significantly important. Although a simpler molecular model of the system (for example, only non-bonded potential is considered) will ensure higher computational efficiency, it may not be adequate for capturing nanoscale phenomenon that significantly affects the macroscopic material responses.

In order to find an appropriate force-field, a closed loop validation using experimental results is necessary. In this work, glass transition temperatures are measured experimentally and compared with estimated Tgs calculated by MD simulations. Based on

these results, MMFF was selected as a classical force-field in this dissertation; detailed selection/validation procedure using experiments will be discussed in Chapter 3.

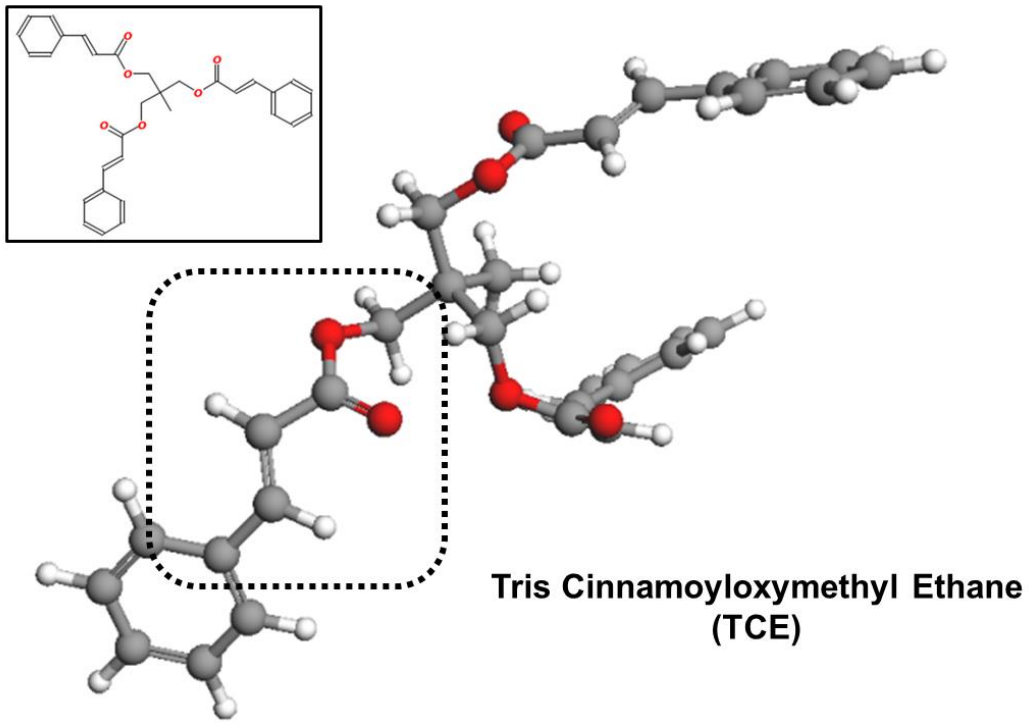

Figure 2.2. Chemical Structure of TCE Monomer,

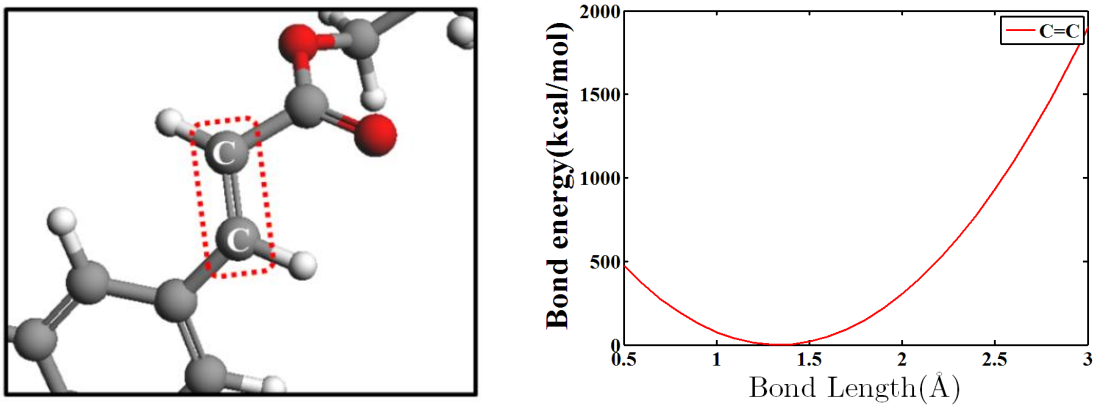

(a) (b)

Figure 2.3. C=C Bond Topology and Potential Energy Plot.

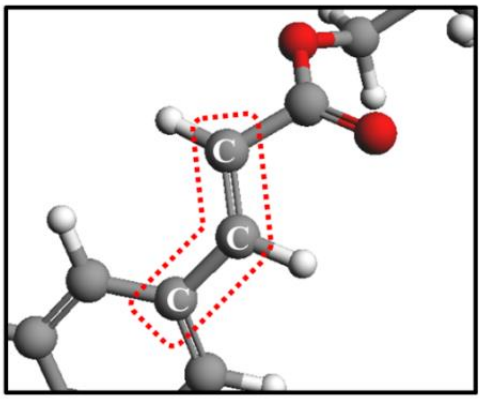

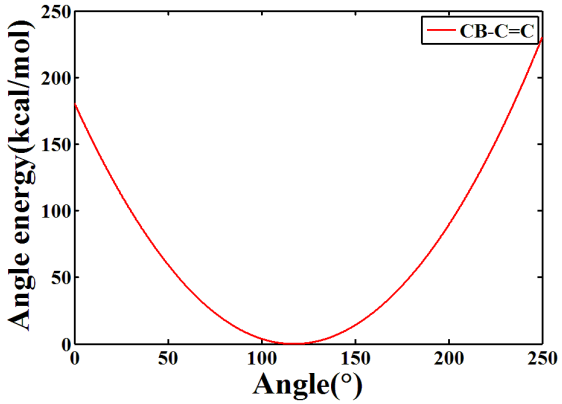

(a) (b)

Figure 2.4. C-C=C Angle Topology and Potential Energy Plot.

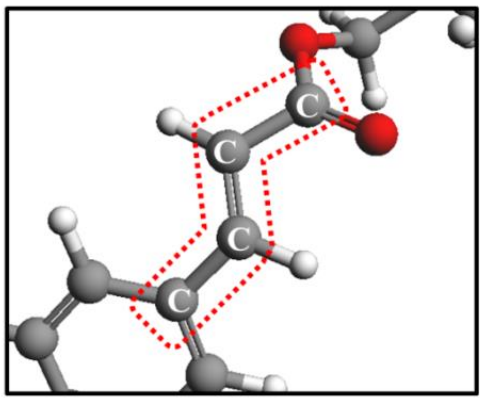

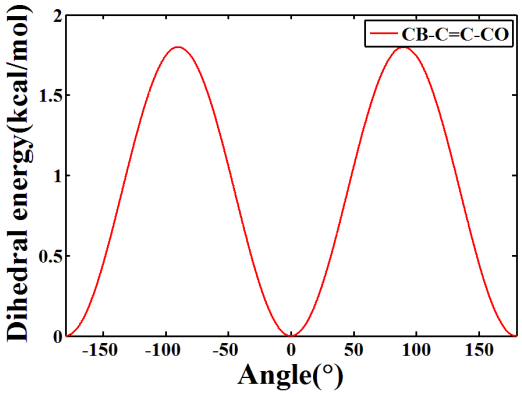

(a) (b)

Figure 2.5. C-C=C-C Dihedral Topology and Potential Energy Plot.

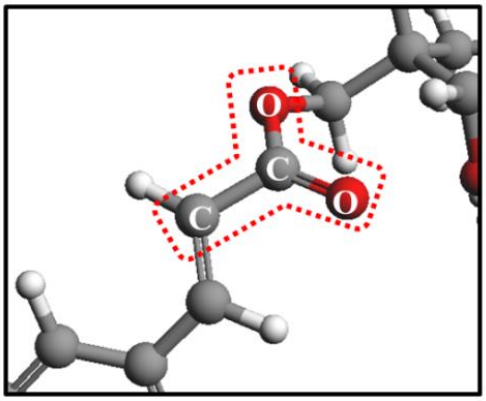

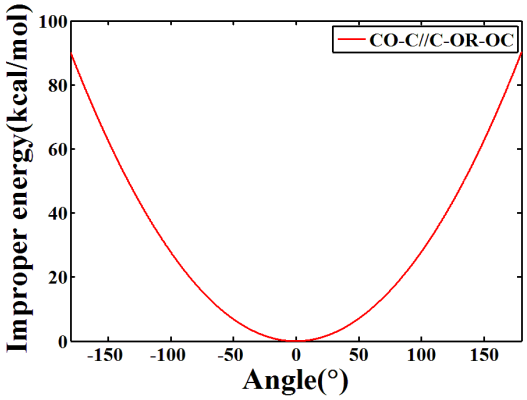

(a) (b)

Figure 2.6. C-O-O-C Improper Topology and Potential Energy Plot.

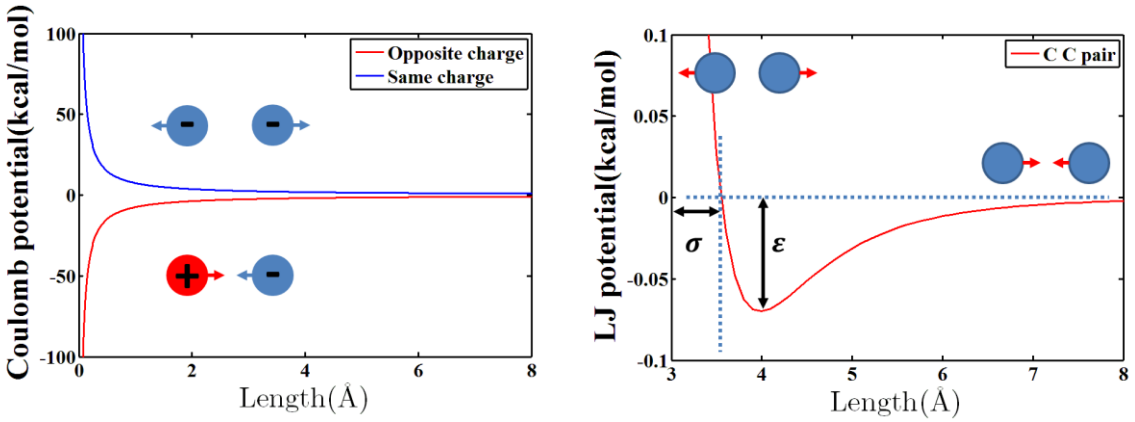

(a) (b)

Figure 2.7. Coulomb Potential (A), and Lennard-Jones (Van Der Waals) Potential (b).

2.3. Hybrid MD Simulation Framework for Mechanochemical Reaction

Traditional MD simulations that implement classical force-fields alone have been utilized to conduct conformational studies of a molecular system, such as a mixture of epoxy resin and hardener. However, the limitation of these traditional MD simulations is that they cannot capture chemical reactions, including covalent bond formation and dissociation. Emulating covalent bond formation is critical for accurately modeling the epoxy network, which directly affects the material properties of the epoxy-based thermoset. In addition, simulating covalent bond dissociation is integral to capturing mechanophore activation, which initiates from the covalent bond breakage of a specific bond in the mechanophore molecules. In this dissertation, the simulation of covalent bond generation is addressed by developing a procedure with in-house codes in conjunction with a bond create command within LAMMPS; detailed discussion is presented in Section 2.3.1. In

addition to bond generation, the simulation of bond dissociation is addressed by employing a special force-field, which is called bond-order based force-field. The bond-order based force-field captures not only the difference between chemical bond orders such as single, double, and triple bonds, but also the critical length at which the bond breaks. In section 2.3.3, detailed information about the bond-order based force-field is presented. Since the framework is developed by integrating two different force-fields, classical force-field, and bond-order based force-field, the term 'hybrid' is coined for the framework. Within this hybrid framework, a virtual loading test method is developed to simulate the mechanical load frame. Concurrently, a local work analysis is devised to explore effective physical parameters that lead to mechanophore activation.

2.3.1. Epoxy Curing Simulation

Unit Cell Development: For MD simulation, atomistic molecular structures of each component in an objective system need to be first defined. This study used commercial products of epoxy resin (FS-A23) and hardener (FS-B412), which is used for manufacturing carbon fiber reinforced composites [115]. Equivalent chemical names of epoxy resin and hardener are DGEBF and DETA (Di-Ethylene Tri-Amine) and their molecular structures are used for constructing the neat epoxy unit cell for MD simulation. The molecular structure of TCE is incorporated into the neat epoxy unit cell to construct the smart polymer unit cell. The numbers of molecules are determined by the weight ratio 100:27 (DGEBF:DETA), which is used for making experimental samples. The weight of TCE is 10% of the total weight of the neat epoxy unit cell. Table 2.2 and Figure 2.8 show the calculated number of molecules and the 3-D molecular structures in smart polymer unit

cell, respectively. Although two mechanophores (TCE and Di-AC) are discussed in this dissertation, only TCE is used to introduce the epoxy curing study.

Table 2.2. Components of Smart Polymer (100:27 and 10% TCE).

	Weight	Formula	Number of Molecules
DGEBF	313 g/mol	$C_{19}H_{20}O_4$	65
DETA	103 g/mol	$C_4H_{13}N_3$	55
TCE	510 g/mol	$C_{32}H_{30}O_6$	5

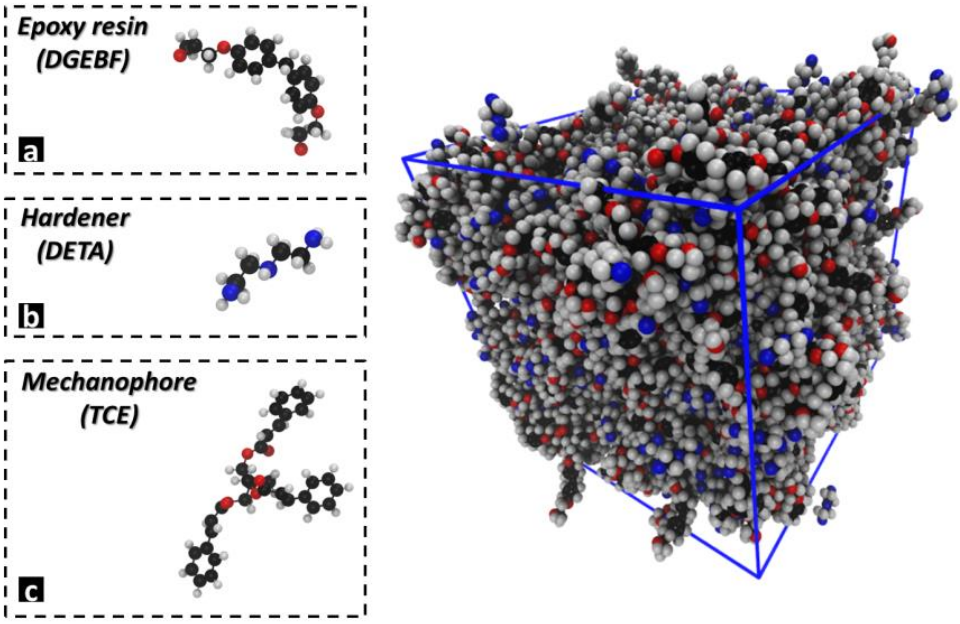

Figure 2.8. Schematic of Smart Polymer (Cyclobutane-Based Mechanophore) Unit Cell.

Simulation of Epoxy Curing Process: In practice, epoxy resin and hardener generate covalent bonds stochastically when the distance between the active sites of epoxy resin and hardener becomes less than a certain distance; Within this space, two active sites share their electrons to make potential energy stable. In polymer science, this is also known as the curing process. Since the quality of the curing process affects the mechanical/thermal properties of an epoxy-based system, modeling this curing process is necessary to improve the reliability of the MD simulation result [116]. Details of the curing process are as follows. First, the epoxide group of DGEBF and the amine group of DETA maintain equilibrium distances by inter/intramolecular potential energy (stage 1 of Figure 2.9). Second, the carbon-oxygen bond in the epoxide group and nitrogen-hydrogen bond in the amine group break. Third, from these separations, oxygen and hydrogen atoms react to generate O-H covalent bond (stage 2 of Figure 2.9). Finally, the carbon of epoxide group and nitrogen of amine group react with each other and generate C-N covalent bond (stage 3 in Figure 2.9). Figure 2.10 shows a 3-D visualization of DGEBF/DETA cross-linked systems. In Figure 2.10(a) the red dotted lines indicate that activated carbon atoms and activated nitrogen atoms that react to generate a C-N covalent bond. DETA has three nitrogen atoms and can generate five C-N covalent bonds; both end nitrogen atoms have two active sites and centered nitrogen atom has one active site (see Figure 2.12(c,d)). In addition to the C-N covalent bond between DGEBF and DETA, a photo-induced covalent bond, named cyclobutane, between TCE monomers is exploited. Figure 2.11 depicts the cyclobutane formation process, known as UV-induced [2 + 2] photocycloaddition, by which TCE monomers generate TCE polymers. After absorbing the UV-light energy, equilibrium of C=C double bonds (named cinnamoyl groups) is broken, which leads to the generation of

cyclobutane. Since the focus is on the epoxy curing process in this chapter, the photo-induced conversion degree is fixed at 40%, as investigated in Oya et al. [26]; the numerical method for cyclobutane generation is discussed in Section 2.3.2 in detail. For the epoxy curing simulation, the conversion degree representing the extent of cure is defined as the ratio of generated covalent bonds to total active sites of the system in MD simulation.

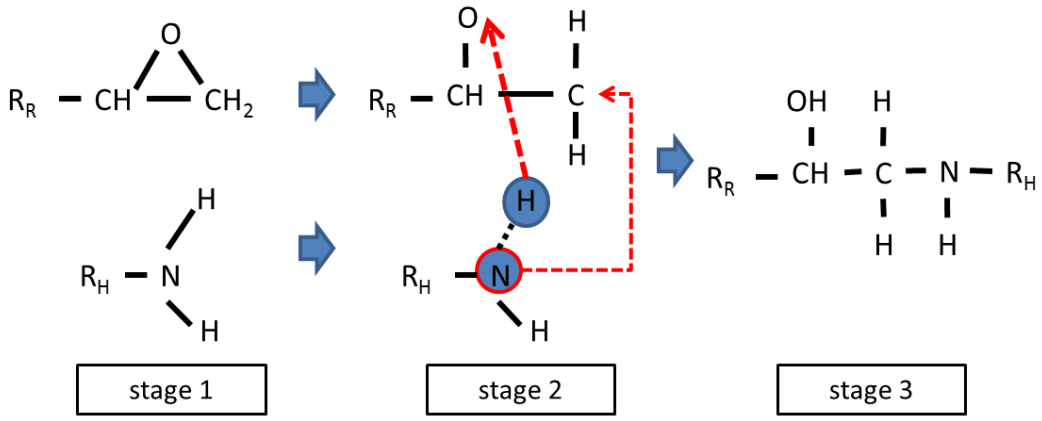

Figure 2.9. Covalent Bond Generation Process, where R_R is the Remaining Part of the Resin, R_H is the Remaining Part of the Hardener, and C, N, H, and O are Carbon, Nitrogen, Hydrogen, and Oxygen Atom, Respectively.

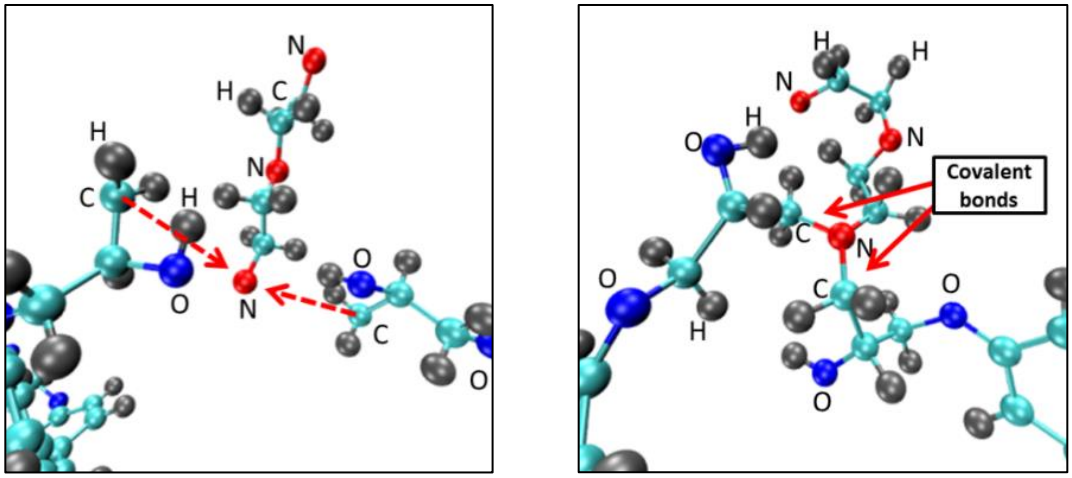

(a) (b)

Figure 2.10. Schematic of the Molecular Structure Before and After Covalent Bond Generation; Gray, Cyan, Blue, Red Sphere Represent Hydrogen, Carbon, Oxygen, and Nitrogen Atoms, Respectively. The Figure also Shows that Nitrogen Makes Two Covalent Bonds with Two DGEBFs.

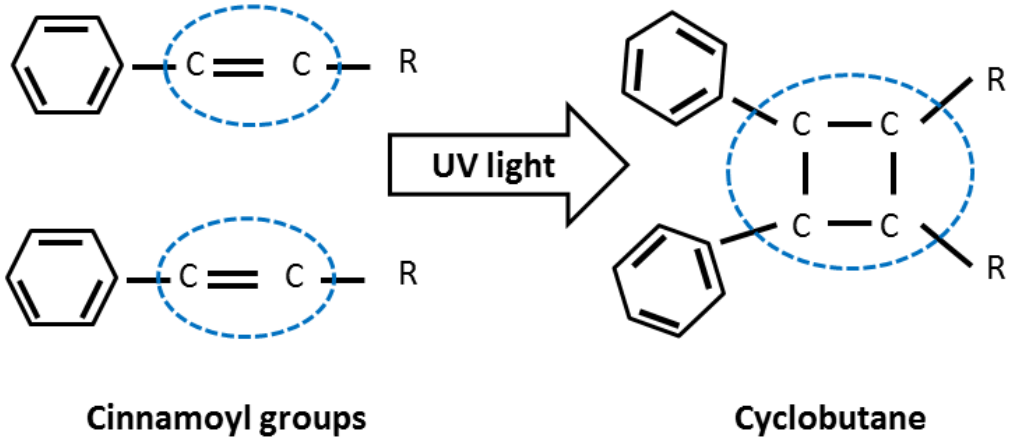

Figure 2.11. Schematic of Cyclobutane Generation Process in TCE Monomers.

Activated DGEBF and DETA molecules are adapted to emulate covalent bond generation between DGEBF and DETA in MD simulation. Activated DGEBF is developed by changing the epoxide group to the methylene group, and activated DETA is produced

by removing five hydrogen atoms from three nitrogen atoms of DETA, as seen in Figure 2.12. Neat epoxy and smart polymer unit cells are constructed using the activated DGEBF and DETA molecules, and 40% cross-linked TCE molecules. PBC are applied to the boundaries of the unit cell in all three directions (initial size of the unit cell is approximately 7 x 7 x 7 nm^3).

Conjugate gradient energy minimization is performed after the initial configuration; this is followed by NPT (isobaric-isothermal) ensemble simulation to equilibrate the unit cells. A Nose-Hoover thermostat and barostat are used to control the temperature and pressure at 300K and 1atm for 150ps. The equilibration of the system is achieved when potential energy shows the fluctuation of a constant mean value. The equilibration step allows for molecules to maintain a minimum distance. Subsequently, the MD simulator generates covalent bonds when the distances between carbon and nitrogen atoms are within the cutoff distance of 4Å. Due to the stochastic nature of the phenomena, there is clearly no validated cutoff distance for covalent bond generation in MD simulation available in the literature. The value of 4Å used in this study has been widely used on various epoxy-based systems [117-119], and also is equivalent to the van der Waals radii, i.e., the closest distance that two molecules can possibly have.

In addition to the cut-off distance, a reasonable curing simulation time needs to be selected to ensure that the conversion degree does not increase/decrease unrealistically and thus arbitrarily determine long/short curing simulation times. Since experimental curing time is in one-hour units and even a one-minute MD simulation is exceedingly difficult to implement, a rational curing simulation time should be addressed. In this work, total energy information is used to determine the rational simulation time (1000 steps with the time step

of 0.1 fs for DGEBF/DETA) wherein the total energy meets the first peak (a clear drop should be observed after this peak) of the total energy, as shown in Figure 2.13. After generating C-N covalent bonds, hydrogen atoms are added to the activated nitrogen atoms that fail to generate a covalent bond with carbon atoms. With the new generated covalent bonds, energy minimization is performed to reduce undesired repulsive forces between atoms.

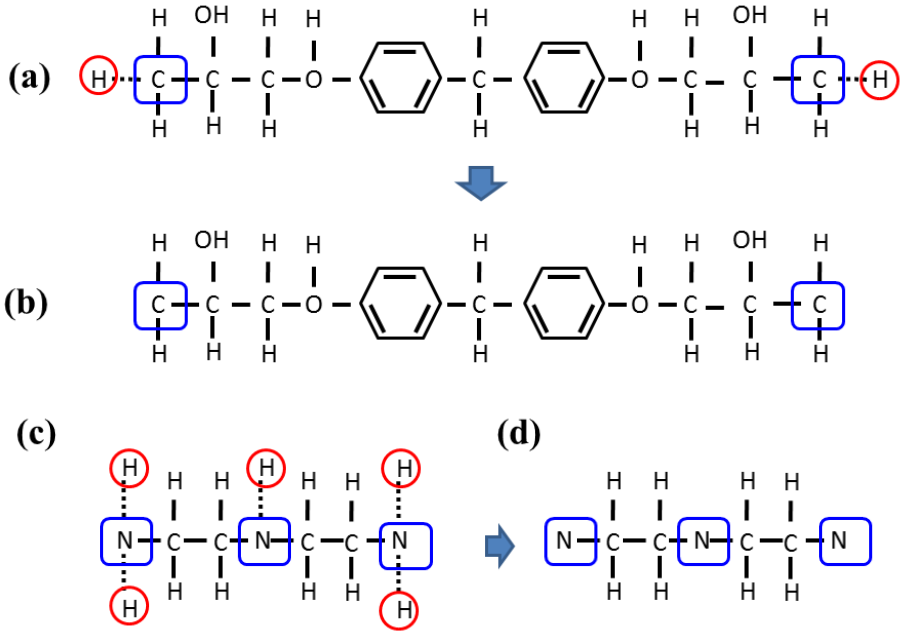

Figure 2.12. Chemical Structures of Activated DGEBF and DETA: a) Pre-activated DGEBF; b) Activated DGEBF After Removing Two Hydrogen Atoms with Red Circle Markings; c) Pre-activated DETA; d) Activated DETA After Removing Five Hydrogen Atoms with Red Circle Markings.

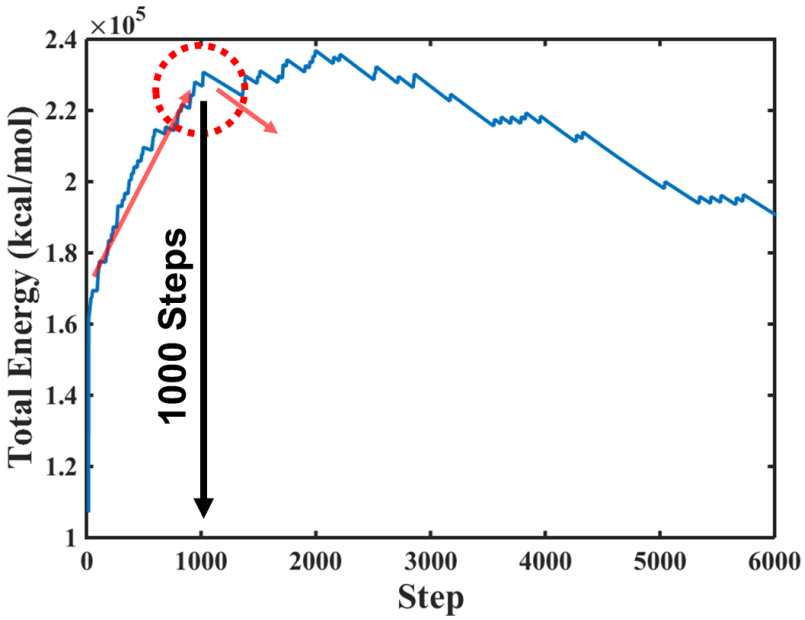

Figure 2.13. Decision of Curing Simulation Time (0.1 fs Time Step).

Estimation of Conversion Degree: As stated earlier, a general method for estimating the conversion degree of the epoxy-based system continues to be a challenging issue since the conversion mechanism is material dependent and also a strong stochastic phenomenon [120-122]. Several numerical studies have been conducted to predict the conversion degree for different epoxy resin and hardener, but very few of the MD simulations have been validated via experimental results [64, 117]. In this study, a purely stochastic approach to predict a most likely conversion degree for epoxy-based system using MD simulation is used. Since this method is based on calculating the inter/intramolecular potential energy, it is expected to be applicable to a range of epoxy-based thermoset systems.

The methodology comprises the following three steps: i) construct multiple unit cells with stochastic initial location of molecules, ii) generate numerical C-N covalent bonds for every unit cell, and iii) find average values of the conversion degree of all the unit cells. In

this study 500 unit cells are constructed and C-N covalent bonds generated for all unit cells using the numerical curing process. The number 500 was determined based on an additional stochastic study using 1000 unit cells to measure the average conversion degree as increasing the number of unit cells. Figure 2.15 shows a large fluctuation of the mean value at the beginning of the plot; this fluctuation, however, is shown to have diminished after using over 500 unit cells.

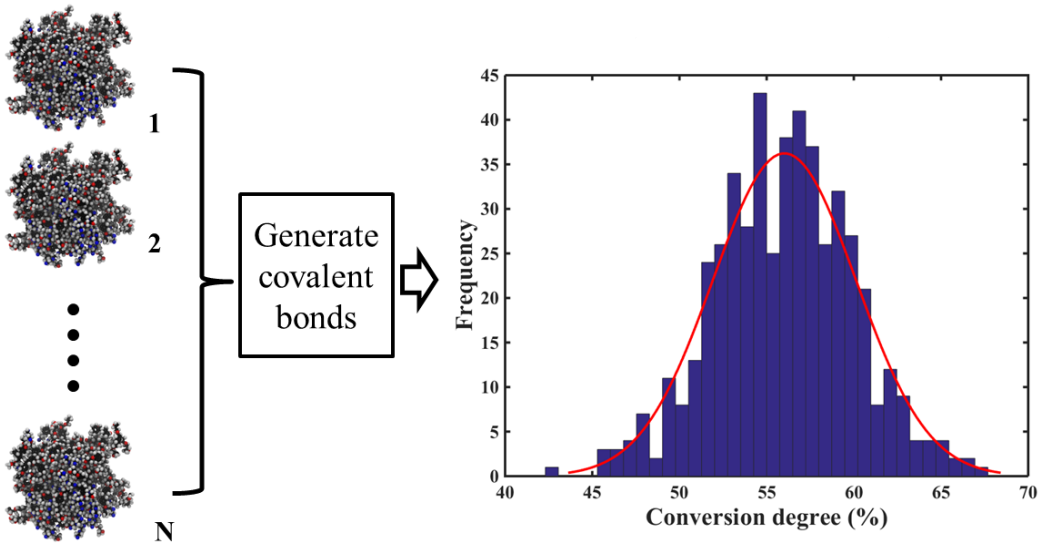

Figure 2.14. Schematic of Conversion Degree Estimation using a Stochastic Approach.

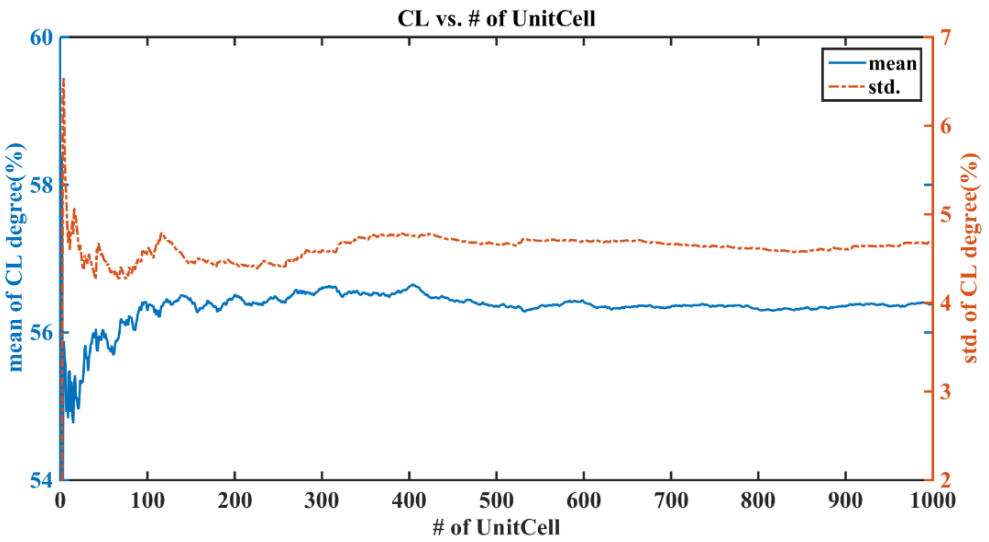

Figure 2.15. Average Values of Conversion Degree vs. the Number of Unit Cells.

Figure 2.16 and Figure 2.17 show two frequency distributions that have been plotted after obtaining conversion degree data from two systems: neat epoxy and smart polymer. Two normal (Gaussian)-like distributions are obtained from the histograms for both neat epoxy (mean is 56% and standard deviation is 4.1%) and smart polymer (mean is 52.7% and standard deviation is 4.2%). Calculated average conversion degrees are considered the most likely conversion degrees in this study. Using these values, representative neat epoxy and smart polymer unit cells are constructed to validate the MD simulation methodologies including epoxy curing and Tg estimation; the validation is discussed in Chapter 3.

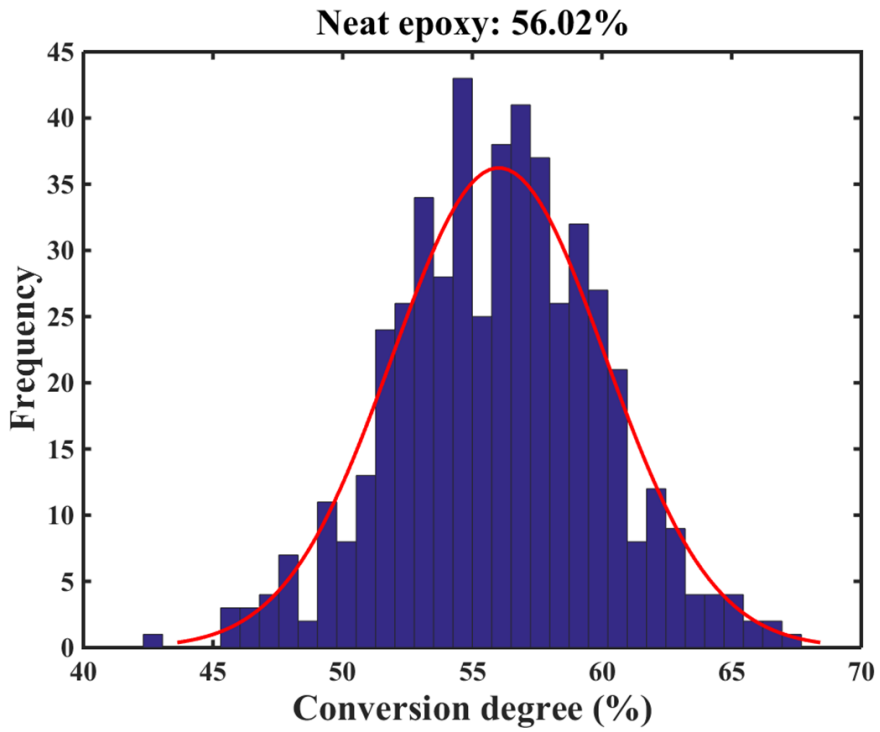

Figure 2.16. Most Likely Conversion Degrees of Neat Epoxy; Solid Red Lines are Fitted Normal Distribution.

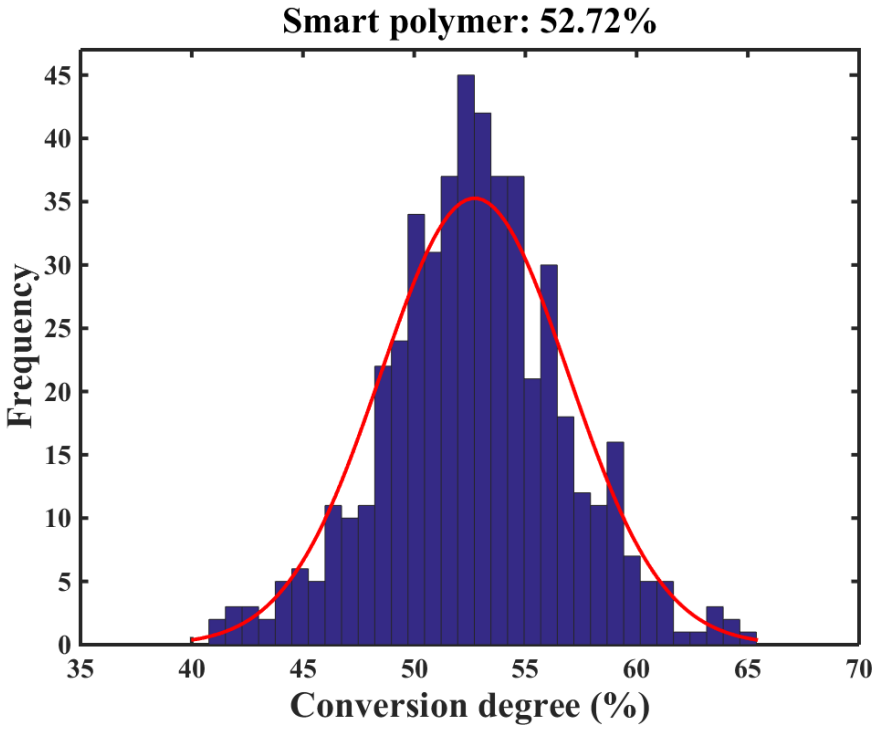

Figure 2.17. Most Likely Conversion Degrees of Smart Polymer; Solid Red Lines are Fitted Normal Distribution.

2.3.2. Numerical Ultraviolet Dimerization

Dimerization: In experiments, the cyclobutane-based mechanophore is synthesized by TCE monomer at room temperature in a thermoset polymer matrix through UV dimerization. The cinnamoyl group within the TCE monomers transforms to cyclobutane (four carbon atom ring structure) due to UV-light energy. It is noted that epoxy curing occurs while the cyclobutanes are synthesized; hence, epoxy curing simulation and numerical UV dimerization must be performed simultaneously. Through this curing process, physical entanglement between the epoxy network and TCE polymer chain also can be simulated. Attaining this physical entanglement in MD simulation is critical because the physical entanglement directly affects the system's mechanical properties as well as its local force distribution. The cut-off distance-based covalent bond generation method for epoxy curing simulation is extended to perform the numerical UV dimerization.

In addition to covalent bond generation, the following two issues should also be addressed for numerical dimerization: i) structural conversion from cinnamoyl group to cyclobutane; ii) transformation of topology information (parametric conversion) between two structures. Figure 2.18 shows the difference in structure and bond length between the TCE monomer and polymer. Huge differences in bond potential energies can be seen despite small differences in bond length between a carbon single bond (348 kJ/mol) and a double bond (614 kJ/mol) based on Ref. [123] (Table 2.3). Assigning the correct topology information after generating the cyclobutane structures, therefore, is critical. Furthermore, the C=C double bonds of the cinnamoyl group affect the topology of the neighboring atom, which changes accordingly when the double bond changes to a single bond.

The numerical UV dimerization method includes the following standard steps: i) introduce two TCE monomers in a simulation unit cell (approximated size of the unit cell is 3 x 3 x 3 nm^3); ii) equilibrate the unit cell using NPT (isobaric-isothermal) ensemble (300K and 1 atm) with Nose-Hoover thermostat/barostat using MMFF; iii) generate covalent bonds when the carbon atoms belonging to the cinnamoyl group are within a pre-defined cutoff distance of 6Å (four times the length of a C-C bond); and iv) assign correct topology information to the newly generated cyclobutane structure. All the MMFF force-field information for cinnamoyl group and cyclobutane are based on the data generated by the SIB [114]. The force-field information of cyclobutane is used when the cinnamoyl groups are transformed to cyclobutane through this dimerization approach. Note that the purpose of this simulation is to show that the numerical UV dimerization enables the synthesis of two cinnamoyl groups into one cyclobutane structure correctly; therefore, only two TCE monomers are involved in this simulation, which results in a small size of unit cell.

In Section 2.3.4, large systems comprising multiple molecules of epoxy resin, hardener, and TCE monomers are used to construct the simulation unit cell of the smart polymer and to perform the epoxy curing simulation and numerical UV dimerization simultaneously. In addition to transforming the structure/topology, the numerical UV dimerization method can potentially lead to the construction of two types of cyclobutane structures, namely, head-to-head and head-to-tail structures, as shown in Figure 2.19. This transformation process is very important because not only does it lead to a variety of numerical dimerization products, but it also allows the generation of a consecutive TCE polymer chain (smart material chain), which then leads to the physical entanglement with the epoxy

network chain (see Figure 2.20). In Chapter 3, this numerical UV dimerization method is verified using a bond dissociation energy calculation method.

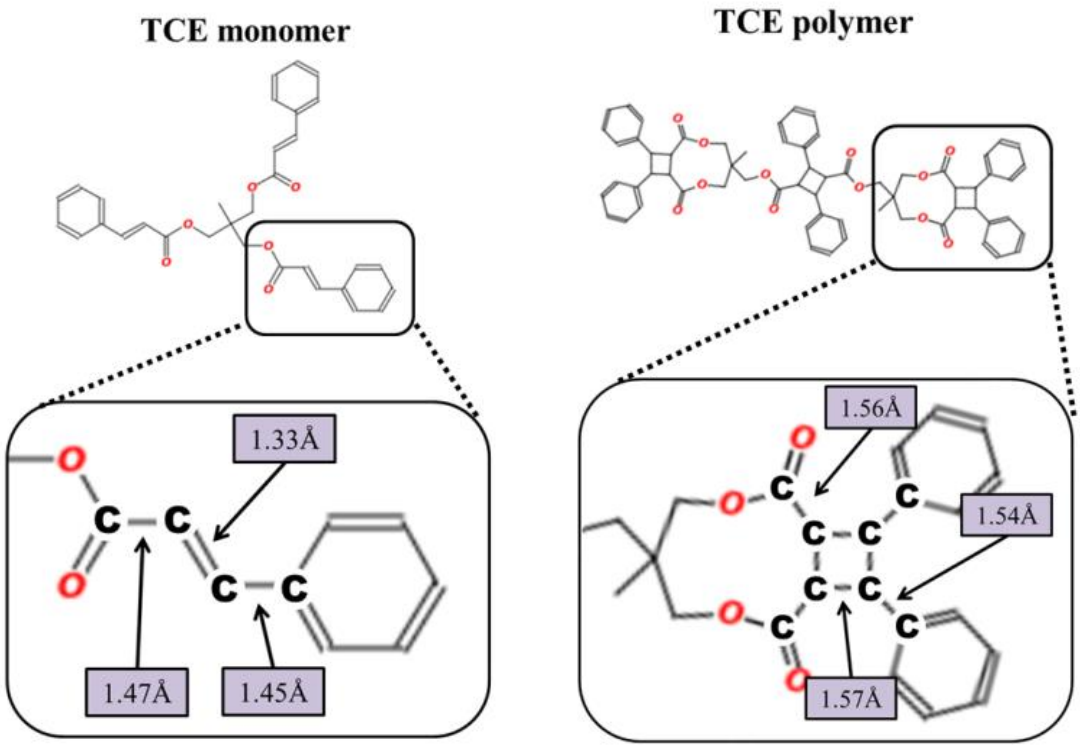

(a) (b)

Figure 2.18. Topological Difference Between Cinnamoyl Group in TCE Monomer (a) and Cyclobutane in TCE Polymer (b).

Table 2.3. Relation of Bond Length and Energy [123].

Bond	Length	Energy
C-C	1.54Å	348kJ/mol
C=C	1.34Å	614kJ/mol
C≡C	1.20Å	839kJ/mol

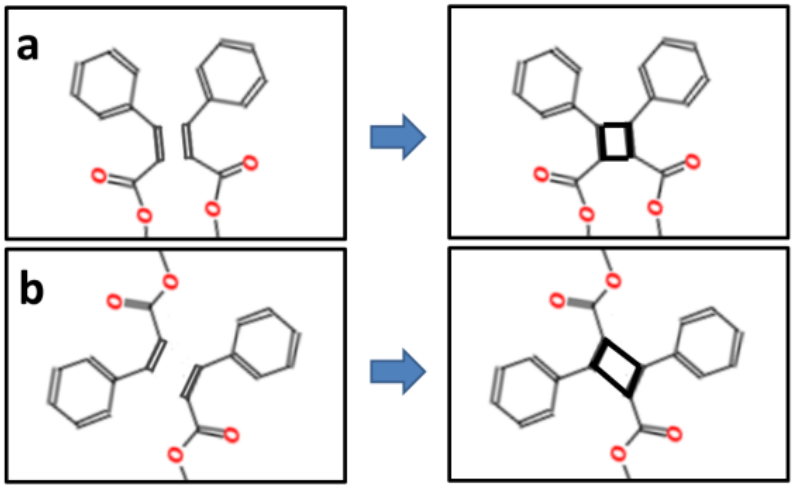

Figure 2.19. Two Types of Possible Cyclobutane Structures; (a) Head-to-Head And (b) Head-to-Tail.

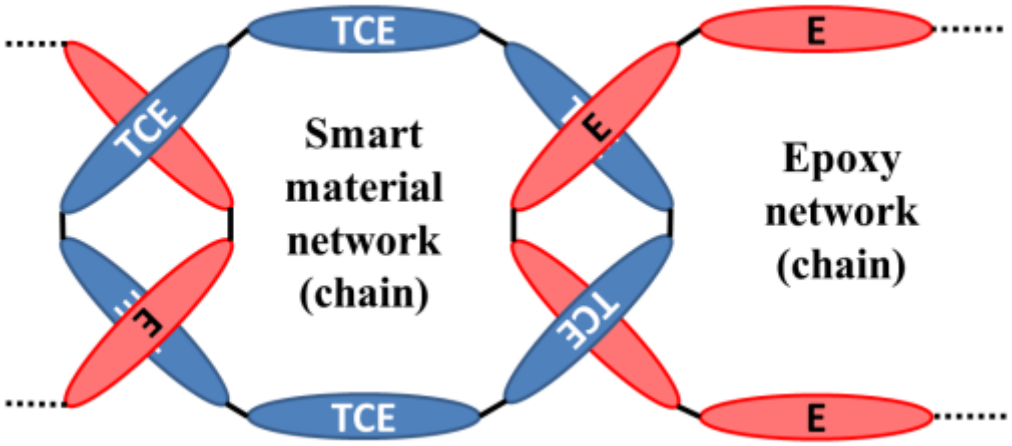

Figure 2.20. Schematic of Entanglement Between Smart Material Network and Epoxy Network ('TCE': TCE Monomers, 'E': Epoxy Molecule).

2.3.3. Simulation of Covalent Bond Dissociation

Reactive Force Field: To capture the covalent bond breakage (interatomic phenomena), a quantum mechanics-based simulation algorithm employed, which requires

significant amounts of computational time, even for a small system. Since the goal of this work is to analyze damage initiation in bulk polymeric system (> 10,000 atoms), quantum mechanics-based algorithms are not necessary. Instead, a special force-field is introduced to capture the covalent bond dissociation. Then, a bond potential functional form of the classical force-fields is approximated in a quadratic function to optimize the covalent bond around the equilibrium bond length. This approximation is very useful and computationally efficient when the system is around the equilibrium state. Although the classical force-field method is more effective for the study of molecular conformation, it does not capture the material response occurring away from the equilibrium point, such as bond breakage. To address this issue, several modified force-fields have been developed [75, 79, 124-126].

$$E_{bond} = E_{repulsive} + E_{attractive} \qquad (2.10)$$

$$E_{repulsive} = 4\,\varepsilon[\left(\frac{\sigma}{r}\right)^{12} - \left(\frac{\sigma}{r}\right)^{6}] \qquad (2.17)$$

$$E_{attractive} = K\,(r - r_1)(r - r_2)r^2 + E_0\,, \quad (r < r_c) \\ = E_0\,, (r \geq r_c) \qquad (2.18)$$

One of examples is to use a modified version of the Kremer-Grest model [124-126]. In the KG model, atoms are bonded together by combining the LJ potential for repulsive interaction and the finite extensible nonlinear elastic (FENE) for attractive interaction. In the modified version of KG, the FENE term was replaced with a quartic bond potential (Equation 2.18) since FENE is optimized for the system around equilibrium state. Equation 2.16 consists of two terms: quartic bond potential and LJ potential (Equation 2.17) where ε is LJ energy coefficient, σ is LJ diameter, r_1 is 2.2589σ, r_2 is 1.5σ, K is 1434 ε/ σ^4, and E_0 is 67.2 ε. In LJ units, ε and σ were taken as unity. This method, however, cannot be applied

to the system with 1-3 atom pairs (angle) or 1-4 atom pairs (dihedral and improper), which are big parts of an epoxy-based thermoset system.

In the literature, there are several bond-order based force-fields available: the embedded atom method (EAM) [124] for crystallographic materials such as metal, the Stillinger and Weber (SW) [127] method for silicon, the Tersoff [128], and the reactive empirical bond-order (REBO) method [129] for carbon nanotubes or graphene. However, due to the complexity of the parameterization of bond-order based force-fields, the challenge has been in the ability to apply these bond-ordered force-fields to complex systems, such as hydrocarbon compounds, epoxy, and protein. Recently, van Duin and coworkers [130] developed ReaxFF for hydrocarbon compounds. In ReaxFF, every functional form for the potential energy such as bonds, angles, dihedrals, and impropers, consists of the bond order (based on the valence bond theory [131, 132]) which is a function of bond length; hence, ReaxFF can describe a range of materials by extracting the parameter set of the bond order, which is strongly material dependent. Parameter sets are available for various multicomponent materials such as organic materials consisting of carbon, oxygen, and hydrogen atoms [130], energetic materials under extreme conduction [133], decomposition of explosives [134], thermal decomposition of polymers [135], heterogeneous catalysts [136], fuel cells [137], crack propagation in silicon crystals [138], catalytic formation of carbon nanotubes [139], and hydrocarbon oxidation [135].

The configuration of ReaxFF potential function is very similar to the classical force-field, but with slight adjustments wherein $E_{R\_torsion}$ represents both dihedral and improper potentials ('R' in $E_{R\_torsion}$ stands for ReaxFF).

$$E_{ReaxFF} = E_{R\_bond} + E_{R\_angle} + E_{R\_torsion} + E_{R\_vdW} + E_{R\_coulomb} \qquad (2.19)$$

Each potential energy term in Equation 2.19 is a function of bond-order (BO) term,

$$BO_{ij} = exp\left[\beta_1 \left(\frac{r_{ij}}{r_0^{\sigma}}\right)^{\beta_2}\right] + exp\left[\beta_3 \left(\frac{r_{ij}}{r_0^{\pi}}\right)^{\beta_4}\right] + exp\left[\beta_5 \left(\frac{r_{ij}}{r_0^{\pi\pi}}\right)^{\beta_6}\right], \qquad (2.20)$$

where $\beta_1 \sim \beta_6$ are bond-order parameter obtained from the optimization process. These parameters are calculated to minimize the error between ReaxFF and DFT. The terms $r_o^{\sigma}, r_o^{\pi}, and\ r_o^{\pi\pi}$ represent the cut-off distance for different bond formations and r_{ij} is the current bond length. In chemistry, three typical covalent bonds exist: σ bond, π bond, and π-π bond (which are also known as single bond (σ bond), double bond (σ + π bond), and triple bond (σ + π- π bond)). In the case of the carbon-hydrogen or hydrogen-hydrogen bonds, which has a single bond, only the first term in Equation 2.20 can exist. Figure 2.21 shows the bond order graph as a function of the bond length of the carbon-carbon bond; therefore, the covalent bond breakage due to physical separation can be described correctly.

However, the bond order equation (Equation 2.20) itself generates an artificial residue, which makes the output of this equation violate the valence bond theory [131, 132], in some cases when modeling a system around equilibrium. An example of this is shown in Figure 2.22. The calculated bond orders of ethane indicate that each carbon has a weak bond order (attraction) with its second nearest neighbor hydrogen atoms due to the equilibrium distance between two atoms (≈ 2.15 Å). Although the corresponding bond order due to this equilibrium distance is 0.1 using Equation 2.20, this causes the carbon to have a total bond order of 4.17 (Figure 2.22a), a phenomenon called ‘over-coordination.' The total bond order of carbon should not exceed 4 based on the valence bond theory; the

incorrect bond order can yield unrealistic behavior and this excess must be adjusted. Figure 2.22(b) shows the corrected version (resulting bond order: 3.88) of the bond order of ethane based on the following two approaches: i) the small bond orders involving the ethane's carbon atom are significantly reduced to minimize their effect if the carbon atom has a bond order of 4 or more; ii) the small bond orders are allowed if the carbon atom has less than 4 bond orders. Complex correction functions are developed to remove the artificial residues, and their presence is not chemically meaningful. As such, the correction functions are not discussed here, and the BO_{ij} in Equation 2.20 will be treated as the corrected version hereafter.

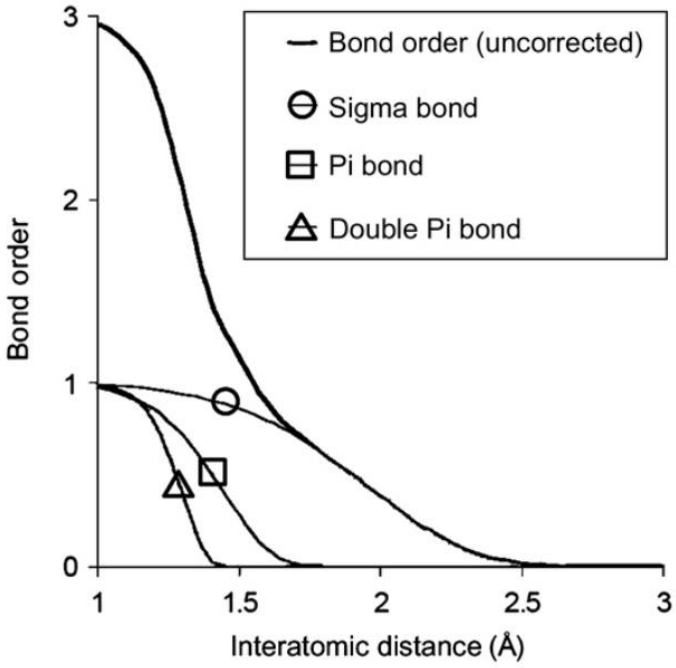

Figure 2.21. Interatomic Distance Dependency of the Carbon-Carbon Bond Order [130, 140].

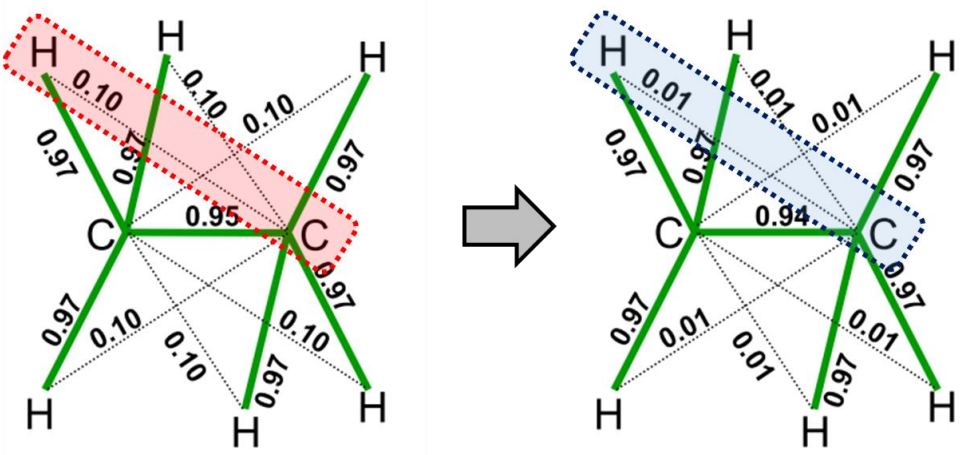

(a) (b)

Figure 2.22. Correction of Unrealistic Bond Order Between the Carbon Atom (C) and the Hydrogen Atom in Valence Angle (H-C-C) Topology; Green Solid Line Represents Covalent Bond and Bond Order is Corrected for Residual 1-3 Bond Orders: BO of 0.1 (Red Dotted Line Box in (a)) is Reduced to 0.01 (Blue Dotted Line Box in (b)) [130, 140]

Using the bond order function BO_{ij}, realistic chemical bond behavior can be captured for bond formation and bond breakage. The traditional harmonic potential functions for bond potential energy between two atoms goes to infinity due to the quadratic function, particularly when the atoms get separated; therefore, it is not physically meaningful and cannot be used for fracture mechanics at the molecular level. This limitation can be addressed by the bond potential of ReaxFF,

$$-\alpha_1 \cdot BO_{ij} \cdot exp\,[\alpha_2(1 - BO_{ij}^{\alpha_3})], \qquad (2.21)$$

where α_1 is bond energy coefficient (kcal/mol) and α_2, α_3 are model parameters, obtained by optimization using a training data set from the DFT calculation. The bond order in the bond potential vanishes when the two atoms separate. Figure 2.23 illustrates the bond potential energies between the classical force-field and ReaxFF by stretching the carbon-carbon bond in ethane molecule. As mentioned previously, the bond energy calculated by

the classical force-field goes up as the bond is stretched; however, the bond energy calculated by the ReaxFF gets saturated when the bond is extended beyond 2.2~2.3 Å, which is used to define the breaking point of the covalent bond.

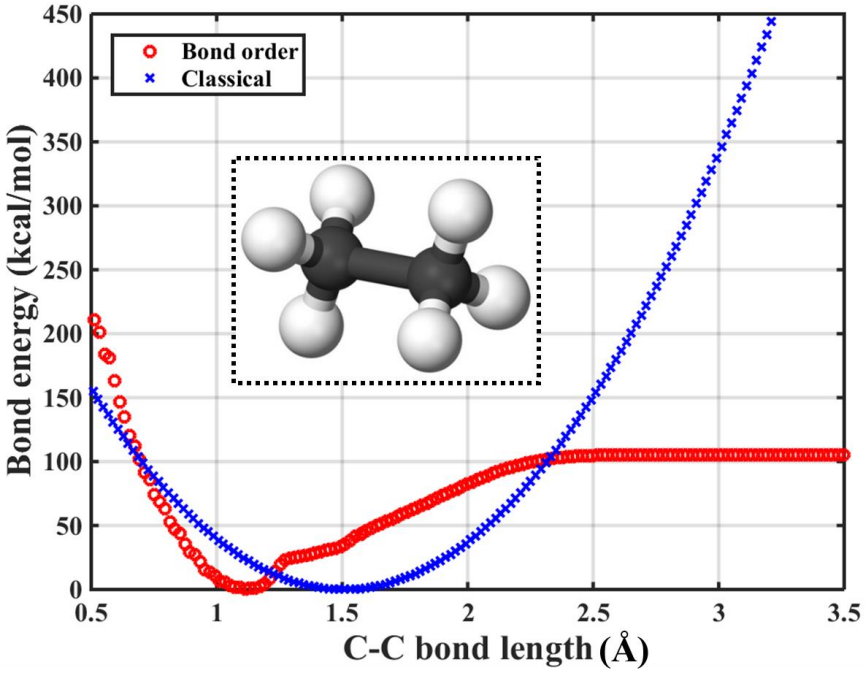

Figure 2.23. Chemical Structure of Ethane and Bond Potential Energy Graphs Calculated using Classical Force-Field (Blue Cross) and Bond-Order Based Force-Field (Red Circle).

The angle term E_{R_angle} in Equation 2.19 has the following form,

$$[1 - exp[\alpha_4\, BO_{ij}^{\alpha_5}]] \cdot [1 - exp[\alpha_4\, BO_{jk}^{\alpha_5}]] \cdot f_{AngleOver} \cdot \left(\alpha_6 - \alpha_6\, exp\left(-\alpha_7 \left(\varphi_{eq} - \varphi_{ijk}\right)^2\right)\right), \quad (2.22)$$

where α_4 and α_5 are model parameters, α_6 is angle energy coefficient (kcal/mol), α_7 is a valence angle parameter $(1/rad)^2$, φ_{eq} is an equilibrium angle, φ_{ijk} is current angle. $f_{AngleOver}$ minimizes the effect of over-coordination in central atom j (i-j-k 3-atom topology) on the

valence angle energy. Similar to bond potential, the angle potential goes to zero as the bond order in the angle term goes to zero.

The torsion term $E_{R\_torsion}$ in Equation 2.19 has the following form,

$$\begin{aligned}[1 - exp[\alpha_8\, BO_{ij}]] \cdot [1 - exp[\alpha_8\, BO_{jk}]] \cdot [1 - exp[\alpha_8\, BO_{kl}]] \cdot \sin(\varphi_{ijk}) \\ \cdot \sin(\varphi_{jkl}) \cdot (\frac{\alpha_9}{2}\, exp\left[\alpha_{10}(BO_{jk} - 3 + f_{TorsionOver})^2\right] \\ \cdot \left(1 - \cos 2\psi_{ijkl}) + \frac{\alpha_{11}}{2}(1 + \cos 3\psi_{ijkl})\right),\end{aligned} \qquad (2.23)$$

where α_8 is a model parameter, α_9 and α_{11} are torsion energy coefficients (kcal/mol), α_{10} is a torsion parameter, ψ_{ijkl} is the current torsional angle, and φ_{ijk} and φ_{jkl} are current valence angles. $f_{TorsionOver}$ minimizes the effect of over-coordination in the atoms j and k (i-j-k-l 4-atom topology). The sine terms imply that the torsion potential vanishes when the valence angles φ_{ijk} and φ_{jkl} are 180°.

Non-bonded interaction terms such as van der Waals and Coulomb potential are also included in ReaxFF; they are independent of bond order. The van der Waals interactions are obtained using a modified Morse potential function,

$$\begin{aligned}D_{ij}[\exp[\delta_{ij} - \frac{1}{r_{vdW}}\left(r_{ij}^{\alpha_{12}} + \left(\frac{1}{r_W}\right)^{\alpha_{12}}\right)^{1/\alpha_{12}}] \\ -2 \cdot \exp[\frac{\delta_{ij}}{2} \cdot (1 - \frac{1}{r_{vdW}}\left(r_{ij}^{\alpha_{12}} + \left(\frac{1}{r_W}\right)^{\alpha_{12}}\right)^{1/\alpha_{12}})]],\end{aligned} \qquad (2.24)$$

where D_{ij} is van der Waals dissociation energy coefficient (kcal/mol) for the atomic pair, α_{12} is a model parameter, r_{vdW} is the van der Waals radius (Å), r_W is van der Waals shielding radius (Å), r_{ij} is current distance between two atoms, and δ_{ij} is van der Waals parameter.

The charge interactions are obtained using a shielded Coulomb's law,

$$D_{Coul} \cdot \left[\frac{q_i \cdot q_j}{\left(r_{ij}^3 + \left(1/\varepsilon_{ij}\right)^3\right)^{1/3}}\right] \quad (2.25)$$

where D_{Coul} is a Coulomb dissociation energy coefficient (kcal/mol), q_i and q_j are atomic charges calculated by the electron equilibration method [141, 142], and ε_{ij} is a shielding parameter to avoid excessive short-range repulsive interaction. This charge calculation scheme is the most expensive aspect of ReaxFF in terms of computational intensity; however, this scheme also leads to successful electrical property estimation.

Selection of ReaxFF Parameter Set: ReaxFF was originally developed by van Duin and co-workers for hydrocarbon compounds [130, 143-146], and many parameter sets have been reported to describe the nonlinear response of diverse materials. Therefore, identifying the most suitable ReaxFF parameter set for the epoxy-based polymer system and mechanophores is an important initial step. First, for the epoxy system, an appropriate ReaxFF parameter set is determined using a bond dissociation energy (BDE) method to calculate the energy required to break a specific C-C bond in the epoxy resin molecule (DGEBF), highlighted by the red box in Figure 2.24. Different ReaxFF parameter sets are considered, and the suitability of each parameter set is evaluated by comparing the calculated BDEs with experimentally measured BDEs. Then BDE calculation is performed using the constrained geometry external force (COGEF) method developed to estimate the strength of covalent bonds by Beyer et al. [147].

The COGEF simulation consists of: i) energy minimization using the conjugate gradient method after constructing a single-molecule unit cell (the size of the simulation unit cell for this COGEF simulation varies with the size of each single molecule); ii) NVT

(isovolume-isothermal) ensemble at 300K equilibration for 20 ps using MMFF (20 ps was sufficient time for the potential energy of the system to reach a certain mean value with adequately small variance); and iii) deformation by moving each atom with constant velocity (0.0005 Å/fs) in the opposite x-direction until the bond breaks (displacement control) using ReaxFF. No constraint is imposed on the y- and z-directions when the COGEF method is executed. Note that all the COGEF simulations are performed with non-periodic boundary conditions since pair potentials caused by molecules in the '*images*' (copy of original unit cell) can affect the BDE calculation indirectly. Using the COGEF method, the trajectories of the atoms are stored every 100 fs, and time average values of every state are stored every 1 fs (0.1 fs time step). The total energy of the system is measured as the geometry deforms, and the results are shown in Figure 2.25. The first total energy drop in each plot represents covalent bond dissociations. The BDEs calculated by different ReaxFF parameter sets (Table 2.4) are compared with the C-C bond energy obtained by pyrolysis experiments [148]; the bond energy was measured to be 389kJ/mol at 298K. Based on the values presented in Table 2.4, the force-field parameters reported by Singh and co-workers [146] show the best correlation with the pyrolysis experimental result; therefore, this parameter set is used for the virtual deformation tests for the epoxy-based system.

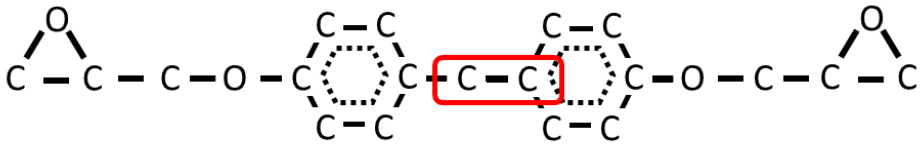

Figure 2.24. Molecular Structure of the Resin (DGEBF) and C-C Bond Used for BDE Calculation.

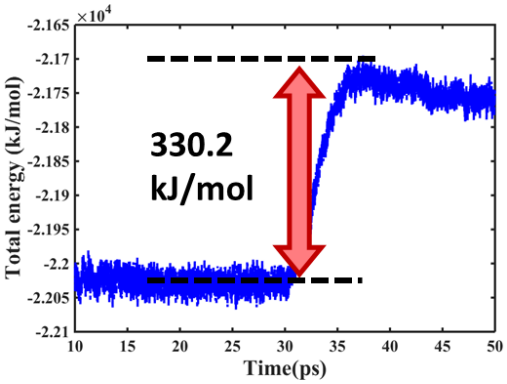

(a) Chenoweth et al. [143]

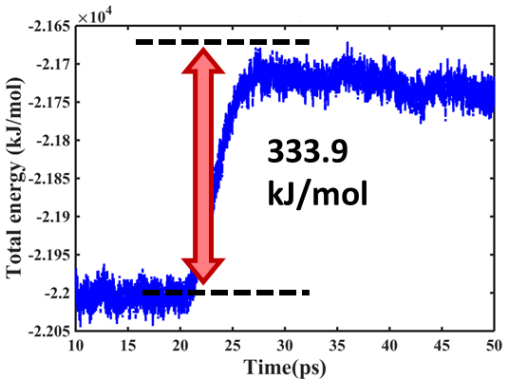

(b) Weismiller et al. [144]

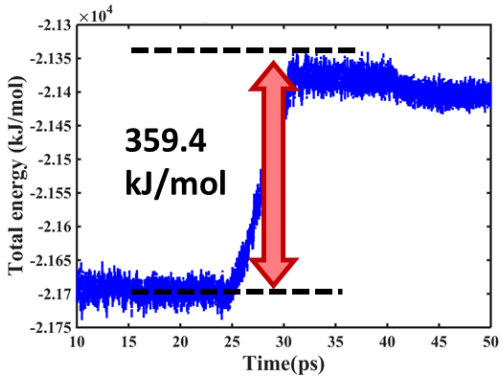

(c) Aryanpour et al. [145]

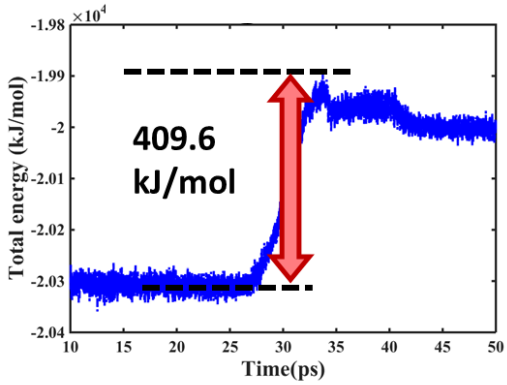

(d) Singh et al. [146]

Figure 2.25. Results of BDE Estimation of C-C Bond in DGEBF using COGEF with Four Different ReaxFF Parameter Sets.

Table 2.4. Calculated BDE with Different Parameter Sets.

ReaxFF Parameter Sets	BDE (kJ/mol)	Error
Chenoweth et al. [143]	330.2	15%
Weismiller et al. [144]	333.9	14%
Aryanpour et al. [145]	359.4	7.6%
Singh et al. [146]	409.6	5.2%

Investigation of the ReaxFF parameter set for mechanophores is also conducted for mechanophore embedded nanocomposites. Since there is no reported ReaxFF parameter set for mechanophores (TCE and Di-AC), dicyano-substituted cyclobutane (DC), which has a structure similar to cyclobutane in TCE polymer, is selected (Figure 2.26). Kryger et al. [28] have estimated the BDE of DC to be 239 kJ/mol using the DFT. BDE of the DC is estimated using the COGEF method through the same procedure used for the C-C bond of DGEBF.

Figure 2.28 shows total energy transition obtained from the COGEF simulations. Table 2.5 presents the BDEs and percentage errors calculated using different ReaxFF parameter sets. The ReaxFF parameter set reported by Singh et al. [146] yields a BDE value of 245.71 kJ/mol and shows the best correlation with Kryger's results (2.8% error). As a result, Singh's parameter set is considered as generating relatively accurate results where the BDE of epoxy resin is validated with the pyrolysis experiments and BDE of cyclobutane is validated with the DFT calculation. Therefore, this parameter set is implemented in this dissertation.

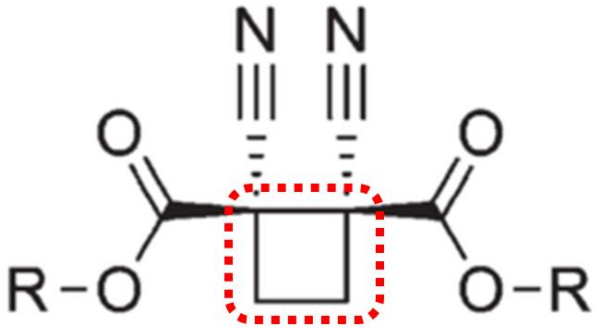

Figure 2.26. Molecular Structure of the DC used for BDE calculation.

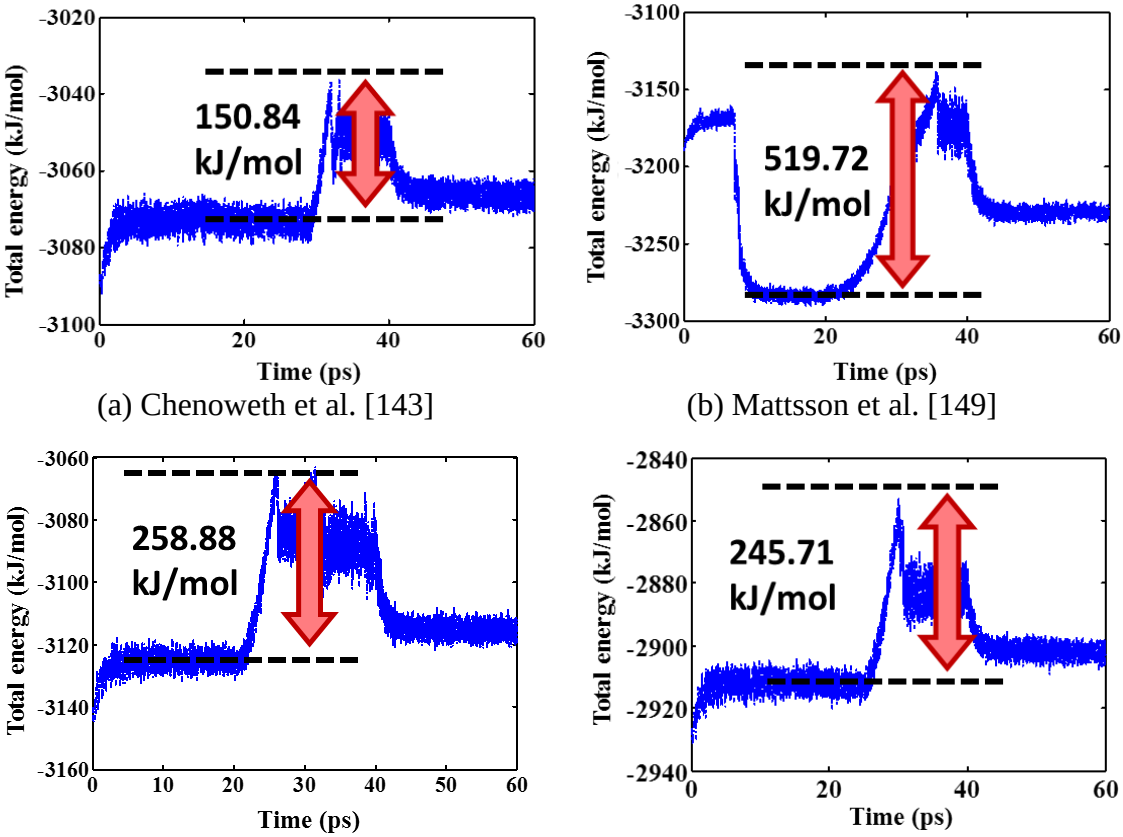

(a) Chenoweth et al. [143] (b) Mattsson et al. [149]

(c) Newsome et al. [150] (d) Singh et al. [146]

Figure 2.27. Results of BDE Estimations of DC using COGEF with Four Different ReaxFF Parameter Sets.

Table 2.5. BDEs of Dicyano-substituted Cyclobutane (DC).

ReaxFF Parameter Sets	BDE (kJ/mol)	Error
Chenoweth et al. [143]	150.83	36%
Mattsson et al. [149]	519.72	117%
Newsome et al. [150]	258.88	8.3%
Singh et al. [146]	245.71	2.8%

2.3.4. Virtual Loading Test

Cyclobutane-based Mechanophore Embedded Thermoset: A representative volume element (RVE) of the smart polymer consists of randomly distributed molecules of the constituents, as shown in Figure 2.8. The weight percentages of the constituents, determined by experiments are as follows: 70 wt% DGEBF, 20 wt% DETA, and 10 wt% TCE monomers. A 100-TCE monomer system is developed and the number of resin/hardener molecules are determined accordingly as shown in Table 2.6 (84,700 atoms). The use of a large number of TCE monomers is ideal since this will improve the likelihood of generating more cyclobutane structures; however, the analysis of a large system will also require considerable computational time. For the trade-off between computational efficiency and likelihood, the 100-TCE monomer system reveals a good number of cyclobutane structures to represent smart polymer with reasonable simulation time.

Epoxy curing/UV dimerization simulations are first performed with MMFF force-field, followed by virtual deformation tests using ReaxFF. Periodic boundary conditions are applied to the boundaries of the RVE (approximate size: $50\times50\times50$ nm^3 at the initial state) along all three directions. Conjugate gradient energy minimization is performed. Subsequently, NPT (isobaric-isothermal) ensemble equilibration is conducted on the RVE at 300K and 1atm (laboratory environment) for 10 ns using the Nose–Hoover thermostat and barostat to control the temperature and pressure, respectively. The 10 ns equilibration of the system allows the potential energy to converge to a mean value with small variance. After equilibration, the simulation of epoxy curing and UV dimerization are performed simultaneously. Degrees of epoxy curing and UV dimerization reaches to around 52% (based on the ratio of the number of new bonds to the maximum possible number of bonds

between carbon atoms of DGEBF and nitrogen atoms of DETA) and around 28% (based on the ratio of the number of new cyclobutane structures to the maximum possible number of cyclobutane structures), respectively. This process is followed by system stabilization using NPT ensemble (300K and 1atm) to reduce the augmented potential energy caused by the newly generated bonds. After system stability is confirmed by checking the potential energy with a mean value and small variance, the virtual deformation tests are performed.

For the virtual deformation test, a novel deformation method using a very high deformation rate (named ultra-high strain rate method) has been used since the quasi-static deformation method [151, 152] implemented by ReaxFF is computationally expensive. This high strain rate method not only allows bond dissociation, but also shows improved computational efficiency. A detailed discussion of this novel deformation method is presented in Chapter 4. During the virtual loading test, the atoms in the volume get remapped to new positions at each time step as the simulation volume deforms (strain rate $2\times10^{13}s^{-1}$). The cyclobutane ring structures are stretched depending on the magnitude of applied force on the carbon atoms of cyclobutane. The atomic forces experienced by the mechanophore molecules are also stored for the local force analysis. It is important to emphasize that the TCE polymer does not generate any covalent bond with the epoxy network. The physical entanglement between the epoxy network and TCE polymer chain allows load transfer, which can lead to mechanophore activation (covalent bond dissociation).

Table 2.6. Components in the Smart Polymer (DGEBF:DETA:TCE=70%:20%:10%)

	Weight	Formula	Number of Molecules
DGEBF	313 g/mol	$C_{19}H_{20}O_4$	1300
DETA	103 g/mol	$C_4H_{13}N_3$	1100
TCE	510 g/mol	$C_{32}H_{30}O_6$	100

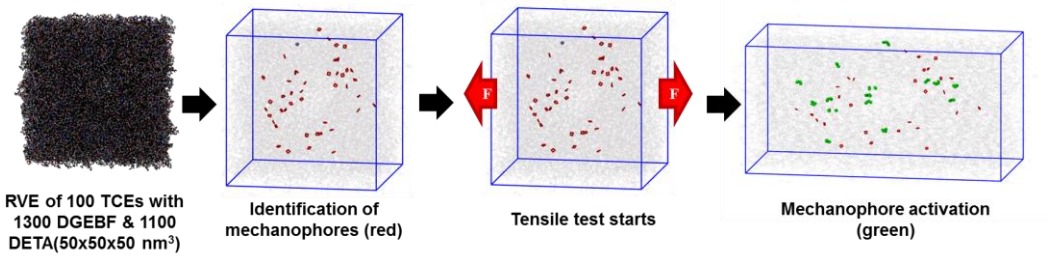

(a) (b) (c)

Figure 2.28. Procedure for Simulation of Mechanophore Activation: a) Prepare Dimerized Smart Polymer RVE, b) Start the Deformation Test (Atoms in Red Represents Healthy Cyclobutanes, Atoms in Green Represents Damaged Cyclobutanes), and c) Observe Atoms in Green as the RVE Deforms.

Anthracene-based Mechanophore Embedded Thermoset: The MD simulation unit cell of the Di-AC embedded nanocomposites is constructed with randomly distributed molecules of the constituents (Figure 2.29). The weight percentages of the constituents in the nanocomposite used for the experiments are 74.8 wt% DGEBF, 20.2 wt% DETA, and 5 wt% Di-AC. The resulting epoxy-based matrix has an extensively crosslinked structure which is generated by the epoxy curing process. As mentioned in Section 2.3.1, the curing of epoxy resin and hardener is simulated using the cut-off distance-based covalent bond

generation method. However, since the Di-AC molecule does not have reactive sites for the epoxy resin or hardener, it can be assumed that there is no covalent bond generation between Di-AC and the epoxy mixture. Fifty (50) Di-ACs are used to build the MD simulation unit cell, and the number of resin/hardener molecules are determined based on the experimental weight percentage (see Table 2.7, 69260 atoms). Periodic boundary conditions are also applied to the boundaries of the unit cell (approximated size of the unit cell is 15×15×15 nm^3 at the initial state) along all three directions. Conjugate gradient-based energy minimization is then performed using MMFF. Subsequently, NPT (isobaric-isothermal) ensemble is used to equilibrate the unit cell at 300 K and 1 atm (laboratory conditions) for 10 ns along with the Nose–Hoover thermostat and barostat to control the temperature and pressure, respectively. The 10 ns equilibration of the system allows the potential energy to converge to a mean value with small variance. After equilibration, the epoxy curing simulation is performed. NPT ensemble (300K and 1atm) is conducted again to reduce the augmented potential energy due to the newly generated bonds. After system equilibration is verified, the virtual loading tests are performed using ReaxFF. The cured Di-AC embedded nanocomposite, e.g., a cyclobutane-based nanocomposite, is deformed by the ultra-high strain rate method, and sequentially bond dissociations are captured. Unlike the COGEF method in which the atom movements cause deformation, the virtual loading test deforms the unit cell volume first, and the atoms' locations are varied according to the volume deformation (also known as affine transformation) [153, 154].

Table 2.7. Components in the Smart Polymer (DGEBF:DETA:Di-AC=74.8%:20.2%:5%)

	Weight	Formula	# of molecules
DGEBF	313 g/mol	$C_{19}H_{20}O_4$	1120
DETA	103 g/mol	$C_4H_{13}N_3$	920
Di-AC	444 g/mol	$C_{30}H_{20}O_4$	50

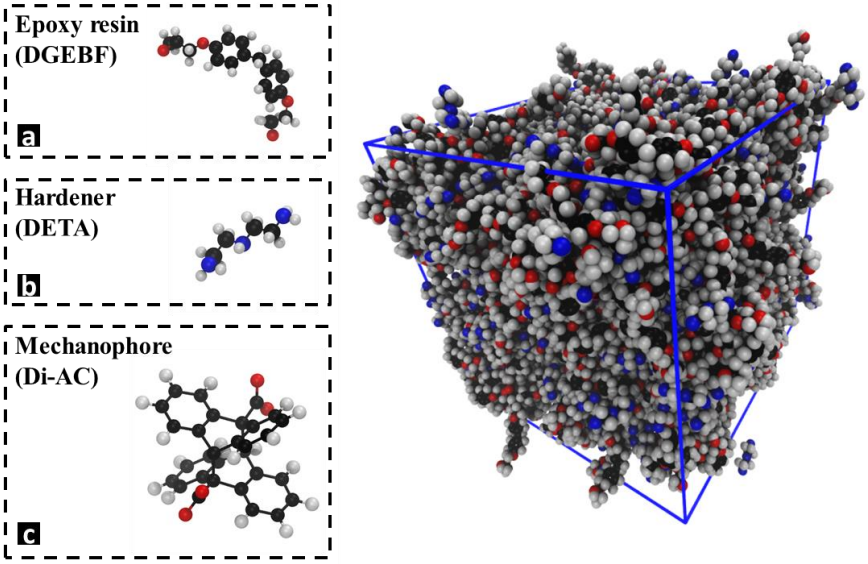

Figure 2.29. Schematic of the MD Simulation Unit Cell: a) Epoxy Resin (DGEBF), b) Hardener (DETA), c) Di-AC Mechanophore.

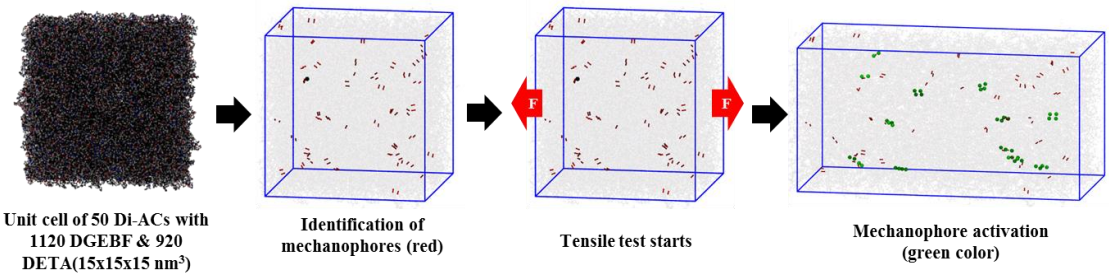

Figure 2.30. Procedure for Simulation of Mechanophore Activation: a) Prepare Bulk Di-AC Embedded Epoxy Polymer Matrix Unit Cell, b) Start Virtual Loading Test (Atoms in Red Color Represents Healthy Di-AC, Atoms in Green Color Represents Damaged Di-AC), and c) Observe Green Color Atoms during the Loading Test.

2.3.5. Local Force/Work Analysis

After the virtual deformation test, the mechanophore activation (color change phenomenon) is simulated using the atoms' trajectory data and by monitoring the C-C bond lengths of mechanophores, as shown in Figure 2.28 and Figure 2.30. The color change from red (healthy mechanophores) to green (damaged mechanophores) is triggered when the C-C bonds are stretched beyond a critical bond length around 2.2Å, as seen in Figure 2.23. However, these simulations are considered only a qualitative visualization approach. To more thoroughly investigate the physical parameters activating mechanophore in an epoxy polymer matrix, a quantitative analysis is more desirable. As physical parameters, two candidates are considered: force and work. In this dissertation, the term 'local' is used to designate the force and work experienced by atoms. In this section, local force/work analysis methods are discussed. Prior to the introduction of the analysis methodologies, the properties of mechanophores, including BDE and bond rupture force (BRF), are

characterized. They are then used as thresholds in the analysis to determine mechanophore activation.

Characterization of Mechanophores: Two mechanophores (TCE and Di-AC) are characterized using the COGEF method with the ReaxFF, since there is no reported experimental/numerical study on BDE or BRF mechanophores. For this investigation, Singh's ReaxFF parameter set is used [146]. The characterization of cyclobutane is conducted first with a pre-dimerized TCE polymer. The COGEF method follows the standard steps: i) energy minimization using the conjugate gradient method with MMFF; ii) NVT (isovolume-isothermal) ensemble at 300K equilibration for 50 ps where the potential energy of the system reaches a certain value with small variance; and iii) deformation by moving each carbon atom with constant velocity (0.0005 Å/fs) in opposite x-direction until the bond breaks (displacement control) using ReaxFF. Figure 2.31 illustrates the boundary condition in terms of the moving directions of atoms (red arrows). No constraint is imposed in the y- and z-directions while the COGEF method is performed. Note that as mentioned in Section 2.3.3, this simulation is performed in non-periodic boundary condition because pair potentials due to the neighbor clone image of the system can indirectly disturb the BDE calculation. The total energy of the system is measured as the geometry deforms, as shown in Figure 2.32. The first drop in total energy is observed around 56 ps, which represents covalent bond dissociation. The simulation results reveal a BDE of 315.05 kJ/mol. In addition, the COGEF method provides the critical bond length (2.16 Å in Figure 2.33) and the magnitude of bond rupture force (BRF) (6.8nN in Figure 2.34) at the bond dissociation moment. These results are used as thresholds for mechanophore activation in the following section.

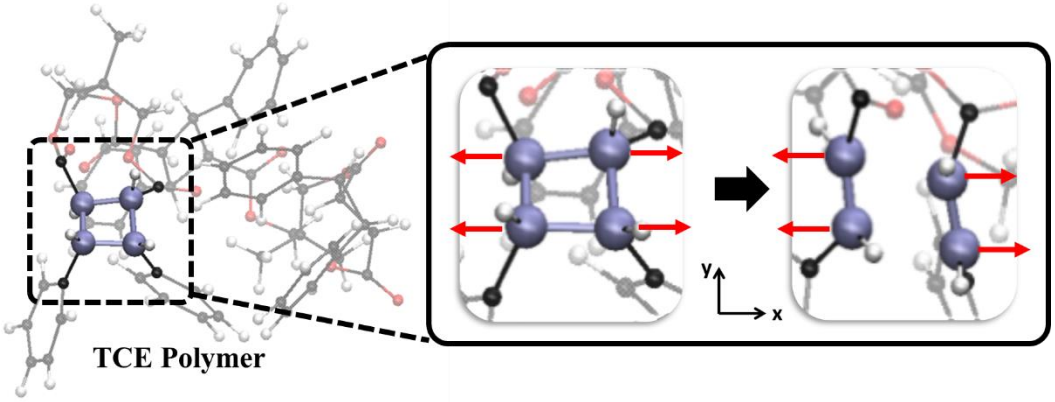

Figure 2.31. Schematic of Boundary Condition for the Tensile Test (Cyclobutane Structure is Emphasized with Bigger Spheres): Constant Velocity (0.0005 Å/Fs) in Opposite X-Direction.

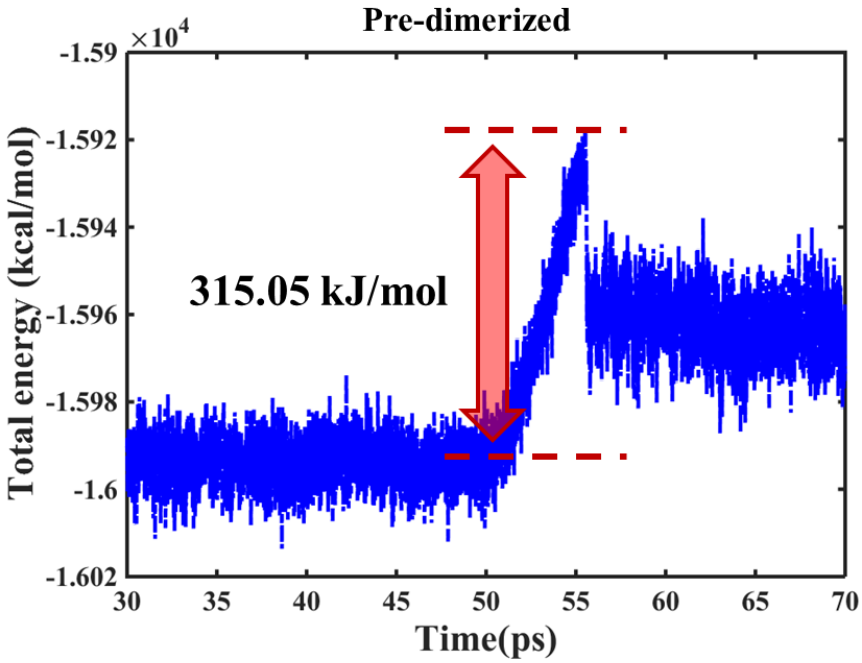

Figure 2.32. BDEs Obtained from Pre-dimerized Cyclobutane Structure (Elongation Starts at 50ps with 0.0005 Å/Fs and Bond Scission Occurs around 56ps).

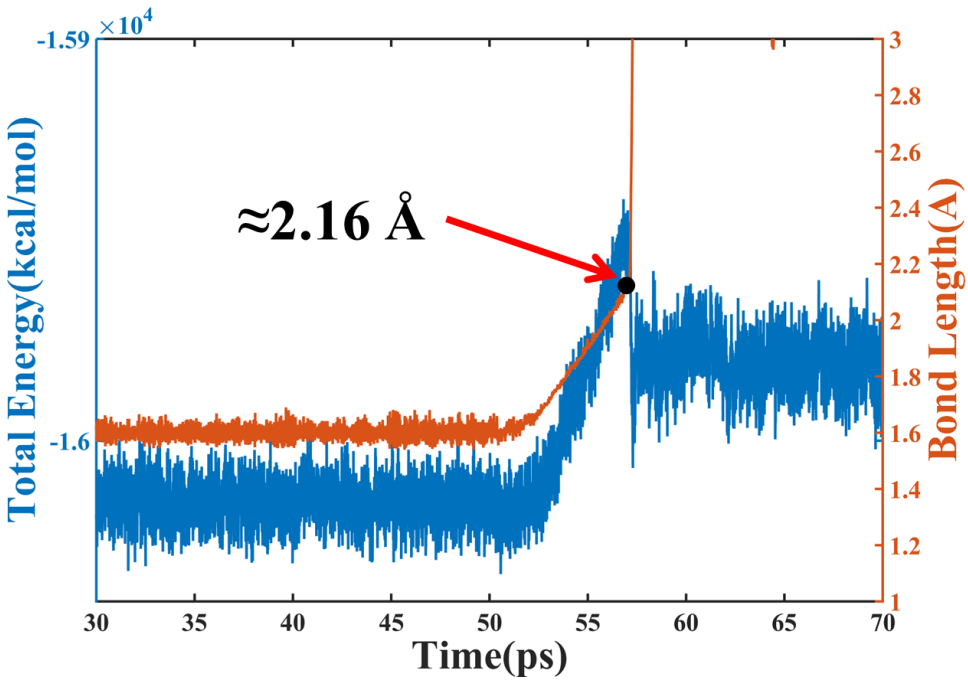

Figure 2.33. C-C Bond Lengths of Cyclobutane and Total Energy Transition of the TCE Polymer during the Tensile Test.

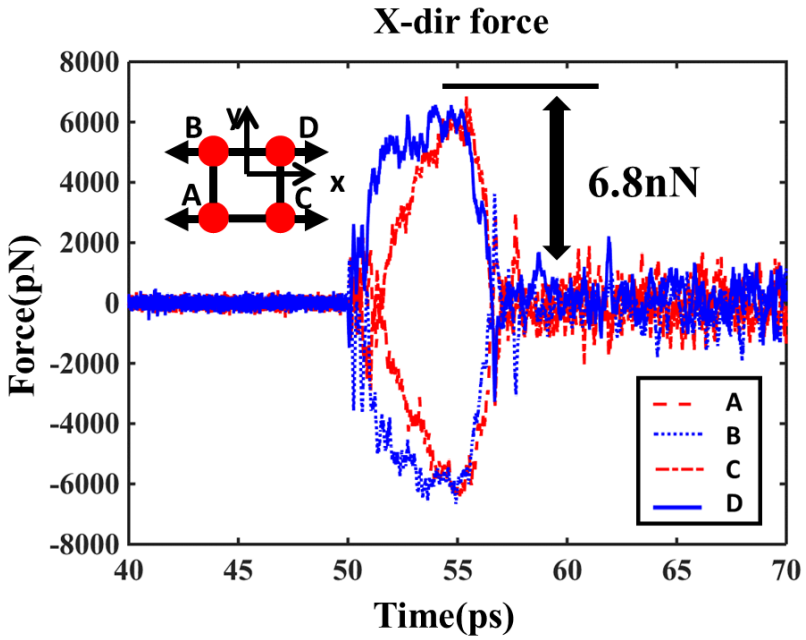

Figure 2.34. BRF of Cyclobutane (≈6.8 nN).

In addition to cyclobutane-based mechanophore, Di-AC's BDE and BRF are characterized using the COGEF. The BDE of Di-AC is 58.5 kcal/mol (244.53 kJ/mol), the critical distance of Di-AC is 2.16 Å (Figure 2.35), and BRF is 6.7nN (Figure 2.36).

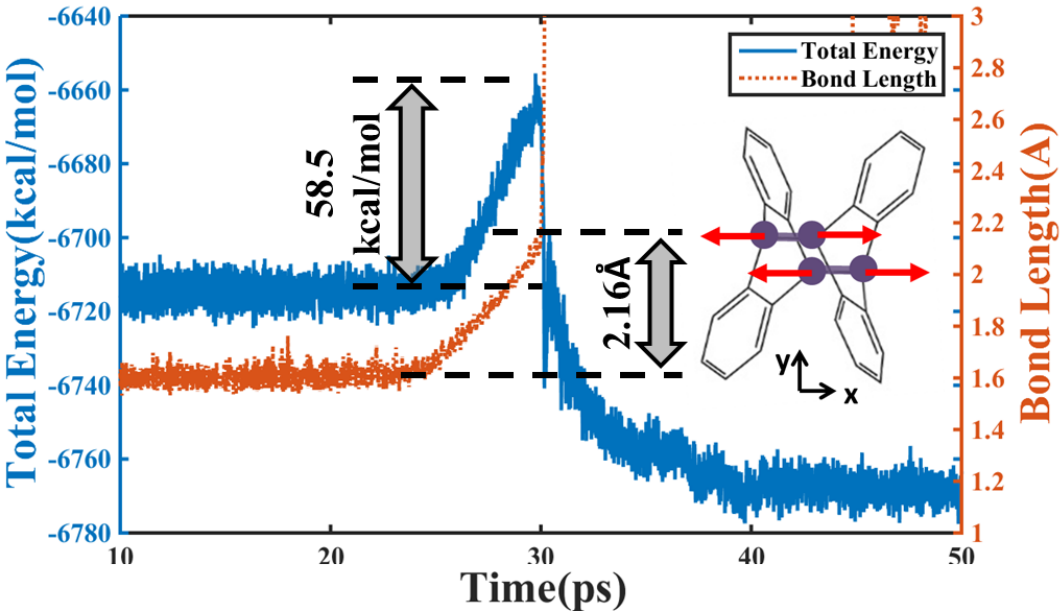

Figure 2.35. Bond Dissociation Energy (58.5 Kcal/Mol) and Critical Length (2.16 Å) of Di-AC; Red Arrows Indicate the Unit Vectors that Represent the Pulling Directions.

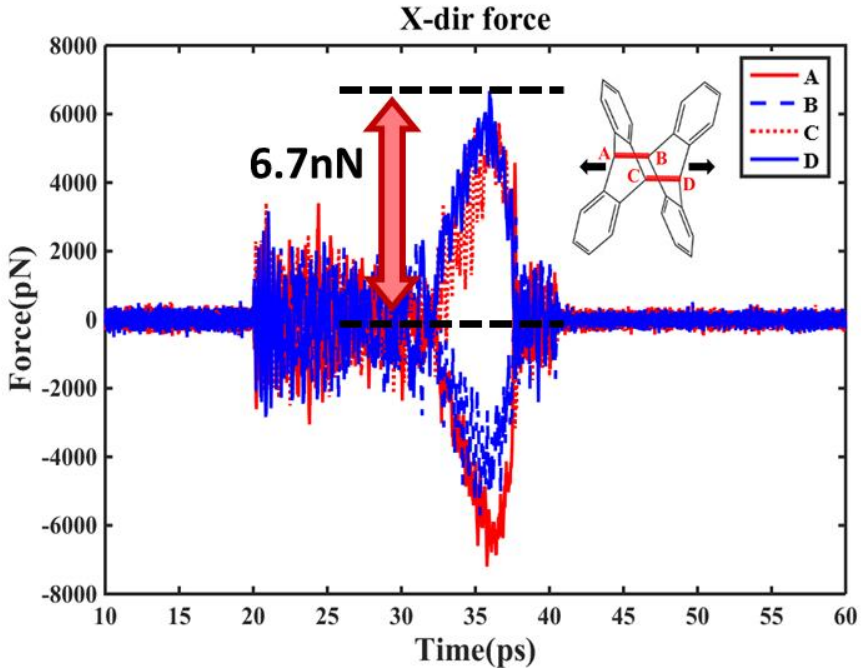

Figure 2.36. BRF of Di-AC (≈6.7 nN).

Cyclobutane-based Mechanophore Embedded Thermoset: For quantitative simulation of the mechanophore activation, the atomic force (a physical parameter candidate) applied on the cyclobutanes' carbon atoms is investigated first. The local force is defined as the amplitude of an internal force that contributes to deformation of the C-C bonds under mechanical loading (Figure 2.37). For example, if bond stretching forces, $\vec{F}_1$ and $\vec{F}_2$, are applied on the cyclobutane in opposite directions as shown in Figure 2.38, the local force is specified by $\min\{|\vec{F}_1|,|\vec{F}_2|\}$, and the bond will move with acceleration, due to net force, $\vec{F}_{net}=\vec{F}_1+\vec{F}_2$. Note that $\vec{F}_1$and $\vec{F}_2$ are pair forces and cancel out if they are equal. However, the zero net force only implies zero acceleration of the bond, and the internal force ($|\vec{F}_1|=|\vec{F}_2|$) contributes to the deformation of the bonds.

The local force definition is summarized in Table 2.8. Using this local force analysis approach, mechanophore activation is said to occur when one of the local forces of four bonds in the cyclobutane becomes greater than RBF (6.8nN). To verify whether local force information of cyclobutanes can be used as a criterion in mechanophore activation, local force information of two different cyclobutanes in the RVE, whose activation states were already obtained from the qualitative visualization analysis, is monitored. The first cyclobutane chosen for this analysis had no activation and the second cyclobutane activated at 50% strain. Figure 2.39 shows the local force trends of the two cyclobutanes. However, the results also indicate that local force analysis is not a reliable approach to identify mechanophore activation because the amplitudes of forces of the first cyclobutane (no activation) spike higher than the BRF (6.8nN) as the strain increases.

To overcome the ambiguous data obtained from the local force analysis, a local work analysis approach is developed by considering the displacement of the C-C bonds. The concept is equivalent to strain energy calculation used in structural analysis. The local work is defined as the work ($\int \vec{F} \cdot d\vec{L}$) done by the applied local force ($\vec{F}$) on the bond with a small deformation, $d\vec{L}$. This local work can be stated as $\int \min\{|\vec{F}_1|, |\vec{F}_2|\} \cdot d\vec{L}$ using the same example as shown in Figure 2.38. The results of local work analysis show that the dashed line AC (green) (see Figure 2.41) in the case of the second cyclobutane, starts to increase at 50% strain, whereas local work estimations of all the bonds are below the threshold in the case of the first cyclobutane (see Figure 2.40). Here, good agreement is observed with the qualitative visualization analysis results. Essentially, a certain amount of force needs to be maintained over a certain amount of time to elongate a covalent bond until it breaks. Therefore, it is reasonable to postulate that the local work is a key factor

governing mechanophore activation, instead of local force. Five samples with different initial locations of molecules and the same weight fraction of constituents are generated and tested to see if this method shows statistically consistent results. The results show that the mechanophores in all the samples are consistently activated at a strain of approximately 20%~25% and the number of activated mechanophores increases as the strain increases (see Figure 2.42).

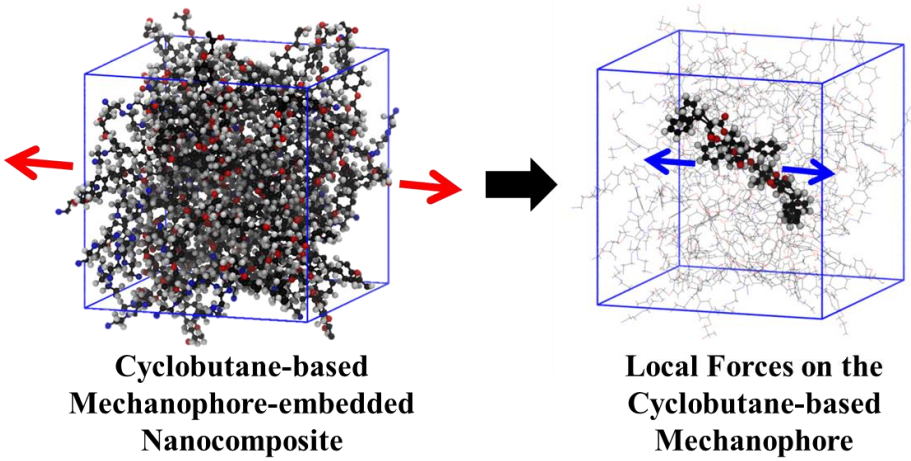

Figure 2.37. Schematic of Local Force Distribution under the Uniaxial Loading Condition.

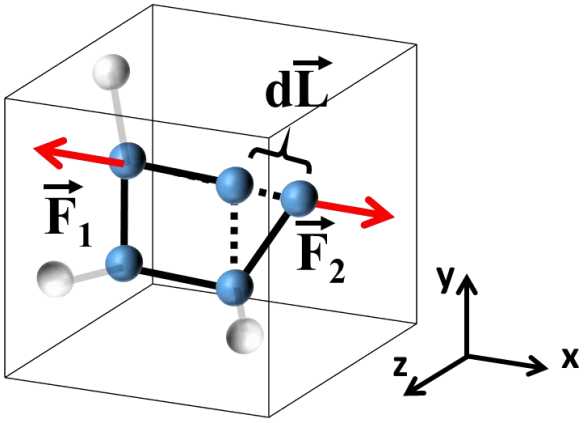

Figure 2.38. Schematic of Cyclobutane under the Applied Atomic Forces ($\vec{F}_1$ and $\vec{F}_2$); Displacement ($d\vec{L}$).

Table 2.8. Definition of Local Force due to $\vec{F}_1, \vec{F}_2$ along X-axis in Opposite Direction (Figure 2.38).

Condition of Atomic Force ($\vec{F}_1, \vec{F}_2$)	Local Force	Motion
$\lvert\vec{F}_1\rvert = \lvert\vec{F}_2\rvert$	$\min\{\lvert\vec{F}_1\rvert, \lvert\vec{F}_2\rvert\}$	zero acceleration
$\lvert\vec{F}_1\rvert \neq \lvert\vec{F}_2\rvert$		acceleration due to $\vec{F}_1 + \vec{F}_2$

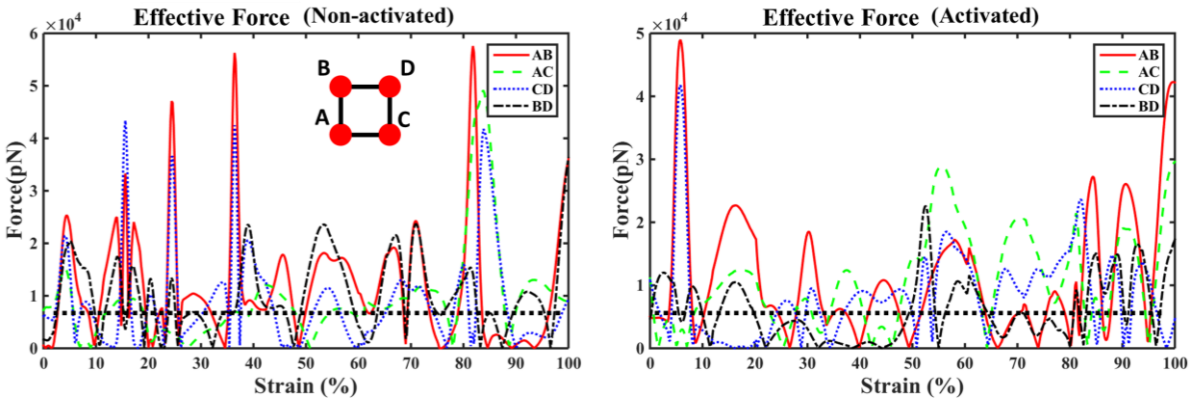

(a) (b)

Figure 2.39. Local Force Plots of Two Cyclobutanes in the Polymer Matrix: a) Cyclobutane with No Activation and b) Activated Cyclobutane at 50% Strain (Dotted Black Line Represents the Threshold of 6.8nN).

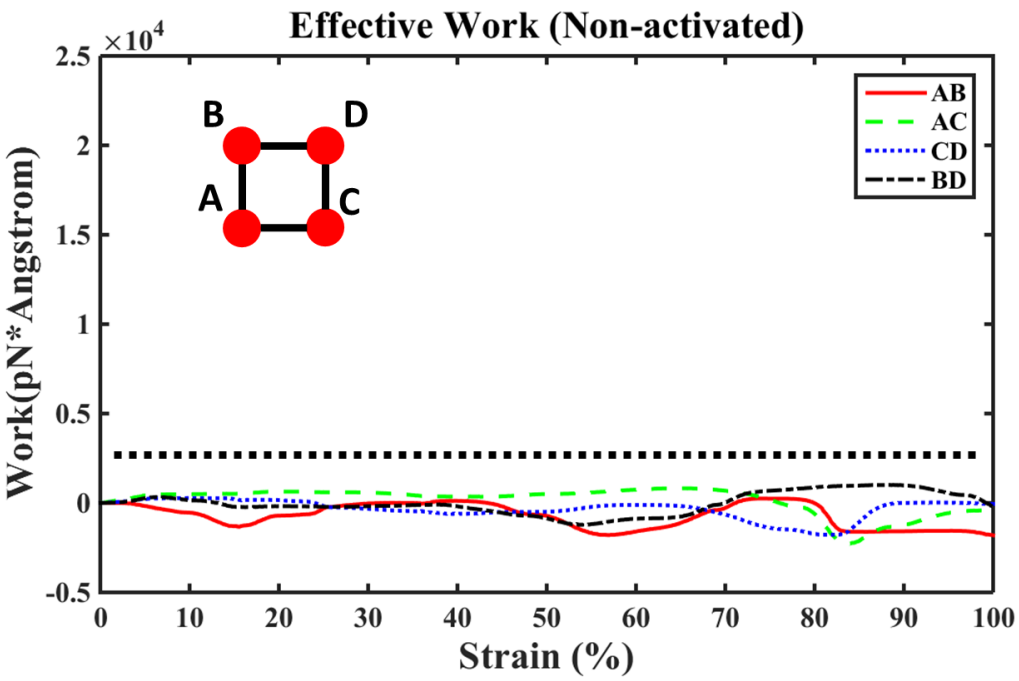

Figure 2.40. Local Work Plots of Non-activated Cyclobutanes in the Polymer Matrix: (Dotted Black Line Represents the Threshold of 315kJ/mol (2,615 pN-Å)).

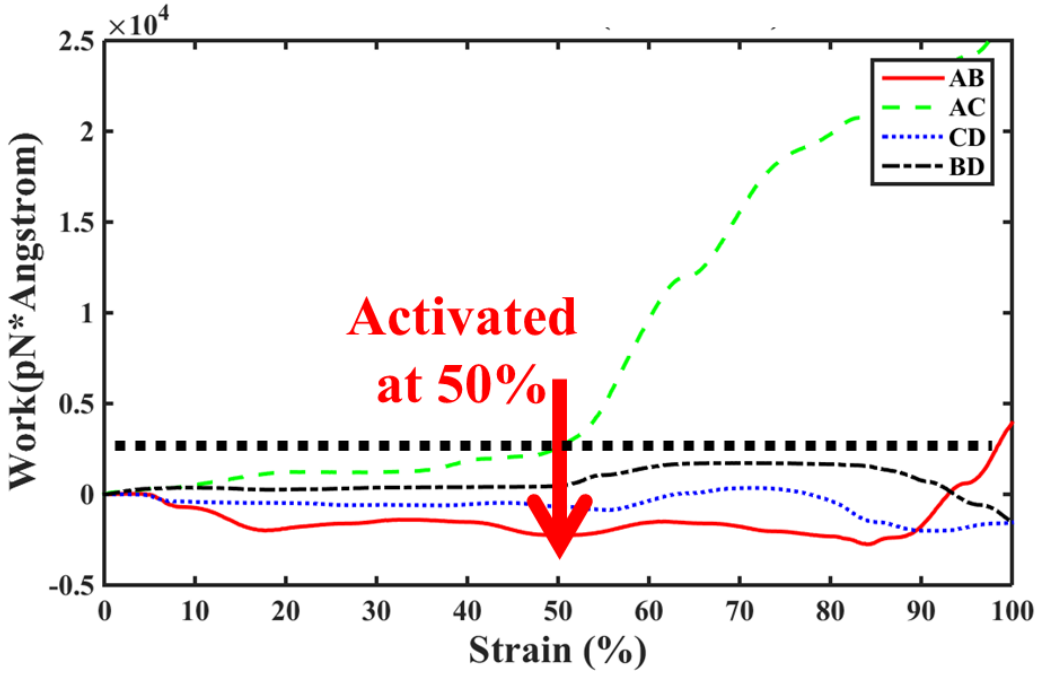

Figure 2.41. Local Work Plots of the Activated Cyclobutanes in the Polymer Matrix at 50% strain (Dotted Black Line Represents the Threshold of 315kJ/mol (2,615 pN-Å)).

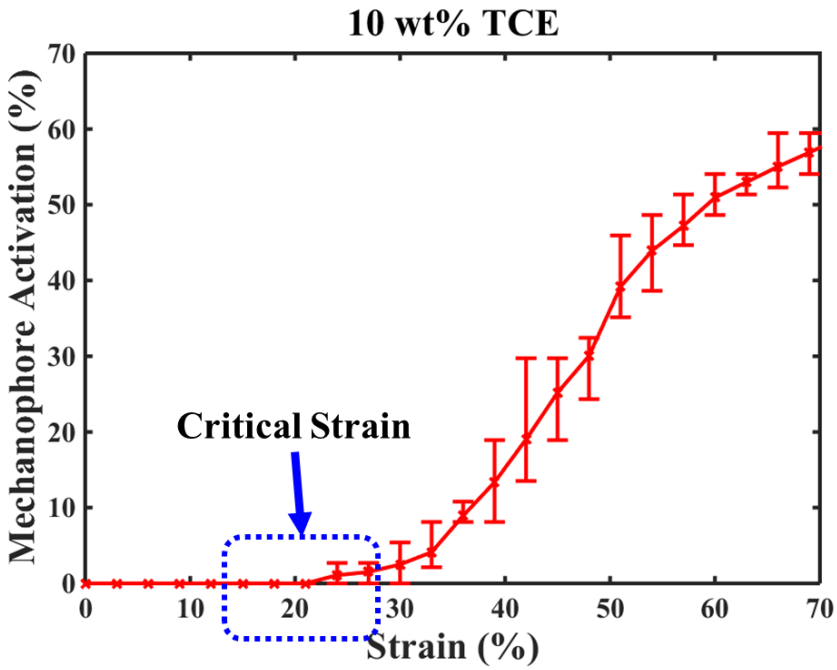

Figure 2.42. Mechanophore Activation vs. Strain Obtained from Five Samples.

Anthracene-based Mechanophore Embedded Thermoset: Local force/work analysis is also applied to Di-AC embedded nanocomposite. In the previous section, it has been shown that local force analysis itself is not relevant in capturing mechanophore activation, whereas local work analysis correctly captures the mechanophore activation. To verify if the local work analysis is valid for Di-AC mechanophore, the same comparison study using two randomly picked Di-AC molecules is conducted. The first Di-AC molecule had no activation and the second Di-AC activated at 30% strain from the qualitative visualization analysis in Figure 2.30. Figure 2.43 shows the local force trends of the two Di-AC molecules. Similar to the results of cyclobutane, local force analysis provides ambiguous data, and the amplitudes of forces of both cyclobutanes spike higher than the

BRF of Di-AC (6.7nN) as the strain increases. On the contrary, the local work analysis approach generates clear data. The output shows that the dashed CD line representing the transition of local work between C and D atoms (blue dotted line) of the second Di-AC starts to increase at 30% strain (Figure 2.45), and all local work calculations of the second Di-AC stay below the threshold (black dotted line), as shown in Figure 2.44. These results from both mechanophores (TCE and Di-AC) indicate that the local work analysis can be a potential tool for evaluating the sensitivity of mechanophores to external mechanical loading. In addition, it proves that mechanophore activation requires not only force, but also deformation induced by the force. Five samples with different initial locations of molecules and the same weight fraction of constituents are generated and tested to see if this method shows statistically consistent results. The results show that the mechanophores in all the samples are consistently activated at a strain of approximately 10%~15% and the number of activated mechanophores increases as the strain increases (see Figure 2.46). It is noteworthy that the Di-AC embedded nanocomposite shows earlier activation than the TCE embedded nanocomposite, which correlates with the fact that the BDE of Di-AC is less than that of TCE. The simulation results are validated using the experimental results in the next chapter. The sensitivity of mechanophore to external stress is also investigated by associating with the experimentally measured ring strain in Chapter 3.

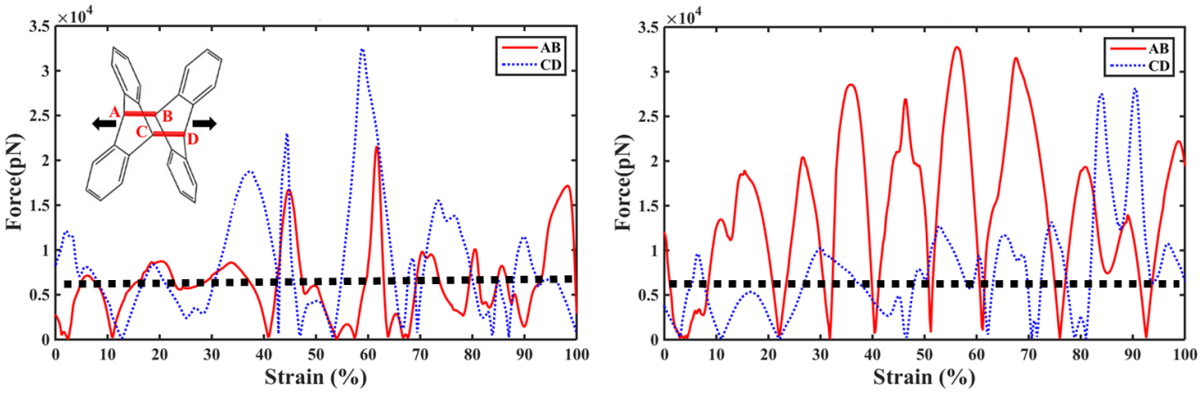

(a) (b)

Figure 2.43. Local Force Plots of Two Cyclobutanes in the Polymer Matrix: a) Cyclobutane with No Activation and b) Activated Cyclobutane at 50% Strain (Dotted Black Line Represents the Threshold of 6.8nN).

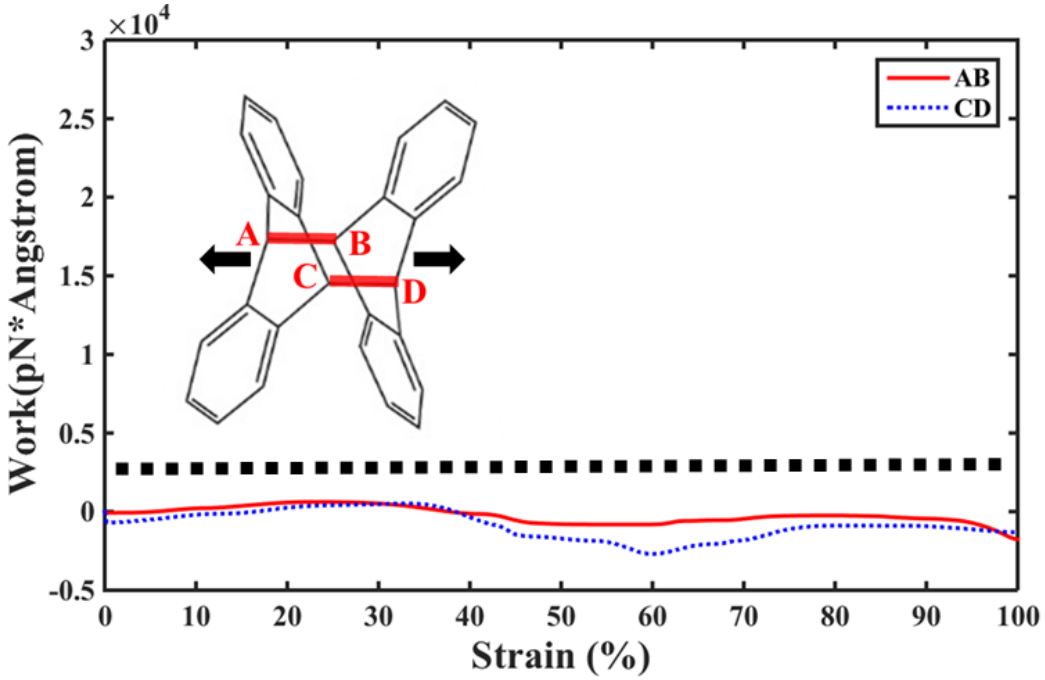

Figure 2.44. Local Work Plots of Non-activated Cyclobutanes in the Polymer Matrix: (Dotted Black Line Represents the Threshold of 244.53 kJ/mol (2,030 pN-Å)).

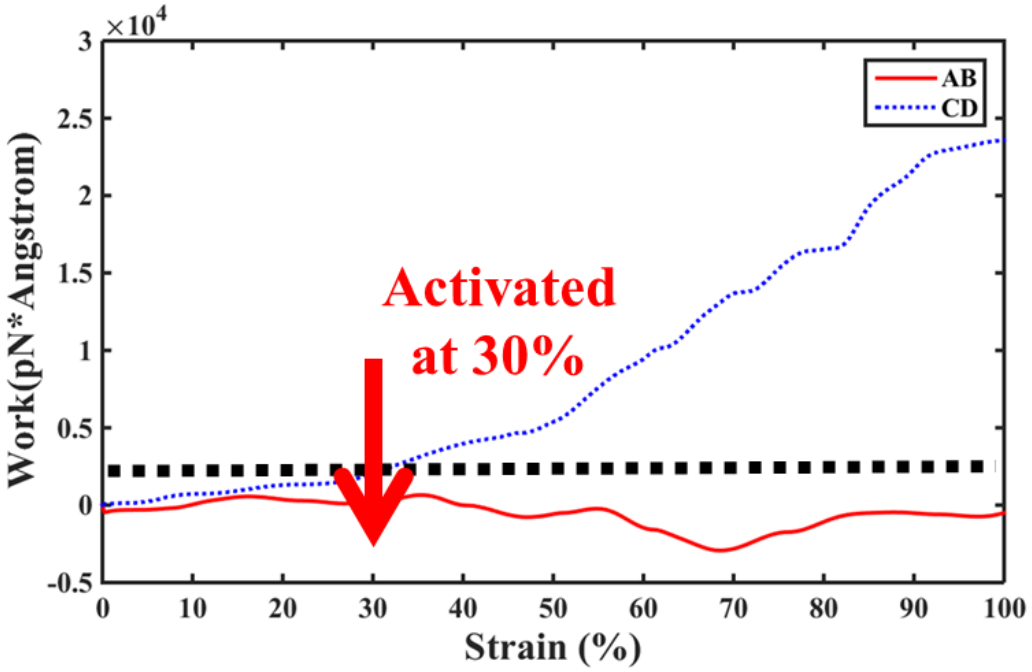

Figure 2.45. Local Work Plots of the Activated Cyclobutanes in the Polymer Matrix at 50% Strain (Dotted Black Line Represents the Threshold of 244.53 kJ/mol (2,030 pN-Å)).

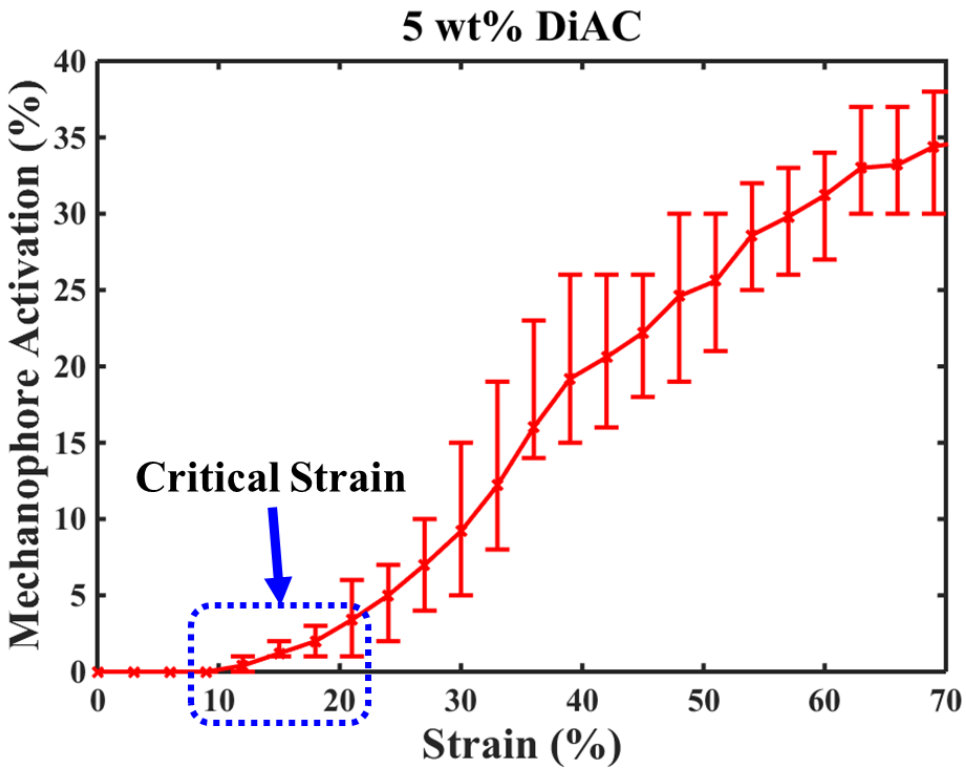

Figure 2.46. Local Work Analysis to Evaluate Mechanophore Activation Performance.

2.4. Chapter Summary

A hybrid MD simulation framework is developed to capture the mechanochemical reaction of mechanophores in an epoxy-based thermoset matrix. An epoxy network required to simulate covalent bond generation was modeled to construct the structure of the host materials. By introducing ReaxFF as a bond-order based force-field, a basic framework for the mechanophore activation simulation was established. The virtual loading test in conjunction with ReaxFF was implemented to activate mechanophore in the thermoset matrix. Local force and work experienced by the mechanophores in the matrix were analyzed to explore the effective physical parameter activating the mechanophore by developing local force/work analysis. The local work analysis results show that anthracene-based mechanophore was activated earlier than cyclobutane mechanophore. These results indicate a good correlation with the BDE study of Di-AC and cyclobutane presented in Section 2.3.5, where the BDE of Di-AC is less than the BDE of cyclobutane. To validate the hybrid MD simulation framework, the output of the framework will be compared with experimental results in Chapter 3.

CHAPTER

3. EXPERIMENTAL VALIDATION OF THE HYBRID MD FRAMEWORK

The principal objective of this research effort is to develop an atomistic model, along with simulation methodologies that provide important insights into the mechanochemical reaction of a mechanophore in a thermoset matrix. The model and methodology framework are then validated through experimental correlations. Specifically, cycloalkane-based mechanophores infused into epoxy-based thermoset matrix, including material preparation (synthesis) and confirmation of mechanophore formation as well as characterization of material properties, including Tg, elastic modulus, loss/storage modulus were experimentally elucidated. Additionally, the fluorescence intensity induced by mechanophore activation after uniaxial loading test was measured using a UV microscope. This experimental study, conducted in collaboration with Dr. Lenore Dai in ASU's chemical engineering department, was then used to validate the atomistic nanocomposite model and the hybrid MD simulation framework.

3.1. Glass Transition Temperature: Estimation and Measurement

3.1.1. Neat Epoxy and Smart Polymer

Tg Estimation and Experimental Validation: In Chapter 2, the most possible conversion degree for each system, namely, 56% for neat epoxy and 52.7% for smart polymer with TCE, was established. In order to validate the curing simulation method and the conversion degree estimations, Tgs were predicted using MD simulations. After measuring Tgs experimentally, the predicted Tgs are compared with experimental results for this validation process.

Tgs for each system were estimated by investigating the change in density at temperatures ranging from 250K to 450K; a detailed simulation process that takes place for Tg estimation is as follows. After generating covalent bonds with the predicted conversion degree, the system becomes unstable due to newly generated bonds. In order to ensure the stability of the system before starting density calculations at different temperatures, additional energy minimization and NPT ensemble simulation (250K and 1atm for 200ps) are required. Once the system is stabilized, a stepwise heating simulation is performed by starting with the equilibrated system (250K and 1atm), and then followed by intervals of 10K with the same pressure. For each temperature, NPT ensemble simulation is conducted for 100ps [155]. When compared to the experimental heating rate, 10K/100ps is very high; however, the high heating rate is inevitable due to the inherent time scale limitation of MD simulation [156].

To address the discrepancy between the experimental process and simulation, an assumption made in this study is that once the system is equilibrated computationally, it will stay in the same state without any significant change. In this instance, 100ps was sufficient time to equilibrate the system. Densities at each temperature are calculated using the time average of densities around equilibration state due to the fluctuation behavior of molecules. Figure 3.1 and Figure 3.2 show trends of densities as a function of temperature for neat epoxy and smart polymer. The error bars in each plot represent MD simulation data. Since the epoxy-based systems are amorphous polymer, there is a transition in density as the temperature varies. The temperature at the transition is defined as Tg, which is determined by locating the intersection of two linearly fitted lines in the two regions: glass

and liquid state region (Figure 3.1 and Figure 3.2). Through this procedure, Tgs of neat epoxy and smart polymer are determined to be 345.2K and 320.8K, respectively.

Table 3.1 shows the root mean squared error (RMSE) and R^2 to evaluate goodness-of-fit for the fitted linear curves. Since the RMSE and R^2 are close to 0 and 1, respectively, linear fit to the MD simulation results is appropriate for each region.

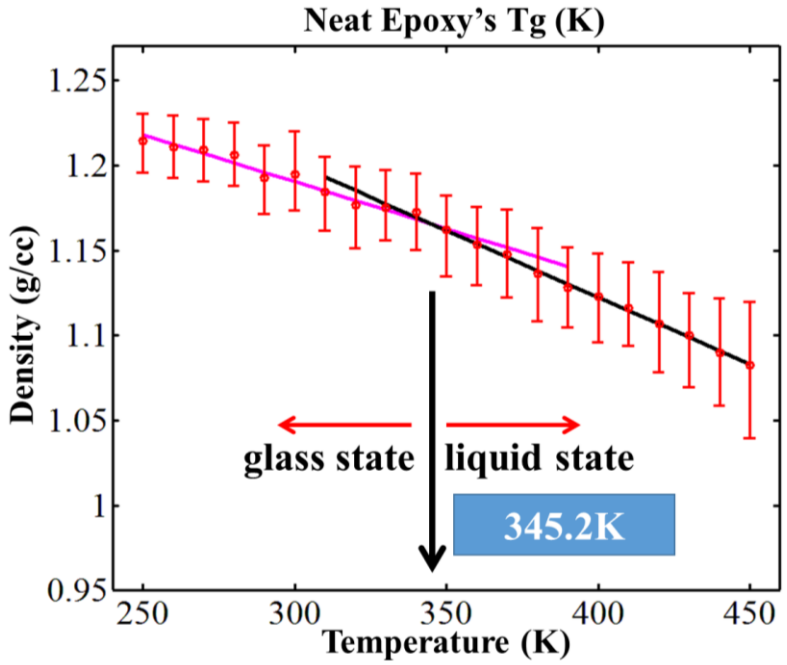

Figure 3.1. MD Simulation Results for Tg Prediction of Neat Epoxy.

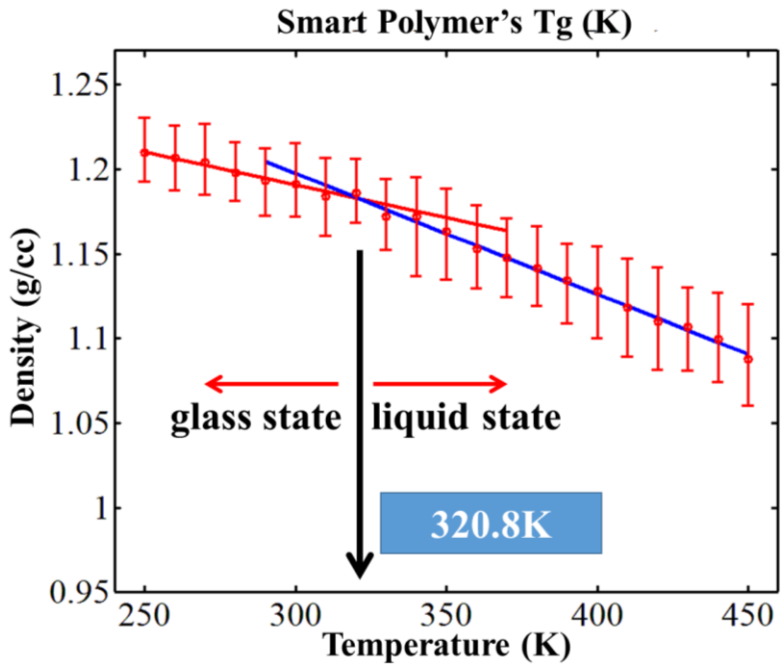

Figure 3.2. MD Simulation Results for Tg Prediction of Smart Polymer.

Table 3.1. Evaluation of Goodness-of-Fit.

	Neat Epoxy		Smart Polymer	
	Glass State	Liquid State	Glass State	Liquid State
RMSE	0.0034	0.0015	0.002	0.0023
R^2	0.97	0.99	0.96	0.99

Next, the numerically estimated Tgs were compared with experimental results to establish experimental validation. Since Tg measurement of smart polymers has yet to be explored, DSC was employed after the synthesis of these novel materials. A set of four experimental samples were fabricated for each material type: neat epoxy and smart

polymer. The averaged values (from the four tests) are presented in Figure 3.3. The comparisons between MD simulations and DSC results are shown in

Table 3.2; Tg estimation shows good agreement with experiments (within 2%). These results indicate that not only does the numerically cured epoxy network and its simulation describe the epoxy-based system accurately, but also a combination of numerically implemented conversion process and force field MMFF is promising for epoxy-based system studies. Furthermore, the results capture the influence of the mechanophore on the neat epoxy which leads to a reduction in the Tg value. Based on these results, it is anticipated that the developed framework will be a reliable numerical method to evaluate the thermal property of other epoxy-based systems. In order to show that this curing simulation and Tg estimation method are applicable to a wide range of epoxy systems, four different epoxy systems are discussed more to estimate Tg points and to compare Tg estimations with experimental results in Section 3.1.2.

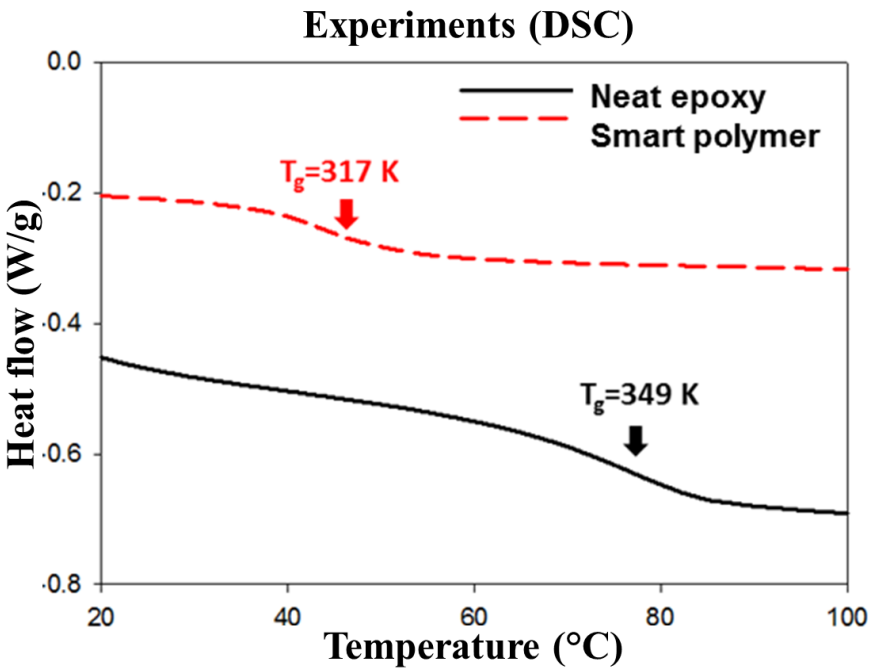

Figure 3.3. Tgs Obtained by DSC: 349K for Neat Epoxy and 317K for Smart Polymer [12].

Table 3.2. Percent Error of Each System.

	MD Simulations	DSC	% Error
Neat Epoxy	345.21K	349K	1.3%
Smart Polymer	320.80K	317K	1.2%

Tg vs. Conversion Degree: There is some research on modeling of the relationship between Tg and the conversion degree. Nielsen et al. [157] introduced the DiBenedetto equation,

$$T_g = \frac{\zeta \alpha T_{g_u} + (1-\alpha) T_{g_u}}{(1-\alpha) + \eta \alpha}, \qquad (3.11)$$

where α is conversion degree ranging from 0 (uncured epoxy system) to 1 (fully cured epoxy system), ζ is a ratio of lattice energies between uncured epoxy system and cured epoxy system, η is a ratio of segmental mobilities between uncured epoxy system and cured epoxy system, and Tg_u is the glass transition temperature of uncured epoxy system. The DiBenedetto equation, however, does not consider Tg of a fully cured epoxy system; therefore, it is not appropriate for use in a highly cured system. Pascault et al. [158], on the other hand, propose an extended DiBenedetto equation by introducing the Tg of a fully cured epoxy system, Tg_f,

$$T_g = \frac{(1-\alpha)T_{g_u} + \alpha\eta T_{g_f}}{(1-\alpha)+\alpha\eta} \quad (3.12)$$

A well-known model describing the relationship between Tg and epoxy conversion degree is the Venditti-Gillham (V-G) equation (Equation 3.3) [122], which is based on an entropy approach introduced by Couchman et al. [159]. It is as follows:

$$T_g = \exp\left(\frac{(1-\alpha)\ln(T_{g_u}) + \alpha\beta\ln(T_{g_f})}{(1-\alpha)+\alpha\beta}\right), \quad (3.13)$$

where β is a ratio of heat capacity change between a fully cured epoxy system and an uncured epoxy system. Venditti et al.[122] also presented comparative studies between the V-G equation and the DSC measurements of several thermosetting epoxy systems, thereby concluding that β ranges from 0.22 to 0.65. Even though most of the β values were obtained from DSC measurements, β is not available for all thermosetting epoxy systems due to the limitations of making fully cured or uncured epoxy system. Therefore, some β values were estimated by fitting the V-G equation to DSC measurements of partially cured epoxy systems.

In this chapter, the V-G equation is used to perform additional validation of the MD simulation framework. This is done by fitting the V-G equation to the MD simulation data. This simulation is meaningful because it shows the efficacy of the MD approach for analyzing the relationship between Tg and the conversion degree, which is a very important factor in modeling the curing mechanism of the thermoset or developing an efficient curing process. Figure 3.4 and Figure 3.5 show that the MD simulation data fits well into the V-G equation in both neat epoxy and smart polymer (R^2 are 0.9917 and 0.9958, respectively, Table 3.3). The ratio β of neat epoxy, 0.6164, is within the range mentioned in Venditti et al. However, the ratio β of smart polymer, 0.7373, is greater than the maximum value of the range. Considering that the V-G equation was derived for neat thermoset epoxy system, the reason for the change can be related to the addition of smart material in the epoxy.

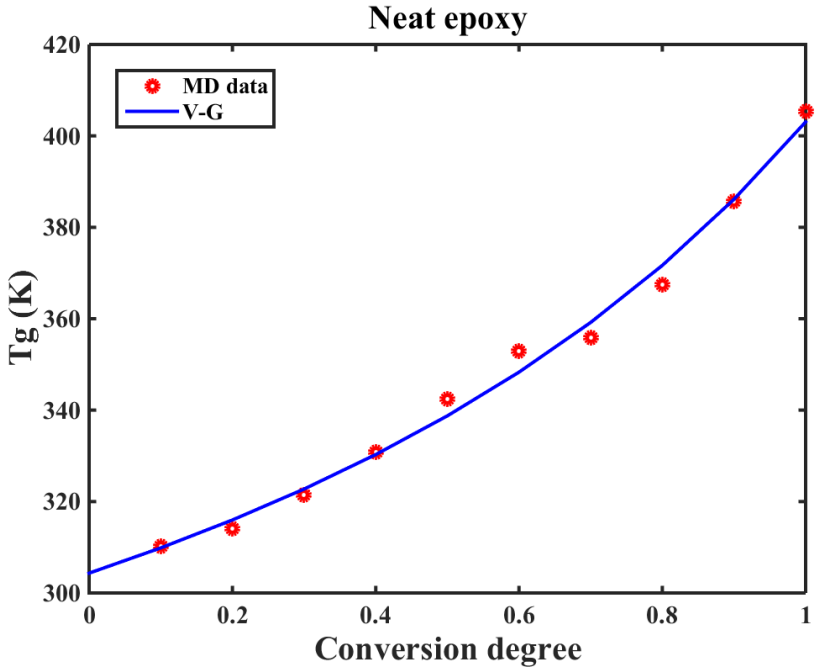

Figure 3.4. Tg Distributions as a Function of Conversion Degree for Neat Epoxy.

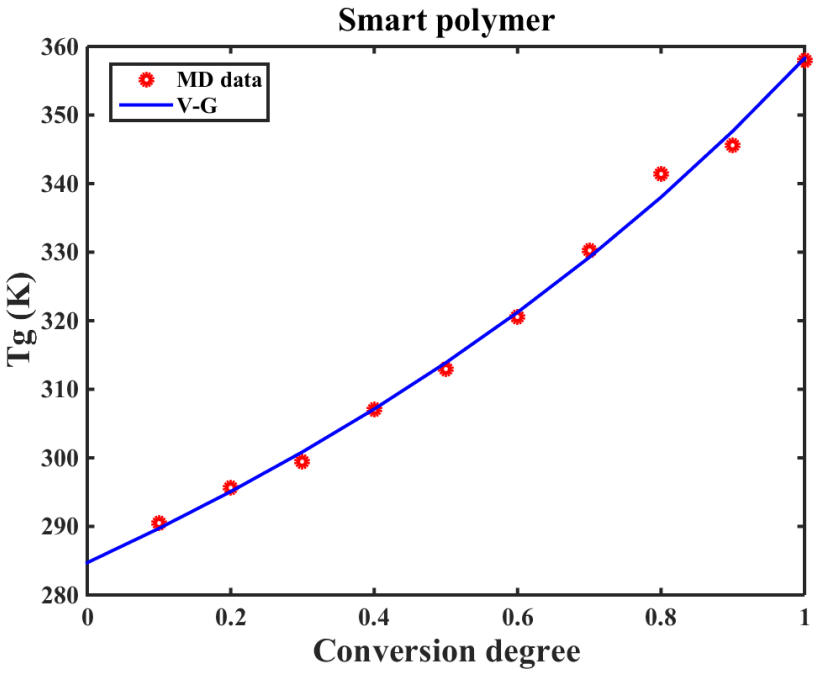

Figure 3.5. Tg Distributions as a Function of Conversion Degree for Smart Polymer.

Table 3.3 Estimated Parameters by Fitting V-G Equation to MD Data.

Material	β	T_{g_u}	R^2
Neat Epoxy	0.6164	304.3K	0.9917
Smart Polymer	0.7373	284.7K	0.9958

3.1.2. Different Epoxy Systems from Literature

The Tg estimation using MD and experimental validation are successfully demonstrated for neat epoxy (DGEBF and DETA) and smart polymer systems in Section 3.2.1. In order to show that the curing simulation methodology and Tg estimation technique are applicable to any epoxy system, four different epoxy resin and hardener systems are

used. The Tgs of each system are estimated and compared with experimentally measured Tgs from the literature [160-163]. Table 2.2 shows each system's constituents, chemical structures and the molecular weights of the constituents: system1 (DGEBF and Di-Ethyl Toluene Di-Amine (DETDA)); system 2 (DGEBF and Tri-Ethylene-Tetr-Amine (TETA)); system 3 (Di-Glycidyl Ether of Bisphenol A (DGEBA) and Iso-Phoron Diamine (IPD)); system 4 (DGEBA and Di-amino Diphenyl Sulfone (DDS)).

The simulation steps are as follows: first, the constituent molecules of each system are mixed stochastically without overlap in the unit cells. The numbers of molecules are determined by the weight ratio used in the literature with experimental results for the corresponding material systems (Table 3.5). Next, in order to mimic the experimental process accurately, the experimental conditions during curing (temperature and pressure) are employed for the curing simulation. Table 3.6 lists the curing temperature used in experiments (pressure is 1 atm for all cases) along with curing simulation times which are determined by the condition where the total energy meets the first peak followed by a distinct drop (please refer to Chapter 2).

Table 3.4. Constituents of Each Epoxy System

System	Resin	Hardener
1	DGEBF ($C_{19}H_{20}O_4$, 313g/mol)	DETDA ($C_{11}H_{18}N_2$, 178g/mol)
2	DGEBF ($C_{19}H_{20}O_4$, 313g/mol)	TETA ($C_6H_{18}N_4$, 146g/mol)
3	DGEBA ($C_{21}H_{24}O_4$, 340g/mol)	IPD ($C_{10}H_{22}N_2$, 170g/mol)
4	DGEBA ($C_{21}H_{24}O_4$, 340g/mol)	DDS ($C_{12}H_{12}N_2O_2S$, 248g/mol)

Table 3.5. Configuration of Epoxy Polymer (Resin/Hardener).

System	Weight Ratio	Molecular Ratio	# of Atoms
1	100/26.4	200/100	11700
2	100/15.4	200/80	10840
3	100/20	200/80	12520
4	100/20	200/60	11540

Table 3.6. Curing Temperature and Curing Simulation Time based on 0.1 fs Time Step.

System	Curing temperature	Curing time in MD
1	450K	1400 steps
2	394K	1640 steps
3	463K	600 steps
4	473K	1160 steps

Preparation of Epoxy Curing Simulation: To emulate covalent bond generation between epoxy resin and hardener in MD simulation, activated resin and hardener molecules are required. This is done by removing two hydrogen atoms from epoxide groups in DGEBF (system 1, 2) and DGEBA (system 3, 4); methylene groups are prepared in resin. DETDA, the hardener for system 1, is activated by removing four hydrogen atoms from the amine group (Figure 3.6c, d). TETA of system 2 is very similar to DETA but with

an additional nitrogen atom as shown in Figure 3.7 c, d; therefore, six hydrogen atoms are removed from the TETA molecule to be activated. Figure 3.8 illustrates the molecules of constituents in system 3; IPD has four hydrogen atoms which need to be eliminated to be activated (Figure 3.8c, d). Lastly, DDS, hardener for system 4 is activated by removing the four hydrogen atoms as shown in Figure 3.9c, d.

Using the activated resin and hardener molecules for each system, the simulation unit cells are constructed by a random distribution of the molecules without overlap with each other. Periodic boundary conditions are applied to the boundaries of the unit cells in all three directions (initial size of the unit cell is approximately 10 x 10 x 10 nm^3). Conjugate gradient energy minimization is then performed followed by NPT ensemble simulation of 10ns to equilibrate the unit cell using the Nose-Hoover thermostat and barostat. The curing temperature is set by the values in Table 3.6. Through the equilibration step, the molecules maintain equilibrium distances between them. Using the same cutoff distance (van der Waal radii of C-N) as used for DGEBF+DETA system, the numerical curing simulation is performed for each system. Subsequently, hydrogenation is performed to saturate the uncured nitrogen atoms for the hardeners in each system. After bond generation and hydrogenation, energy minimization process is performed for each system until they become stable.

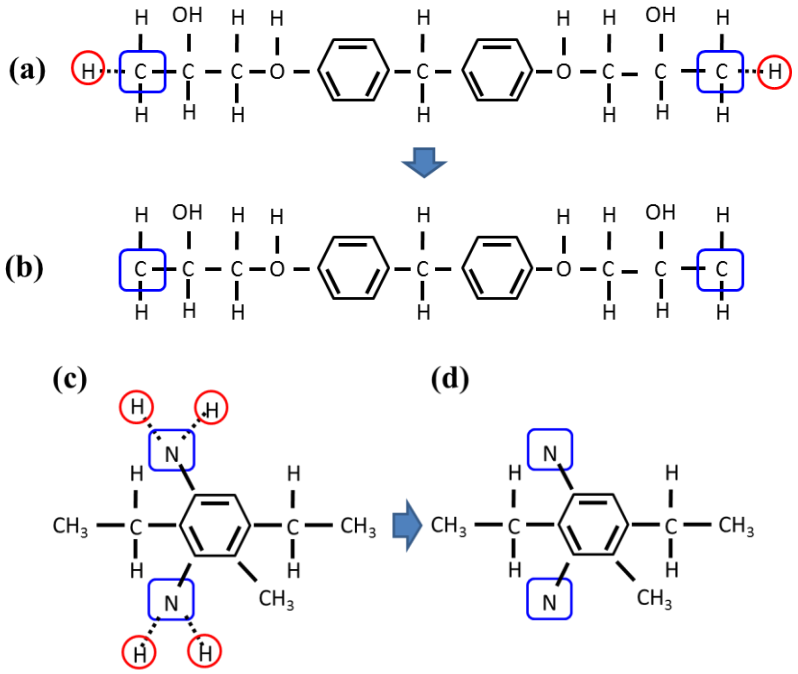

Figure 3.6. System 1: (a) Pre-Activated DGEBF; (b) Activated DGEBF After Removing Two Hydrogen Atoms with Red Circle Markings; (c) Pre-activated DETDA; (d) Activated DETDA after Removing Four Hydrogen Atoms with Red Circle Markings.

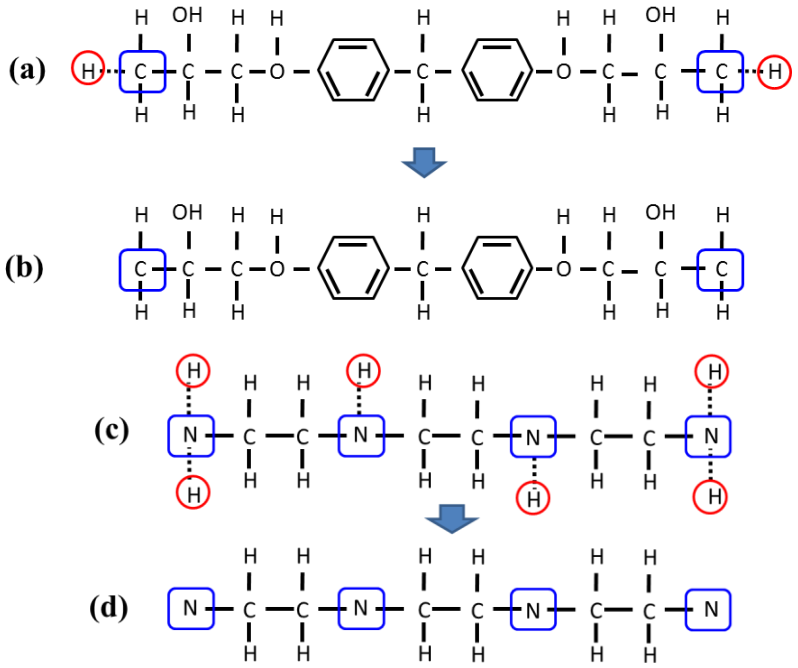

Figure 3.7. System 2: (a) Pre-activated DGEBF; (b) Activated DGEBF after Removing Two Hydrogen Atoms with Red Circle Markings; (c) Pre-activated TETA; (D) Activated TETA after Removing Six Hydrogen Atoms with Red Circle Markings.

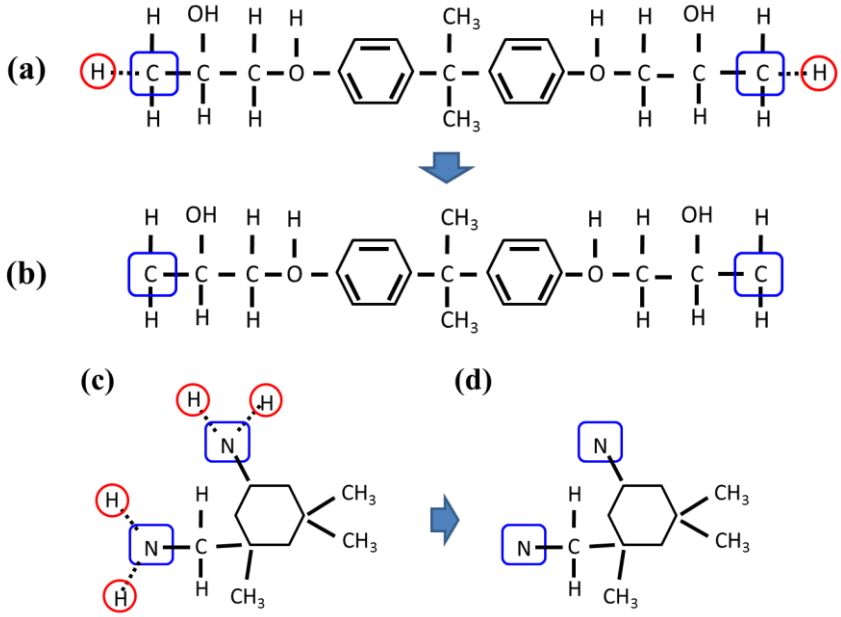

Figure 3.8. System 3: (a) Pre-activated DGEBA; (b) Activated DGEBA after Removing Two Hydrogen Atoms with Red Circle Markings; (c) Pre-activated IPD; (d) Activated IPD After Removing Four Hydrogen Atoms with Red Circle Markings.

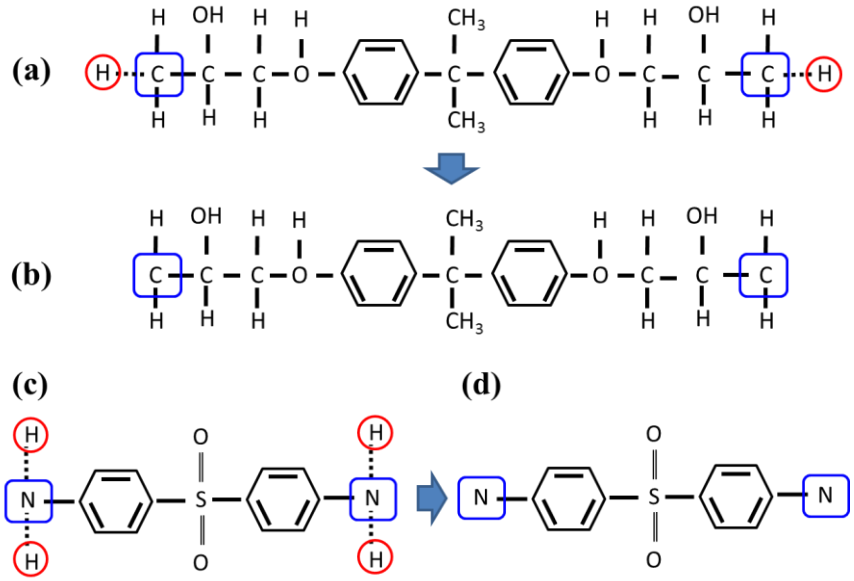

Figure 3.9. System 4: (a) Pre-activated DGEBA; (b) Activated DGEBA after Removing Two Hydrogen Atoms with Red Circle Markings; (c) Pre-activated DDS; (d) Activated DDS After Removing Four Hydrogen Atoms with Red Circle Markings.

Estimation of Conversion Degree: The method to estimate the conversion degree of the neat epoxy system using multiple unit cells is applied to these four epoxy systems. In the previous section, curing simulation conditions including temperature, simulation time, and hydrogenation method are determined for each system. This curing simulation condition is applied to multiple unit cells. In Chapter 2, 500 unit cells are generated for the DGEBF+DETA (neat epoxy) system. Likewise, the four epoxy systems generate 500 unit cells and each unit cell goes through corresponding curing simulation procedures. The most possible conversion degree for each system is estimated by calculating average values of 500 unit cells' conversion degree.

After obtaining conversion degree values from the multiple unit cell simulations, frequency distributions of the conversion degree for each system is provided as shown in Figure 3.10-Figure 3.13. The average conversion degrees for each system is listed in Table 3.7, which are considered the most likely conversion degrees. Based on these values, representative epoxy cured systems are constructed. These cured systems are used to estimate the Tg points.

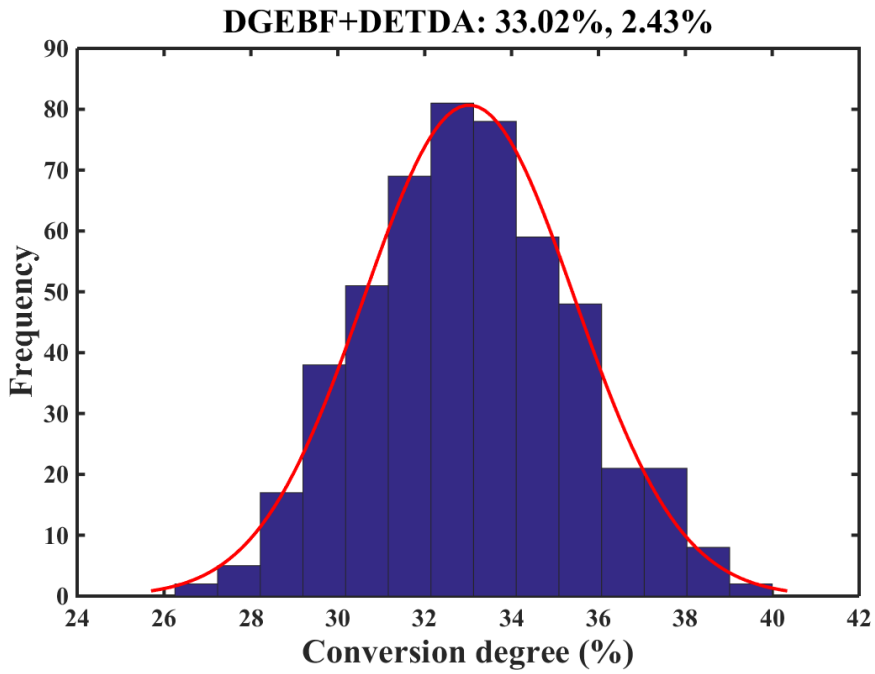

Figure 3.10. Conversion Degree Estimation for System 1 (DGEBF+DETDA); Solid Red Lines are Fitted Normal Distributions.

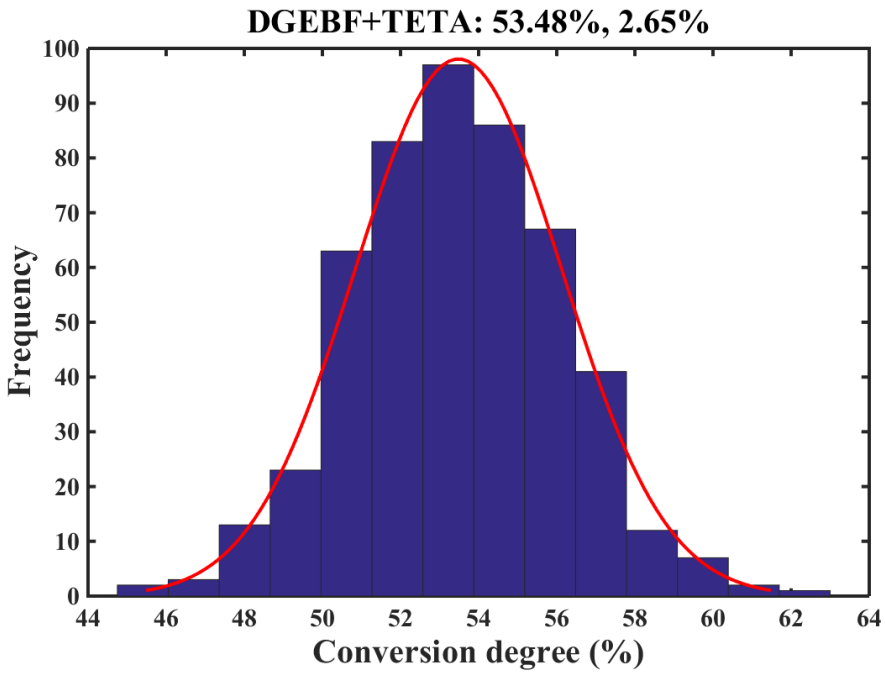

Figure 3.11. Conversion Degree Estimation for System 2 (DGEBF+TETA); Solid Red Lines are Fitted Normal Distributions.

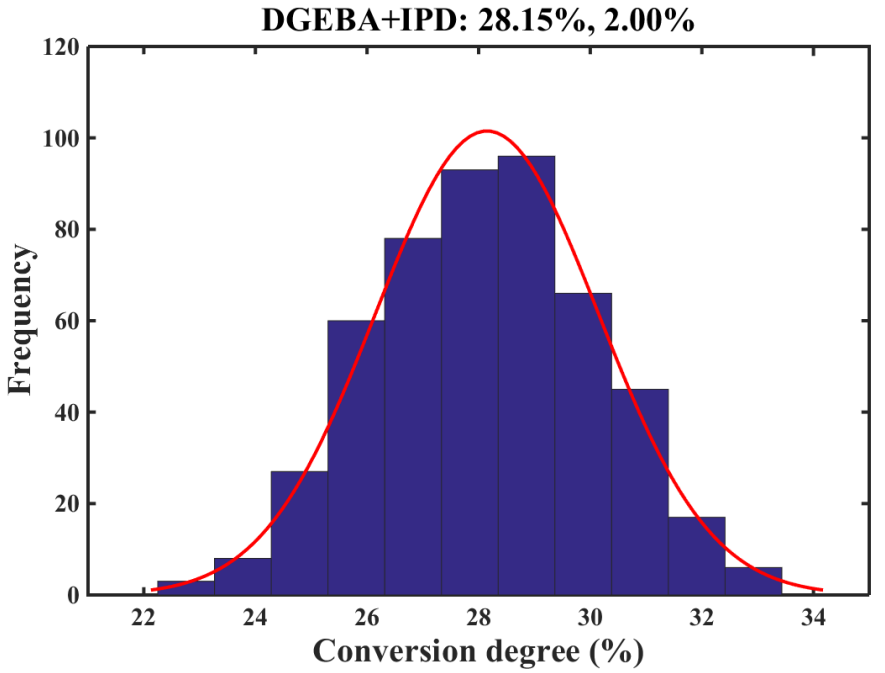

Figure 3.12. Conversion Degree Estimation for System 3 (DGEBA+IPD); Solid Red Lines are Fitted Normal Distributions.

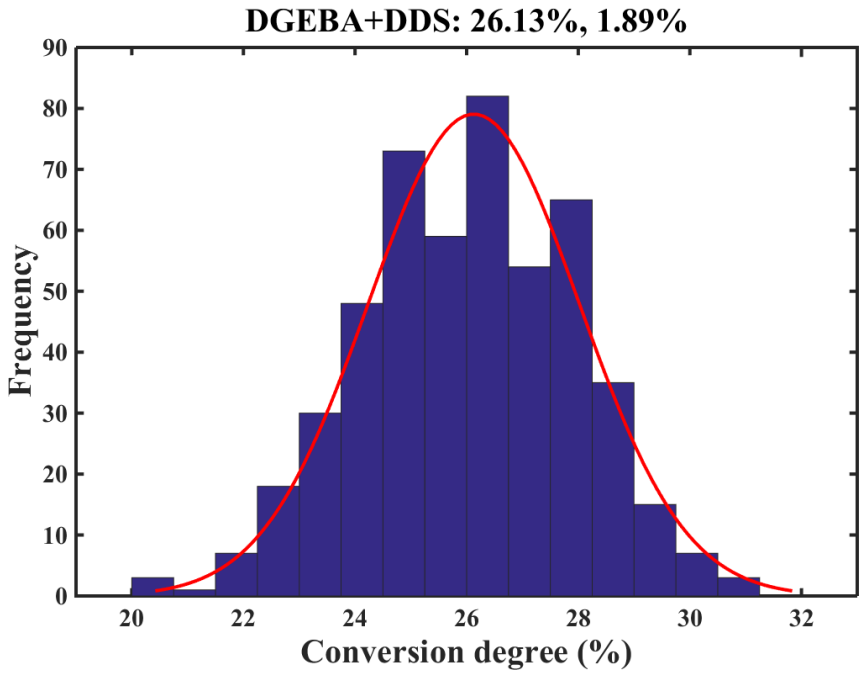

Figure 3.13. Conversion Degree Estimation for System 4 (DGEBA+DDS); Solid Red Lines are Fitted Normal Distributions.

Table 3.7. Average and Standard Deviation of Conversion Degree for Each System.

System	Average	Standard Deviation
1	33.02%	2.43%
2	53.48%	2.65%
3	28.15%	2%
4	26.13%	1.89%

Tgs are investigated by calculating densities at different temperatures, ranging from 250K to 600K using MD simulations and identifying a phase transition. A stepwise heating simulation method is performed starting with an equilibrated system (250K and 1atm) and

followed by intervals of 10K. For each temperature, NPT ensemble simulation is conducted for 100ps [155]. Densities at each temperature are calculated using time average of densities around equilibration state due to molecular vibration.

Figure 3.14-Figure 3.17 show trends of densities as a function of temperature for four epoxy systems. The error bars in each plot correspond to the MD simulation data. In order to determine the temperature at the transition of phase from liquid to glass, two linear regressions are performed and used to identify the intersection of two lines. The accuracy of the linear regression performed here is confirmed by the root mean squared error (RMSE) and R^2 estimation for each system presented in Table 3.8. Through this procedure, Tgs of each system are calculated. Table 3.9 lists the MD-estimated Tgs as well as the Tgs measured by DSC or DMA from the literature to evaluate the accuracy of the MD results; MD simulations estimate the Tg within 2% error. In addition, the results indicate that Tg estimations performed in this dissertation are more accurate than existing MD aided Tg estimation studies. Tack and co-worker [164] estimated DGEBF+DETDA epoxy system's Tg to be 412K, which has a 4.1% error, whereas the same system (system 1) was estimated to be 422.9K (1.6% error). Li et al. [163] estimated the Tg of DGEBA+DDS epoxy system at 7.4% error; however, the Tg of the same system (system 4) is estimated at 0.4% error. Fan and co-worker [161] calculated the Tg of DGEBF+TETA to be 378K which has a 4% error with experiments. In this work, the same system (DGEBF+TETA)'s Tg is estimated to be 401.3K (1.8% error). Through these experimental validations, it is evident that the combination of the proposed MD simulation methods (conversion degree and Tg estimations), and MMFF force field is very suitable for thermal property estimation of a wide range of epoxy-based thermoset systems.

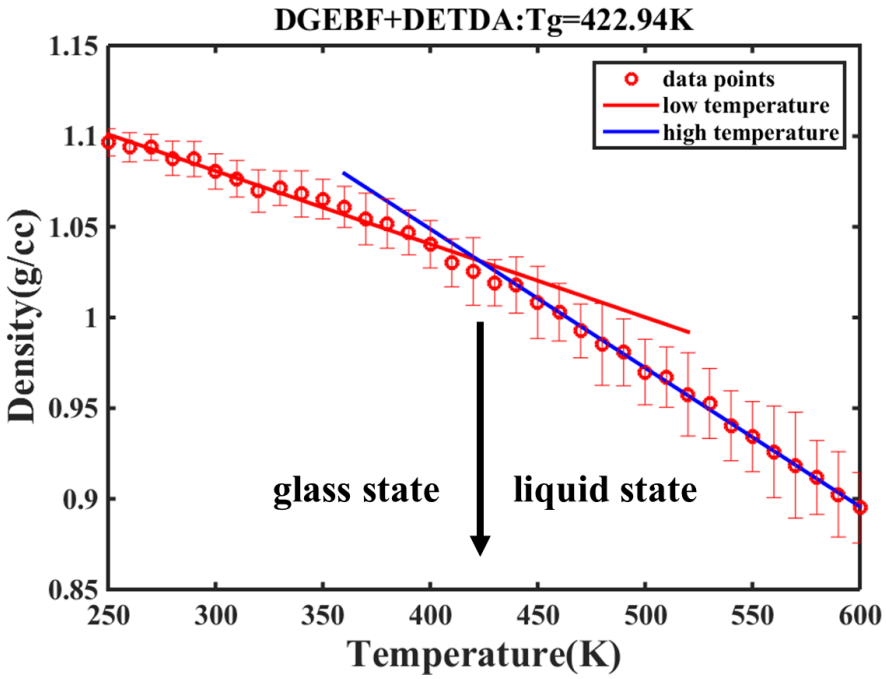

Figure 3.14. MD Simulation Results for Tg Prediction of System 1 (DGEBF+DETDA).

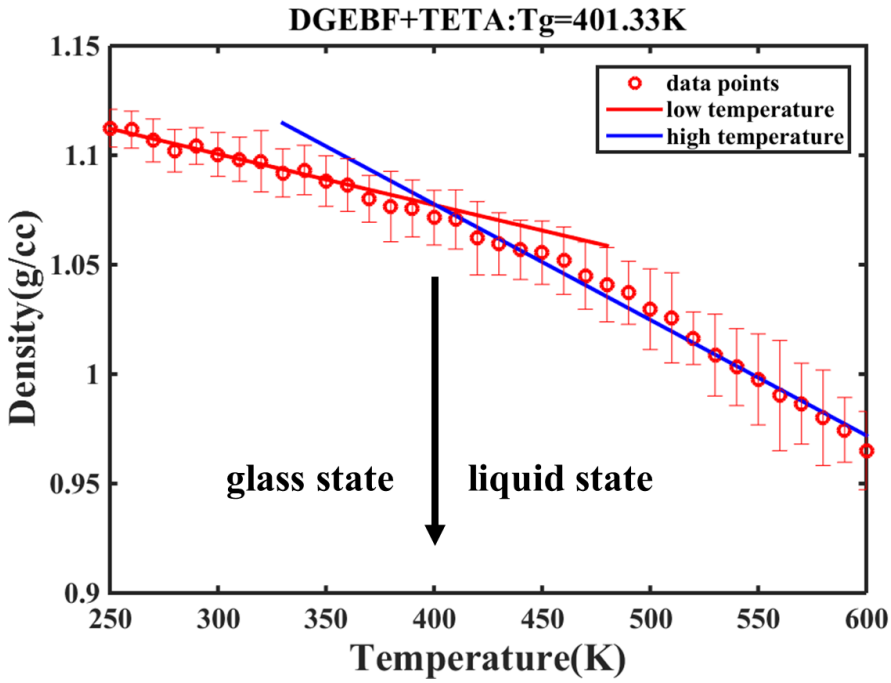

Figure 3.15. MD Simulation Results for Tg Prediction of System 2 (DGEBF+TETA).

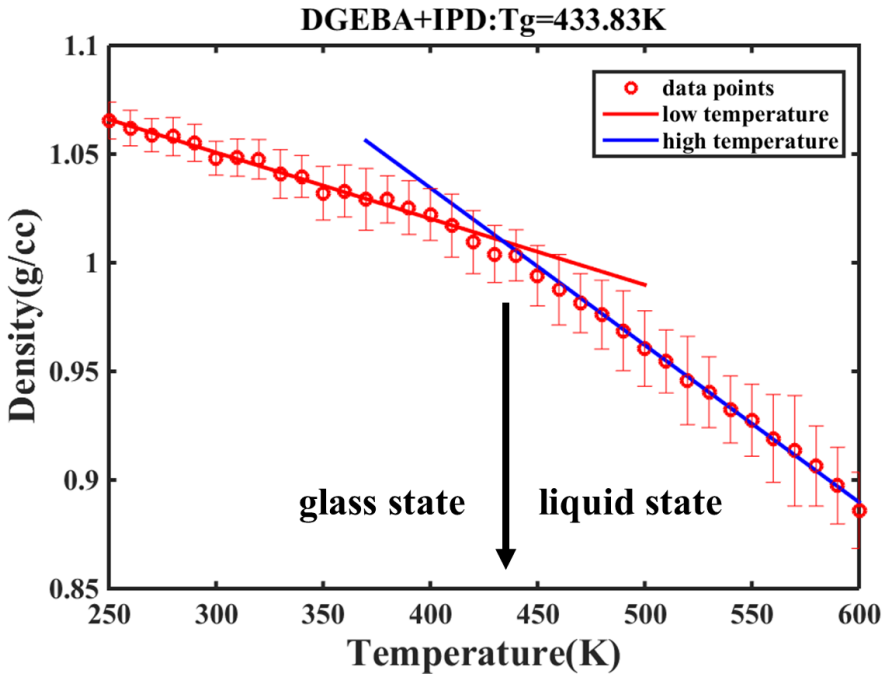

Figure 3.16. MD Simulation Results for Tg Prediction of System 3 (DGEBA+IPD).

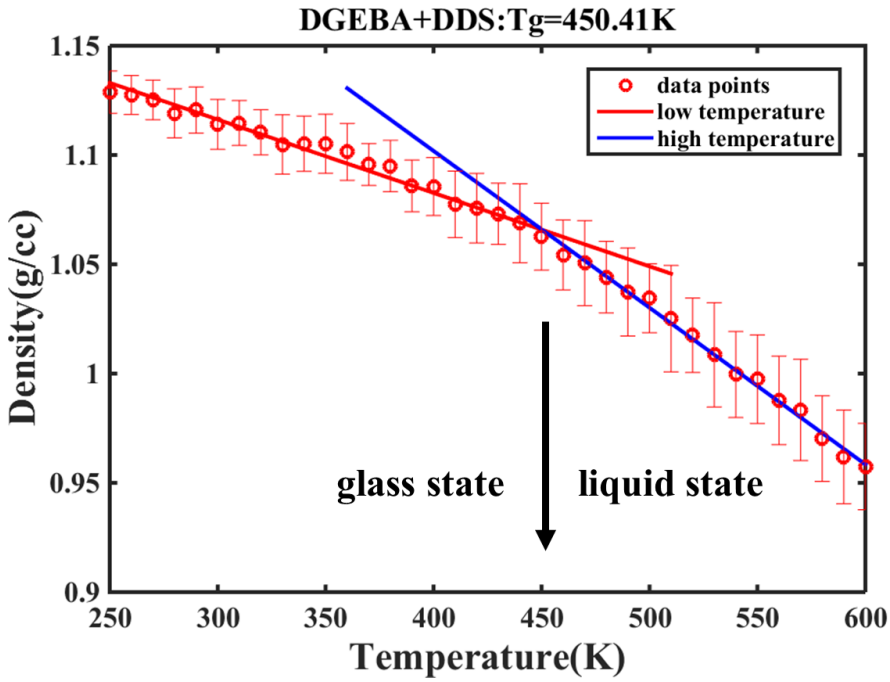

Figure 3.17. MD Simulation Results for Tg Prediction of System 4 (DGEBA+DDS).

Table 3.8. Evaluation of Goodness-of-Fit.

System	R^2		RMSE	
	Glass State	Liquid State	Glass State	Liquid State
1	0.97	0.99	0.0037	0.0017
2	0.97	0.98	0.0016	0.0045
3	0.98	0.99	0.0022	0.0021
4	0.97	0.99	0.0035	0.0027

Table 3.9. Estimated Tgs and Percent Error.

System	MD Simulations	DSC	% Error
1	422.9K	430K[165]	1.6%
2	401.3K	394K[161]	1.8%
3	433.8K	436K[162]	0.5%
4	450.4K	448K[163]	0.4%

3.2. Fluorescence Signal Detection: Experiments and Simulations

3.2.1. Synthesis and Testing

Sample Preparation and Test Methods: The dimeric anthracene-based mechanophore, Di-AC, was synthesized by 9-anthracene carboxylic acid (AC) using photosynthesis with a 302 nm wavelength UV lamp. After the photosynthesis, white Di-

AC powder particles were obtained and added to a mixture of epoxy resin and hardener with 5 wt% Di-AC (DGEBF and DETA, weight ratio 100:27). Once the mixture was homogenized, it was poured into silicone rubber molds and allowed to cure at room temperature. Neat epoxy samples were prepared in a similar manner, but without Di-AC. The average dimensions of the samples for the compression test were 3×4×8 mm^3. A compression test system (TestResources 800L) was used to compress the samples to different strains and obtain stress-strain plots for the epoxy samples. The tests were run in displacement control in the longitudinal direction at a loading rate of 1 mm/min and conducted at room temperature. The fluorescence generation from the compressed samples was observed under a Nikon Eclipse TE300 inverted video fluorescence microscope by excitation under 340-380 nm UV light with a filter cube to capture the emission of light between 435-485 nm. An image analysis software package was used to quantify the fluorescence intensity of the images taken from this study [166].

Damage Precursor Detection: Compression tests were performed on the mechanophore-embedded composite; 10 fluorescence microscopy images at specific strains (0%, 2%, 4%, 6%, 10%, and 15%) were obtained. Figure 3.18 shows the stress-strain curve along with representative fluorescence images at the selected strains. The image of the samples at 0% strain was taken prior to any compression and provides a baseline to confirm the capability of Di-AC mechanophore as a damage sensor. When it comes to the image of the sample at 4% strain, there is little distinguishable difference between the 0% and 4% images to the naked eye. However, the dark green color shown in the image of the samples at 6% strain, just after the yield point, is indicative of scattered

local damage, which activates the Di-AC mechanophores. The green fluorescence emission becomes more apparent as the stress-strain curve progresses into the plastic regime as indicated by the images of the samples at 10% and 15% strains. The same testing was performed on the neat epoxy to compare with the previous smart polymer test, and no change in fluorescence was observed from all the images as expected. Comparing the images of smart polymer and neat epoxy verifies that Di-AC can be used as a mechanophore in the epoxy system. Along with the image comparison, Figure 3.19 illustrates the average and the standard deviation of fluorescence intensity from two smart polymer samples at the specific strains. As seen in Figure 3.19, 4% strain is still in the elastic regime, but the average intensity of fluorescence at this strain increases compared to the 0% strain state; this indicates that Di-AC has the capability to be a damage precursor detector. It is also true that average intensities of 0% and 2% strain cases are statistically different; however, the fluorescence intensity of Sample 1 in Figure 3.19 shows some overlap in the error bar between 0% and 2% strains. This overlap is not present in the intensity information between 0% and 4% strain images. Since plastic deformation and material failure are accelerated drastically after the yield point, it is imperative to be aware of the impending material failure before yielding occurs. This allows the material to be repaired before catastrophic failure. This is also a significant improvement to the results of the cyclobutane-based mechanophore embedded epoxy polymer, for which fluorescence emission was only observed after the yield point [12].

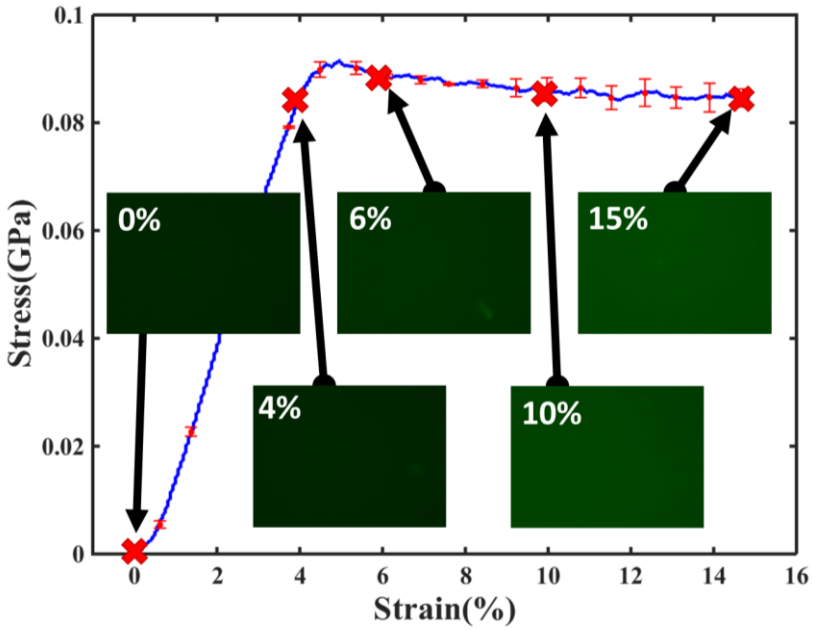

Figure 3.18. Stress-Strain Curve and Fluorescence Images from the Compression Test.

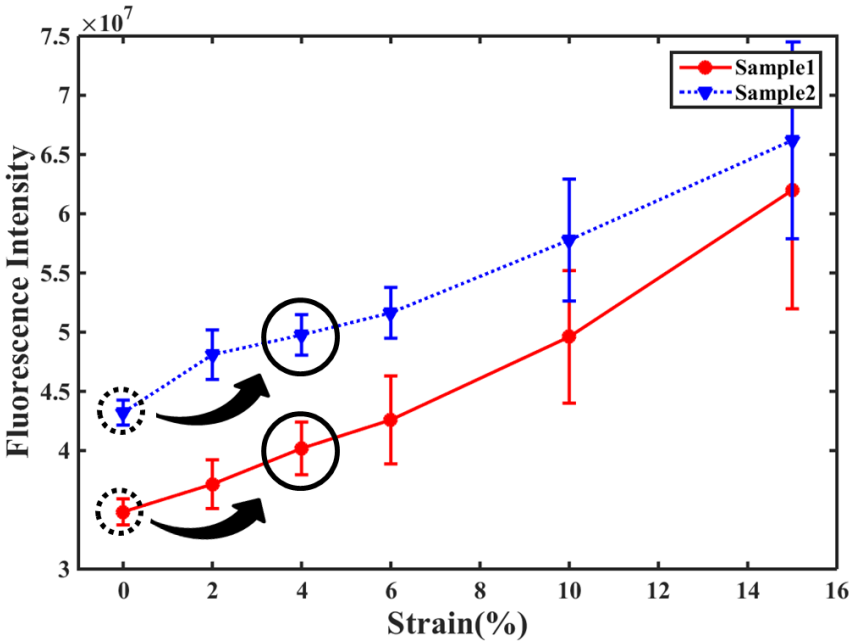

Figure 3.19. Intensity of Fluorescence in Two Samples from Compression Test.

3.2.2. Damage Precursor Detection Simulation

In this study, damage precursor is defined as an indication of impending material failure prior to the yield strain. The yield strain can be obtained from stress-strain curve computationally using MD simulation, and this strain value can be compared with the critical strain estimated from the mechanophore activation results to investigate the capability of damage precursor detection. MMFF, the classical force-field, is employed to estimate the stress-strain response of the smart polymer since this comparative study is focused on the elastic regime (from zero strain to yield strain) and classical force-fields have shown tremendous success in capturing elastic behavior of polymer systems [65, 163, 167-171]. It is noteworthy that ReaxFF can also be used for this estimation; however, ReaxFF is relatively well optimized to simulate plastic behavior. A few studies in the literature have used ReaxFF to estimate the elastic behavior of epoxy polymer system, but appropriate experimental validation was not provided [172].

Using MMFF, the dynamic method (constant-stress deformation) developed by Berendsen et al. [173] is applied to the epoxy-cured unit cell. The crosslinked smart polymer unit cell is deformed gradually at a constant rate of 10^{10} s^{-1} along the x-axis in the NPT ensemble (300 K and zero pressure on y and z-axis). The strain rate is significantly high compared to that of experiments ($\approx 10^{-3}$ s^{-1}) due to the limitation of feasible time step in MD simulations. However, this strain rate has been used in the MD research field and have estimated experimentally comparable stress-strain curves [169-171]. It is also noted that the simulation time is appropriately long (100,000 steps, 1 fs time step) for the system size under consideration (69260 atoms) to ensure that the thermodynamic parameters are well averaged. Hence, the mechanical properties estimated through virial stress

information from the simulation results are comparable to the mechanical properties measured by experiments based on the ergodic theory [174, 175]. The results from mechanophore activation are added to the stress-strain curve to compare the critical strain and yield strain.

As highlighted with a dotted red box in Figure 3.20, the hybrid MD methodology illustrates that the critical strain (14% strain) from mechanophore activation occurs prior to the yield strain (15% strain). Good agreement is observed with experimental results (Figure 3.18 and Figure 3.19): both simulations and experiments indicate that mechanophores are activated before the yield strain. Although there is a difference in absolute strain value between experiments and simulations due to the huge length scale discrepancy, the significance of this computational result is that the occurrence of the critical strain for mechanophore prior to the yield strain (damage precursor detection), which is strongly dependent on interatomic and intermolecular interaction in the composite system, is captured. In order to verify the effectiveness of this comparative method as a means to verify damage precursor detection capability, the comparative method is also applied to the cyclobutane-based mechanophore (TCE) study. In the experiments using cyclobutane, the fluorescence emission signal (6% strain in Figure 3.22) was only observed subsequent to yield strain (5% strain in Figure 3.21) [12], implying that cyclobutane-based mechanophore does not possess damage precursor detection capability. The results from the comparative method to the cyclobutane mechanophore simulation data also show good agreement with the corresponding experimental results; the critical strain for mechanophore activation (26% strain) occurs after yield strain (18% strain) as shown in Figure 3.32. The comparative method using the hybrid MD simulation results successfully

identifies the damage precursor detection capability of two different mechanophores (TCE and Di-AC); it is anticipated that this comparative method can be expanded for the study of various mechanophores.

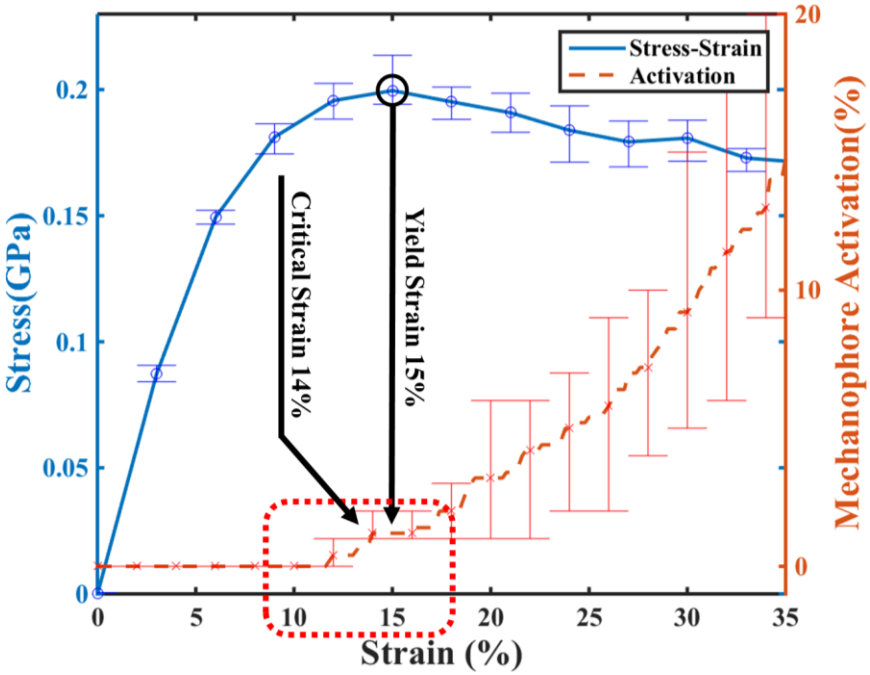

Figure 3.20. Simulation Results: Stress-Strain Curves vs. Mechanophore Activation Plot for the Di-AC Embedded Nanocomposite.

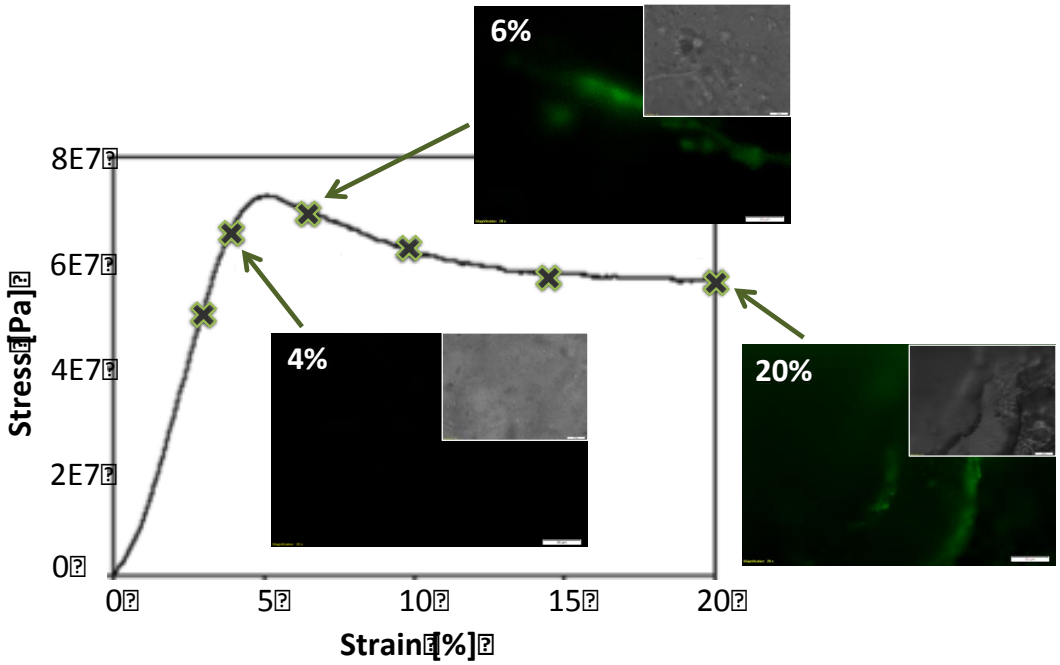

Figure 3.21. Experimental Results: Stress-Strain Curves vs. Fluorescence Images from the Compression Test for the TCE Embedded Nanocomposite [12].

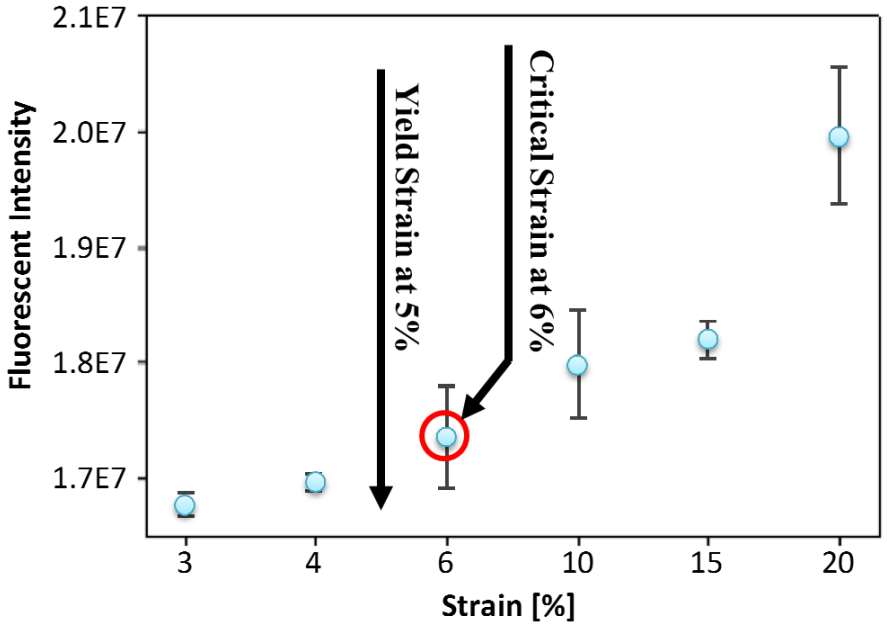

Figure 3.22. Experimental Results: Intensity of Fluorescence from the Compression Test for the TCE Embedded Nanocomposite [12].

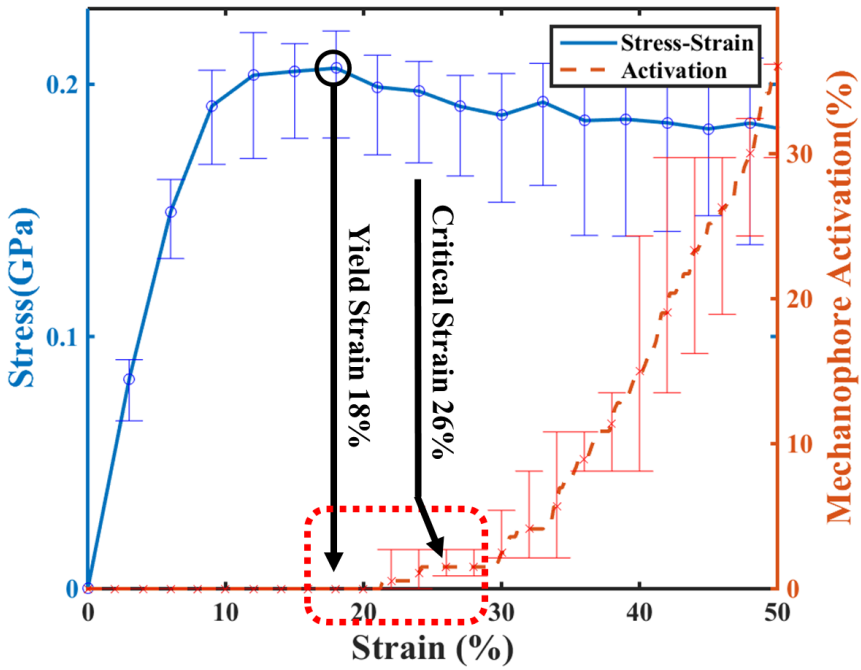

Figure 3.23. Stress-Strain Curves vs. Mechanophore Activation Plot of Cyclobutane-Based Mechanophore Embedded Polymer.

Comparative Study for Mechanophore Sensitivity: Experimental results have demonstrated the improved sensitivity of Di-AC as a damage sensor compared to the cyclobutane-based mechanophore. However, a reasonable physics-based justification, which might be supported by existing experimental knowledge, has not been provided. Although the 'ring strain' analysis based on 'heat of combustion' measurement has been used to evaluate the instability of cycloalkane (Table 3.10), ring strain analysis of Di-AC has not been reported due to its complex structure for the 'heat of combustion' experiments [176]. As an alternative to 'ring strain' analysis, the BDE calculation is used to analyze the instability of mechanophores. It has been shown that Di-AC's BDE is less than that of TCE in the previous chapter; therefore, addressing the correlation between BDE and ring strain

is critical. Furthermore, the reason for the lower BDE of Di-AC can be justified by an understanding based on nanoscale physics.

Cyclobutane and cyclooctane are selected from the ring strain table (see Table 3.10). Cyclobutane is selected because of the TCE comprising three cyclobutanes, and cyclooctane is selected due to its similarity to the Di-AC chemical structure, which contains a derivative of cyclooctane (Figure 2.34). The ring strain of cyclobutane (26.4 kcal/mol) was found to be greater than the ring strain of cyclooctane (9.6 kcal/mol), implying that cyclobutane is more sensitive to external stimulation than cyclooctane. Note that the BDE calculation should show inverse proportionality to ring strain analysis because the BDE calculation computes the energy required to break the structure. Low BDE implies that the structure is weak (unstable) and sensitive to external loads. The BDE calculation using COGEF is performed with Singh's ReaxFF parameter set (please refer Chapter 2). The COGEF simulation is conducted following the same procedure as used in the previous chapter. Only the boundary conditions for the deformation is different. Red arrows in Figure 3.24 and Figure 3.25 indicate the unit vectors of the pulling directions. The total energy of the system is measured as the geometry deforms. The simulation results reveal that the BDE of cyclobutane and cyclooctane are 71.7 kcal/mol and 159.95 kcal/mol, respectively. The BDE of cyclooctane (159.95 kcal/mol) is greater than BDE of cyclobutane (71.7 kcal/mol); it is successfully correlated with the inverse proportionality of the ring strain. Therefore, it becomes possible to use the BDE calculation as an alternative to the ring strain analysis.

The sensitivity of Di-AC to external loads is characterized hereby using the BDE results. From the previous BDE calculation of Di-AC, it is found that the BDE of Di-AC is 58.5

kcal/mol (Figure 2.35), which is lower than the BDE of cyclobutane (71.7 kcal/mol). This implies both that the Di-AC will have higher ring strain than cyclobutane and it requires less energy for bond breakage than cyclobutane. Additionally, the cyclooctane, which was chosen due to its structural similarity to Di-AC as a comparative study, requires higher energy to break the bond than Di-AC. In order to understand the relatively low BDE of Di-AC compared to cyclobutane and cyclooctane, it is noteworthy that Di-AC has a unique structure: two cyclooctane ring shapes share two covalent bonds, which is called [4+4] cyclodimer (Figure 2.34). Although there is no experimental evidence to support the following conclusion, it might be reasonable to hypothesize that the improved sensitivity of Di-AC is due to the unique structure: [4+4] cyclodimer through the BDE analysis.

Table 3.10. Ring Strain of Cycloalkane [176].

Cycloalkane $(CH_2)_n$	CH_2 Units (n)	Ring Strain (kcal/mol)
Cyclopropane	n = 3	27.6
Cyclobutane	n = 4	26.4
Cyclopentane	n = 5	6.5
Cyclohexane	n = 6	0
Cycloheptane	n = 7	6.3
Cyclooctane	n = 8	9.6

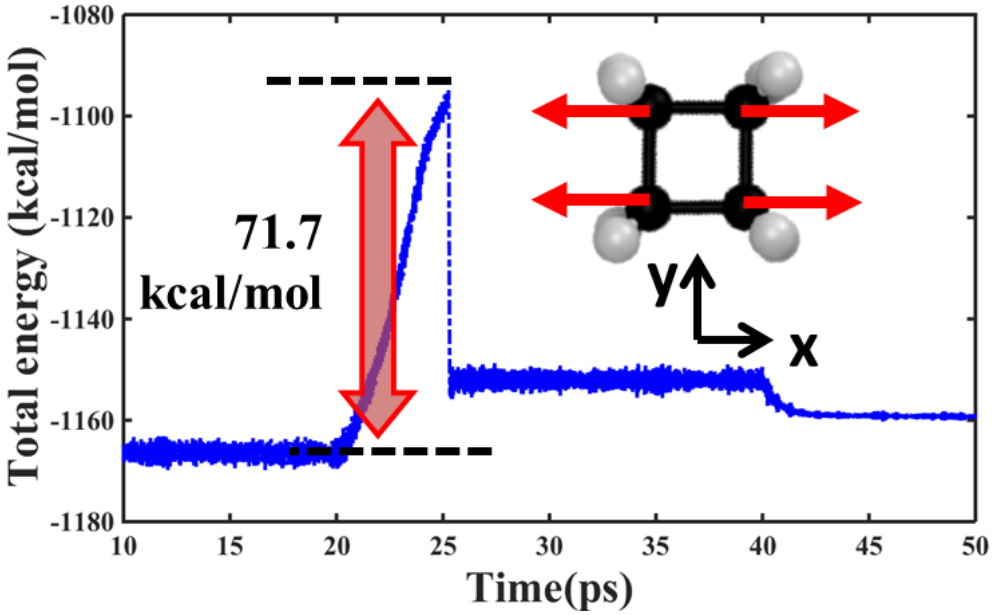

Figure 3.24. Bond Dissociation Energies of Cyclobutane (71.7 Kcal/mol); Red Arrows Indicate the Unit Vectors Representing the Pulling Directions.

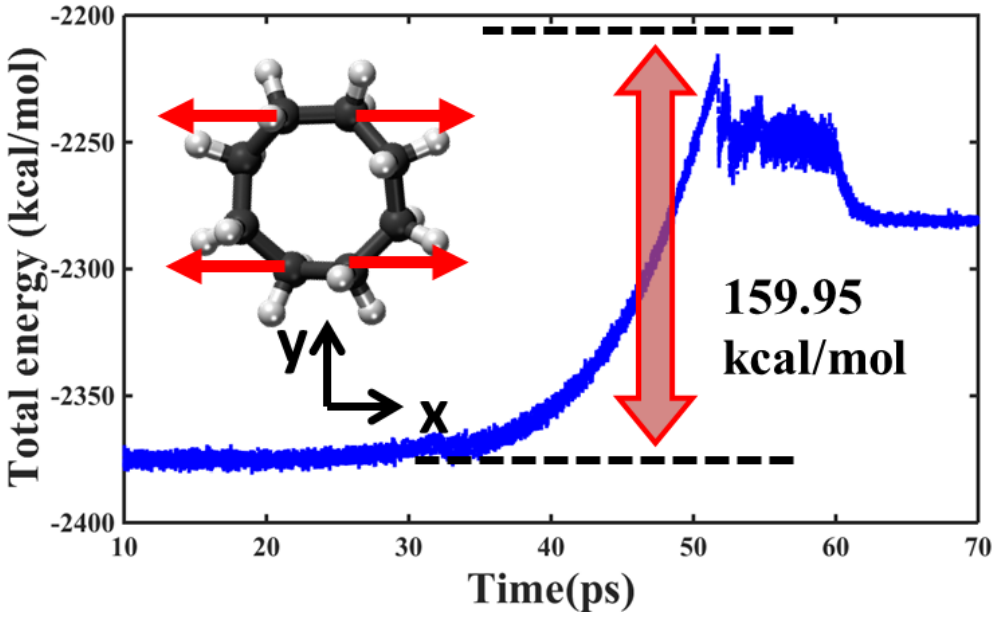

Figure 3.25. Bond Dissociation Energies of Cyclooctane (159.95 Kcal/mol); Red Arrows Indicate the Unit Vectors Representing the Pulling Directions.

3.3. Mechanical Properties

3.3.1. Cyclobutane-based Mechanophore Embedded Thermoset

The mechanical properties are measured via uniaxial/triaxial deformation tests conducted using the MD simulator. For the deformation test, 52.7% crosslinked smart polymer and 56% crosslinked neat epoxy are used; specifically, the same unit cell used in Section 2.3.1 is utilized in this virtual deformation test. In addition, the classical force-field, is employed to estimate the stress-strain response of the two systems due to the same reason mentioned in the previous section (Section 3.2.2). After generating covalent bonds in each unit cell under the same experimental curing condition (300K and 1 atm), these unit cells were equilibrated under zero-atmospheric pressure to remove predefined pressure on all the axes. Subsequently, the unit cell was deformed along the x-axis with constant strain rate ($10^{10}s^{-1}$) under NPT ensemble (300K and zero pressure on y and z-axis); MD simulator measures the stress and strain about the x-axis. The raw stress data obtained after 30% deformation shows huge fluctuation due to the intrinsic atomic vibration and is shown in Figure 3.26-Figure 3.29.

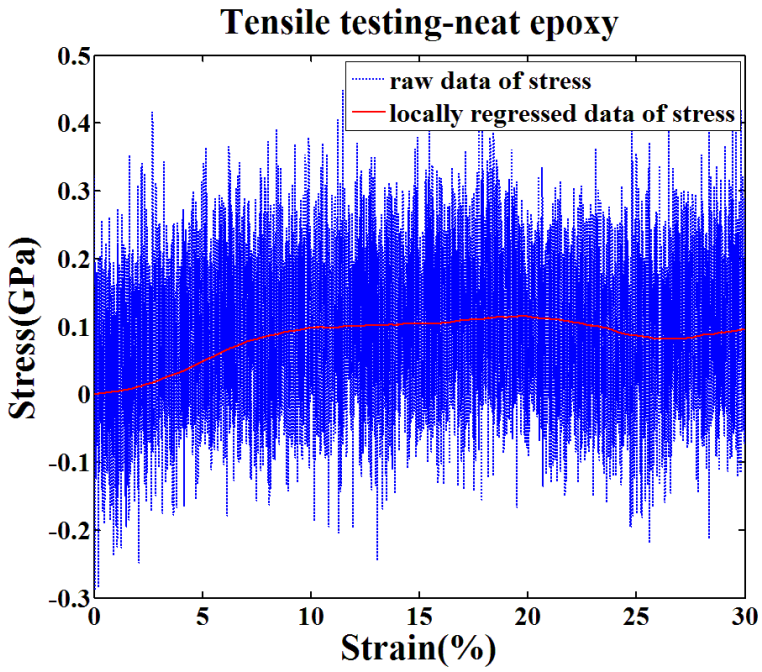

Figure 3.26. Uniaxial Tensile Tests in MD Simulation with the Conversion Degree of 56% for Neat Epoxy.

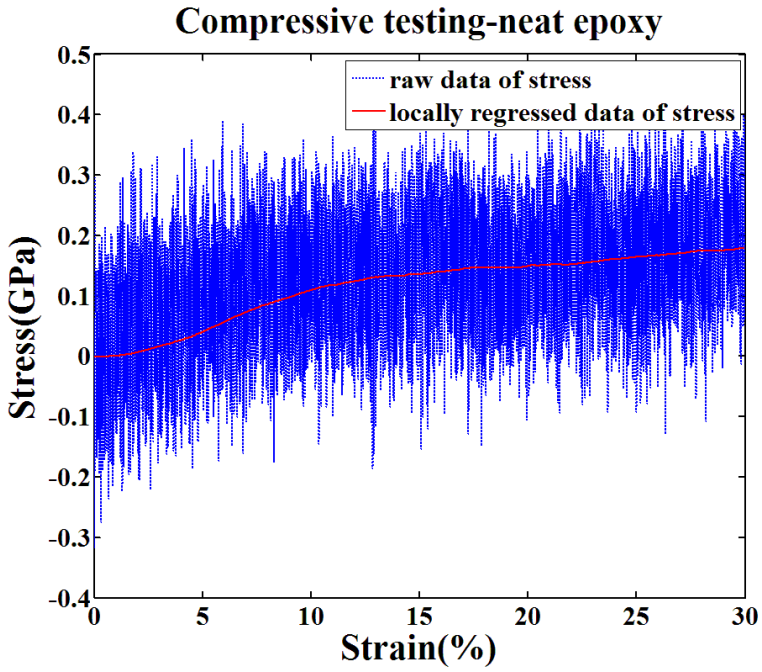

Figure 3.27. Uniaxial Compression Tests in MD Simulation with the Conversion Degree of 56% for Neat Epoxy.

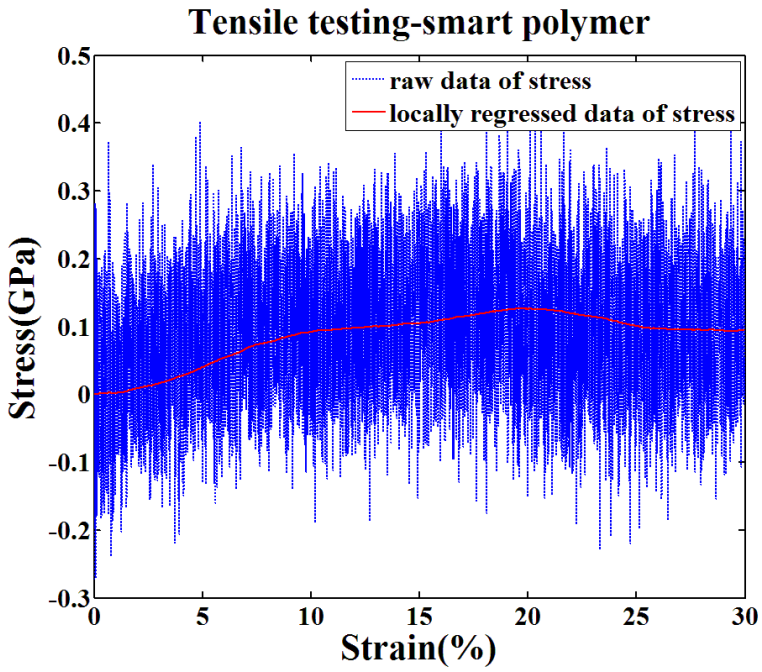

Figure 3.28. Uniaxial Tensile Tests in MD Simulation with the Conversion Degree of 52.7% for Smart Polymer.

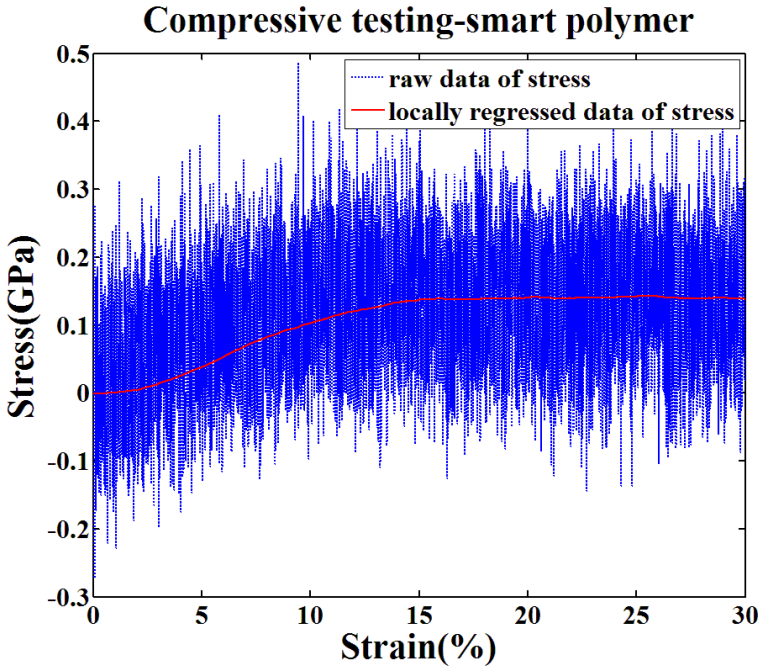

Figure 3.29. Uniaxial Compression Tests in MD Simulation with the Conversion Degree of 52.7% for Smart Polymer.

A local regression of linear polynomial model has been used to reduce the fluctuation. Each plot has raw stress data (blue dotted line) and locally regressed data (red solid line). Based on the locally regressed stress-strain curve, Young's modulus is computed by finding maximum local slope through the stress-strain curve from zero strain until 15% strain, at which the curve usually starts to show the strain-hardening behavior. In addition, it is worth noting that since an epoxy based system has an amorphous structure, the dynamic response corresponding to the tensile test and the compressive test might be different. The stress-strain curve in tension and compression for both neat epoxy and smart polymer are shown in Figure 3.30 and Figure 3.31. Since each unit cell is not homogeneous, a uniaxial deformation test was also conducted for y and z-axes independently. For bulk modulus estimation, a triaxial deformation test was conducted, which is relatively simple compared to the uniaxial deformation test. After increasing the hydrostatic pressure on each unit cell from 0 atm to 5000 atm at room temperature, the MD simulator measures the volume change of each unit cell to calculate the bulk modulus using Equation 3.4.

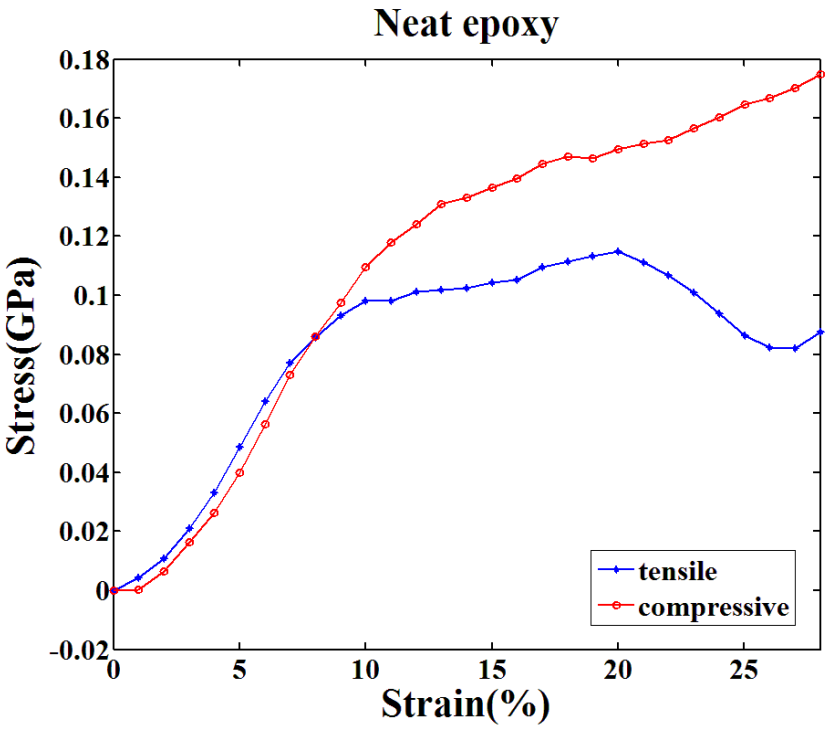

Figure 3.30. Locally Regressed Stress-Strain Curves of Neat Epoxy.

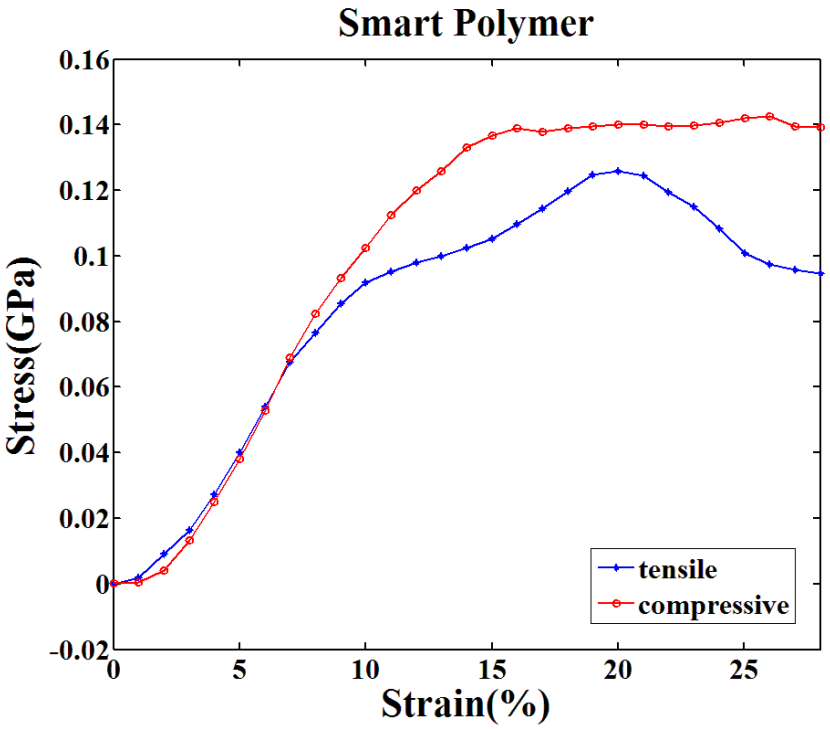

Figure 3.31. Locally Regressed Stress-Strain Curves of Neat Epoxy.

$$K = \frac{\Delta p}{\Delta V / V_0} \quad (3.14)$$

Based on Young's modulus (E) and bulk modulus (K) achieved from MD simulation, shear modulus and Poisson's ratio are calculated using two basic equations in mechanics of material under isotropic material assumption,

$$G = \frac{3KE}{9K - E}, \text{ and } \upsilon = \frac{3K - E}{6K} \quad (3.15)$$

where G is shear modulus and υ is Poisson's ratio. Table 3.11 shows the prediction of mechanical properties of both neat epoxy and smart polymer.

Table 3.11. Prediction of Mechanical Properties.

	Neat Epoxy (56%)		Smart Polymer (52.7%)	
	Tension	Compression	Tension	Compression
Young's Modulus	1.64GPa	1.80GPa	1.53GPa	1.73GPa
Bulk Modulus	6.47GPa	6.47GPa	5.90GPa	5.90GPa
Shear Modulus	0.56GPa	0.62GPa	0.53GPa	0.59 GPa
Poisson's Ratio	0.4578	0.4536	0.4567	0.4511

The relationship between the conversion degree and the mechanical properties is investigated next. The same uniaxial/triaxial deformation tests have been conducted at conversion degrees ranging from 10% to 100%. Figure 3.32-Figure 3.35 show the MD

simulation results of Young's modulus and linearly regressed Young's modulus as a function of conversion degree. Because the number of atoms in each unit cell (≈4000 atoms) is not enough to represent continuum model, the MD simulation results do not show a linear trend as the conversion degree increases. For this reason, finding a relationship describing Young's modulus as a function of conversion degree is more meaningful. Linearly fitted lines show a proportional relationship between Young's modulus and the conversion degree, which is physically intuitive (high conversion degree means high stiffness). The solid blue lines are defined as a linear equation, such as Equation 3.6. Substituting a specific conversion degree into Equation 3.6, elastic modulus of the epoxy system cured with a specific degree can be predicted.

$$E = \delta x + \varepsilon, \qquad (3.16)$$

where E is Young's modulus (GPa), x is conversion degree (0~1), δ and ε are fitted parameters listed in Table 3.12. These predicted results would be extended to compute mechanical properties in a future study.

Table 3.12. Parameters for Fitted Linear Lines for Young's Modulus of Both Neat Epoxy and Smart Polymer.

	Neat Epoxy		Smart Polymer	
	Tension	Compression	Tension	Compression
δ	1.258	1.913	0.994	1.243
ε	0.851	0.810	1.029	1.178

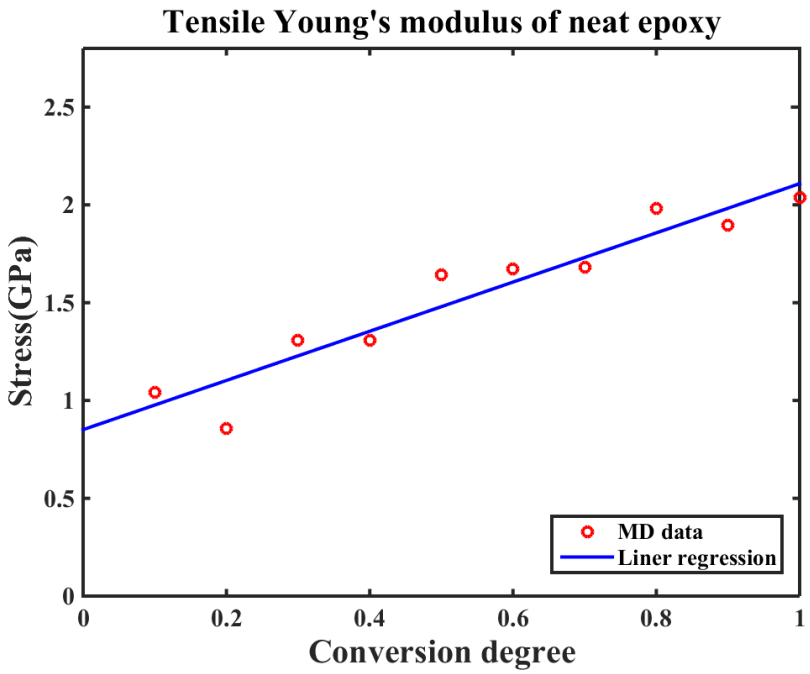

Figure 3.32. Tensile Young's Modulus vs. Conversion Degree for Neat Epoxy

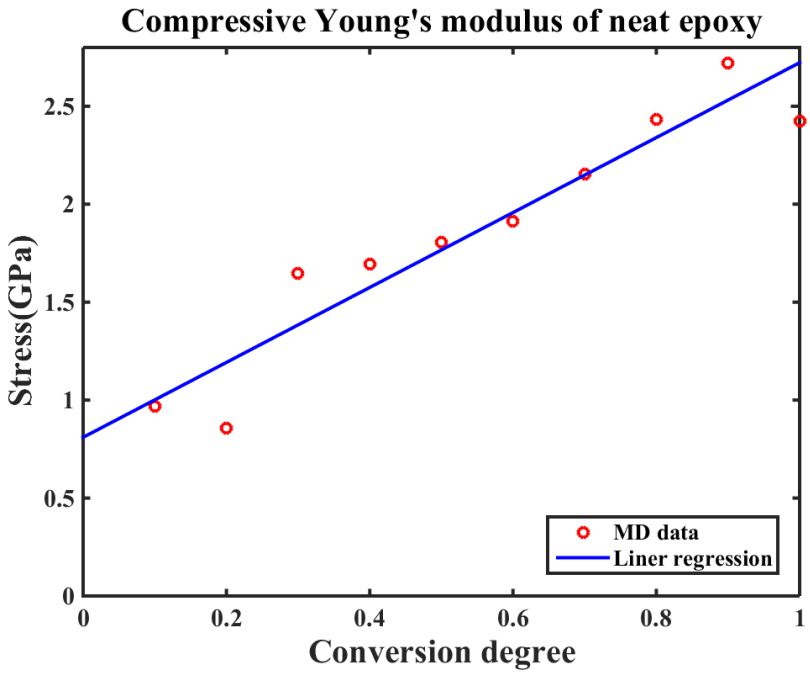

Figure 3.33. Compressive Young's Modulus vs. Conversion Degree of Neat Epoxy

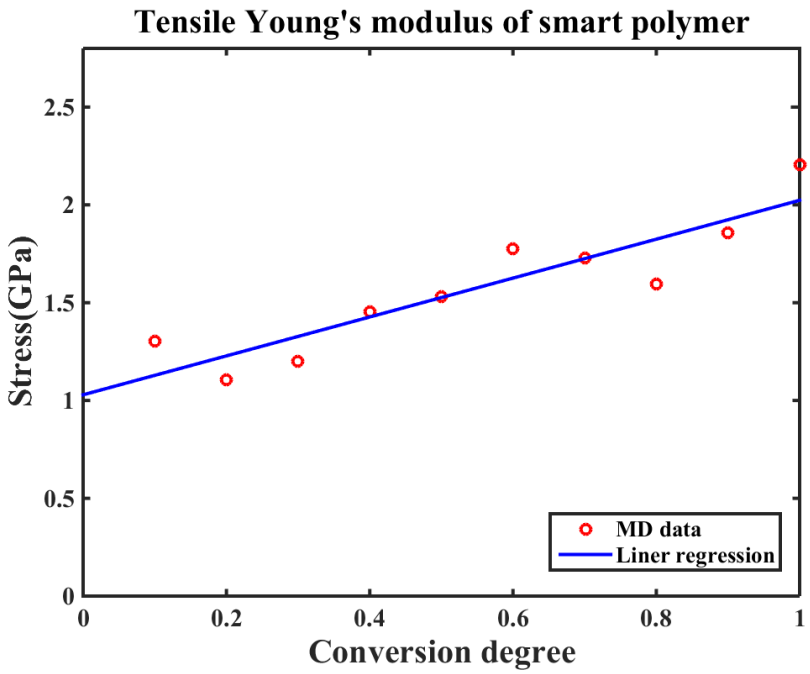

Figure 3.34. Tensile Young's Modulus vs. Conversion Degree of Smart Polymer

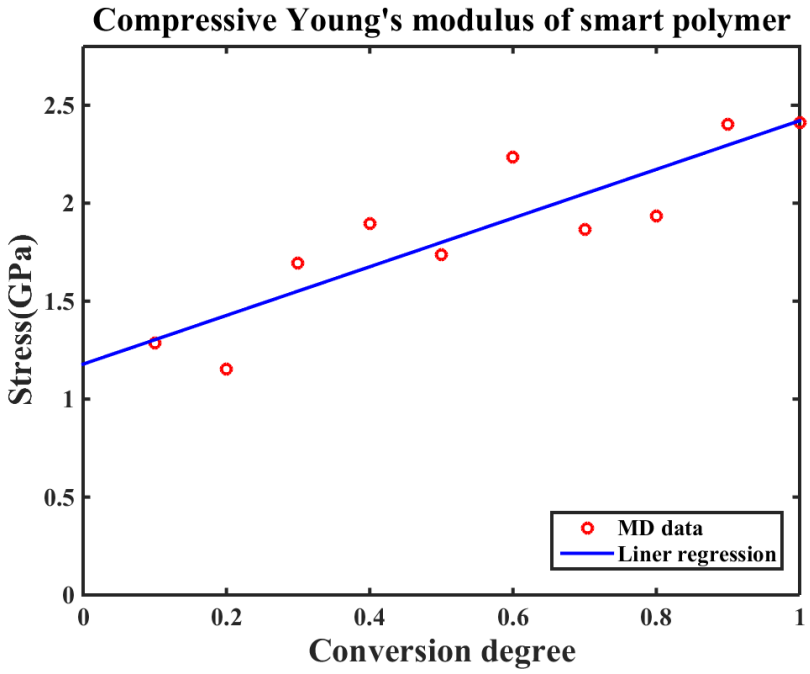

Figure 3.35. Compressive Young's Modulus vs. Conversion Degree of Smart Polymer

3.3.2. Anthracene-based Mechanophore Embedded Thermoset

In addition to damage precursor detection described in Section 3.2, changes in mechanical properties due to Di-AC inclusion observed from experiments (see Figure 3.36) is also captured by the MD simulations. MD simulations estimate a difference of 12.5 MPa in the yield strength between neat epoxy and smart (Di-AC embedded) polymer (see Figure 3.37). The experiments showed 11.55 MPa degradation in the yield strength. The Young's modulus in both cases (neat epoxy and the smart polymer) is also estimated. A small difference in modulus (3.9%) is observed between the two cases, which correlates well with experimentally measured modulus difference of 4.2%. It should be noted that due to the length scale discrepancy between experiments and atomistic simulation, the absolute strain and stress values (magnitude of yield strain and stress) do not correlate with the experimental results. However, the MD simulation results demonstrate that the modeling framework estimates the mechanical property variation induced by Di-AC inclusion successfully. These close correlations in important physical phenomena indicate that the computational framework can be used to guide the experiments by estimating the effects of variability in the design parameters on material properties with some level of accuracy.

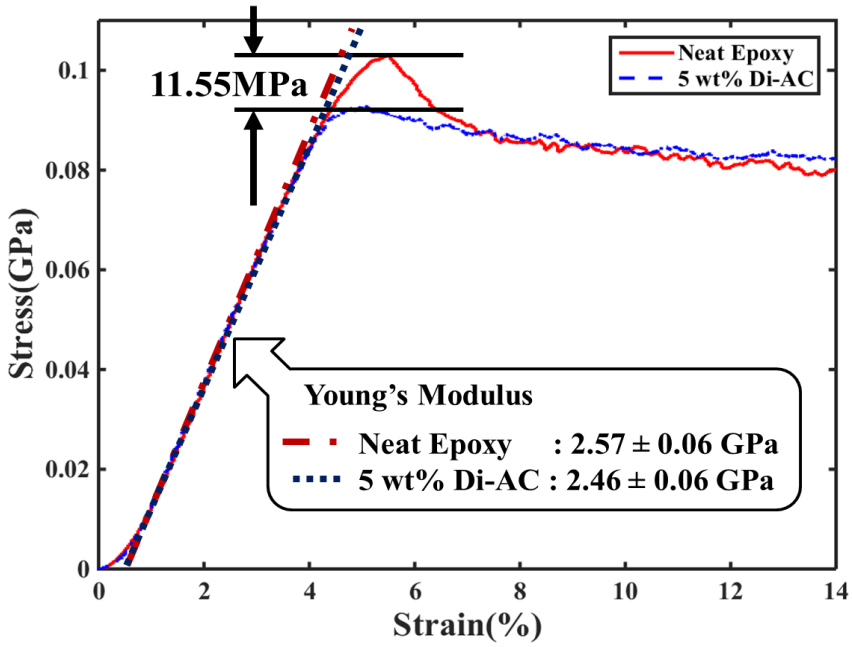

Figure 3.36. Experimental Results: Stress-Strain Curves of Neat Epoxy and Smart Polymer (5 wt% Di-AC Epoxy).

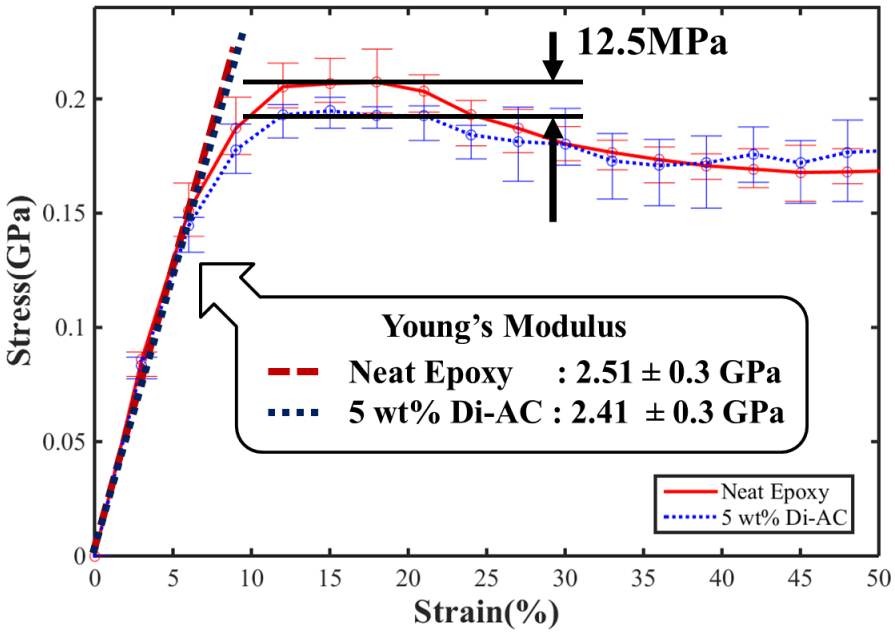

Figure 3.37. Simulation Results: Stress-Strain Curves of Neat Epoxy and Smart Polymer (5 wt% Di-AC Epoxy).

3.4. Verification of Numerical Dimerization Algorithm

The accuracy of the developed numerical UV dimerization method (refer to Chapter 2) needs to be established, since incorrect topology information leads to inaccurate dynamic behavior. Unlike previous experimental validation, this section is about verification of the algorithm developed for topology transformation. For this verification, the BDE of two molecules (pre-dimerized and numerically dimerized TCE polymers) are compared. BDEs are calculated using COGEF with ReaxFF (refer to Chapter 2).

After performing the numerical UV dimerization to create the numerically dimerized TCE polymer, its BDE is calculated. The pre-dimerized TCE polymer, which has the same structure as the numerically dimerized TCE polymer, is also prepared for the BDE calculation for the comparative study. As the pre-dimerized TCE has been characterized in Section 2.3.5 for the local work analysis, the numerically dimerized TCE is also analyzed using the same method. The total energy of the numerically dimerized TCE system is measured here as the geometry deforms (see Figure 3.38). The first drop in total energy is observed around 56 ps from both systems (the results for the pre-dimerized TCE is presented in Chapter 2); the drop represents covalent bond dissociation. The simulation results reveal a BDE of 315.05 kJ/mol from the pre-dimerized TCE polymer and 315.4 kJ/mol from the numerically dimerized TCE polymer. The percentage error between the two systems is less than 0.001%; this indicates that the numerical UV dimerization method transforms the cinnamoyl groups to cyclobutane correctly.

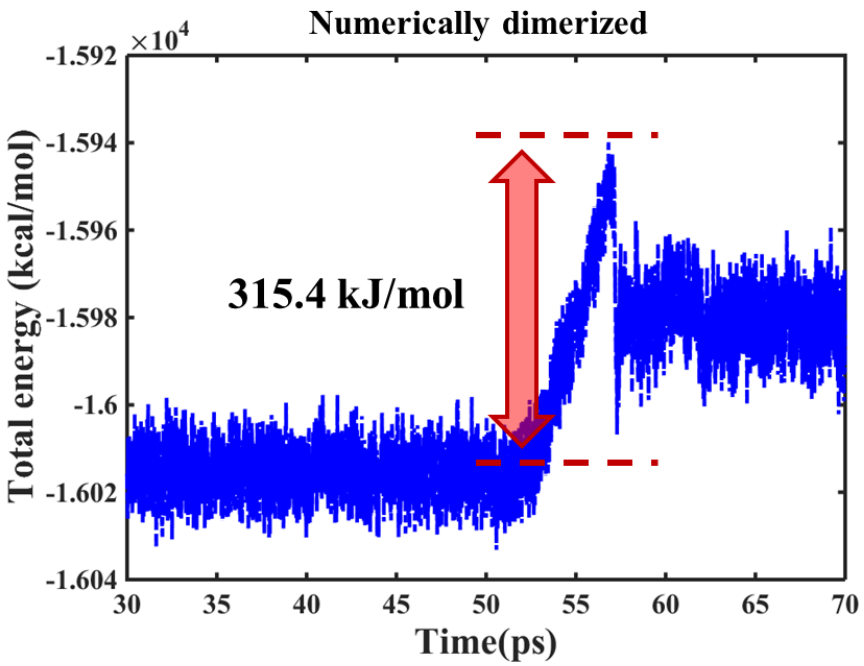

Figure 3.38. BDEs Obtained from Numerically Dimerized Cyclobutane Structure (Elongation Starts at 50ps with 0.0005 Å/fs and Bond Scission Occurs around 56ps).

3.5. Chapter Summary

In this chapter, experiments and MD simulations results are presented to validate the molecular model of mechanophore embedded nanocomposites and the hybrid MD simulation framework. The influence of mechanophores (stress-sensitive material) on the conversion degree and Tgs of neat epoxy was investigated numerically and experimentally. Tgs estimated by the hybrid MD simulation framework were compared with experimental results from DSC. In order to show the suitability of the hybrid MD framework to predict thermal property for general epoxy system, four different epoxy systems were introduced and their Tgs were estimated within 2% error. In addition, early damage signal detection capability of the mechanophore was demonstrated by obtaining UV excited images from the damaged specimens (TCE and Di-AC embedded nanocomposites) subjected to

mechanical loading. Along with the experimental results, the simulation results from the hybrid framework captured the capability of early damage signal detection. In this chapter, the reliability of the hybrid MD simulation framework has been validated experimentally; therefore, it is expected that this framework can provide a guideline for the design of mechanophoric material systems with a limited number of experiments.

CHAPTER

4. ATOMISTIC SIMULATION METHOD FOR DAMAGE EVOLUTION IN THERMOSET POLYMER

In this chapter, a novel atomistic simulation methodology is developed to accurately capture the brittle behavior of epoxy based thermoset polymer. An appropriate bond-order based force-field is necessary to capture bond dissociation during the deformation test. A bond-order based force-field was used by Odegard et al. [172] previously to capture material degradation of an epoxy polymer system during deformation test; however, their results were inconclusive as to whether the material degradation was due to conformational change (molecular sliding) or due to covalent bond dissociation.

It is noteworthy that using a bond-order based force-field as in the deformation test by Odegard et al. [1] is only a necessary condition to capture bond dissociation. In order to capture bond dissociation properly during the deformation simulation in MD, a method to decouple molecular thermal vibration from the deformation simulation along with using an appropriate bond-order based force-field is explored. Two deformation methods are hypothesized to suppress the effect of thermal vibration: zero-temperature deformation (also called quasi-continuum method) and ultra-high strain rate (UHSR $\approx 10^{13}$ s^{-1}). In the zero-temperature method, the energy minimization process maintains the system at ground state, free of thermal effects, whereas the UHSR method allows molecular vibration, but deforms the simulation volume with a higher strain rate than the bond vibration frequency of the covalent bonds.

The zero-temperature and UHSR methods both implicitly produce time-independent behavior resembling quasi-static systems because the thermal activation of molecular

motion is decoupled from the virtual mechanical deformation [152]. The virtual mechanical deformation results show that the two deformation methods with the appropriate bond-order based force-field capture brittle fracture in an epoxy-based polymer system at a small strain (~10%), which correlates well with experimental results [48-50].

4.1. Molecular Model and Simulation Method

To construct a simulation volume, molecular structures of DGEBF (epoxy resin) and DETA (hardener) were used based on the weight fraction (M_{DGEBF}:M_{DETA}=100:27). Table 4.1 contains the number of molecules in the simulation volume (66,560 atoms), and Figure 4.1 shows a schematic of the 3D molecular structure of the volume. The classical force-field MMFA was implemented to equilibrate the epoxy system and perform the curing simulation (crosslink formation) [47, 114]. A stochastic crosslink formation approach, based on a cutoff distance for covalent bond generation between active sites, was adopted to simulate the epoxy curing process [177]. Note that while MD simulations with a classical force-field are very effective for studying processes in a system around its equilibrium state (e.g., curing), they are not appropriate for investigating covalent bond dissociation occurring away from the equilibrium state (e.g., deformation tests). In order to capture the bond dissociation phenomenon, a popular bond-order based force-field method called ReaxFF was used. The ReaxFF parameter set developed by Singh et al. [146] was identified as an appropriate force-field for the epoxy system. BDE of C-C bond in epoxy resin (DGEBF) was calculated and validated with experiments (pyrolysis experiments [148]) for the ReaxFF parameter set investigation, which is elaborated in Chapter 2. The

experimentally validated parameter set was then used for the virtual deformation tests in this chapter.

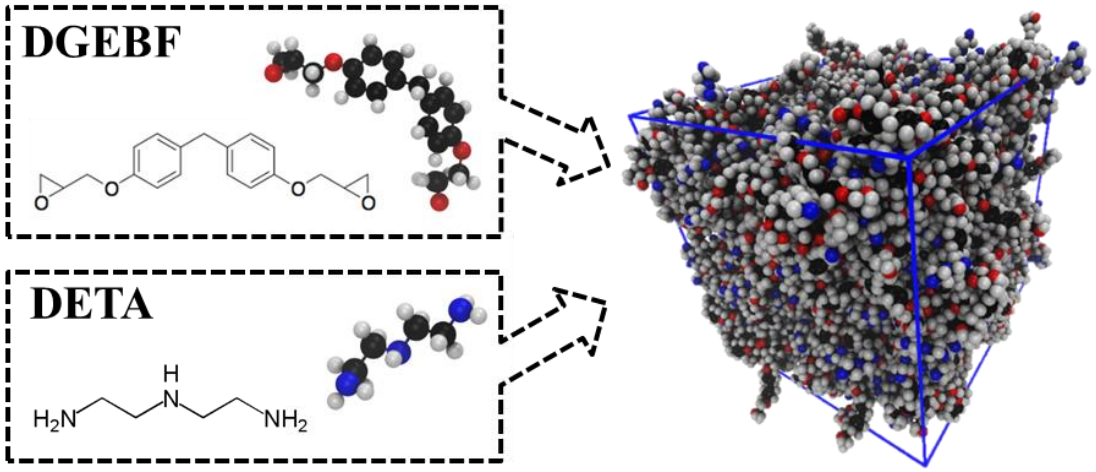

Figure 4.1. Schematic of the MD Simulation Volume Containing DGEBF (Epoxy Resin) and DETA (Hardener).

Table 4.1. Components in the Simulation Volume (M_{DGEBF}:M_{DETA}=100:27).

	Weight	Formula	Number of Molecules
DGEBF	313 g/mol	$C_{19}H_{20}O_4$	1120
DETA	103 g/mol	$C_4H_{13}N_3$	920

4.2. Effect of Thermal Vibration on Potential Energy under Deformation Test

Temperature is related to the kinetic energy of the molecular system directly; however, in MD simulations, temperature can also cause potential energy variation. Temperature changes affect not only the frequency, but also the amplitude of molecular vibration leading

to changes in the potential energy. This phenomenon is verified in the following simulations: The potential energy of 100 ps NPT ensemble of the epoxy-based thermoset polymer at different temperatures (0K, 100K, and 500K) is measured with MMFF force-field after the epoxy curing process. The epoxy curing process, introduced in Chapter 2, is performed using the cutoff distance based covalent bond generation method [177], after performing energy minimization (conjugate gradient method) and subsequent equilibration for 10 ns with the NPT ensemble (300K and 1atm, Nose-Hoover thermostat/barostat) on the initial system (size of the volume is 15 x 15 x 15 nm^3) with periodic boundary conditions. The timescale discrepancy between experiments and simulation is addressed with an assumption that once the system reaches a steady state of potential energy through equilibration, it will stay at the same state. The NPT simulation time of 100 ps was sufficient to equilibrate the potential energy of the molecular systems to their steady states. Figure 4.2 shows that the temperature affects the variations in potential energy. It is noted that the ensemble simulations with absolute 0K setting cause instability in LAMMPS; therefore, near-zero temperature (≈1K) is used for equilibration. As shown in Figure 4.2, the system equilibrated at 500K has higher potential energy than others. In the subsequent simulations, the effect of the simulation volume deformation on potential energy is addressed. The initial hypothesis is that *potential energy increases as simulation volume deforms because the covalent bonds, angles, dihedrals, and impropers also deform during this deformation test*.

The epoxy-cured simulation volume deforms gradually at a constant rate. During this process, the atoms in the volume are remapped to new positions at each time step. This deformation of the simulation volume and subsequent remapping of atoms causes the bond

length between atoms to vary based on the local force experienced by the atoms. The simulation volume is deformed along the x axis with a strain rate of 10^{10} s^{-1} in the NPT ensemble (three different temperatures and zero pressure on y and z axes). Interestingly, Figure 4.3 shows that the deformation of the simulation volume does not vary the potential energy for all three cases, indicating that the initial hypothesis is incomplete. This observation also implies that the deformation test fails to capture plastic behavior of the material system. Two possible interpretations can account for this: i) the bond length is being re-equilibrated between time steps due to thermal vibration of molecules during the deformation test, and ii) the re-equilibration occurs because the frequency of bond vibration is significantly higher than the deformation strain rate. Using these two interpretations, the initial hypothesis is updated as follows: *The potential energy increases as the simulation volume deforms when the inherent molecular thermal vibration is decoupled.*

The renewed hypothesis is evaluated by studying the frequency of bond vibration at different temperatures, especially for the molecular vibration at near-zero temperatures. Table 4.2 shows the frequencies of bond vibration estimated from MD simulations by performing NPT equilibration at room temperature (300K) and near-zero temperatures (≈1K) at 1 atm. The bond vibration frequency analysis is conducted on three typical bonds of the constituent molecules in the epoxy system (DGEBF and DETA): carbon-carbon (C-C), carbon-nitrogen (C-N), and carbon-oxygen (C-O) bonds. The frequency is calculated using fast Fourier transform (FFT) by plotting the fluctuation in bond length around its equilibrium value. The peak value of frequency determines the primary vibration frequencies of the corresponding bonds. Since the molecular system is at a near-

equilibrium state throughout the equilibration, MMFF force-field is used to extract the bond vibration frequency.

Table 4.2. Comparison of Bond Vibration Frequencies at Different Temperatures ($1THz=10^{12}s^{-1}$).

Bond Type	Bond Vibration Frequency (THz)	
	300K	≈1K
C-C	33.4	0.65
C-N	37.3	0.68
C-O	38	0.71

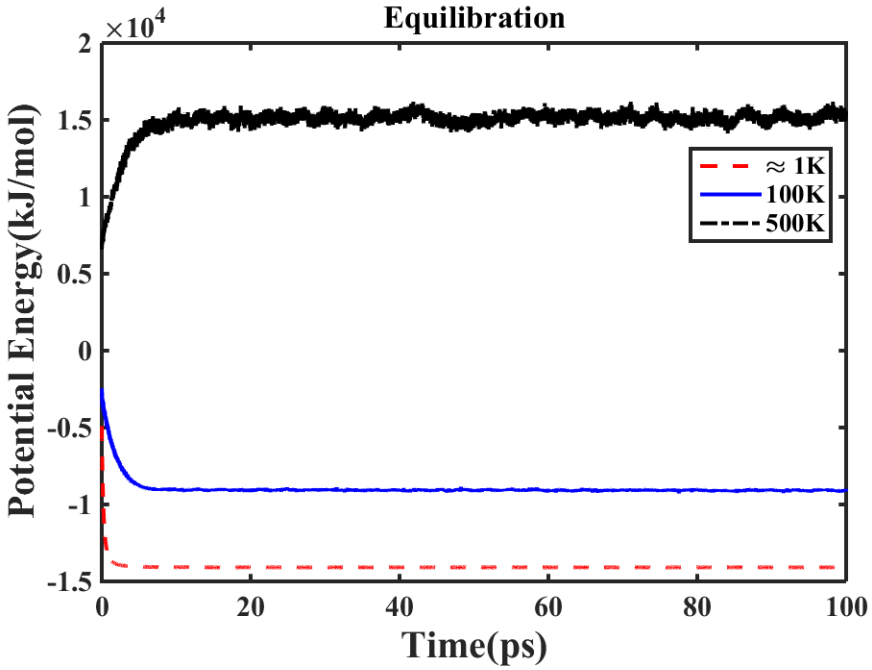

Figure 4.2. Potential Energies of Epoxy-Cured System at Different Temperatures During Equilibration.

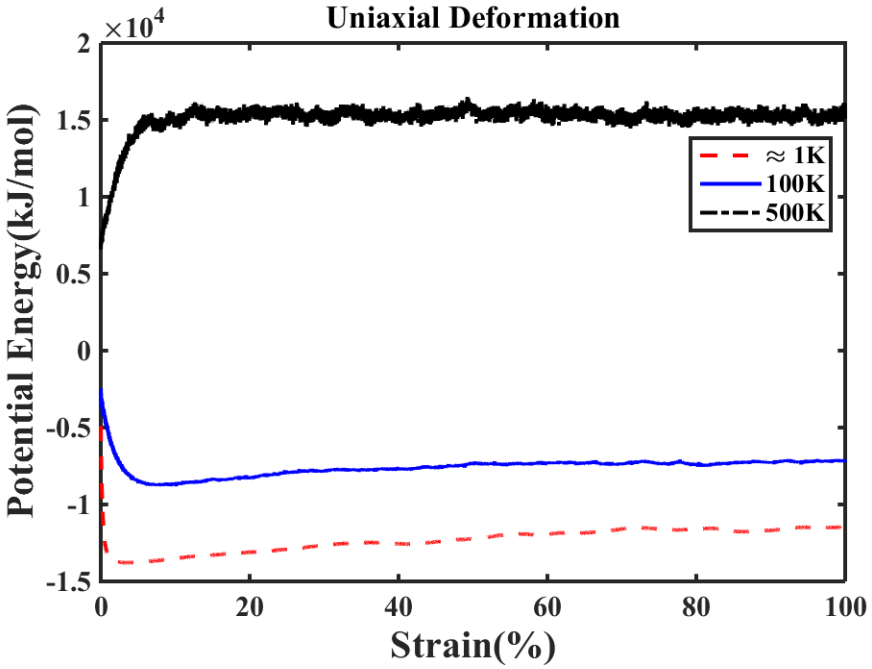

Figure 4.3. Potential Energies of Epoxy-Cured System at Different Temperatures During Uniaxial Deformation.

4.3. Deformation Test at Zero Temperature

Deformation tests at zero-temperature are performed to decouple thermal vibration from mechanical deformation. As mentioned in Section 4.2, NPT ensemble simulations with absolute 0K setting makes the system unstable in LAMMPS. Introducing an energy minimization step into the virtual deformation test maintains the system temperature at zero. This idea is borrowed from the quasi-continuum method, which was originally developed as a multiscale modeling method to bridge molecular scale to continuum scale by decoupling temperature effect [178]. The simulation volume is deformed by gradually varying the strain using ReaxFF; the atom coordinates in the volume are then remapped from a previously stored box shape to a new deformed one based on an affine

transformation followed by energy minimization [153, 154]. By using this simulation method, the absolute zero temperature condition successfully allows the decoupling of the thermal vibration from the MD simulations, and plastic deformation induced by covalent bond breakage can be observed. However, the energy minimization conducted at every small strain deformation makes the method computationally expensive. This zero-temperature deformation method is applied to the epoxy-cured system (66,560 atoms) for 1000 tensile strain steps resulting in 50% final strain. This simulation is performed on a computing node with Intel(R) Xeon(R) CPU E5-2640 v2 @ 2.00GHz processors using 8 CPU cores. The total CPU hours for a single simulation was well over 1000 hours. This prohibitively large computational time associated with energy minimization warrants the development of a numerical framework that can reliably and efficiently simulate fracture in epoxy-based thermoset polymer.

4.4. Deformation Test with Ultra-High Strain Rate

The feasibility of performing deformation tests at USHRs (>> 10^{10} s^{-1}) is explored as an alternative to the computationally intensive zero-temperature method. The average bond vibration frequency (0.68THz=0.68×10^{12} s^{-1}) is calculated to be higher than deformation strain rates, 10^{8}-10^{10} s^{-1}, which are normally used in the literature pertaining to MD simulations [65-68]. Hence, it is expected that these UHSRs, higher than the average vibration frequency of the bonds present in the molecular system of interest, deform the simulation volume faster than bond vibrations. Therefore, elongated bond lengths overcome thermally-induced re-equilibration during the deformation test. Here, the term

UHSR is used to differentiate from the 'high strain rate' used in the current MD research field [65-68].

Tensile deformation simulations are performed at different temperatures with different strain rates to analyze the effect of strain rate and temperature on potential energy. After the equilibrations of the system for 100 ps at two different temperatures (≈1K and 100K), tensile deformations are performed until 100% strain at these two temperatures with multiple strain rates ranging from 1×10^{10} s^{-1} to 2×10^{13} s^{-1}. Figure 4.4-Figure 4.7 show the variation of potential energy along the strain. As mentioned in Section 4.2 the systems that were equilibrated at two different temperatures have different potential energies (see Figure 4.4). The trends observed from Figure 4.4-Figure 4.7 indicate the interplay of two important phenomena causing variation in potential energy: 1) increase in temperature causes geometric distortions in the molecular system and indirectly leads to an increase in potential energy; 2) application of strain to the simulation volume leads to bond elongation and a corresponding increase in potential energy. Depending on the values of temperature and the applied strain rate, one of these phenomena dominates over the other. In Figure 4.4, the applied strain rate is less than the value of bond vibration frequencies at ≈1K and 100K; therefore, case (1) dominates in this range of strain rate. In Figure 4.5, the applied strain rate is higher than bond vibration frequencies at ≈1K but lower than the bond vibration frequencies at 100K, which makes two energy trends intersect around 65% strain (inset in Figure 4.5). This indicates that case (2) is dominant in the ≈1K simulations whereas case (1) plays a more important role in the 100K simulation.

At higher strain rates (≈10^{13} s^{-1}), as shown in Figure 4.6 and Figure 4.7, the influence of temperature is reduced significantly because the applied strain rate is higher than the bond vibrational frequencies in both the ≈1K and the 100K simulations. If the strain rate of the deformation is faster than the bond stretching vibration, the effect of re-equilibration of the stretched bond due to thermal vibration is reduced. Therefore, the applied strain is transferred completely to the atomic bonds and case (2) dominates over case (1). Figure 4.7 shows that the potential energy values almost converge in spite of the difference in temperature, indicating that the potential energy is invariant to temperature at UHSRs. Thus, the effects of temperature on the deformation test are reduced at UHSRs, and the variation in potential energy can be fully attributed to the increase in strain in the system causing bond elongation and bond dissociation.

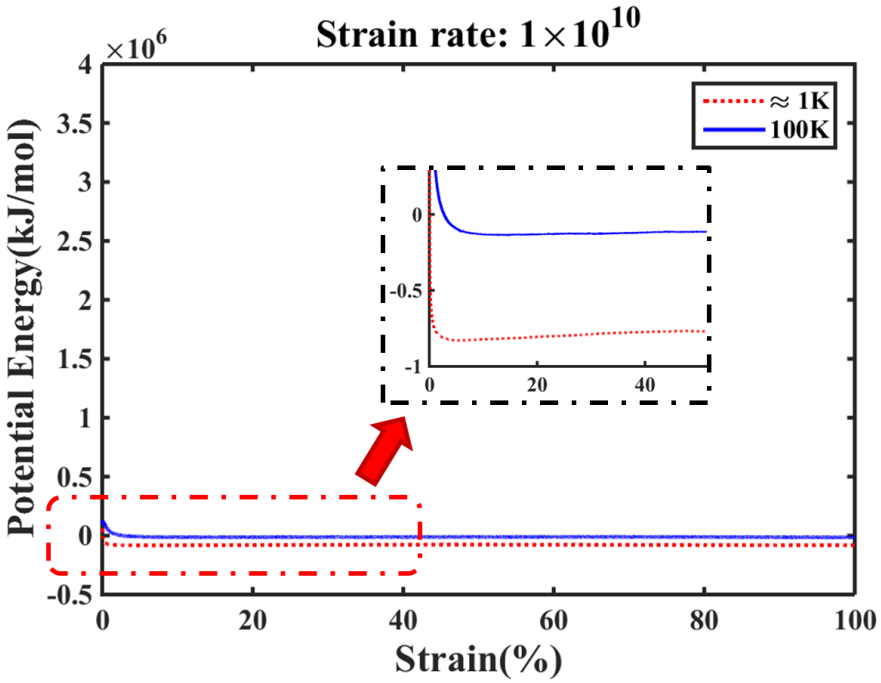

Figure 4.4. Effect of Temperature on Potential Energy at Different Strain Rates of 1×10^{10} s^{-1}.

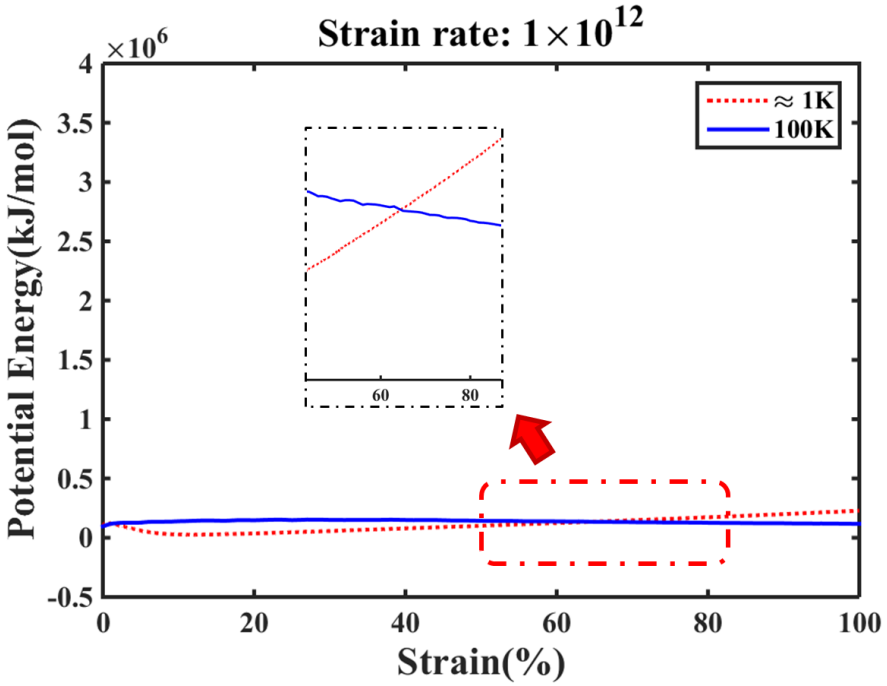

Figure 4.5. Effect of Temperature on Potential Energy at Different Strain Rates of 1×10^{12} s^{-1}.

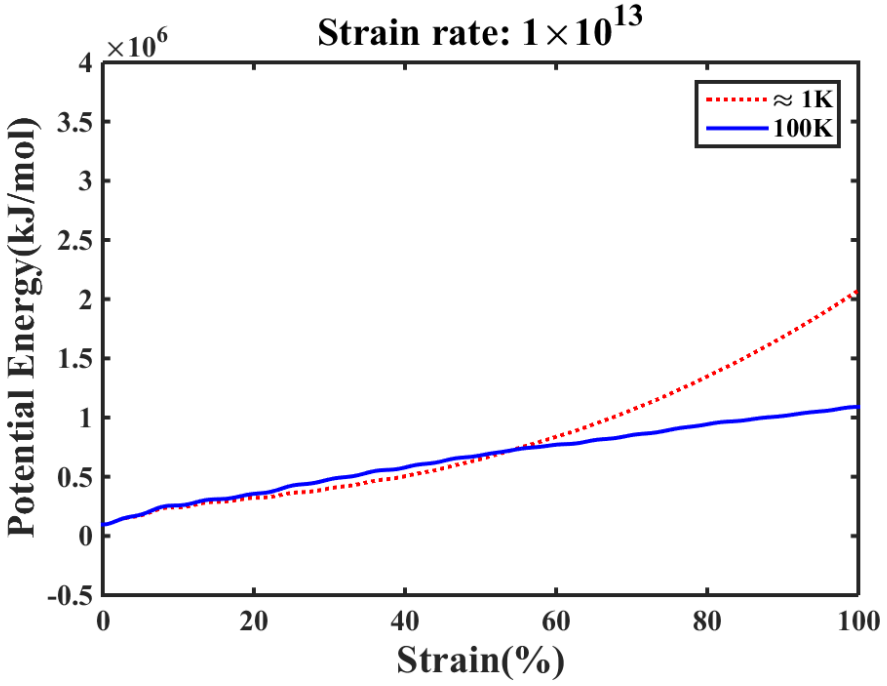

Figure 4.6. Effect of Temperature on Potential Energy at Different Strain Rates of 1×10^{13} s^{-1}.

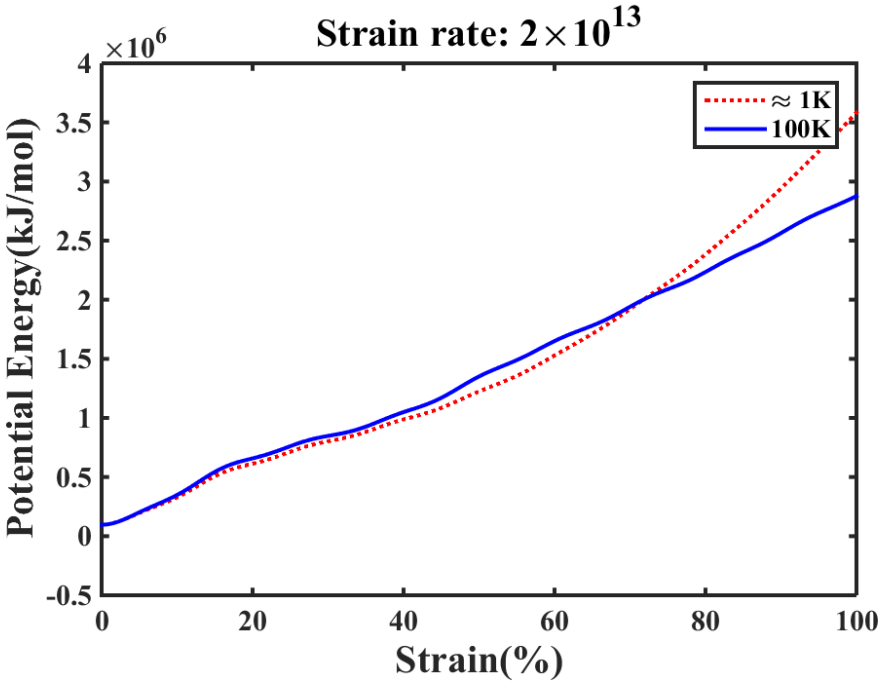

Figure 4.7. Effect of Temperature on Potential Energy at Different Strain Rates of 2×10^{13} s^{-1}.

4.4.1. Compatibility Between Zero-Temperature and UHSR Methods

The equivalence of the UHSR approach with zero-temperature method is verified by comparing the deformation test results using a small system comprising 3 DGEBF and 1 DETA molecules (149 atoms). The resin and hardener are connected by carbon-nitrogen (C-N) covalent bonds. Subsequent to energy minimization and NPT equilibration with periodic boundary conditions, the tensile deformation tests are performed using the two methods. Figure 4.8 and Figure 4.9 show the variation in bond energy calculated by zero-temperature and UHSR methods using ReaxFF, respectively; in both cases, the bond energies increase until bond dissociation occurs. The strain value at which bond dissociation occurs is called ‘critical strain.’ The critical strains are different for the zero-

temperature (≈80%) and the UHSR (≈60%) cases since the energy minimization at every small deformation step in the zero-temperature method brings the geometry of the system to its ground state abruptly, and thus the weakest points where the stresses are concentrated in the system are periodically relaxed. Therefore, the critical strain in the zero-temperature case is slightly higher than that in the UHSR case.

Morphological transformation along the strain in the two cases is also studied using snapshots taken at specific strains (see Figure 4.10). Two systems are stretched in a similar way at the beginning of the strain; they show different locations of weakest points as strain increases. Consequently, the UHSR method exhibits the potential to capture plastic deformation of covalent bond similar to the zero-temperature method, particularly in the tendency towards variation in bond energy that is demonstrated in both methods. Through this small system test, the UHSR method also confirms higher computational efficiency over the zero-temperature method.

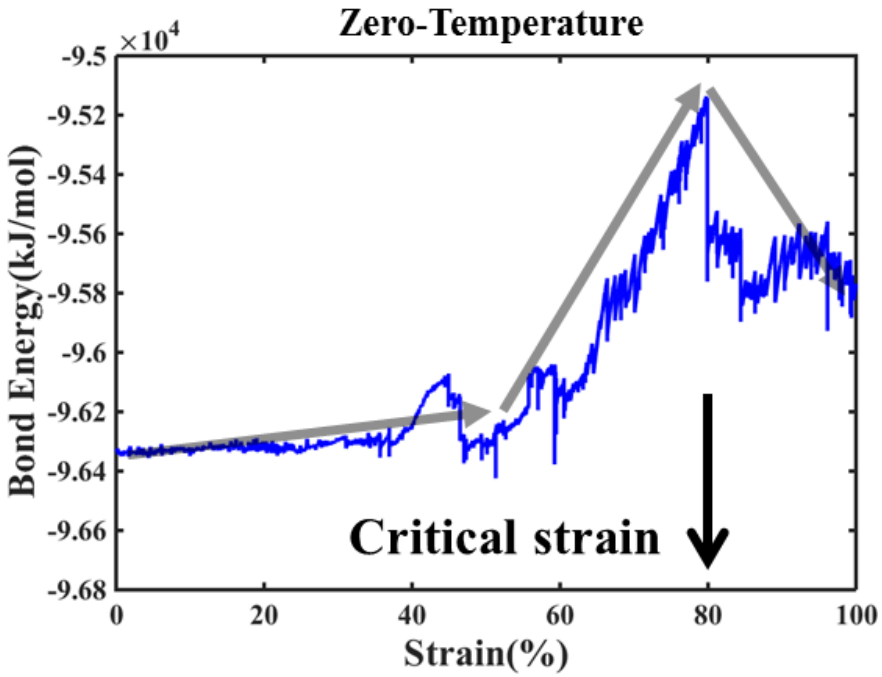

Figure 4.8. Bond Energies Calculated by Zero-Temperature during the Deformation Test.

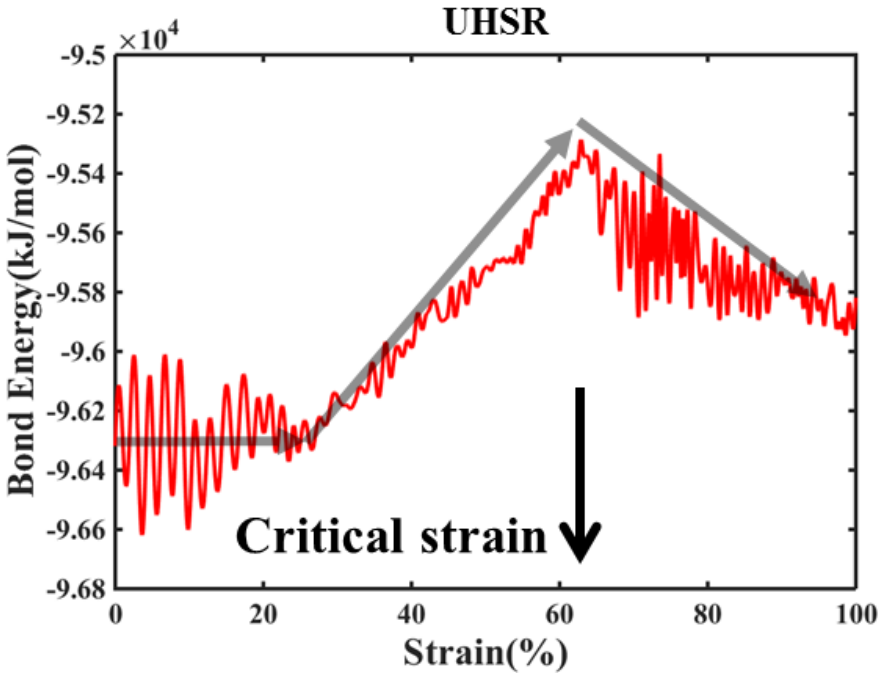

Figure 4.9. Bond Energies Calculated by UHSR Methods during the Deformation Test; Strain Rate for the UHSR Method is 10^{13} s^{-1}.

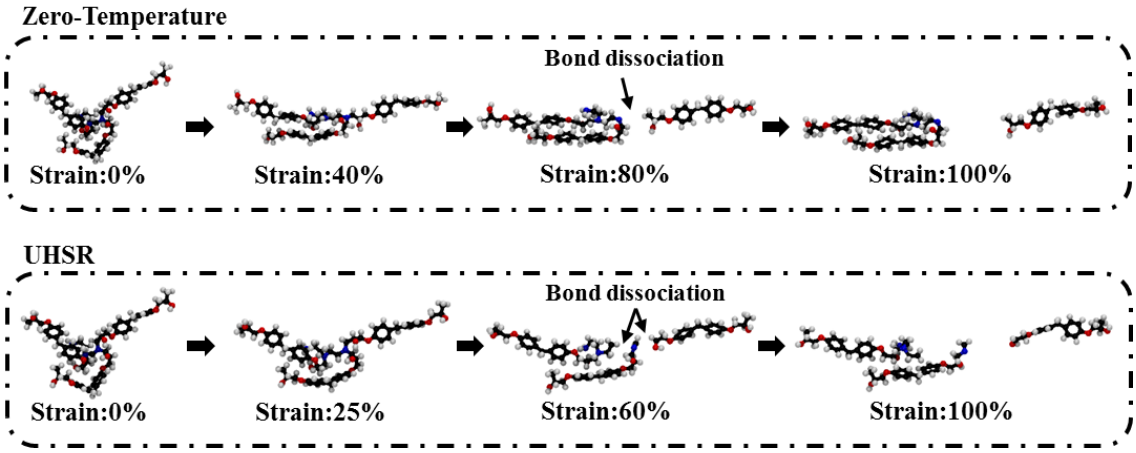

Figure 4.10. Snapshots of Deformation Tests from Zero-Temperature and UHSR Methods; the Strain Information Corresponds to the Plots in Figure 4.8 and Figure 4.9.

4.4.2. Results from the UHSR Method

The UHSR method is applied to the same epoxy system used in the application of the zero-temperature approach (described in Section 4.1). The simulation volume containing cured epoxy is deformed along the x axis in the NPT ensemble (≈1K and zero pressure on y and z axes) at a strain rate of 10^{13} s^{-1} with ReaxFF. During the deformation, the atoms in the volume get remapped to new positions based on the local atomic forces at each time step. In order to investigate the effect of spatial randomness, five simulation unit cells with stochastic initial configuration of molecules are constructed, and the virtual deformation test for each unit cell is performed. The engineering stress-strain response, presented in Figure 4.11, clearly exhibits an average yield strain below 10%. The yield stress is over-estimated due to the strain rate discrepancy between experiments and MD simulations

[179]; however, the yield strains show good correlation with experimental results found in the literature [48-50].

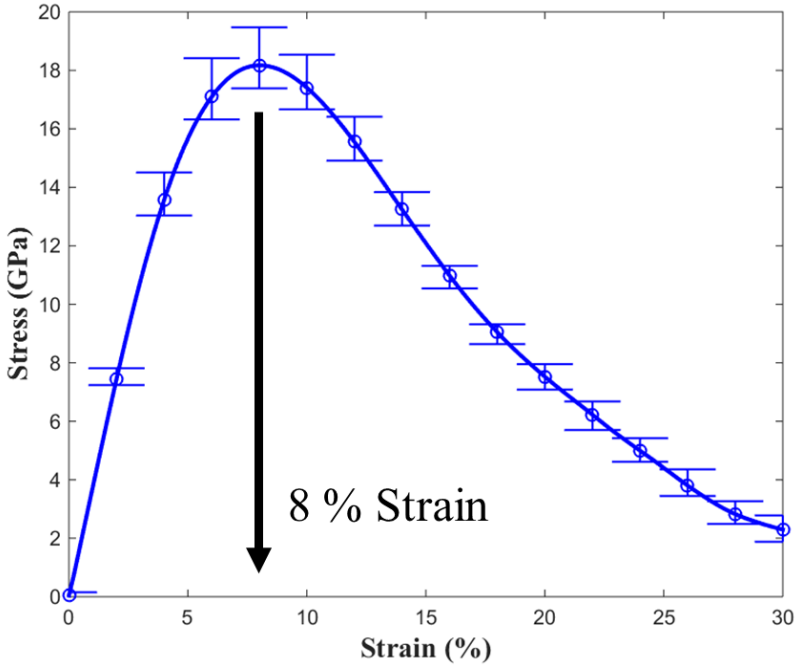

Figure 4.11. Stress-Strain Response from Simulations with Different Initial Location of Molecules.

The BDE of the epoxy system (bulk thermoset polymer matrix) is calculated through additional deformation tests in order to investigate material failure due to covalent bond breakage. The BDE is normalized by the system volume to obtain BDE density. Figure 4.12 illustrates the variation in BDE density for the bulk thermoset polymer matrix as simulation volume deforms at two different strain rates (10^{12} s^{-1} and 10^{13} s^{-1}). The increase in BDE density verifies that covalent bond breakage causes material failure. The curve pertaining to 10^{12} s^{-1} deformation test in Figure 4.12 exhibits only slight increase in BDE

density owing to most of the elongated bonds affected by thermal equilibration. However, the deformation test conducted at strain rate 10^{13} s^{-1} successfully overcomes thermal vibration and substantial increase in BDE density is observed at low strains.

The snapshots shown in the Figure 4.12 were taken at specific strain values (20%, 40%, 60%, and 80%), and the highlighted dots represent atoms of damaged bonds. The plot shows significant increase in BDE density from the initiation of deformation to 50% strain, which correlates with 'burst of bond breakage events' also observed in experiments [180]. The results also reveal that bond breakage events initiate around yield strain and accelerate subsequently until complete material failure. Furthermore, the comparisons show that strain rate 10^{13} s^{-1} is appropriate for observing brittle fracture in the epoxy-based thermoset polymer matrix. The BDE density and yield strain information estimated by the physics-based molecular simulations are expected to provide valuable insight and input into continuum level fracture analyses.

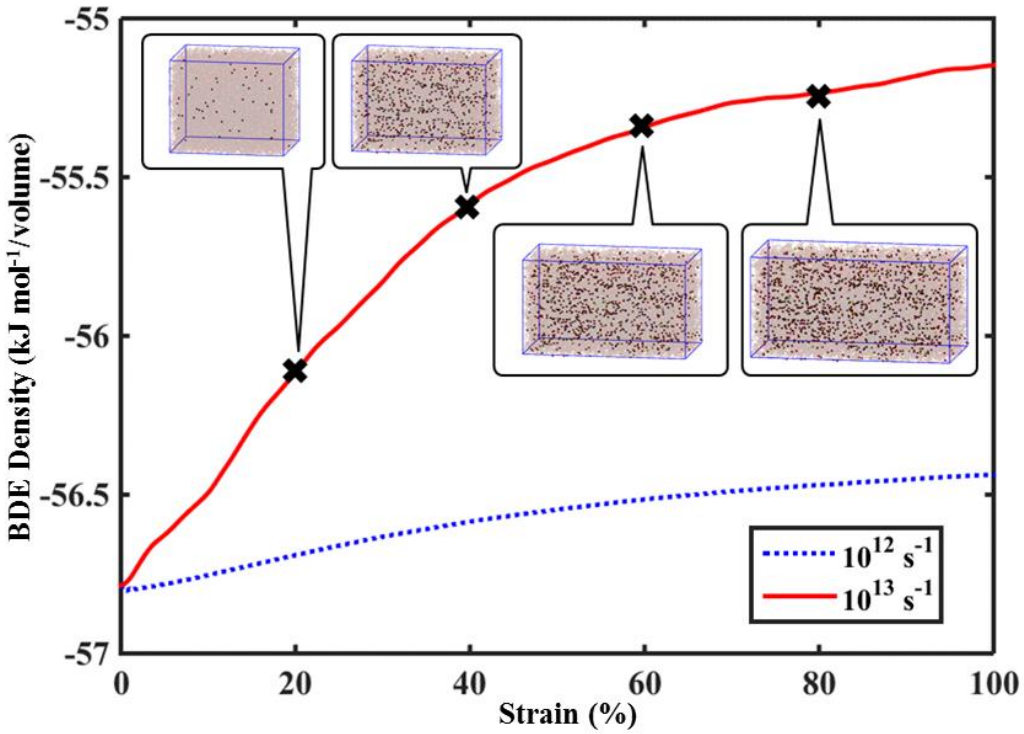

Figure 4.12. Variation of BDE Density with Strain at Near-Zero Temperature with Different Strain Rates.

4.5. Chapter Summary

A novel atomistic simulation methodology was developed to capture brittle failure in epoxy-based thermoset polymers using ReaxFF. This study primarily addressed the effects of temperature on potential energy during the virtual deformation tests, since it was observed that thermal vibrations led to relaxation of bonds, and subsequent bond elongation was impeded. In order to decouple the thermal effects, a computationally prohibitive zero-temperature method was first explored. An alternative approach to the zero-temperature method was then devised to improve computational efficiency while maintaining accuracy. An alternative approach, i.e., the UHSR method, enabled the study of bond dissociation (brittle behavior) of a bulk polymer system (large system size) using ultra-high strain rates

($\approx 10^{13}$ s^{-1}), which are higher than the average vibration frequency of the bonds in the molecular system of interest. The UHSR method produced very similar results as the zero-temperature method, but with significant computational benefits using a combination of low temperature (≈1K) and ultra-high strain rate. The UHSR method also provides a platform to quantify both the BDE and BDE density in a bulk polymer system; these parameters are capable of describing the extent of damage in continuum level fracture analysis of thermoset polymer systems.

CHAPTER

5. MOLECULAR FIBER/MATRIX INTERPHASE MODEL

In this chapter, a physics-based molecular interphase model is developed and integrated within a micromechanics modeling method to establish a multiscale modeling framework. The resultant novel molecular interphase model accounts for structural variation and physical entanglement between the carbon fiber surface and the polymer matrix by introducing voids in the graphene layers. The numerical epoxy curing process mentioned in Chapter 2, is applied to the thermoset polymer constituent. The curing process, combined with the semi-crystalline carbon fiber surface, allows the generation and entanglement of polymer chains through the voids of the graphene layers. Several configurations of the interphase model are discussed, including variations in the boundary conditions and structure of the interphase. Virtual transverse tensile tests are performed using the interphase models, and the mechanical properties estimated from the results are integrated into the high fidelity generalized method of cells (HFGMC) theory [181, 182] for larger length scale analyses. Multiscale failure and microdamage theories that have been applied to a sectional micromechanical model [183] are used for the current modeling framework. The interphase properties predicted by the atomistically informed multiscale framework in this work are compared to those obtained from several available studies [82, 84, 85].

5.1. Nanoscale Constituent Models

5.1.1. Polymer Matrix Model

In this study, an epoxy-based thermoset polymer consisting of DGEBF resin and Di-DETA hardener is simulated in the interphase model using a cutoff distance based covalent bond generation method, described in Chapter 2. MD simulations are performed using

LAMMPS [109] with a classical all-atom force-field, MMFF [47, 114]. A resin to hardener weight ratio of 100:27 (DGEBF: DETA) is specified by the manufacturer and used to determine the number of molecules for the polymer unit cell, as seen in Table 2.6. Molecular structures of neat epoxy are the same as the structures in Figure 4.1 since the same epoxy system (DGEBF+DETA) is used in this interphase study.

5.1.2. Carbon Fiber Surface Model

The molecular interphase model replicates the semi-crystalline structure of the carbon fiber surface by intentionally creating voids in several protruded graphene layers. Similar processes for defect creation have been applied to CNT models in multiscale FEA analyses [184]. The carbon fiber surface model is constructed by stacking a number of pristine graphene (PG) layers (N_{pg}) and the graphene with void (GV) layers (N_{gv}). A N_{pg}:N_{gv}:N_{pg} (5:5:5) stacking sequence is used as shown in the schematic in Figure 5.1. For graphene layers, an all-atom (AA) force-field is implemented using the optimized potential for liquid simulation (OPLS) potential to characterize the atomic and molecular interactions. The OPLS-AA parameter set [46] was chosen based on the potential energy calculations for a single CNT molecule whose structure is compatible with graphene. However, the OPLS-AA only contains functional forms for bond, angle, and dihedral deformations among bonded interactions. In graphene, the out-of-plane distortions (improper distortions) play a non-negligible role in the potential calculations. Therefore, the functional form of the improper distortion was included from the consistent valence force-field (CVFF) parameter set [185]. Thus, the bond and angle distortions are described by a harmonic functional form, which are identical to MMFF potential functions; the dihedral and improper distortions, on

the other hand, are described between quadruplets of atoms (Table 5.2). Since the functional forms for the non-bonded van der Waals and Coulomb interactions are the same as those of MMFF, they are not included in Table 5.2. For the interphase model, a combination of the MMFF, OPLS, and CVFF force-fields are used.

Table 5.1. Neat Epoxy Components.

	Weight	Formula	Number of Molecules
DGEBF	313 g/mol	$C_{19}H_{20}O_4$	260
DETA	103 g/mol	$C_4H_{13}N_3$	220

Table 5.2. Functional Form for Potential Energy Calculations.

	Functional Form
Bond	$\mathrm{E_{bond}} = K_{bond}(r - r_0)^2$
Angle	$\mathrm{E_{angle}} = K_{angle}(\theta - \theta_0)^2$
Dihedral	$\mathrm{E_{dihedral}} = \frac{1}{2}K_1(1 + cos\phi) + \frac{1}{2}K_2(1 - cos2\phi) + \frac{1}{2}K_3(1 + cos3\phi) + \frac{1}{2}K_4(1 - cos4\phi)$
Improper	$\mathrm{E_{improper}} = \mathrm{K_{improper}}[1 + d_i \cos(n_i\phi)]$

In addition to the force-field information, preparation of appropriate graphene structure is significantly crucial. Graphene layer can be generated by the tool 'Nanotube Builder' in the visualization molecular dynamics (VMD) program [186]. Although VMD is generally used to visualize molecular trajectories calculated by MD simulation, a diverse set of tools to build molecular system, such as graphene, CNT, and simple crystalline structures are included in VMD. However, the nanotube builder generates only a pristine graphene layer, which does not have voids. Thus, the 'atomselect' function in VMD is used to build a graphene layer with voids, which is accomplished by a unique method of deselecting a cluster of carbon atoms in a specific area. Figure 5.2 shows the process of void generation in the pristine graphene layer; the carbon atoms in the red box are deselected.

After generating a graphene layer with a void, a hydrogenation process is required. Although the nanotube builder generates the graphene layer, the carbon atoms at the edge of the graphene layer are not hydrogenated, which causes open valence on the edge carbon atoms. As a result, these carbon atoms try to generate covalent bonds with the neighboring polymer atoms when ReaxFF is implemented. Since the graphene carbon atoms at the edge of the graphene are hydrogenated, in reality, this implies that bond generation between the edge atoms and neighboring atoms due to open valence are not physically correct. Moreover, these bond generations lead to unrealistically high stress when the deformation test is performed in MD simulations; hence, the graphene layer must be hydrogenated. In VMD a tool called 'Molefacture' can add atoms to a molecular system. Thus, hydrogen atoms are added to the carbon atoms in open valence state. Figure 5.3 shows the graphene layer before and after the hydrogenation.

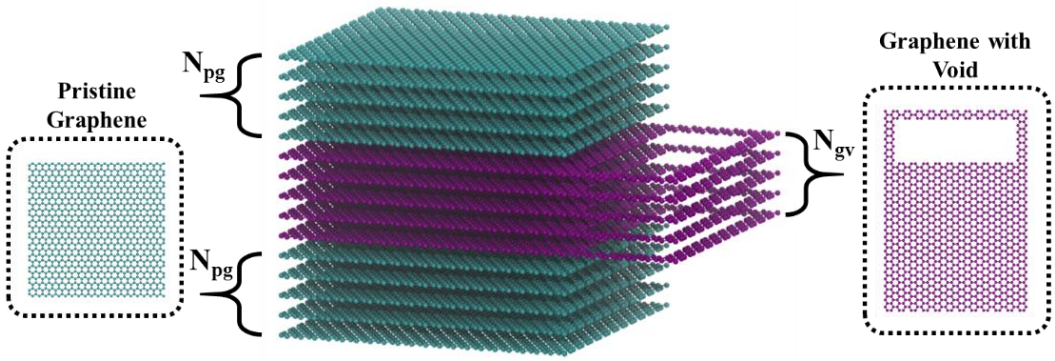

Figure 5.1. Molecular Representation of the Carbon Fiber Surface using a Number of PG Layers (Npg) and a Number of GV Layers (Ngv).

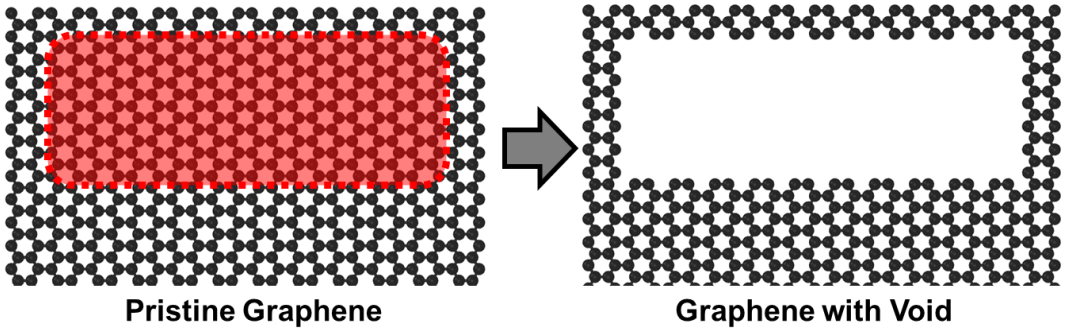

Figure 5.2. Schematic of Void Generation in the Pristine Graphene Layer.

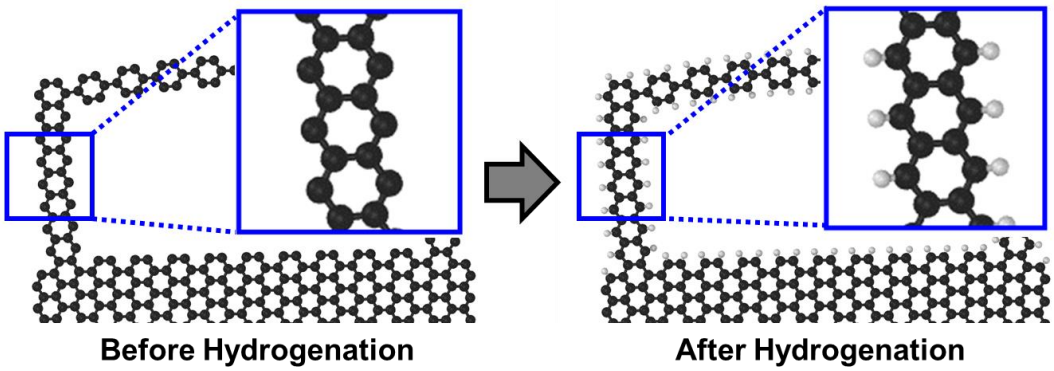

Figure 5.3. Hydrogenation for Graphenes: Carbon Atoms (Black) and Hydrogen Atoms (White).

5.2. Interphase Models

The individual constituent models are combined to create a molecular interphase model with graphene layers and a polymer matrix (left and right sides, respectively, in Figure 5.4). The numerical curing of the resin and hardener allows the polymer network to form through the void, while capturing the entanglement between the carbon fiber surface and the polymer matrix. Due to the entanglement of polymer chains with the GV layers, a large amount of energy is required to break these bonds compared to the non-bonded interactions simulated by the van der Waals potential energy. To illustrate the effect of the physical entanglement on the mechanical properties, a variation of the interphase model was developed by replacing the center layers with PG layers, referred to as the PG interphase model. The initial dimensions of the interphase model are 100×65×50 $Å^3$, containing 15,000 atoms in the polymer matrix and 15,840 atoms in the carbon fiber surface. As shown in Figure 5.5, periodic boundary conditions are applied along the y and z axes. Periodic boundary condition is not applicable to the x axis since there is phase discontinuity representing interphase along the x axis. Energy minimization of the interphase model is performed using the conjugate gradient method. Subsequently, NPT (isobaric-isothermal) ensemble equilibration is performed at 300K and 1 atm for 10 ns (1fs time step) using the Nose-Hoover thermostat and barostat. During the 10 ns NPT simulation, the potential energy of the interphase model converges to a mean value with minimal variance, which is considered to be the initial, equilibrated state. The cutoff distance based covalent bond generation method demonstrated in Chapter 2, is applied to the equilibrated model to generate covalent bonds between the carbon atoms in the resin and the nitrogen atoms in the hardener (C-N bond).

To ensure stability in the numerically cured interphase model, additional NPT ensemble simulations (300K and 1 atm) are performed until the total energy converges to a stable value. Since the classical force-fields used for the numerical curing process cannot capture inelastic behavior (bond breakage) of the molecular model, a bond-order based force-field is introduced in the equilibrated model to capture covalent bond breakage during the virtual tensile test. ReaxFF as the bond-order based force-field is used in this work [146]. Virtual testing of the interphase model is performed using MD simulations incorporating the ReaxFF force-field. It is important to note that the reason for not using the bond-order based force-field for the numerical curing and equilibration is because of the computational intensity of this approach. Figure 5.6 and Figure 5.7 illustrate the loading conditions for the virtual transverse tensile test where the graphene layers are constrained by a roller joint condition, as shown by the black dotted box, which depicts movement only in the y and z axes. The red dotted box indicates the displacement condition applied to the polymer matrix along the x axis by displacing either all (Figure 5.6) or half of the polymer atoms (Figure 5.7). Figure 5.8 shows the boundary and loading conditions for the PG interphase model. Virtual tests are conducted using these models to obtain MD generated elastic and failure properties of the interphase, which are then used in the high-fidelity micromechanics theory presented in the following section.

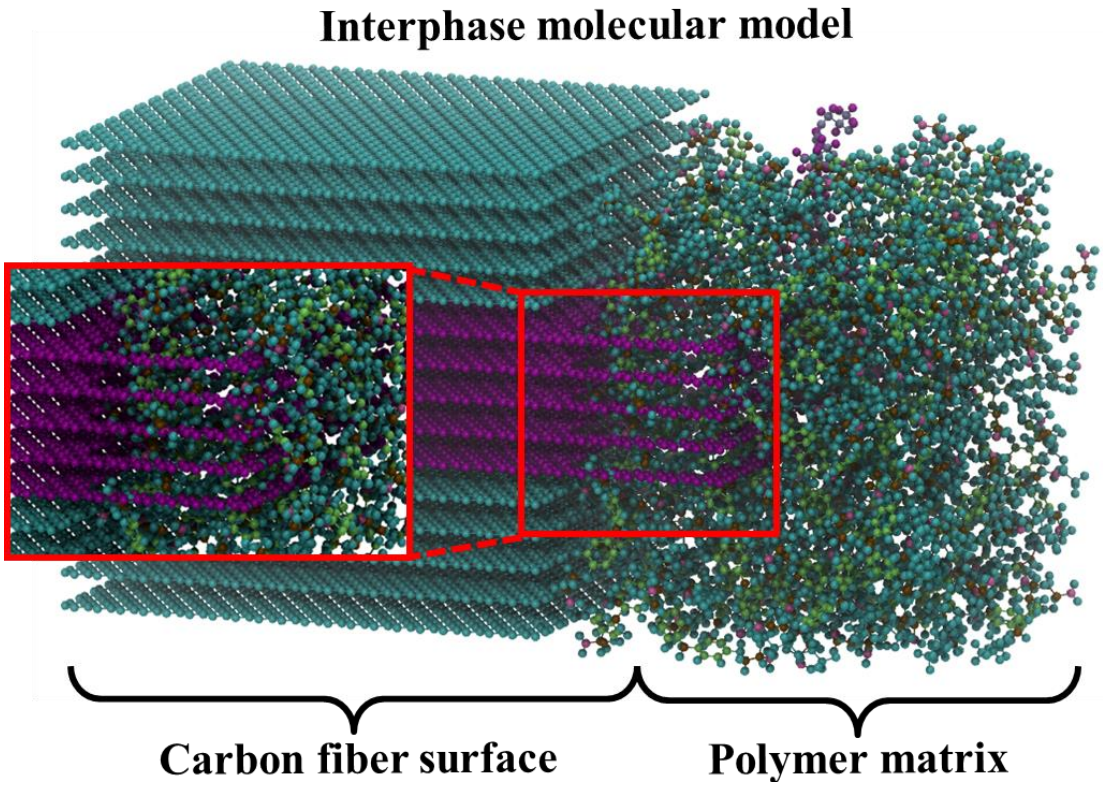

Figure 5.4. Molecular Structure of the Interphase Model.

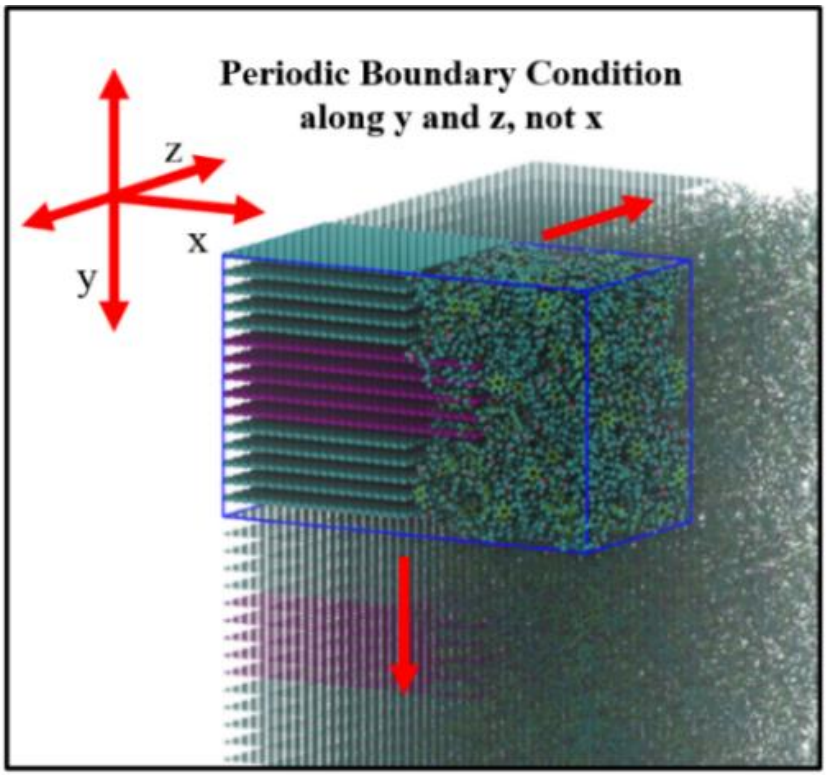

Figure 5.5. Periodic Boundary Conditions of the Interphase Model.

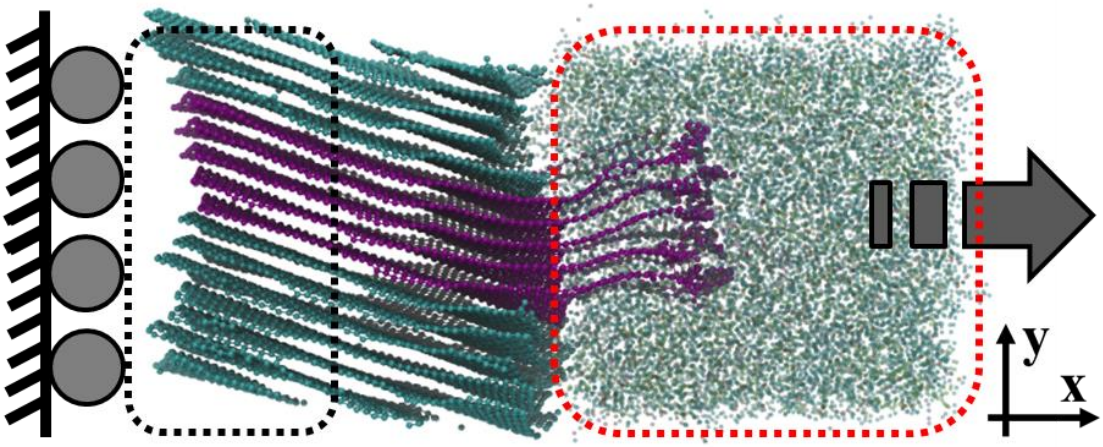

Figure 5.6. Boundary Conditions for the Virtual Tensile Tests of The Interphase Model with GV Layers where the Displacement Condition is Applied to All the Polymer Atoms.

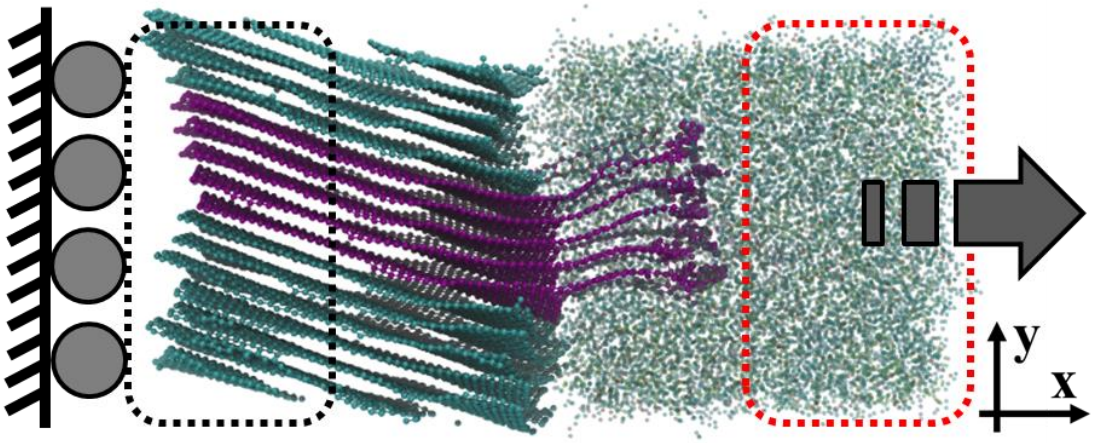

Figure 5.7. Boundary Conditions for the Virtual Tensile Tests of the Interphase Model with GV Layers where the Displacement Condition is Applied to Half of the Polymer Atoms.

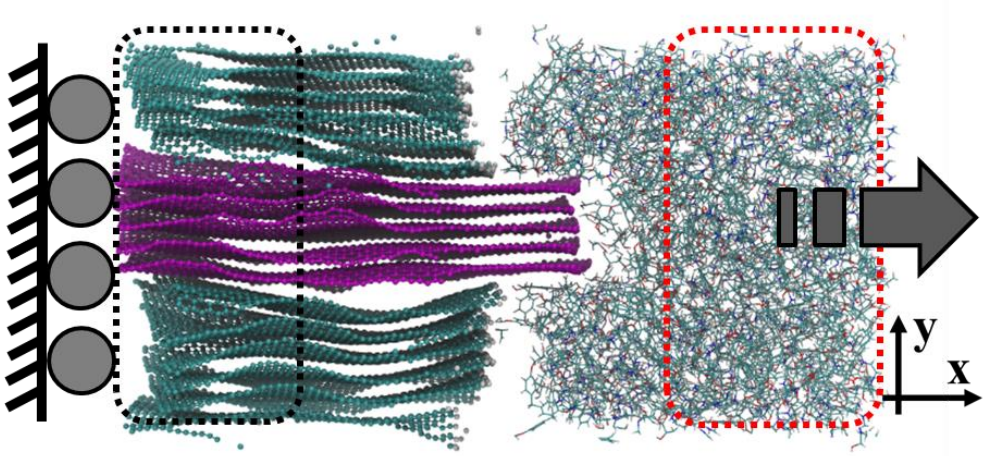

Figure 5.8. Schematic of Loading Conditions for the Virtual Tensile Test of the Interphase Model with Only PG Layers.

5.3. Micromechanical Modeling

The HFGMC micromechanics theory is employed in the multiscale modeling framework. This micromechanical theory assumes that the composite microstructure is ordered and can be represented by a repeating unit cell consisting of a single fiber in

polymer matrix. The unit cell is assumed to be periodically distributed in a space defined by a global coordinate system as illustrated in Figure 5.9. A discretization method is used to divide the unit cell into an arbitrary number of rectangular sub-volumes called subcells where each subcell can contain a distinct set of material properties.

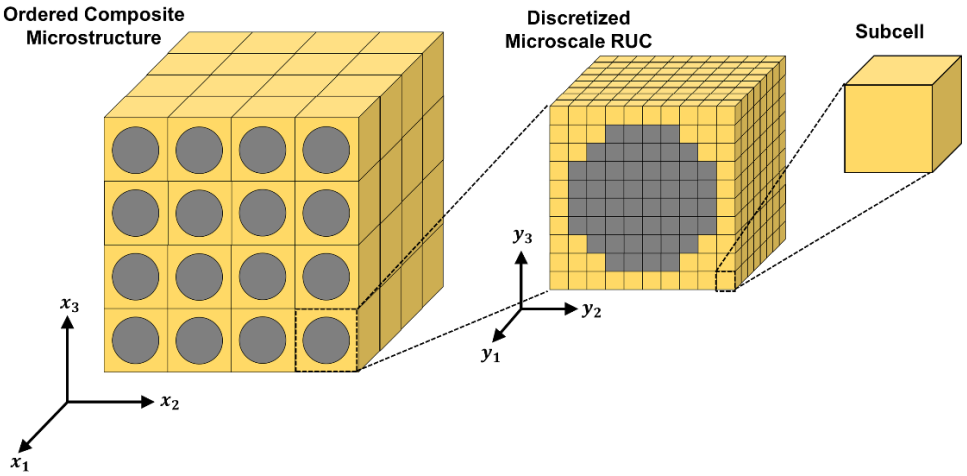

Figure 5.9. Schematic Showing the Discretization Process of a Fiber PMC Microstructure.

Since the composite unit cell is defined by a continuous carbon fiber, the computational costs of the microscale simulations are reduced by setting the unit cell thickness in the y_1 axis to be one subcell thick. The interphase subcells are created by replacing the polymer subcells that are immediately adjacent to the fiber subcells, as illustrated in Figure 5.10. A unit cell discretized into 256 subcells shown in Figure 5.10 is one of examples. Through a convergence study, the appropriate number of subcells needed to represent the unit cell is determined in the results in Section 5.4. The HFGMC theory enables shear coupling between the subcells through the application of a higher order displacement field, which accurately captures the effect of the interphase on the composite response and failure. The

displacement field for each subcell is solved by assigning equilibrium, boundary conditions, and interfacial continuity conditions. The derivations and the solution procedure used here are those detailed in [181, 182]. The properties determined from the nanoscale MD simulations of the interphase are incorporated into the HFGMC micromechanics approach to obtain the unit cell response of the composite.

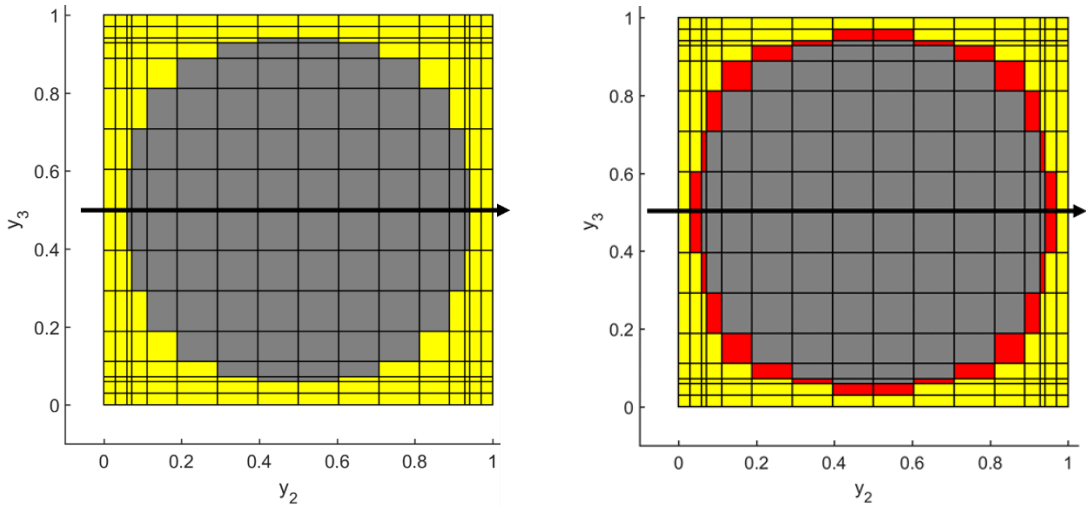

Figure 5.10. Discretization of a Microscale Unit Cell (a) without an Interphase and (b) with an Interphase into Polymer (Yellow), Fiber (Gray), and Interphase (Red) Subcells.

The constitutive equations for the fiber subcells are defined with a transversely isotropic, linear elastic constitutive law (Equation 5.1). The polymer subcells are represented by a modified Bodner-Partom viscoplastic state variable model [187, 188] described by Equations 5.2 and 5.3, and incorporated within the constitutive law in Equation 5.4.

$$d\varepsilon_i^f = S_{ij}^f d\sigma_j^f \qquad i, j = 1 \cdots 6 \tag{5.1}$$

$$\dot{\varepsilon}_{ij}^{I} = 2D_0 \exp\left[-\frac{1}{2}\left(\frac{Z}{\sigma_e}\right)^{2n}\right]\left(\frac{\sigma_{ij}^{dev}}{2\sqrt{J_2}} + \alpha\delta_{ij}\right) \quad (5.2)$$

$$\sigma_e = \sqrt{3J_2} + \sqrt{3}\alpha\sigma_{kk} \quad (5.3)$$

$$d\varepsilon_i^m = S_{ij}^m d\sigma_j^m + d\varepsilon_i^I \quad i, j = 1\cdots 6 \quad (5.4)$$

In Equation 5.1, the variables $d\varepsilon^f$ and $d\sigma^f$ represent the strain and stress increments of the fiber subcells, respectively, and S^f contains the components of the compliance matrix for the fiber subcells. In Equations 5.2 and 5.3, Z and α are variables related to resistance of molecular flow and the hydrostatic stress effects, respectively, D_0 is the maximum inelastic strain rate, and the variable n controls the material rate dependency. The σ^{dev} tensor contains the deviatoric stress components, J_2 is the second invariant of the deviatoric stress tensor, and σ_{kk} is the summation of normal stress components. The variables $d\varepsilon^m$ and $d\sigma^m$ represent the strain and stress increments of the polymer matrix subcells, respectively, and S^m contains the components of the compliance matrix for the polymer matrix subcells. de^I is the inelastic strain increment of the polymer matrix subcells, which is obtained through explicit solutions. A linear elastic model is used in the interphase subcells and the constitutive equations are similar to that of the fiber subcells described in Equation 5.1. For the interphase properties obtained from previous studies, the material symmetry of the interphase is defined as either isotropic or transversely isotropic based on the assumptions outlined in the respective studies.

In the current model, damage and failure criteria are applied to the subcells and the unit cell. Progressive damage is modeled using a work potential theory [189], which captures microscale damage by discretizing the strain energy into elastic and damage components. In earlier studies, the work potential theory has been integrated into the GMC theory

through a progressive damage model with plane stress conditions [190]. A 3D form of this progressive damage theory was incorporated into a sectional micromechanical model [191]. This microscale damage theory is applied to the 3D constitutive law of the polymer subcells where the damage parameters, calculated at each time step, degrade the elastic modulus of the polymer. The microscale failure modes of the polymer and interphase subcells are determined through a maximum strain and maximum stress criterion, respectively. The maximum strain criterion is used for the polymer subcells due to the highly nonlinear response caused by the viscoplastic behavior of the polymer. The macroscale failure criteria of the unit cell are based on a modified Hashin failure theory that incorporates shear stress terms in the compressive fiber failure mode [192, 193].

5.4. Results and Discussion

5.4.1. Molecular Interphase Results

The nanoscale properties of the interphase are estimated through the virtual tensile testing of the atomistic interphase model. Deformation is applied to the polymer matrix at a constant rate of 0.001 Å/fs (displacement condition) with the previously described boundary conditions. High displacement rates are needed in MD simulations to account for molecular interactions. However, the total time of the simulations with these high displacement rates is constrained to a few nanoseconds due to computational limitations. Figure 5.11 and Figure 5.12 show how the different displacement configurations affect the straining of the GV layers and polymer matrix, and that the GV interphase model configuration displacing half the polymer atoms depicts a more accurate representation of the physical loading mechanisms in the material. The simulation results (Figure 5.13) of

the PG interphase demonstrate straining of only the polymer matrix. Additionally, the polymer atoms near the protruded graphene layers in the PG interphase results show less deformation compared to the polymer atoms away from the graphene layers; this shows the effect of structural variation on the material response.

Figure 5.14 shows the stress-stain plots of the MD simulations based on the spatially and temporally averaged virial stress calculation [174]. The results show that displacing all the polymer atoms in the GV interphase model yields minimal straining of the polymer matrix molecules resulting in a high stress concentration at the carbon chains around the void and lower failure strain of 5%. By displacing half of the polymer atoms in the GV interphase, the polymer matrix molecules in the void and adjacent to the carbon fiber surface are strained, which relieves the stress concentration and causes a decrease in stiffness. The stress-strain results for the PG interphase model produce low stiffness and failure values indicating a dependence on the Lennard-Jones potential due to the void-free structure of the model, which prevents entanglement between the carbon fiber surface and the polymer matrix. The dotted red box in Figure 5.14 shows irregularities at the initial stage of the stress-strain plots caused by a temporary lack of contact between the carbon fiber surface and the polymer matrix. Additionally, due to the potential energy caused by the formation of bonded and non-bonded interactions during the equilibration simulation, the stress-strain plots have an initial stress value. Therefore, the portion of the stress-strain curve ranging from 1% to 3% strain is used to calculate the transverse moduli.

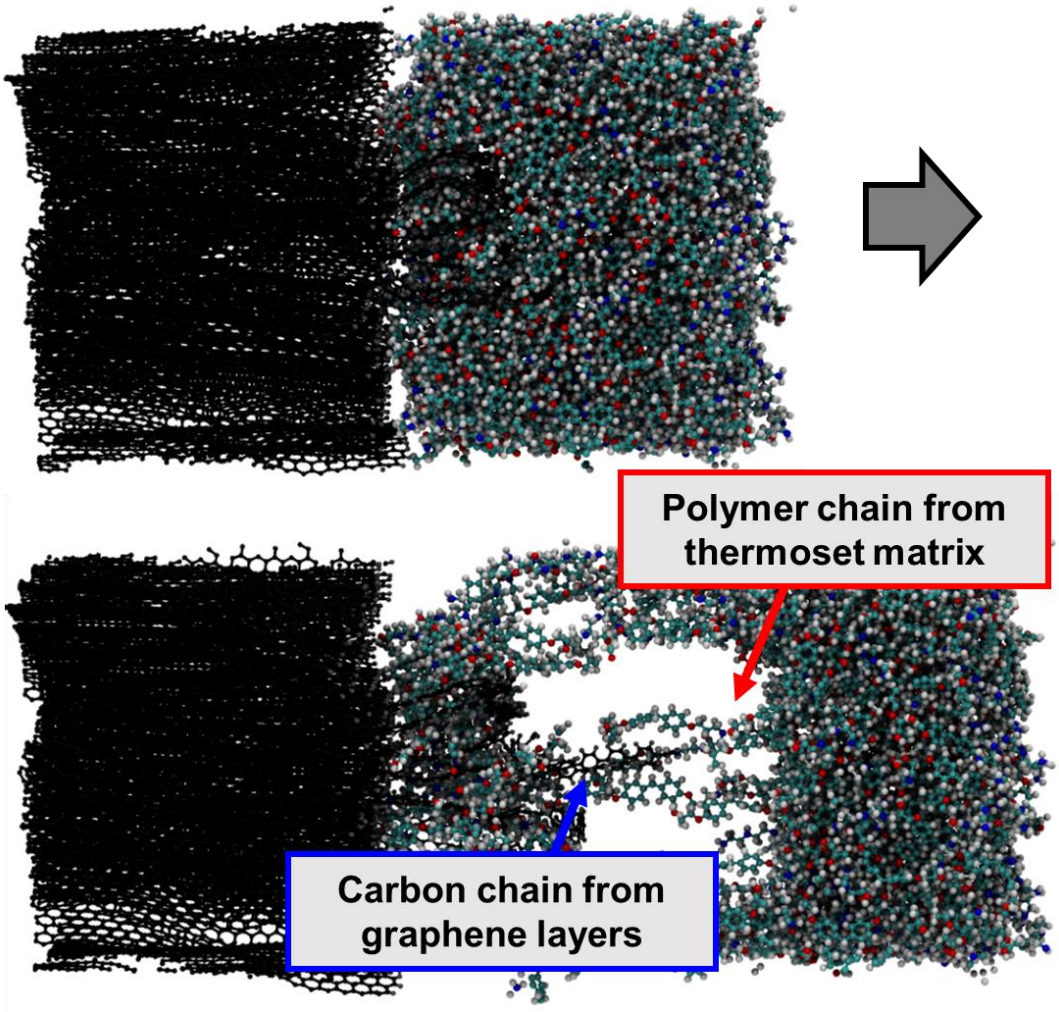

Figure 5.11. Virtual Test Results of the Equilibrated Molecular Interphase Models Showing the Position of the Atoms Before (Left) and After (Right) Testing: Graphene with Void (GV) Interphase Model Displacing *Half the Polymer*.

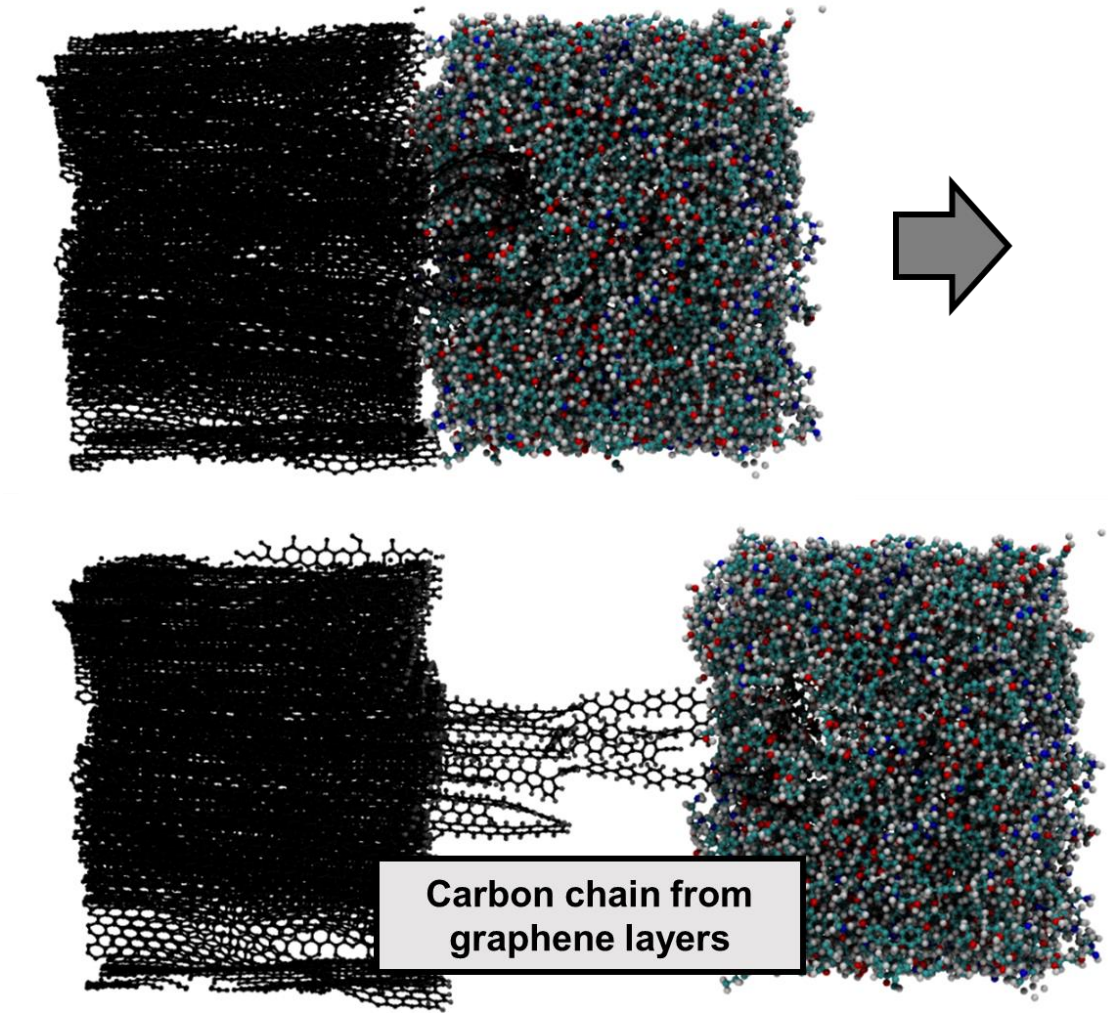

Figure 5.12. Virtual Test Results of the Equilibrated Molecular Interphase Models Showing the Position of the Atoms Before (Left) and After (Right) Testing: Graphene with Void (GV) Interphase Model Displacing *All the Polymer*.

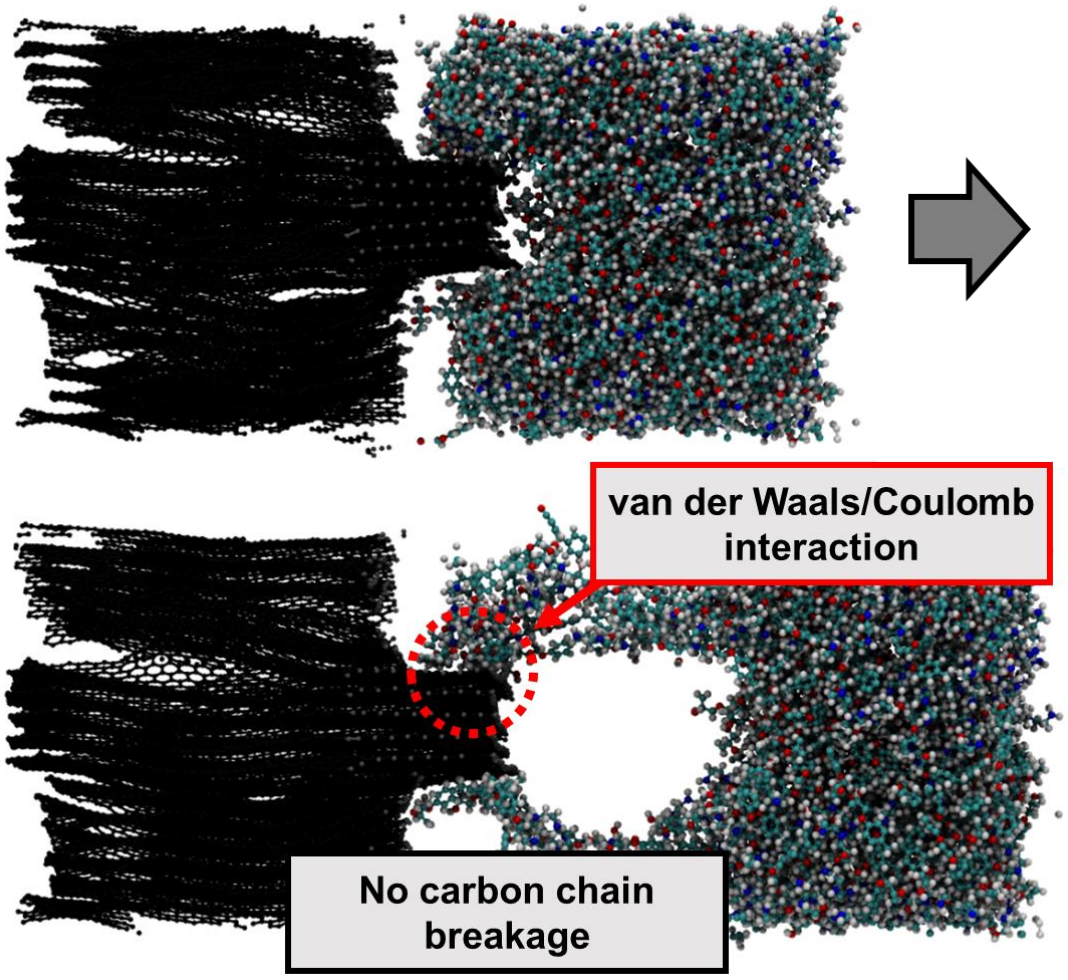

Figure 5.13. Virtual Test Results of the Equilibrated Molecular Interphase Models Showing the Position of the Atoms Before (Left) and After (Right) Testing: Pristine Graphene (PG) Interphase Model.

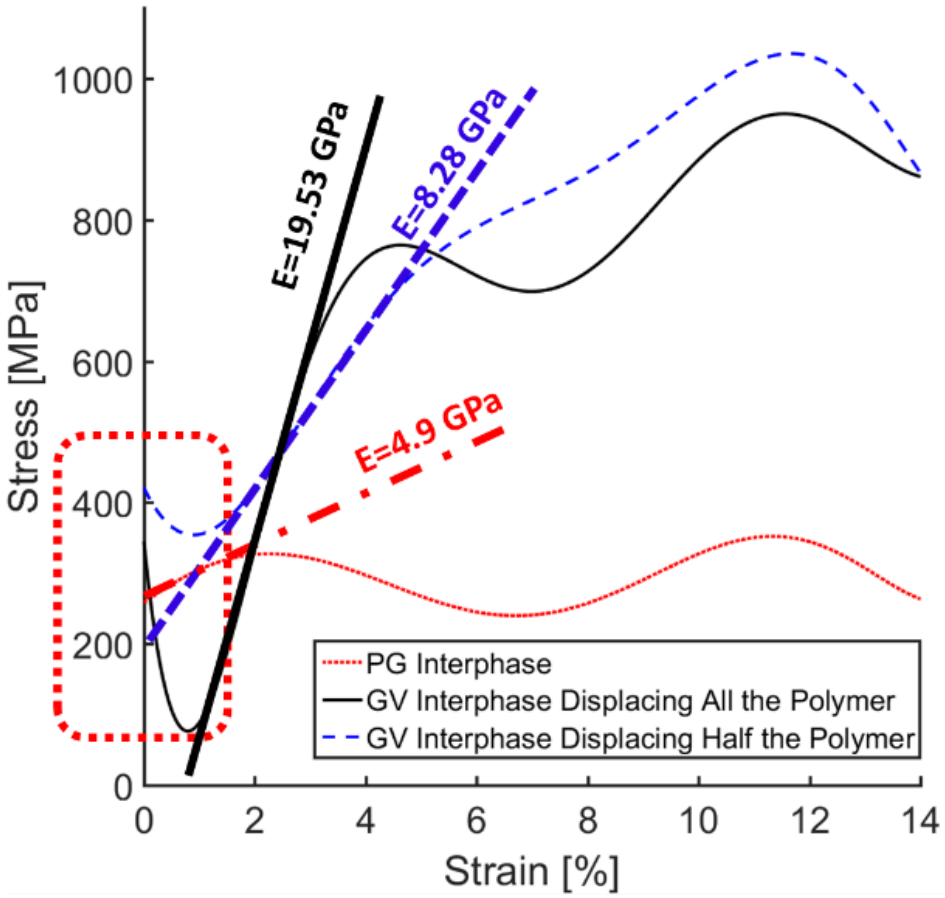

Figure 5.14. Stress-Strain Plots from the Virtual Loading Test Results of the Interphase Models.

5.4.2. High Fidelity Micromechanics Results

Various interphase properties from the literature are investigated using the micromechanics technique to compare with those obtained using the MD simulated properties. Table 5.3 displays the transverse properties for each interphase type including the current MD simulated properties. The first interphase type refers to the properties obtained by Wang et al. [84] using dynamic modulus imaging methods. The interphase properties from Zhang et al. [85] are calculated using a cohesive law derived from the non-

bonded potential only and they applied factors to capture microscopic defects. The third interphase model uses an intermediate modulus from a parametric study performed by Asp et al. [82]. The transverse tensile modeling results are obtained by applying a strain rate of 1.05 s^{-1} to the PMC microscale unit cell.

Table 5.3. Interphase Material Properties.

	Transverse Modulus (GPa)	Transverse Tensile Strength (MPa)
Wang et al. [84]	12.7	50
Zhang et al. [85]	3.37	53
Asp et al. [82]	34	50*
Current Model – GV Displacing All the Polymer	19.53	783.5
Current Model – GV Displacing Half the Polymer	8.28	1024
Current Model – PG	4.9	377.5
* Value assumed; not available in reference		

A convergence study is performed to determine an appropriate time increment and the number of subcells required for the micromechanics simulations. The GV interphase model with half the polymer atoms being displaced was used in this convergence study. The stress-strain responses of the unit cell for various time increments are shown in Figure 5.15(a) and convergence of the response, including failure, is achieved with a time

increment of 5×10^{-6}. The convergence study for the number of subcells is presented in Figure 5.15(b) and shows that the unit cell stress-strain response converges with a simulation containing 256 subcells. The converged parameters are used in the subsequent simulations to compare the different interphase models and properties.

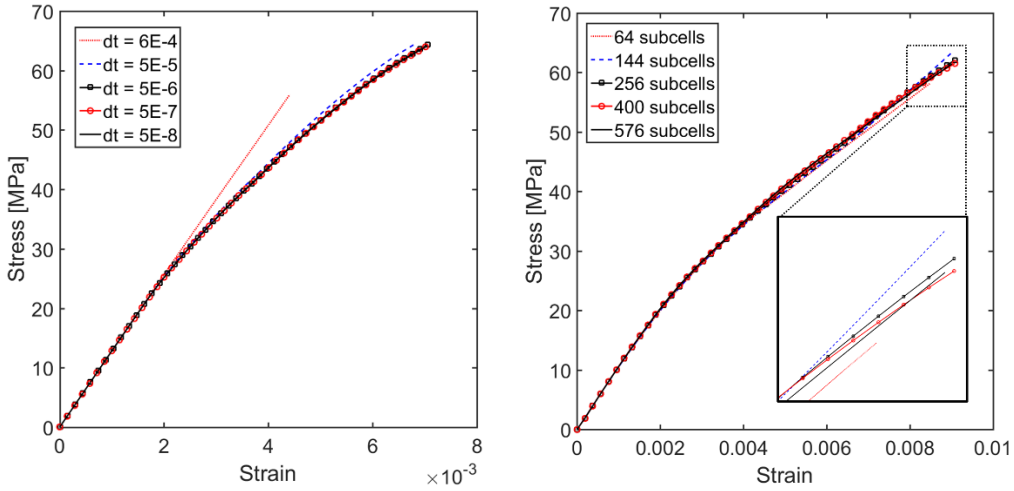

(a) (b)

Figure 5.15. Micromechanics Convergence Study of (a) the Time Increment and (b) the Number of Subcells.

Transverse tensile stress-strain plots of unit cell simulations with different interphase types are depicted in Figure 5.16. For comparison, these results are plotted with simulation results obtained from a unit cell without interphase subcells. The stress-strain response for the simulations with interphase properties from the literature (Table 5.3) shows smaller failure strains compared to the simulation without interphase subcells. In contrast, the simulations with the current interphase models result in a 5% lower transverse tensile strength and increased nonlinearity causing 25% larger failure strains. To plot the

transverse tensile stress as a function of normalized unit cell width, subcell stress values are extracted as shown by the arrow bisecting the unit cell in the y_2 axis in Figure 5.10. The subcell stress-width data for the simulations with the interphase types from literature, presented in Figure 5.17(a), shows local failure of the interphase subcells. In contrast, Figure 5.17(b) demonstrates that local failure in the unit cell simulation results, obtained using the current interphase models, occurs in the polymer subcells. Additionally, the simulations with the current interphase models show a larger stress gradient across the interphase due to the properties and material symmetry applied to these models (Figure 5.18(a) and (b)). The large stress gradients and local failure modes increase the viscoplastic straining of the polymer subcells, which causes the large nonlinearity in the unit cell simulations with the current interphase models. It is important to note that the large variations in transverse elastic moduli of different interphase types do not affect the mode of local failure, whereas the interphase strength and structure do affect the mode of local failure.

Similar results were obtained in Maligno et al. [194] where a finite element model of a composite RVE was simulated and parametric studies were performed using interphase strength as a variable. For interphase strengths less than about 60 MPa, Maligno's results showed that local failure initiated in the interphase elements and, for higher values of interphase strengths, local failure occurred in the polymer elements. These results were obtained using varying interphase transverse elastic moduli and the modulus variations did not have an effect on the mode of local failure, which agrees with the results from the simulations in this study.

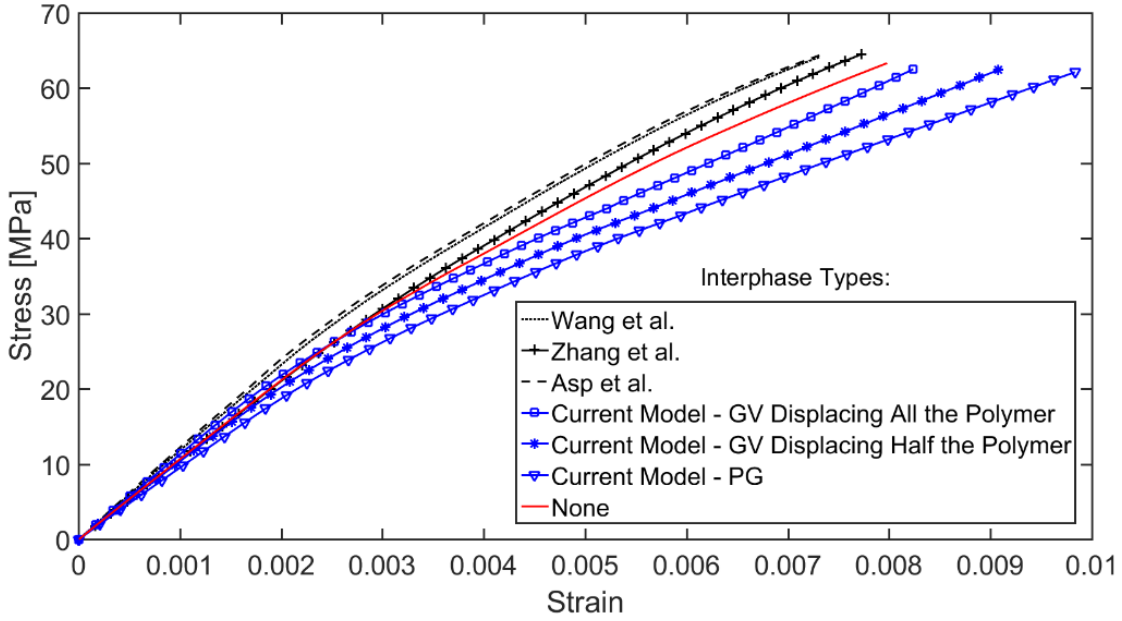

Figure 5.16. Transverse Tensile Stress-Strain Plots for Unit Cells with Different Interphase Properties.

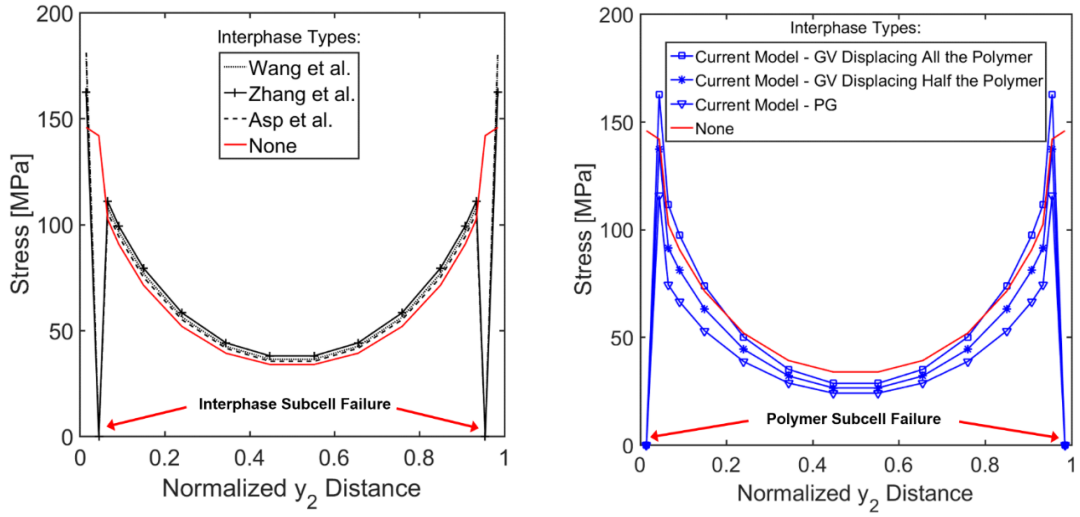

(a) Literature interphases (b) Current interphases

Figure 5.17. Subcell Stress-Width Plots for Unit Cell Simulations with 0.74% Strain.

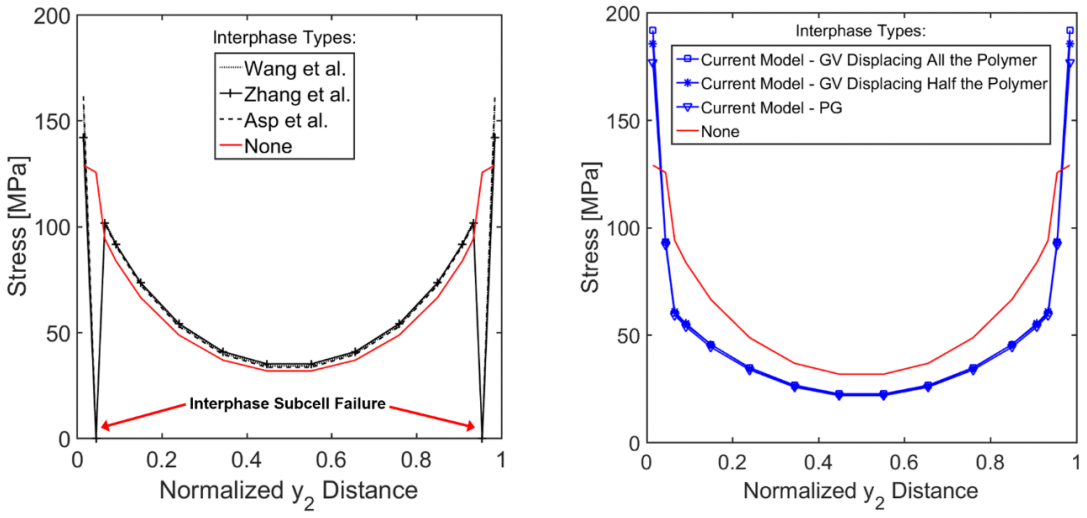

(a) Literature interphases (b) Current interphases

Figure 5.18. Subcell Stress-Width Plots for Unit Cell Simulations with 0.64% Strain.

5.5. Chapter Summary

In this chapter, a nanoscale interphase model composed of multiple GV layers and a thermoset polymer matrix to represent the physical molecular structure of the interphase is presented. The GV layers were created by removing carbon atoms, which caused voids in the layers. The results from the MD simulations show that strong carbon fiber/polymer matrix interactions exist in the GV interphase models yielding larger stiffness and strength compared to the PG interphase model. A multiscale framework was developed to integrate the interphase models with a high-fidelity micromechanics theory. The complex interactions shown in the MD results, due to voids and structural variation, cause large stress gradients across the interphase and increased viscoplastic behavior in the microscale simulations. A comparison of the microscale results showed that the unit cell response obtained using the current interphase model predicts a slightly lower composite tensile

strength (about 5%) and a maximum difference of 25% in failure strain compared to the results obtained using interphase properties from the literature.

CHAPTER

6. CONTRIBUTIONS AND FUTURE WORK

6.1. Contributions

An atomistic model and simulation methodology that captures mechanochemical reaction of mechanophores in thermoset polymer matrix is developed in this dissertation. The developed atomistic model and simulation methodology, herein named hybrid MD simulation framework, are validated by comparing the estimated simulation results with the experimental work. The hybrid MD framework was validated by comparing experimental results obtained through active collaboration with the chemical engineering research group at ASU, as well as experiments conducted in the literature to measure material properties of a range of thermoset polymers. The development of the hybrid MD framework offers four major contributions to the area of computational materials design, specifically for mechanochemical materials in epoxy polymer. They include: i) an experimentally validated thermoset polymer matrix generation method that uses van der Waals radii as a cutoff distance, thus allowing for estimation of conversion degrees of epoxy-based thermosets; ii) the ability to capture mechanophore activation induced by covalent bond breakage via introduction of ReaxFF, which is a bond order based force-field; iii) an experimentally validated mechanical loading test simulation method which matches the performance of the QC method with improved computational efficiency; iv) development of a local work analysis method that enables a quantitative analysis of the sensitivity of mechanophore activation. Ultimately, this dissertation shows that the experimentally validated hybrid MD framework has excellent potential to provide physically/chemically meaningful material design guidelines of experimental design

parameters that can lead to optimized material performance while significantly reducing labor and cost involved in experiments required for the novel mechanochemical material development.

As a part of this research, a fiber/matrix interphase model was also developed to capture the nanoscale phenomena at the interphase region. The primary goal of this mechanochemical reaction study was to extend the atomistic framework to model mechanophore embedded PMCs and to achieve comprehensive understanding of the damage initiation and progression that often initiate in this region. The interphase modeling methodology will be combined with mechanophore embedded thermoset polymer modeling method in future work.

6.2. Future Work

The research presented here provides a new method to capture mechanochemical reaction of mechanophores in nanocomposites while offering a preliminary insight on how to estimate fiber/matrix interphase properties. The novel methodology can be extended to model the mechano-chemical interactions in a wide range of polymeric material systems. Following are some future research topics based on the challenges that emerged in the course of this work:

1. A mechanophore embedded PMC model would need to be developed; mechanophore activation mechanism in the interphase region and dynamic/static response in this region also needs to be investigated in depth. A critical challenge in this area is the boundary condition mismatch between the nanocomposite model and the interphase model during the virtual loading test, which also needs to be

addressed. A novel boundary condition for the combined system (mechanophore embedded nanocomposites + interphase model) needs to be explored since the UHSR method, which enables covalent bond breakage during the loading test, is only applicable under the three directional periodic boundary conditions.

2. The simulation results show good agreement with experiments (early damage signal detection and yield strength variation due to mechanophore inclusion); however, there are still some limits to using MD simulation results as values that can be directly compared with experimental output. For example, yield strengths and strain showed overestimated values when compared to the experimental results. This may have been caused by unit cell constructed using defect-free assumption and by the length scale discrepancy, which is an inherent limitation of MD simulations. The first limitation can be addressed by stochastically introducing manufacturing damage, such as void and clustering constituents, in the unit cells. The second scale-related limitation could be investigated by developing a coarse-grained model that can increase the range of the length scale from nanometers to micrometers. However, it is important to note that current coarse-grained methods cannot capture the chemical reaction such as covalent bond breakage and bond formation which are essential for the mechanophore activation simulation. Therefore, there is a need to develop advanced coarse-grained methods to capture the mechanochemical reaction of mechanophores.
3. The effect of physical and chemical aging on the performance of mechanophore embedded nanocomposites, i.e., more realistic estimations of time-dependent material properties such as residual life expectancy and degraded performance due

to extreme (high temperature and moisture) environmental condition, is another area that could benefit from additional study.

4. Using this simulation framework, a parametric study could be performed to investigate the effect of variability of input parameters on mechanophore performance and mechanical response, and further to provide experimental design guidelines that could reduce the number of cost and labor intensive experiments. This study could be extended to include other parameters such as different weight fractions of mechanophores, different types of epoxy resins and hardeners, as well as a varying range of curing conditions (temperature and pressure).
5. The developed framework is applicable to an experimentally synthesized material, primarily because this framework is not based on QM. However, new material design requires more computational capabilities; this can possibly be addressed by implementing QM method within the current hybrid MD framework.

REFERENCES

[1] Board, U. C., 1988, "Advanced Materials by Design," *Office of Technology Assessment, Washington, DC.*

[2] Gibson, R.F., 2016, "Principles of composite material mechanics," CRC press.

[3] Sohn, H., Swenson, E. D., Olson, S. E., DeSimio, M. P., and Dutta, D., 2010, "Delamination detection in composite structures using laser vibrometer measurement of Lamb waves," SPIE Smart Structures and Materials Nondestructive Evaluation and Health Monitoring, Anonymous International Society for Optics and Photonics, pp. 76500P-76500P-10.

[4] Hiche, C., Coelho, C. K., Chattopadhyay, A., and Seaver, M., 2010, "Impact localization on complex structures using FBG strain amplitude information," SPIE Smart Structures and Materials Nondestructive Evaluation and Health Monitoring, Anonymous International Society for Optics and Photonics, pp. 764903-764903-10.

[5] Zhang, Y., 2005, "Piezoelectric paint sensor for real-time structural health monitoring," Smart Structures and Materials, Anonymous International Society for Optics and Photonics, pp. 1095-1103.

[6] Neerukatti, R., Hensberry, K., Kovvali, N., and Chattopadhyay, A., 2015, "A Novel Probabilistic Framework for Damage Localization and Prognosis Including Temperature Compensation," *J.Intell.Mater.Syst.Struct,* **27**(5) pp. 592-607.

[7] Knauss, W.G., Emri, I., and Lu, H., 2008, "Mechanics of polymers: viscoelasticity," Springer.

[8] Mascarenhas, W. N., 2011, "A Damage Model for the Ductile Failure Analysis of Plastic Components."

[9] Riande, E., Diaz-Calleja, R., Prolongo, M., Masegosa, R., and Salom, C., 1999, "Polymer viscoelasticity: stress and strain in practice," CRC Press.

[10] Datta, S., Fard, M. Y., and Chattopadhyay, A., 2015, "High-Speed Surfactant-Free Fabrication of Large Carbon Nanotube Membranes for Multifunctional Composites," *Journal of Aerospace Engineering,* pp. 04015060.

[11] Liu, Y., Rajadas, A., and Chattopadhyay, A., 2012, "A Biomimetic Structural Health Monitoring Approach using Carbon Nanotubes," *Jom,* **64**(7) pp. 802-807.

[12] Zou, J., Liu, Y., Shan, B., Chattopadhyay, A., and Dai, L. L., 2014, "Early Damage Detection in Epoxy Matrix using Cyclobutane-Based Polymers," *Smart Materials and Structures,* **23**(9) pp. 095038.

[13] Nofen, E. M., Wickham, J., Koo, B., Chattopadhyay, A., and Dai, L. L., 2016, "Dimeric Anthracene-Based Mechanophore Particles for Damage Precursor Detection in Reinforced Epoxy Matrix Composites," *Materials Research Express,* **3**(3) pp. 035701.

[14] Davis, D. A., Hamilton, A., Yang, J., Cremar, L. D., Van Gough, D., Potisek, S. L., Ong, M. T., Braun, P. V., Martínez, T. J., and White, S. R., 2009, "Force-Induced Activation of Covalent Bonds in Mechanoresponsive Polymeric Materials," *Nature,* **459**(7243) pp. 68-72.

[15] Song, Y., Lee, K., Hong, W., Cho, S., Yu, H., and Chung, C., 2012, "Fluorescence Sensing of Microcracks Based on Cycloreversion of a Dimeric Anthracene Moiety," *Journal of Materials Chemistry,* **22**(4) pp. 1380-1386.

[16] Cho, S., Kim, J., and Chung, C., 2008, "A Fluorescent Crack Sensor Based on Cyclobutane-Containing Crosslinked Polymers of Tricinnamates," *Sensors and Actuators B: Chemical,* **134**(2) pp. 822-825.

[17] Crenshaw, B. R., Burnworth, M., Khariwala, D., Hiltner, A., Mather, P. T., Simha, R., and Weder, C., 2007, "Deformation-Induced Color Changes in Mechanochromic Polyethylene Blends," *Macromolecules,* **40**(7) pp. 2400-2408.

[18] Chen, Y., Spiering, A., Karthikeyan, S., Peters, G. W., Meijer, E., and Sijbesma, R. P., 2012, "Mechanically Induced Chemiluminescence from Polymers Incorporating a 1, 2-Dioxetane Unit in the Main Chain," *Nature Chemistry,* **4**(7) pp. 559-562.

[19] Berkovic, G., Krongauz, V., and Weiss, V., 2000, "Spiropyrans and Spirooxazines for Memories and Switches," *Chemical Reviews,* **100**(5) pp. 1741-1754.

[20] Kobatake, S., and Irie, M., 2003, "8Photochromism," *Annual Reports Section" C"(Physical Chemistry),* **99**pp. 277-313.

[21] Crano, J.C., and Guglielmetti, R.J., 1999, "Organic Photochromic and Thermochromic Compounds: Volume 2: Physicochemical Studies, Biological Applications, and Thermochromism," Springer Science & Business Media.

[22] Kingsbury, C. M., May, P. A., Davis, D. A., White, S. R., Moore, J. S., and Sottos, N. R., 2011, "Shear Activation of Mechanophore-Crosslinked Polymers," *Journal of Materials Chemistry,* **21**(23) pp. 8381-8388.

[23] Gossweiler, G. R., Hewage, G. B., Soriano, G., Wang, Q., Welshofer, G. W., Zhao, X., and Craig, S. L., 2014, "Mechanochemical Activation of Covalent Bonds in Polymers with Full and Repeatable Macroscopic Shape Recovery," *ACS Macro Letters,* **3**(3) pp. 216-219.

[24] Cho, S., Kim, J., and Chung, C., 2010, "Photochemical Crack Healing in Cinnamate-Based Polymers," *Journal of Nanoscience and Nanotechnology,* **10**(10) pp. 6972-6976.

[25] Chung, C., Roh, Y., Cho, S., and Kim, J., 2004, "Crack Healing in Polymeric Materials Via Photochemical [2 2] Cycloaddition," *Chemistry of Materials,* **16**(21) pp. 3982-3984.

[26] Oya, N., Sukarsaatmadja, P., Ishida, K., and Yoshie, N., 2012, "Photoinduced Mendable Network Polymer from Poly (Butylene Adipate) End-Functionalized with Cinnamoyl Groups," *Polymer Journal,* **44**(7) pp. 724-729.

[27] Cintas, P., and Cravotto, G., 2012, "Mechanochemistry: Measuring the Force of Sound," *Nature Chemistry,* **4**(2) pp. 77-78.

[28] Kryger, M. J., Munaretto, A. M., and Moore, J. S., 2011, "Structure–mechanochemical Activity Relationships for Cyclobutane Mechanophores," *Journal of the American Chemical Society,* **133**(46) pp. 18992-18998.

[29] Ma, Z., Yang, F., Wang, Z., and Jia, X., 2015, "Mechanically Induced Color Change Based on the Chromophores of Anthracene and Rhodamine 6G," *Tetrahedron Letters,* **56**(2) pp. 393-396.

[30] Brichkin, S., Razumov, V., Bogdanova, L., and Rozenberg, B., 2000, "Luminescent Labels for the Study of Phase Separation in Cured Epoxy Polymer Systems," *Polymer Science Series Ac/C of Vysokomolekuliarnye Soedineniia,* **42**(5) pp. 516-521.

[31] Froimowicz, P., Frey, H., and Landfester, K., 2011, "Towards the Generation of Self-Healing Materials by Means of a Reversible Photo-induced Approach," *Macromolecular Rapid Communications,* **32**(5) pp. 468-473.

[32] Defize, T., Riva, R., Jérôme, C., and Alexandre, M., 2012, "Multifunctional Poly (E-caprolactone)-Forming Networks by Diels–Alder Cycloaddition: Effect of the Adduct on the Shape-Memory Properties," *Macromolecular Chemistry and Physics,* **213**(2) pp. 187-197.

[33] Xing, J., Zheng, M., Chen, W., Dong, X., Takeyasu, N., Tanaka, T., Zhao, Z., Duan, X., and Kawata, S., 2012, "C 2v Symmetrical Two-Photon Polymerization Initiators with Anthracene Core: Synthesis, Optical and Initiating Properties," *Physical Chemistry Chemical Physics,* **14**(45) pp. 15785-15792.

[34] Sottos, N. R., 2014, "Polymer Mechanochemistry: Flex, Release and Repeat," *Nature Chemistry,* **6**pp. 381-383.

[35] Li, J., Nagamani, C., and Moore, J. S., 2015, "Polymer Mechanochemistry: From Destructive to Productive," *Accounts of Chemical Research,* **48**(8) pp. 2181-2190.

[36] Brantley, J. N., Wiggins, K. M., and Bielawski, C. W., 2013, "Polymer Mechanochemistry: The Design and Study of Mechanophores," *Polymer International,* **62**(1) pp. 2-12.

[37] Buehler, M. J., 2013, "Materials by design—A Perspective from Atoms to Structures," *MRS Bulletin,* **38**(02) pp. 169-176.

[38] Li, C., Browning, A. R., Christensen, S., and Strachan, A., 2012, "Atomistic Simulations on Multilayer Graphene Reinforced Epoxy Composites," *Composites Part A: Applied Science and Manufacturing,* **43**(8) pp. 1293-1300.

[39] Zhu, R., Pan, E., and Roy, A., 2007, "Molecular Dynamics Study of the Stress–strain Behavior of Carbon-Nanotube Reinforced Epon 862 Composites," *Materials Science and Engineering: A,* **447**(1) pp. 51-57.

[40] Subramanian, N., Koo, B., Rai, A., and Chattopadhyay, A., 2015, "A Multiscale Damage Initiation Model for CNT-Enhanced Epoxy Polymers," *Proc. ICCM, Copenhagen, Denmark.*

[41] Rai, A., Subramanian, N., Koo, B., and Chattopadhyay, A., 2016, "Multiscale Damage Analysis of Carbon Nanotube Nanocomposite using a Continuum Damage Mechanics Approach," *Journal of Composite Materials,* pp. 0021998316654304.

[42] Silberstein, M. N., Min, K., Cremar, L. D., Degen, C. M., Martinez, T. J., Aluru, N. R., White, S. R., and Sottos, N. R., 2013, "Modeling Mechanophore Activation within a Crosslinked Glassy Matrix," *Journal of Applied Physics,* **114**(2) pp. 023504.

[43] Mayo, S. L., Olafson, B. D., and Goddard, W. A., 1990, "DREIDING: A Generic Force Field for Molecular Simulations," *Journal of Physical Chemistry,* **94**(26) pp. 8897-8909.

[44] Pearlman, D. A., Case, D. A., Caldwell, J. W., Ross, W. S., Cheatham III, T. E., DeBolt, S., Ferguson, D., Seibel, G., and Kollman, P., 1995, "AMBER, a Package of Computer Programs for Applying Molecular Mechanics, Normal Mode Analysis, Molecular Dynamics and Free Energy Calculations to Simulate the Structural and Energetic Properties of Molecules," *Computer Physics Communications,* **91**(1) pp. 1-41.

[45] Kaminski, G. G. A., 2001, "Evaluation and Reparametrization of the OPLS-AA Force Field for Proteins Via Comparison with Accurate Quantum Chemical Calculations on Peptides," *The Journal of Physical Chemistry.B,* **105**(28) pp. 6474; 6474-6487; 6487.

[46] Jorgensen, W. W. L., 1996, "Development and Testing of the OPLS all-Atom Force Field on Conformational Energetics and Properties of Organic Liquids," *Journal of the American Chemical Society,* **118**(45) pp. 11225; 11225-11236; 11236.

[47] Halgren, T. A., 1996, "Merck Molecular Force Field. I. Basis, Form, Scope, Parameterization, and Performance of MMFF94," *Journal of Computational Chemistry,* **17**(5-6) pp. 490-519.

[48] Kinloch, A.J., 2013, "Fracture behaviour of polymers," Springer Science & Business Media.

[49] Cook, W. D., Mayr, A. E., and Edward, G. H., 1998, "Yielding Behaviour in Model Epoxy thermosets—II. Temperature Dependence," *Polymer,* **39**(16) pp. 3725-3733.

[50] Dlubek, G., Pointeck, J., Shaikh, M. Q., Hassan, E., and Krause-Rehberg, R., 2007, "Free Volume of an Oligomeric Epoxy Resin and its Relation to Structural Relaxation: Evidence from Positron Lifetime and Pressure-Volume-Temperature Experiments," *Physical Review E,* **75**(2) pp. 021802.

[51] Sun, C., and Vaidya, R., 1996, "Prediction of Composite Properties from a Representative Volume Element," *Composites Science and Technology,* **56**(2) pp. 171-179.

[52] Asp, L., Berglund, L. A., and Talreja, R., 1996, "Prediction of Matrix-Initiated Transverse Failure in Polymer Composites," *Composites Science and Technology,* **56**(9) pp. 1089-1097.

[53] Trias, D., Costa, J., Mayugo, J., and Hurtado, J., 2006, "Random Models Versus Periodic Models for Fibre Reinforced Composites," *Computational Materials Science,* **38**(2) pp. 316-324.

[54] Totry, E., González, C., and LLorca, J., 2008, "Failure Locus of Fiber-Reinforced Composites Under Transverse Compression and Out-of-Plane Shear," *Composites Science and Technology,* **68**(3) pp. 829-839.

[55] Vaughan, T., and McCarthy, C., 2011, "Micromechanical Modelling of the Transverse Damage Behaviour in Fibre Reinforced Composites," *Composites Science and Technology,* **71**(3) pp. 388-396.

[56] Moncada, A. M., Reynolds, W. D., Chattopadhyay, A., Bednarcyk, B. A., and Arnold, S. M., 2009, "An Explicit Multiscale Model for Progressive Failure of Composite Structures," 50th AIAA/ASME/ASCE/AHS/ASC Structures, Structural Dynamics, and Materials Conference 17th AIAA/ASME/AHS Adaptive Structures Conference 11th AIAA No, Anonymous pp. 2549.

[57] Raghavan, P., and Ghosh, S., 2005, "A Continuum Damage Mechanics Model for Unidirectional Composites Undergoing Interfacial Debonding," *Mechanics of Materials,* **37**(9) pp. 955-979.

[58] Ghosh, S., Lee, K., and Raghavan, P., 2001, "A Multi-Level Computational Model for Multi-Scale Damage Analysis in Composite and Porous Materials," *International Journal of Solids and Structures,* **38**(14) pp. 2335-2385.

[59] Groves, S., Harris, C., Highsmith, A., Allen, D., and Norvell, R., 1987, "An Experimental and Analytical Treatment of Matrix Cracking in Cross-Ply Laminates," *Experimental Mechanics,* **27**(1) pp. 73-79.

[60] Bader, M., Bailey, J., Parvizi, A., and Curtis, P., 1980, "The Mechanisms of Initiation and Development of Damage in Multi-Axial Fibre-Reinforced Plastics Laminates," *Mechanical Behaviour of Materials,* pp. 227-239.

[61] Wang, A. S., 1984, "Fracture Mechanics of Sublaminate Cracks in Composite Materials," *Journal of Composites, Technology and Research,* **6**(2) pp. 45-62.

[62] Das, S., Reddy, N., and Raju, G., 2015, "Damage Evolution Studies in Carbon Fiber Reinforced Polymer Composites using Active and Passive Thermography."

[63] Rodriguez, B., Galleguillos, C., Fernández, R., and Lasagni, F., 2014, "Passive Infrared Thermography for Damage Monitoring during Structural Testing of CFRP Parts," *No.June,* pp. 22-26.

[64] Li, C., and Strachan, A., 2010, "Molecular Simulations of Crosslinking Process of Thermosetting Polymers," *Polymer,* **51**(25) pp. 6058-6070.

[65] Li, C., and Strachan, A., 2011, "Molecular Dynamics Predictions of Thermal and Mechanical Properties of Thermoset Polymer EPON862/DETDA," *Polymer,* **52**(13) pp. 2920-2928.

[66] Li, C., Jaramillo, E., and Strachan, A., 2013, "Molecular Dynamics Simulations on Cyclic Deformation of an Epoxy Thermoset," *Polymer,* **54**(2) pp. 881-890.

[67] Valavala, P., Odegard, G., and Aifantis, E., 2009, "Influence of Representative Volume Element Size on Predicted Elastic Properties of Polymer Materials," *Modelling and Simulation in Materials Science and Engineering,* **17**(4) pp. 045004.

[68] Bandyopadhyay, A., Valavala, P. K., Clancy, T. C., Wise, K. E., and Odegard, G. M., 2011, "Molecular Modeling of Crosslinked Epoxy Polymers: The Effect of Crosslink Density on Thermomechanical Properties," *Polymer,* **52**(11) pp. 2445-2452.

[69] Shiu, S., and Tsai, J., 2014, "Characterizing Thermal and Mechanical Properties of Graphene/Epoxy Nanocomposites," *Composites Part B: Engineering,* **56**pp. 691-697.

[70] Shin, H., Chang, S., Yang, S., Youn, B. D., and Cho, M., 2016, "Statistical Multiscale Homogenization Approach for Analyzing Polymer Nanocomposites that Include Model Inherent Uncertainties of Molecular Dynamics Simulations," *Composites Part B: Engineering,* **87**pp. 120-131.

[71] Rahman, R., and Haque, A., 2013, "Molecular Modeling of Crosslinked Graphene–epoxy Nanocomposites for Characterization of Elastic Constants and Interfacial Properties," *Composites Part B: Engineering,* **54**pp. 353-364.

[72] Ionita, M., 2012, "Multiscale Molecular Modeling of SWCNTs/Epoxy Resin Composites Mechanical Behaviour," *Composites Part B: Engineering,* **43**(8) pp. 3491-3496.

[73] Zhang, J., Koo, B., Subramanian, N., Liu, Y., and Chattopadhyay, A., 2015, "An Optimized Cross-Linked Network Model to Simulate the Linear Elastic Material Response of a Smart Polymer," *Journal of Intelligent Material Systems and Structures,* pp. 1045389X15595292.

[74] Zhang, J., Koo, B., Liu, Y., Zou, J., Chattopadhyay, A., and Dai, L., 2015, "A Novel Statistical Spring-Bead Based Network Model for Self-Sensing Smart Polymer Materials," *Smart Materials and Structures,* **24**(8) pp. 085022.

[75] Panico, M., Narayanan, S., and Brinson, L., 2010, "Simulations of Tensile Failure in Glassy Polymers: Effect of Cross-Link Density," *Modelling and Simulation in Materials Science and Engineering,* **18**(5) pp. 055005.

[76] Sliozberg, Y. R., Hoy, R. S., Mrozek, R. A., Lenhart, J. L., and Andzelm, J. W., 2014, "Role of Entanglements and Bond Scission in High Strain-Rate Deformation of Polymer Gels," *Polymer,* **55**(10) pp. 2543-2551.

[77] Hoy, R. S., and Robbins, M. O., 2007, "Strain Hardening in Polymer Glasses: Limitations of Network Models," *Physical Review Letters,* **99**(11) pp. 117801.

[78] Rottler, J., and Robbins, M. O., 2003, "Growth, Microstructure, and Failure of Crazes in Glassy Polymers," *Physical Review E,* **68**(1) pp. 011801.

[79] Moller, J., Barr, S., Schultz, E., Breitzman, T., and Berry, R., 2013, "Simulation of Fracture Nucleation in Cross-Linked Polymer Networks," *Jom,* **65**(2) pp. 147-167.

[80] Schoeppner, G., Tandon, G., and Pochiraju, K., 2008, "Multiscale Modeling and Simulation of Composite Materials and Structures," Springer, pp. 359-462.

[81] Reifsnider, K., 1994, "Modelling of the Interphase in Polymer-Matrix Composite Material Systems," *Composites,* **25**(7) pp. 461-469.

[82] Asp, L., Berglund, L. A., and Talreja, R., 1996, "Effects of Fiber and Interphase on Matrix-Initiated Transverse Failure in Polymer Composites," *Composites Science and Technology,* **56**(6) pp. 657-665.

[83] Souza, F., Allen, D., and Kim, Y., 2008, "Multiscale Model for Predicting Damage Evolution in Composites due to Impact Loading," *Composites Science and Technology,* **68**(13) pp. 2624-2634.

[84] Wang, X., Zhang, J., Wang, Z., Zhou, S., and Sun, X., 2011, "Effects of Interphase Properties in Unidirectional Fiber Reinforced Composite Materials," *Materials & Design,* **32**(6) pp. 3486-3492.

[85] Zhang, B., Yang, Z., Sun, X., and Tang, Z., 2010, "A Virtual Experimental Approach to Estimate Composite Mechanical Properties: Modeling with an Explicit Finite Element Method," *Computational Materials Science,* **49**(3) pp. 645-651.

[86] Zhandarov, S., and Mäder, E., 2005, "Characterization of Fiber/Matrix Interface Strength: Applicability of Different Tests, Approaches and Parameters," *Composites Science and Technology,* **65**(1) pp. 149-160.

[87] Broutman, L., 1969, "Measurement of the Fiber-Polymer Matrix Interfacial Strength," *Interfaces in Composites,* **452**pp. 27.

[88] Ageorges, C., Friedrich, K., Schüller, T., and Lauke, B., 1999, "Single-Fibre Broutman Test: Fibre–matrix Interface Transverse Debonding," *Composites Part A: Applied Science and Manufacturing,* **30**(12) pp. 1423-1434.

[89] Hadden, C. M., Klimek-McDonald, D. R., Pineda, E. J., King, J. A., Reichanadter, A. M., Miskioglu, I., Gowtham, S., and Odegard, G. M., 2015, "Mechanical Properties of Graphene Nanoplatelet/Carbon Fiber/Epoxy Hybrid Composites: Multiscale Modeling and Experiments," *Carbon,* **95**pp. 100-112.

[90] Jiang, L., Tan, H., Wu, J., Huang, Y., and Hwang, K., 2007, "Continuum Modeling of Interfaces in Polymer Matrix Composites Reinforced by Carbon Nanotubes," *Nano,* **2**(03) pp. 139-148.

[91] Mousavi, A. A., Arash, B., Zhuang, X., and Rabczuk, T., 2016, "A Coarse-Grained Model for the Elastic Properties of Cross Linked Short Carbon Nanotube/Polymer Composites," *Composites Part B: Engineering,* **95**pp. 404-411.

[92] Edwards, I.A., Menendez, R., and Marsh, H., 2013, "Introduction to carbon science," Butterworth-Heinemann.

[93] Johnson, D., 1987, "Structure-Property Relationships in Carbon Fibres," *Journal of Physics D: Applied Physics,* **20**(3) pp. 286.

[94] Guigon, M., and Oberlin, A., 1986, "Heat-Treatment of High Tensile Strength PAN-Based Carbon Fibres: Microtexture, Structure and Mechanical Properties," *Composites Science and Technology,* **27**(1) pp. 1-23.

[95] Zhang, Y., Xu, F., Zhang, C., Wang, J., Jia, Z., Hui, D., and Qiu, Y., 2016, "Tensile and Interfacial Properties of Polyacrylonitrile-Based Carbon Fiber After Different Cryogenic Treated Condition," *Composites Part B: Engineering.*

[96] Kulkarni, M. M., 2009, "Prediction of Elastic Properties of a Carbon Nanotube Reinforced Fiber Polymeric Composite Material using Cohesive Zone Modeling."

[97] Beyerlein, I. J., Amer, M. S., Schadler, L. S., and Phoenix, S. L., 1998, "New Methodology for Determining in Situ Fiber, Matrix and Interface Stresses in Damaged Multifiber Composites," *Science and Engineering of Composite Materials,* **7**(1-2) pp. 151-204.

[98] Shokrieh, M. M., and Rafiee, R., 2010, "Prediction of Mechanical Properties of an Embedded Carbon Nanotube in Polymer Matrix Based on Developing an Equivalent Long Fiber," *Mechanics Research Communications,* **37**(2) pp. 235-240.

[99] Hua, Y., Gu, L., Premaraj, S., and Zhang, X., 2015, "Role of Interphase in the Mechanical Behavior of Silica/Epoxy Resin Nanocomposites," *Materials,* **8**(6) pp. 3519-3531.

[100] Alder, B., and Wainwright, T., 1957, "Phase Transition for a Hard Sphere System," *The Journal of Chemical Physics,* **27**(5) pp. 1208.

[101] Kirkwood, J., Smoluchowski, R., Mayer, J., and Weyl, W., 1951, "Phase Transformations in Solids," *Wiley, New York,* pp. 6.

[102] Metropolis, N., Rosenbluth, A. W., Rosenbluth, M. N., Teller, A. H., and Teller, E., 1953, "Equation of State Calculations by Fast Computing Machines," *The Journal of Chemical Physics,* **21**(6) pp. 1087-1092.

[103] Swope, W. C., Andersen, H. C., Berens, P. H., and Wilson, K. R., 1982, "A Computer Simulation Method for the Calculation of Equilibrium Constants for the Formation of Physical Clusters of Molecules: Application to Small Water Clusters," *The Journal of Chemical Physics,* **76**(1) pp. 637-649.

[104] Gibbs, J.W., Bumstead, H.A., Ralph Gibbs Van Name, and Longley, W.R., 1928, "The collected works of J. Willard Gibbs: In two volumes," Longmans, Green and Company.

[105] Halgren, T. A., 1996, "Merck Molecular Force Field. II. MMFF94 Van Der Waals and Electrostatic Parameters for Intermolecular Interactions," *Journal of Computational Chemistry,* **17**(5-6) pp. 520-552.

[106] Halgren, T. A., 1996, "Merck Molecular Force Field. III. Molecular Geometries and Vibrational Frequencies for MMFF94," *Journal of Computational Chemistry,* **17**(5-6) pp. 553-586.

[107] Halgren, T. A., and Nachbar, R. B., 1996, "Merck Molecular Force Field. IV. Conformational Energies and Geometries for MMFF94," *Journal of Computational Chemistry,* **17**(5-6) pp. 587-615.

[108] Halgren, T. A., 1996, "Merck Molecular Force Field. V. Extension of MMFF94 using Experimental Data, Additional Computational Data, and Empirical Rules," *Journal of Computational Chemistry,* **17**(5-6) pp. 616-641.

[109] Plimpton, S., 1995, "Fast Parallel Algorithms for Short-Range Molecular Dynamics," *Journal of Computational Physics,* **117**(1) pp. 1-19.

[110] Tou, W. I., Chang, S., Lee, C., and Chen, C. Y., 2013, "Drug Design for Neuropathic Pain Regulation from Traditional Chinese Medicine," *Scientific Reports,* **3**.

[111] Ericksen, S. S., Cummings, D. F., Teer, M. E., Amdani, S., and Schetz, J. A., 2012, "Ring Substituents on Substituted Benzamide Ligands Indirectly Mediate Interactions with Position 7.39 of Transmembrane Helix 7 of the D4 Dopamine Receptor," *The Journal of Pharmacology and Experimental Therapeutics,* **342**(2) pp. 472-485.

[112] Shim, J., and MacKerell Jr, A. D., 2011, "Computational Ligand-Based Rational Design: Role of Conformational Sampling and Force Fields in Model Development," *MedChemComm,* **2**(5) pp. 356-370.

[113] Allen, F. H., 2002, "The Cambridge Structural Database: A Quarter of a Million Crystal Structures and Rising," *Acta Crystallographica Section B: Structural Science,* **58**(3) pp. 380-388.

[114] Zoete, V., Cuendet, M. A., Grosdidier, A., and Michielin, O., 2011, "SwissParam: A Fast Force Field Generation Tool for Small Organic Molecules," *Journal of Computational Chemistry,* **32**(11) pp. 2359-2368.

[115] Liu, Y., Fard, M. Y., Chattopadhyay, A., and Doyle, D., 2012, "Damage Assessment of CFRP Composites using a Time–frequency Approach," *Journal of Intelligent Material Systems and Structures,* **23**(4) pp. 397-413.

[116] Ellis, B., 1993, "Chemistry and technology of epoxy resins," Blackie Academic & Professional.

[117] Varshney, V., Patnaik, S. S., Roy, A. K., and Farmer, B. L., 2008, "A Molecular Dynamics Study of Epoxy-Based Networks: Cross-Linking Procedure and Prediction of Molecular and Material Properties," *Macromolecules,* **41**(18) pp. 6837-6842.

[118] Yu, S., Yang, S., and Cho, M., 2009, "Multi-Scale Modeling of Cross-Linked Epoxy Nanocomposites," *Polymer,* **50**(3) pp. 945-952.

[119] Wu, C., and Xu, W., 2006, "Atomistic Molecular Modelling of Crosslinked Epoxy Resin," *Polymer,* **47**(16) pp. 6004-6009.

[120] Aronhime, M.T., and Gillham, J.K., 1986, "Epoxy Resins and Composites III," Springer, pp. 83-113.

[121] Enns, J. B., and Gillham, J. K., 1983, "Time–temperature–transformation (TTT) Cure Diagram: Modeling the Cure Behavior of Thermosets," *Journal of Applied Polymer Science,* **28**(8) pp. 2567-2591.

[122] Venditti, R., and Gillham, J., 1997, "A Relationship between the Glass Transition Temperature (Tg) and Fractional Conversion for Thermosetting Systems," *Journal of Applied Polymer Science,* **64**(1) pp. 3-14.

[123] McNaught, A.D., and McNaught, A.D., 1997, "Compendium of chemical terminology," Blackwell Science Oxford.

[124] Kremer, K., and Grest, G. S., 1990, "Dynamics of Entangled Linear Polymer Melts: A Molecular-dynamics Simulation," *The Journal of Chemical Physics,* **92**(8) pp. 5057-5086.

[125] Sides, S. W., Grest, G. S., and Stevens, M. J., 2001, "Surface-Tethered Chains Entangled in a Polymer Melt: Effects on Adhesion Dynamics," *Physical Review E,* **64**(5) pp. 050802.

[126] Stevens, M. J., 1999, "Thoughts on the Structure of Alkylsilane Monolayers," *Langmuir,* **15**(8) pp. 2773-2778.

[127] Stillinger, F. H., and Weber, T. A., 1985, "Computer Simulation of Local Order in Condensed Phases of Silicon," *Physical Review B,* **31**(8) pp. 5262.

[128] Tersoff, J., 1988, "Empirical Interatomic Potential for Carbon, with Applications to Amorphous Carbon," *Physical Review Letters,* **61**(25) pp. 2879.

[129] Brenner, D. W., Shenderova, O. A., Harrison, J. A., Stuart, S. J., Ni, B., and Sinnott, S. B., 2002, "A Second-Generation Reactive Empirical Bond Order (REBO) Potential Energy Expression for Hydrocarbons," *Journal of Physics: Condensed Matter,* **14**(4) pp. 783.

[130] Van Duin, A. C., Dasgupta, S., Lorant, F., and Goddard, W. A., 2001, "ReaxFF: A Reactive Force Field for Hydrocarbons," *The Journal of Physical Chemistry A,* **105**(41) pp. 9396-9409.

[131] Pauling, L., 1960, "The nature of the chemical bond and the structure of molecules and crystals: an introduction to modern structural chemistry," Cornell university press.

[132] Slater, J. C., 1931, "Molecular Energy Levels and Valence Bonds," *Physical Review,* **38**(6) pp. 1109.

[133] Strachan, A., van Duin, A. C., Chakraborty, D., Dasgupta, S., and Goddard III, W. A., 2003, "Shock Waves in High-Energy Materials: The Initial Chemical Events in Nitramine RDX," *Physical Review Letters,* **91**(9) pp. 098301.

[134] van Duin, A. C., Zeiri, Y., Dubnikova, F., Kosloff, R., and Goddard, W. A., 2005, "Atomistic-Scale Simulations of the Initial Chemical Events in the Thermal Initiation of Triacetonetriperoxide," *Journal of the American Chemical Society,* **127**(31) pp. 11053-11062.

[135] Chenoweth, K., van Duin, A. C., and Goddard, W. A., 2008, "ReaxFF Reactive Force Field for Molecular Dynamics Simulations of Hydrocarbon Oxidation," *The Journal of Physical Chemistry A,* **112**(5) pp. 1040-1053.

[136] Goddard III, W. A., Van Duin, A., Chenoweth, K., Cheng, M., Pudar, S., Oxgaard, J., Merinov, B., Jang, Y. H., and Persson, P., 2006, "Development of the ReaxFF Reactive Force Field for Mechanistic Studies of Catalytic Selective Oxidation Processes on BiMoO X," *Topics in Catalysis,* **38**(1-3) pp. 93-103.

[137] Goddard III, W., Merinov, B., Van Duin, A., Jacob, T., Blanco, M., Molinero, V., Jang, S., and Jang, Y., 2006, "Multi-Paradigm Multi-Scale Simulations for Fuel Cell Catalysts and Membranes," *Molecular Simulation,* **32**(3-4) pp. 251-268.

[138] Buehler, M. J., van Duin, A. C., and Goddard III, W. A., 2006, "Multiparadigm Modeling of Dynamical Crack Propagation in Silicon using a Reactive Force Field," *Physical Review Letters,* **96**(9) pp. 095505.

[139] Nielson, K. D., van Duin, A. C., Oxgaard, J., Deng, W., and Goddard, W. A., 2005, "Development of the ReaxFF Reactive Force Field for Describing Transition Metal Catalyzed Reactions, with Application to the Initial Stages of the Catalytic Formation of Carbon Nanotubes," *The Journal of Physical Chemistry A,* **109**(3) pp. 493-499.

[140] Russo, M. F., and van Duin, A. C., 2011, "Atomistic-Scale Simulations of Chemical Reactions: Bridging from Quantum Chemistry to Engineering," *Nuclear Instruments and Methods in Physics Research Section B: Beam Interactions with Materials and Atoms,* **269**(14) pp. 1549-1554.

[141] Mortier, W. J., Ghosh, S. K., and Shankar, S., 1986, "Electronegativity-Equalization Method for the Calculation of Atomic Charges in Molecules," *Journal of the American Chemical Society,* **108**(15) pp. 4315-4320.

[142] Janssens, G. O., Baekelandt, B. G., Toufar, H., Mortier, W. J., and Schoonheydt, R. A., 1995, "Comparison of Cluster and Infinite Crystal Calculations on Zeolites with the Electronegativity Equalization Method (EEM)," *The Journal of Physical Chemistry,* **99**(10) pp. 3251-3258.

[143] Chenoweth, K., Cheung, S., Van Duin, A. C., Goddard, W. A., and Kober, E. M., 2005, "Simulations on the Thermal Decomposition of a Poly (Dimethylsiloxane) Polymer using the ReaxFF Reactive Force Field," *Journal of the American Chemical Society,* **127**(19) pp. 7192-7202.

[144] Weismiller, M. R., Duin, A. C. v., Lee, J., and Yetter, R. A., 2010, "ReaxFF Reactive Force Field Development and Applications for Molecular Dynamics Simulations of Ammonia Borane Dehydrogenation and Combustion," *The Journal of Physical Chemistry A,* **114**(17) pp. 5485-5492.

[145] Aryanpour, M., van Duin, A. C., and Kubicki, J. D., 2010, "Development of a Reactive Force Field for Iron− Oxyhydroxide Systems," *The Journal of Physical Chemistry A,* **114**(21) pp. 6298-6307.

[146] Singh, S. K., Srinivasan, S. G., Neek-Amal, M., Costamagna, S., van Duin, Adri C. T., and Peeters, F. M., 2013, "Thermal Properties of Fluorinated Graphene," *Prb,* **87**(10) pp. 104114.

[147] Beyer, M. K., 2000, "The Mechanical Strength of a Covalent Bond Calculated by Density Functional Theory," *The Journal of Chemical Physics,* **112**(17) pp. 7307-7312.

[148] Dean, J.A., 1985, "Lange's handbook of chemistry," McGraw Hill Book Co., New York, NY.

[149] Mattsson, T. R., Lane, J. M. D., Cochrane, K. R., Desjarlais, M. P., Thompson, A. P., Pierce, F., and Grest, G. S., 2010, "First-Principles and Classical Molecular Dynamics Simulation of Shocked Polymers," *Physical Review B,* **81**(5) pp. 054103.

[150] Newsome, D. A., Sengupta, D., Foroutan, H., Russo, M. F., and van Duin, A. C., 2012, "Oxidation of Silicon Carbide by O2 and H2O: A ReaxFF Reactive Molecular Dynamics Study, Part I," *The Journal of Physical Chemistry C,* **116**(30) pp. 16111-16121.

[151] Theodorou, D. N., and Suter, U. W., 1986, "Atomistic Modeling of Mechanical Properties of Polymeric Glasses," *Macromolecules,* **19**(1) pp. 139-154.

[152] Mott, P., Argon, A., and Suter, U., 1993, "Atomistic Modelling of Plastic Deformation of Glassy Polymers," *Philosophical Magazine A*, **67**(4) pp. 931-978.

[153] Sommer, J., and Lay, S., 2002, "Topological Structure and Nonaffine Swelling of Bimodal Polymer Networks," *Macromolecules*, **35**(26) pp. 9832-9843.

[154] Basu, A., Wen, Q., Mao, X., Lubensky, T., Janmey, P. A., and Yodh, A., 2011, "Nonaffine Displacements in Flexible Polymer Networks," *Macromolecules*, **44**(6) pp. 1671-1679.

[155] Fox, J. R., and Andersen, H. C., 1984, "Molecular Dynamics Simulations of a Supercooled Monatomic Liquid and Glass," *The Journal of Physical Chemistry*, **88**(18) pp. 4019-4027.

[156] Buehler, M. J., Hartmaier, A., Gao, H., Duchaineau, M., and Abraham, F. F., 2004, "Atomic Plasticity: Description and Analysis of a One-Billion Atom Simulation of Ductile Materials Failure," *Computer Methods in Applied Mechanics and Engineering*, **193**(48) pp. 5257-5282.

[157] Nielsen, L. E., 1969, "Cross-Linking–effect on Physical Properties of Polymers."

[158] Pascault, J., and Williams, R., 1990, "Glass Transition Temperature Versus Conversion Relationships for Thermosetting Polymers," *Journal of Polymer Science Part B: Polymer Physics*, **28**(1) pp. 85-95.

[159] Couchman, P., and Karasz, F., 1978, "A Classical Thermodynamic Discussion of the Effect of Composition on Glass-Transition Temperatures," *Macromolecules*, **11**(1) pp. 117-119.

[160] Hexion Specialty Chemicals, Product Bulletin EPON Resin 863, (http://www.hexion.com/Products/TechnicalDataSheet.aspx?id=3958) .

[161] Fan, H. B., and Yuen, M. M., 2007, "Material Properties of the Cross-Linked Epoxy Resin Compound Predicted by Molecular Dynamics Simulation," *Polymer*, **48**(7) pp. 2174-2178.

[162] Sindt, O., Simon, S., McKenna, G., and Liang, E., 1998, "Cure, shrinkage and properties of an epoxy material," TECHNICAL PAPERS OF THE ANNUAL TECHNICAL CONFERENCE-SOCIETY OF PLASTICS ENGINEERS INCORPORATED, Anonymous SOCIETY OF PLASTICS ENGINEERS INC, **2,** pp. 1658-1662.

[163] Li, C., Medvedev, G. A., Lee, E., Kim, J., Caruthers, J. M., and Strachan, A., 2012, "Molecular Dynamics Simulations and Experimental Studies of the Thermomechanical Response of an Epoxy Thermoset Polymer," *Polymer*.

[164] Tack, J. L., and Ford, D. M., 2008, "Thermodynamic and Mechanical Properties of Epoxy Resin DGEBF Crosslinked with DETDA by Molecular Dynamics," *Journal of Molecular Graphics and Modelling,* **26**(8) pp. 1269-1275.

[165] Hexion Specialty Chemicals, Product Bulletin EPIKOTE Resin 862/ EPIKURE Curing Agent W System., (http://www.miller-stephenson.com/wp-content/uploads/2016/08/W.pdf) .

[166] Abràmoff, M. D., Magalhães, P. J., and Ram, S. J., 2004, "Image Processing with ImageJ," *Biophotonics International,* **11**(7) pp. 36-42.

[167] Bouvard, J., Francis, D. K., Tschopp, M. A., Marin, E., Bammann, D., and Horstemeyer, M., 2013, "An Internal State Variable Material Model for Predicting the Time, Thermomechanical, and Stress State Dependence of Amorphous Glassy Polymers Under Large Deformation," *International Journal of Plasticity,* **42**pp. 168-193.

[168] Tschopp, M., Bouvard, J., Ward, D., Bammann, D., and Horstemeyer, M., 2013, "Influence of Ensemble Boundary Conditions (Thermostat and Barostat) on the Deformation of Amorphous Polyethylene by Molecular Dynamics," *arXiv Preprint arXiv:1310.0728.*

[169] Hossain, D., Tschopp, M., Ward, D., Bouvard, J., Wang, P., and Horstemeyer, M., 2010, "Molecular Dynamics Simulations of Deformation Mechanisms of Amorphous Polyethylene," *Polymer,* **51**(25) pp. 6071-6083.

[170] Frankland, S., Harik, V., Odegard, G., Brenner, D., and Gates, T., 2003, "The Stress–strain Behavior of Polymer–nanotube Composites from Molecular Dynamics Simulation," *Composites Science and Technology,* **63**(11) pp. 1655-1661.

[171] Min, K., Silberstein, M., and Aluru, N., 2014, "Crosslinking PMMA: Molecular Dynamics Investigation of the Shear Response," *Journal of Polymer Science Part B: Polymer Physics,* **52**(6) pp. 444-449.

[172] Odegard, G. M., Jensen, B. D., Gowtham, S., Wu, J., He, J., and Zhang, Z., 2014, "Predicting Mechanical Response of Crosslinked Epoxy using ReaxFF," *Chemical Physics Letters,* **591**pp. 175-178.

[173] Berendsen, H. J., Postma, J. P. M., van Gunsteren, W. F., DiNola, A., and Haak, J., 1984, "Molecular Dynamics with Coupling to an External Bath," *The Journal of Chemical Physics,* **81**pp. 3684.

[174] Subramaniyan, A. K., and Sun, C., 2008, "Continuum Interpretation of Virial Stress in Molecular Simulations," *International Journal of Solids and Structures,* **45**(14) pp. 4340-4346.

[175] Agarwal, A., Zhu, J., Hartmann, C., Wang, H., and Delle Site, L., 2015, "Molecular Dynamics in a Grand Ensemble: Bergmann–Lebowitz Model and Adaptive Resolution Simulation," *New Journal of Physics,* **17**(8) pp. 083042.

[176] Wiberg, K. B., 1986, "The Concept of Strain in Organic Chemistry," *Angewandte Chemie International Edition in English,* **25**(4) pp. 312-322.

[177] Koo, B., Liu, Y., Zou, J., Chattopadhyay, A., and Dai, L., 2014, "Study of Glass Transition Temperature (Tg) of Novel Stress-Sensitive Composites using Molecular Dynamic Simulation," *Modelling and Simulation in Materials Science and Engineering,* **22**(6) pp. 065018.

[178] Tadmor, E. B., Ortiz, M., and Phillips, R., 1996, "Quasicontinuum Analysis of Defects in Solids," *Philosophical Magazine A,* **73**(6) pp. 1529-1563.

[179] Fratzl, P., 2008, "Collagen: structure and mechanics, an introduction," Springer.

[180] Zhurkov, S., Zakrevskyi, V., Korsukov, V., and Kuksenko, V., 1972, "Mechanism of Submicrocrack Generation in Stressed Polymers," *Journal of Polymer Science Part A-2: Polymer Physics,* **10**(8) pp. 1509-1520.

[181] Aboudi, J., Pindera, M., and Arnold, S. M., 2002, "High-Fidelity Generalization Method of Cells for Inelastic Periodic Multiphase Materials," *Paper no. NASA-TM-2002-211469.*

[182] Aboudi, J., Arnold, S.M., and Bednarcyk, B.A., 2012, "Micromechanics of composite materials: a generalized multiscale analysis approach," Butterworth-Heinemann.

[183] Johnston, J., and Chattopadhyay, A., 2015, "Effect of Material Variability on Multiscale Modeling of Rate-Dependent Composite Materials," *Journal of Aerospace Engineering,* pp. 04015003.

[184] Gupta, A., and Harsha, S., 2016, "Analysis of Mechanical Properties of Carbon Nanotube Reinforced Polymer Composites using Multi-Scale Finite Element Modeling Approach," *Composites Part B: Engineering,* **95**pp. 172-178.

[185] Zang, J., Yuan, Q., Wang, F., and Zhao, Y., 2009, "A Comparative Study of Young's Modulus of Single-Walled Carbon Nanotube by CPMD, MD and First Principle Simulations," *Computational Materials Science,* **46**(3) pp. 621-625.

[186] Humphrey, W., Dalke, A., and Schulten, K., 1996, "VMD: Visual Molecular Dynamics," *Journal of Molecular Graphics,* **14**(1) pp. 33-38.

[187] Bodner, S.R., 2002, "Unified plasticity for engineering applications," Springer Science & Business Media.

[188] Goldberg, R. K., Roberts, G. D., and Gilat, A., 2005, "Implementation of an Associative Flow Rule Including Hydrostatic Stress Effects into the High Strain Rate Deformation Analysis of Polymer Matrix Composites," *Journal of Aerospace Engineering*, **18**(1) pp. 18-27.

[189] Schapery, R., 1990, "A Theory of Mechanical Behavior of Elastic Media with Growing Damage and Other Changes in Structure," *Journal of the Mechanics and Physics of Solids*, **38**(2) pp. 215-253.

[190] Pineda, E. J., Waas, A. M., Bednarcyk, B. A., Collier, C. S., and Yarrington, P. W., 2009, "Progressive Damage and Failure Modeling in Notched Laminated Fiber Reinforced Composites," *International Journal of Fracture*, **158**(2) pp. 125-143.

[191] Johnston, J., and Chattopadhyay, A., 2015, "Effect of Material Variability on Multiscale Modeling of Rate-Dependent Composite Materials," *Journal of Aerospace Engineering*, **28**(6) pp. 04015003.

[192] Zhu, L., Chattopadhyay, A., and Goldberg, R. K., 2008, "Failure Model for Rate-Dependent Polymer Matrix Composite Laminates Under High-Velocity Impact," *Journal of Aerospace Engineering*, **21**(3) pp. 132-139.

[193] Hashin, Z., 1980, "Failure Criteria for Unidirectional Fiber Composites," *Journal of Applied Mechanics*, **47**(2) pp. 329-334.

[194] Maligno, A., Warrior, N., and Long, A., 2009, "Effects of Inter-Fibre Spacing on Damage Evolution in Unidirectional (UD) Fibre-Reinforced Composites," *European Journal of Mechanics-A/Solids*, **28**(4) pp. 768-776.